

Plasma deposition of carbon materials

Citation for published version (APA):

Buuron, A. J. M. (1993). *Plasma deposition of carbon materials*. [Phd Thesis 1 (Research TU/e / Graduation TU/e), Applied Physics and Science Education]. Technische Universiteit Eindhoven.
<https://doi.org/10.6100/IR405971>

DOI:

[10.6100/IR405971](https://doi.org/10.6100/IR405971)

Document status and date:

Published: 01/01/1993

Document Version:

Publisher's PDF, also known as Version of Record (includes final page, issue and volume numbers)

Please check the document version of this publication:

- A submitted manuscript is the version of the article upon submission and before peer-review. There can be important differences between the submitted version and the official published version of record. People interested in the research are advised to contact the author for the final version of the publication, or visit the DOI to the publisher's website.
- The final author version and the galley proof are versions of the publication after peer review.
- The final published version features the final layout of the paper including the volume, issue and page numbers.

[Link to publication](#)

General rights

Copyright and moral rights for the publications made accessible in the public portal are retained by the authors and/or other copyright owners and it is a condition of accessing publications that users recognise and abide by the legal requirements associated with these rights.

- Users may download and print one copy of any publication from the public portal for the purpose of private study or research.
- You may not further distribute the material or use it for any profit-making activity or commercial gain
- You may freely distribute the URL identifying the publication in the public portal.

If the publication is distributed under the terms of Article 25fa of the Dutch Copyright Act, indicated by the "Taverne" license above, please follow below link for the End User Agreement:

www.tue.nl/taverne

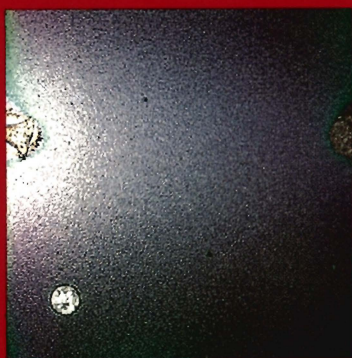
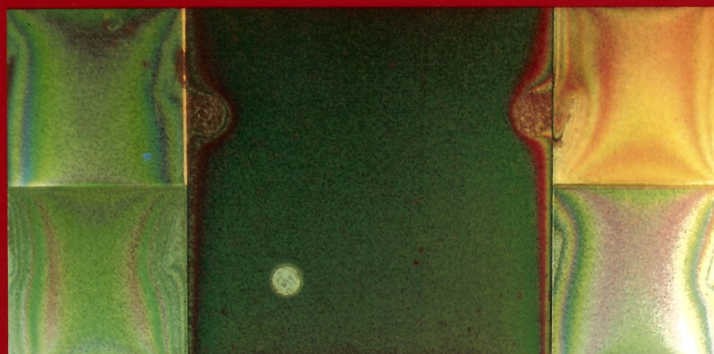
Take down policy

If you believe that this document breaches copyright please contact us at:

openaccess@tue.nl

providing details and we will investigate your claim.

PLASMA DEPOSITION OF CARBON MATERIALS



A.J.M. Buuron

PLASMA DEPOSITION OF CARBON MATERIALS

PROEFSCHRIFT

ter verkrijging van de graad van doctor aan de
Technische Universiteit Eindhoven, op gezag van de
Rector Magnificus, prof. dr. J.H. van Lint, voor een commissie
aangewezen door het College van Dekanen in het openbaar te
verdedigen op vrijdag 1 oktober 1993 om 16.00 uur

door

Adrianus Jacobus Maria Buuron

geboren te Roosendaal



Dit proefschrift is goedgekeurd
door de promotoren

prof. dr. ir. D.C. Schram
en
prof. dr. M.J.A. de Voigt

co-promotor
dr. ir. M.C.M. van de Sanden

Errata

On page	expression	should be
31, 32	two orientations: as a CFC or as CFC _⊥	two orientations: as a CFC or as CFC _⊥
41, 43	CFC	CFC
59	$\frac{\dots f_{ki}}{4\epsilon_0 \dots}$ (4.10) $4\epsilon_0 \dots$ (4.12)	$\frac{\dots f_{ik}}{4\epsilon_0 \dots}$ (4.10) $\epsilon_0 \dots$ (4.12)
70	$A_m = \dots$ (4.27)	$-A_m = \dots$ (4.27)
82	<i>Figure 4.11 (c) s₄ radial density profiles of Fig. (a)</i>	<i>Figure 4.11 (c) 4s radial density profiles of Fig. 4.15</i>
88	$\Lambda(k\bar{R}) = \frac{\sqrt{\ln 2}}{k_L \bar{R} \sqrt{\pi}} = \dots$ $\frac{\Delta \lambda_L}{\Delta \lambda_D} \leq \frac{100}{k\bar{R}}$ $\Delta \nu_L = \frac{1}{2\pi\tau} = \frac{A}{2\pi\nu}$ $\Lambda(k\bar{R}) = \sqrt{\frac{2g_p}{g_q n_p \lambda_{qp}^2} \mu R}$	$\Lambda(k\bar{R}) = \frac{\sqrt{\ln 2}}{k_L \bar{R} \sqrt{\pi}} = \dots$ $\frac{\Delta \lambda_L}{\Delta \lambda_D} \geq \frac{100}{k\bar{R}}$ $\Delta \nu_L = \frac{1}{2\pi\tau} = \frac{A}{2\pi}$ $\Lambda(k\bar{R}) = \sqrt{\frac{2g_p}{g_q n_p \lambda_{qp}^2} \mu R}$
94	For K_4 no data are available. K'_4	For K_2 no data are available. K'_2
97, 98 (,54)	chamber pressure of 10^3 Pa in $58 \text{ cm}^3 \text{ s}^{-1}$ argon	chamber pressure of 10^2 Pa in $100 \text{ cm}^3 \text{ s}^{-1}$ argon
100	ref. [18]	ref. [7]
139	$\chi^2 = \frac{1}{N} \sum_{i=1}^N (a_i^{\text{exp}} - a_i^{\text{calc}})^2 - \dots$	$\chi^2 = \frac{1}{N} \sum_{i=1}^N (a_i^{\text{exp}} - a_i^{\text{calc}})^2 + \dots$
147, 157	$d(\mu\text{m})$	$d(\text{nm})$
151	15 nm s^{-1}	1 nm s^{-1}
155	E9, H2 and F2	E9, H2 and F1
173	CF ₄ , C ₂ H ₂ , CF ₄ , ...	CH ₄ , C ₂ H ₂ , CF ₄ , ...

Aan mijn ouders

Front page: Photographs of carbon coated steel substrates.

Contents

1	General introduction	1
2	Thick carbon deposition by cascaded arcs	7
	Abstract	7
2.1	Introduction	8
2.2	Experimental configuration	9
2.3	Different types of carbon deposits	11
	2.3.1 a-C:H films	12
	2.3.2 Diamond	13
2.4	Graphite deposition	15
	2.4.1 Specific experimental data	16
	2.4.2 Results and discussion	17
	Conclusions	22
	Acknowledgement	23
	Bibliography	23
3	Plasma deposited carbon films as a possible means for divertor repair	25
	Abstract	25
3.1	Introduction	26
3.2	Design of the next step fusion reactors	27
3.3	Carbon deposition by an expanding cascaded arc plasma	28
	3.3.1 The expanding cascaded arc set-up	28
	3.3.2 Deposition conditions and materials	30
3.4	Diagnostics	33
	3.4.1 Raman spectroscopy set-up	33
	3.4.2 Set-up for thermal shock experiments	33
3.5	Results and discussion	35
	3.5.1 Introduction	35
	3.5.2 Morphology and crystallinity of the coatings; hydrogen admixture, the principal determining factor.	35

3.5.3	Macroscopic properties of the films: appearance, cohesion and adhesion, density	37
3.5.4	Relations of the Raman spectra parameters and the thermal shock resistance with the deposition conditions.	39
3.5.5	Summary and evaluation of the results of the diagnostics	43
3.5.6	Growth rate and efficiency considerations.	45
3.5.7	Qualitative study of thermal shock damage	47
3.5.8	Diamond conditions	48
3.6	Conclusions	49
	Acknowledgement	50
	Bibliography	51
4	Absorption spectroscopy on the expanding cascaded arc plasma jet	53
	Abstract	53
4.1	Introduction	54
4.2	General description of absorption spectroscopy	55
4.2.1	Techniques of absorption spectroscopy	55
4.2.2	Absorption coefficient of spectral lines	57
4.2.3	Spectral line shapes and broadening mechanisms	59
4.2.4	Total absorption of spectral lines	61
4.2.5	Measurement and data analysis techniques in the case of spatially inhomogeneous absorbing media	63
4.3	Experimental	64
4.3.1	The cascaded arc set-up for deposition	64
4.3.2	The spectroscopic set-up	66
4.3.3	Measurement conditions	70
4.3.4	Treatment of experimental data	73
4.4	Results and discussion	79
4.4.1	Absolute density of the Ar($3p^5 4s$) states in a pure argon plasma	79
4.4.2	Absolute density of Ar($3p^5 4s$) states in plasmas used for carbon deposition	91
4.4.3	Density of H($2s$) states in an argon/hydrogen plasma	97
4.5	Conclusions	98
	Acknowledgement	99
	Bibliography	99
5	Diamond deposition by an expanding cascaded arc plasma	103
	Abstract	103
5.1	Introduction	104

5.2	Structure and properties of diamond	105
5.3	Diamond nucleation and growth	106
5.4	Experimental set-up	111
5.5	Raman Spectroscopy	112
5.5.1	Introduction	112
5.5.2	Theory of the Raman effect	113
5.6	Results and discussion	117
5.6.1	Deposition conditions	117
5.6.2	Crystallinity, morphology and deposition rate of the deposited diamond	118
5.7	Conclusions	130
	Acknowledgement	131
	Bibliography	131
6	Fast deposition of amorphous hydrogenated carbon by an expanding cascaded arc plasma	135
	Abstract	135
6.1	Introduction	136
6.2	Techniques and evaluation methods for analysis of the optical properties of the films	137
6.2.1	Spectroscopic ellipsometry	137
6.2.2	Infrared absorption spectroscopy	139
6.3	Experimental	141
6.3.1	The expanding cascaded arc set-up for deposition	141
6.3.2	Adhesion improvement by pretreatment	142
6.3.3	Diagnostic arrangements	143
6.4	Results and discussion	146
6.4.1	The optical parameters	146
6.4.2	The H/C and O/C ratio	154
6.4.3	The application of a-C:H layers for anti-corrosion protection	157
	Acknowledgement	164
	Conclusions	165
	Bibliography	166
	Summary	169
	Samenvatting	172
	Dankwoord	175
	Curriculum vitae	177

Chapter 1

General introduction

The element carbon occurs in various appearances ('allotropes'), each of these with a number of useful properties, such as a high hardness, low friction coefficients, chemical inertness, biocompatibility, and (in some forms) a high thermal conductivity and/or optical transparency. Compared to other elements or compounds with comparable properties, carbon has the additional property that it is not poisonous and, not detrimental to the environment. Over the last decades the research on the synthetic production of carbon materials, particularly in the shape of thin films, has grown explosively. Initially, the common techniques for depositing thin films of a material on a substrate were Chemical Vapour Deposition (CVD) and the hot filament technique. In these methods a carbon containing gas is dissociated by a hot substrate or a hot filament respectively, leading to the deposition of carbonaceous materials on the substrate. In the last decades, with the advance of plasma techniques, this method has largely been replaced by Plasma Enhanced Chemical Vapour Deposition (PECVD), in which the dissociation of the feed gas is promoted by electronic impact. Initially, plasmas like radio-frequency (RF) and direct current (DC) glow discharges were employed. Gradually reactors using various types of plasmas, among others microwave cavities and magnetrons were adapted for deposition purposes. Most methods have the drawback that the transport of the active particles occurs by diffusion, resulting in limited deposition rates of maximum up to about 10 μm per hour (for amorphous carbon). The most recent development is the employment of expanding plasma jets. In these methods, the convective transport of particles to the substrate results in deposition rates which are higher by orders of magnitude. As a source, mostly a DC arc, an acetylene-oxygen flame or an Inductively Coupled Plasma (ICP) is used. In the group Equilibrium and Transport in Plasmas (ETP) of the Department of Physics of the Eindhoven University of Technology, a flowing cascaded arc is used as a particles source. In this type of arc, a plasma is generated in a channel, composed of a number of annular plates, the arc being

stabilized by the water cooled channel walls. The power dissipation is relatively high, typically of the order of 5 kW, and the carrier gas argon is flowing at a high rate of typically $100 \text{ standard cm}^3\text{s}^{-1}$. The main feature of a technique like this is that the three functions, production, transport and deposition are spatially separated and the optimization of these functions can occur more or less independently. Besides for carbon deposition, this technique is also in use for fast deposition of amorphous hydrogenated silicon for solar cell applications [1]. In Fig. 1.1 an outline of the deposition reactor is shown. For carbon deposition, a hydrocarbon is admixed in the argon carrier gas, and by charge exchange and dissociative recombination a plasma of excited and ionized carbon and hydrocarbon particles is created. The anode side of the arc is connected to a vacuum vessel in which the arc plasma expands towards a substrate, where the deposition of different types of carbon occurs.

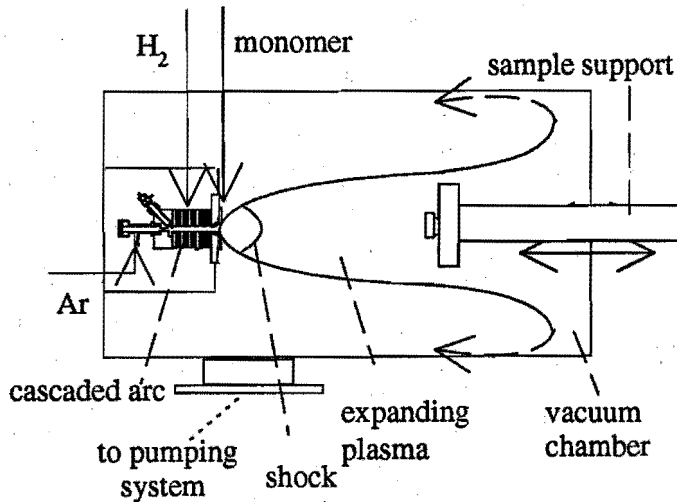


Figure 1.1: Outline of the deposition reactor.

Depending on reactor and substrate parameters, various forms of carbon can be deposited from amorphous carbon to the crystalline forms graphite and diamond. A specific carbon allotrope is characterized by the prevalent bonding type in the bulk material. Carbon has four valence electrons, two in the $2s$ -subshell and two in the $2p$ -subshell. The wave functions of the electrons can overlap in various degrees, and form three hybrid states, denoted as sp^3 , sp^2 and sp^1 hybridization.

Examples of the resulting bonding types are the diamond bonding, the graphitic bonding and the carbyne bonding respectively. The sp^1 bonding type can be found in polymers, and is only of limited importance in the present work.

Graphite is an example of sp^2 hybridization, with three strong σ bonds (bond energy 7.43 eV [2]) and one weaker and delocalized π bond. The structure is shown in Fig. 1.2 (a). The strong σ bonds are trigonally directed in one plane, leading to planes with two-dimensional hexagonal configurations, the basal planes. Bulk graphite consists of a stacking of these planes, with a weak interplanar bonding (energy 0.86 eV). This structure explains the anisotropic properties of graphite.

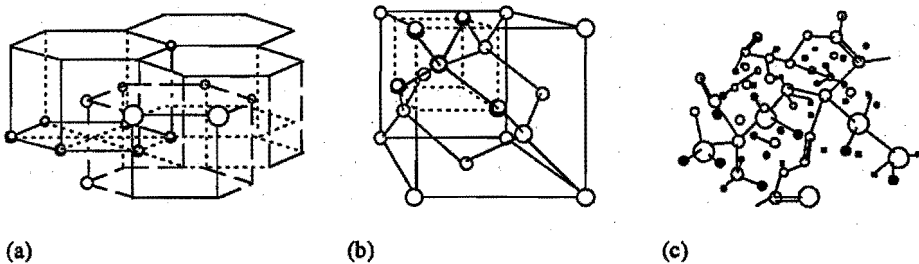


Figure 1.2: Schematic representation of the structure of (a) graphite, (b) diamond and (c), with hydrogen depicted by the solid symbols, a-C:H.

Within the plane the electrons of the π bonding types are more or less free, and lead to the metallic behavior of a high electrical and thermal conduction in the planes. Between the planes the conductive properties are poor, the bonding is weak, leading to the practical applications of graphite like in pencils and as a lubricant. A particular carbon form based on the sp^2 bonding type are the recently discovered Buckminster fullerenes ('bucky-balls') [3]. Up to now, the presence of this form of carbon could not be demonstrated in the films deposited with the expanding cascaded arc. As the practical relevance of this carbon allotrope is still limited, no specific research has been done on depositing this form of carbon.

In this thesis the thermoconductive and thermomechanical properties of plasma deposited graphite are studied for a novel application: The protection against and repair of erosion damage on the plasma exposed components of future fusion reactors. This project is treated in Chapter II and III of this thesis. These chapters have also been published in *Fusion Technology* 19 (1991) 2049, and *Thin Solid Films* 212 (1992) 282 respectively.

The sp^3 hybridization leads to four equivalent, strong σ -bondings in a tetrahedral configuration, the diamond bonding, with a C-C bond energy of 7.41 eV

[2]. In Fig. 1.2 (b) the structure of the resulting diamond crystal is shown. The structure is Face Centered Cubic (FCC), with a cubic unit cell. Macroscopically, a number of crystal types occur, ranging from purely cubic to octahedral, depending on the conditions during the formation of the diamond. Diamond has a high optical band gap and is extremely hard. Applications of diamond films can be found in the tribologic field, as wear resistant and low friction coatings, and in the IC technology, as insulating layers and as a heat sink. Plasma deposited films of diamond are in general polycrystalline which limits their practical application for optical purposes. Depositing a monocrystalline (epitaxial) film on a non-diamond substrate is a worldwide issue, unsolved up-to-date. The solving of this problem is also out of the scope of this thesis. The present work, presented in Chapter V of this thesis, was primarily aimed at further optimizing the deposition of diamond films with the expanding cascaded arc technique.

An increasingly important branch of the carbon materials is the group of the amorphous hydrogenated carbon (a-C:H) materials. In Fig. 1.2 (c) the structure of a-C:H is shown. All three bonding types are present, and the structure can be considered as a random network of graphitic and diamondlike bondings, with hydrogen saturation of the dangling bonds. The amount of sp^1 bondings is mostly small. The properties of a-C:H are mainly determined by the ratio of the amount of sp^3 and sp^2 bonds, and the hydrogen content. With increasing sp^3/sp^2 ratio and decreasing hydrogen content, the material changes from soft, polymer-like to hard diamond-like. Particularly diamond-like carbon (DLC) has properties resembling those of diamond, such as a high hardness, low friction coefficients and chemical inertness. In contrast to the polycrystalline diamond films, a-C:H films are smooth, which makes them more suited for optical applications. This typical combination of properties makes the importance of a-C:H films comparable, and in some fields complementary, to that of diamond films. In Chapter VI of this thesis the field of the deposition of a-C:H layers with the expanding cascaded arc method is further explored and optimized. As an application the anti-corrosion performance of plasma-deposited amorphous carbon layers was investigated. In Table 1.1 some important properties of the three types of carbon under investigation are summarized.

In the past, extensive studies have already been carried out on the arc plasma, the expanding plasma and the reactor parameters for deposition. Extensive theoretical modelling has been carried out, and by means of Thomson and Rayleigh scattering experiments [4, 5] and emission spectroscopy [6, 7, 8] temperatures and densities of species present in the expanding plasma jet have been determined. An issue in the plasma deposition is the role of metastables in energy transfer processes to the hydrocarbon feed gas. In this thesis, using absorption spectroscopy, densities of the argon $4s$ metastables, which are not observable in emission, are

presented. The theory and the results of the absorption spectroscopy are addressed in Chapter IV.

Table 1.1: *Room-temperature electrical conductivity σ_{RT} , thermal conductivity λ_c , optical band gap E_g , density and hardness of diamond, graphite (in-plane) and a-C:H (adopted from [9, 10, 11])*

	σ_{RT} ($\Omega^{-1}\text{cm}^{-1}$)	λ_c ($\text{W m}^{-1}\text{K}^{-1}$)	E_g (eV)	density (g cm^{-3})	hardness (kg mm^{-2})
diamond	10^{-18}	800	5.5	3.515	10^4
graphite	$2.5 \cdot 10^4$	1600-2000	-0.04	2.267	-
a-C:H	$10^{-7}-10^{-16}$	<100	1-4	1.3-2.4	1250-6000

The structure of this thesis reflects the progress of the research on the deposition of carbon in the course of time. Each chapter can be regarded as the result of a more or less independent study, and can also be read independently from the others. This structure has been chosen aimed at a systematic presentation of the papers which were already published (Ch. II and III), and of the other results in the approximate shape in which they will be submitted for publication.

Bibliography

- [1] G.J. Meeusen *et al.*, *9th Int. Coll. on Plasma Processes CIP 93, Antibes (France), june 6-11 1993*, la Groupe de Recherche 57 du CNRS & Société Francaise du Vide, Paris, 99, (1993).
- [2] J. Mort and F. Jansen (eds.), *Plasma Deposited Thin Films*, CRC Press, Inc., Boca Raton, Florida, (1986).
- [3] H.W. Kroto, J. R. Heath, S.C. O'Brien, R.F. Curl and R.E. Smalley, *Nature*, **318**, 162, (1985).
- [4] M.C.M. van der Sanden, *Ph. D. thesis*, Eindhoven University of Technology, (1991).
- [5] M.C.M. van de Sanden, G.M. Janssen, J.M. de Regt, D.C. Schram, J.A.M. van der Mullen and B. Van der Sijde, *Rev. Sci. Instrum.*, **63** (6), 3369, (1992).
- [6] G.M.W. Kroesen, *Ph.D. Thesis*, Eindhoven University of Technology, (1988).
- [7] J.J. Beulens, *Ph. D. thesis*, Eindhoven University of Technology, (1991).
- [8] J.J. Beulens, C. Gastineau, N. Guerassimov, J. Koulidiati and accepted for publication in D.C. Schram, *Plasma Chem. Plasma Process*, febr (1993).
- [9] J. Robertson, *Adv. Phys.*, **35** (4), 317, (1986).
- [10] P.L. Walker and P.A. Thrower (eds.), *Chemistry and Physics of Carbon; A Series of Advances, Vol. 11*, Marcel Dekker, New York, (1984).
- [11] B. Dischler, A. Bubenzer and P. Koidl, *Appl. Phys. Lett.*, **42** (8), 636, (1983).

Chapter 2

Thick carbon deposition by cascaded arcs ¹

A.J.M. Buuron, J.J. Beulens, M.J.F. v.d. Sande
and D.C. Schram

*Eindhoven University of Technology, Dept. of Physics
5600 MB Eindhoven, The Netherlands.*

J.G. v.d. Laan

*Netherlands Energy Research Foundation, ECN, 1755 ZG Petten, The
Netherlands.*

abstract

An expanding cascaded arc plasma is used for the deposition of different types of carbon layers at high growth rates. In the past amorphous hydrogenated carbon films have been deposited at rates of up to 200 nm s^{-1} on areas of about 100 cm^2 . Single diamond crystals of $60 \mu\text{m}$ and $25\text{-}\mu\text{m}$ -thick continuous films were deposited within one hour on areas of $\sim 3 \text{ cm}^2$. In recent experiments pyrolytic graphite films have been deposited. The film type and growth rate depend on the choice of the optimum reactor parameter settings. To maximize the growth rate and crystallinity of the film, the reactor settings are varied. High growth rates (maximum of 762 nm s^{-1}) have been obtained at high temperatures ($600\text{-}1000 \text{ }^\circ\text{C}$). Films of up to $200 \mu\text{m}$ thick have been produced within 20 minutes on an area of $\sim 12 \text{ cm}^2$. Several diagnostic techniques are used to analyze the films. The purity of the films has been confirmed by means of Auger electron spectroscopy.

¹This article has been published in *Fusion Technol.* 19 (1991) 2049

2.1 Introduction

During the last decades, many different types of discharges have been used in the field of plasma surface modification, etching and deposition. The most current method is the application of a low-pressure radio-frequency or DC glow discharge [1]. In this method, the substrate is immersed in an argon/hydrocarbon plasma and the deposition process is governed by diffusion. The deposition rates are relatively low, of the order of $1\text{-}20\ \mu\text{m h}^{-1}$.

In 1981 the flowing cascaded arc was introduced as a powerful particle source [2]. A hydrocarbon gas can effectively be dissociated in CH radicals and in excited and ionized carbon particles. Combined with the supersonic expansion of the plasma into a vacuum chamber toward the substrate, deposition rates of hundreds of nanometers per second have been reached for amorphous hydrogenated carbon films (a-C:H films). The main feature of the method is the separation of the three functions of production, transport, and deposition. The type, quality and growth rate of the films can be controlled by variation of the reactor parameters. The growth rate can be raised by increasing the flux of active particles on the substrate, e.g. by increasing the arc power. With this configuration, very high growth rates ($200\ \text{nm s}^{-1}$) have been reached for amorphous carbon films at low substrate temperatures ($20\text{-}100\ ^\circ\text{C}$) with argon/CH₄ and argon/C₂H₂ plasmas (ratio typically 100/1, flow rates in cm^3s^{-1}). For higher deposition temperatures and with addition of H₂ to the gas flow, the growth rate is strongly reduced [3, 4]. Diamond films have been deposited at $1000\ ^\circ\text{C}$ in an argon/hydrogen/methane environment (ratio 20/20/0.2) at a rate of $\sim 10\ \text{nm s}^{-1}$. The main factors determining the crystallinity of the film are the substrate temperature and the amount of hydrogen admixture in the argon flow.

The growth rate, the refractive index and the thickness of the film are monitored *in situ*, with helium-neon (He-Ne) ellipsometry [2]. *Ex situ*, the layers are analyzed by a number of techniques. Ultraviolet-visible-infrared spectroscopic ellipsometry [5] gives information on the band gap, the absorption bands (presence and type of carbon-hydrogen bonds) and the refractive index. Raman scattering is applied to determine the carbon-carbon bond type and the degree of crystallinity in the film. Information on the morphology is also obtained by scanning electron microscopy (SEM). Additional techniques are electron spectroscopy for chemical analysis to determine the type of film, Rutherford back scattering to determine hydrogen content and depth profile, low energy electron diffraction to determine crystallinity, and Auger electron spectroscopy to determine impurities.

In a joint effort among Eindhoven University of Technology, the Netherlands Energy Research Foundation and the Next European Torus (NET) team, a fea-

sibility study is being performed on the possibility of *in situ* repair of erosion damage on divertor plates in NET [6] by means of fast carbon deposition by a cascaded arc. Graphitic or diamond-like layers may be particularly suitable candidates, because of their high thermal conductivity and shock resistance and their mechanical strength. Deposition experiments with a variety of plasma and deposition parameter settings have been carried out based on the experience acquired during the amorphous carbon and diamond deposition experiments. A brief survey of these earlier projects is given first.

2.2 Experimental configuration

Fig. 2.1 shows a schematic of the arc. The arc consists of three cathodes, a stack of ten insulated copper plates, and an end plate with a ring shaped copper anode, the nozzle. Only one cathode is shown in Fig. 2.1; the other two are situated circumferentially at 120-deg angles to each other. The components are all water cooled. The cathodes are 1 mm diameter tungsten thorium tips for currents up to 30 A/cathode. The cascade plates have a 4-mm inner bore and are 5 mm thick. Together with the 1-mm-thick insulation plates, they form a 60-mm-long plasma channel. The carrier gas argon is injected at a pressure of 0.5 bar at the beginning of the arc channel at room temperature at a flow rate of typically $100 \text{ cm}^3\text{s}^{-1}$. The electron temperature is approximately constant in the axial direction and is $\sim 15\,000 \text{ K}$ for standard operating conditions (arc current of 50 A, argon flow rate of $100 \text{ cm}^3\text{s}^{-1}$). The heavy particle temperature reaches a value of about $12\,000 \text{ K}$ in the middle of the arc channel and decreases slightly again toward the exit of the channel [7]. The ionization degree is typically about $\sim 10\%$, rendering an electron density in the order of 10^{22} m^{-3} . Hydrogen can be added in the middle of the channel. To prevent obstruction of the arc channel by graphite formation, the monomer gas is injected through the nozzle at the end of the anode. The condition of the cathodes can be inspected through the viewing port.

The position of the cascaded arc in the vacuum chamber is shown in Fig. 2.2. A movable sample support, with an additional sample pedestal is mounted opposite the arc. The plasma mixture is extracted into the vacuum vessel. Consequently, a beam of ions and electrons (10%), atoms and radicals (argon, carbon, hydrogen and CH) emerges, directed toward the substrates on the sample support. A carbon ion flux of typically 8.10^{18} s^{-1} is obtained through charge exchange with the argon ions [2]. Three regions can be distinguished in this expanding beam, a region of supersonic expansion, a shock region and a subsonic expansion region. In the past model calculations and measurements [2, 8] have been carried out on the plasma parameters in these regions, using the reactor settings

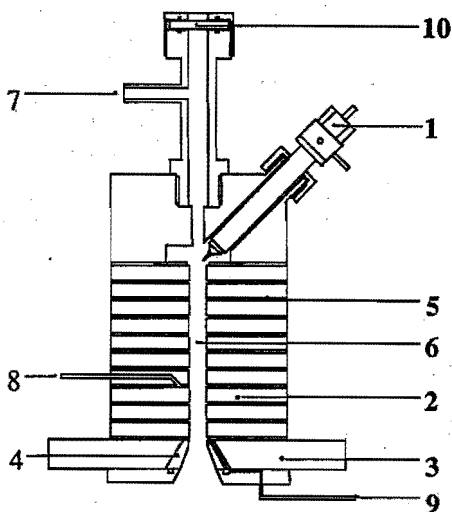


Figure 2.1: Schematic of the cascaded arc: (1) cathode, (2) copper plate, (3) end plate, (4) nozzle, (5) insulation plate, (6) plasma channel, (7) argon injection site, (8) hydrogen injection site, (9) monomer injection site, and (10) viewing port.

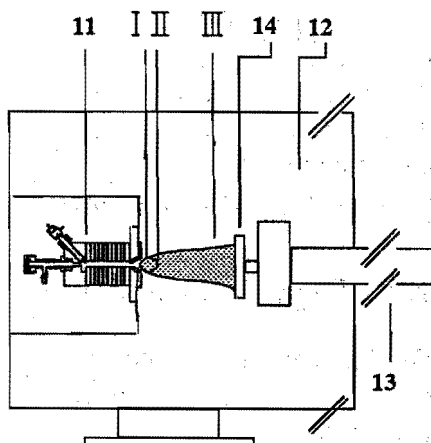


Figure 2.2: Schematic of the deposition reactor: (11) position of the arc in the vacuum chamber, (12) vacuum chamber, (13) movable sample support, and (14) sample pedestal. I: supersonic expansion region; II: shock region; III: subsonic expansion region.

summarized above. In region I, the particles are accelerated to supersonic velocities (~ 4000 m/s). During this expansion the electron and the heavy particle temperatures decrease to ~ 4000 K, and the electron density decreases strongly to the order of 10^{19} m^{-3} . At a distance of about 10 cm from the nozzle (depending on the chamber pressure) a shock (region II) exists. The temperatures and the electron density rise again to about 8000 K and typically 10^{20} m^{-3} respectively. Beyond the shock (region III) the plasma expands subsonically and the plasma composition remains constant ("frozen"). The temperatures drop to values in the range of 2000 to 4000 K.

The particles are transported further toward the substrate at subsonic velocities. More recent measurements [9], have shown that the subsequent changes in the temperatures in the respective regions are less explicit when the reactor settings are different. With an arc current of 45 A, an argon flow of 3.5 l min^{-1} and a chamber pressure of 40 Pa the temperatures drop to ~ 2500 K in the supersonic expansion region, rise to ~ 3500 K in the shock and decrease again in the subsonic region, to values of the order of 2000 K at 50 cm from the nozzle.

On the addition of the monomer gas cooling of the plasma takes place and

the power and flow settings should be adjusted to prohibit "overloading", i.e. incomplete dissociation of the monomer into active CH and carbon species. A typical value for the monomer flow is 1% of the argon flow. The chamber pressure is variable from 1 to 10^4 Pa, the nozzle to sample distance from 2 to 80 cm. More information on the cascaded arc, the reactor and the expanding plasma can be found elsewhere [2, 8, 10, 11].

2.3 Different types of carbon deposits

As pointed out earlier, there is a direct relationship between the different reactor settings and type and growth rate of the film. To characterize this relationship the following parameters (and definitions) are of interest:

- | | | |
|---|--|---|
| 1. The power flow product P | $P = \text{arc power} \times \text{argon flow rate}$ | $(\text{W} \cdot \text{cm}^3 \text{ s}^{-1})$ |
| 2. The hydrocarbon flow rate | $\{\text{C}_x\text{H}_y\}$ | $(\text{cm}^3 \text{ s}^{-1})$ |
| 3. The type of hydrocarbon | $\text{CH}_4, \text{C}_2\text{H}_2 \text{ or } \text{C}_7\text{H}_8$ | |
| 4. The inverse power factor Q | $Q = \text{carbon flow rate}/P$ | (W^{-1}) |
| 5. The hydrogen flow rate, expressed as the hydrogen-carbon ratio | (H/C) | |
| 6. The chamber pressure | p_c | (Pa) |
| 7. The substrate temperature | T_s | $(^\circ\text{C})$ |
| 8. The nozzle to sample distance | d_{n-s} | (cm) |

The growth rate is a function of all of these parameters. For the film type, parameters 4, 5, and 7 are of particular interest. This dependence may be summarized in Fig. 2.3. The inner part of the triangle represents the whole spectrum of possible a-C:H compounds. With an increasing H/C ratio in the beam and an increasing substrate temperature, the hydrogen content in the film tends toward zero, resulting in the limiting cases of graphite and diamond. The hydrogen radicals in the beam etch away hydrogen atoms from carbon-hydrogen bonds. Under specific conditions, the radicals etch graphitic carbon-carbon bonds so that diamond may be obtained. In the opposite case of a low substrate temperature and no hydrogen admixture highly polymer-like films with a high hydrogen content ($> 40\%$) can be deposited.

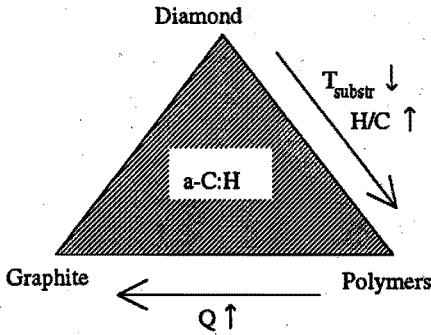


Figure 2.3: Relationship between film type and deposition parameters. In this figure H/C indicates the film H/C ratio.

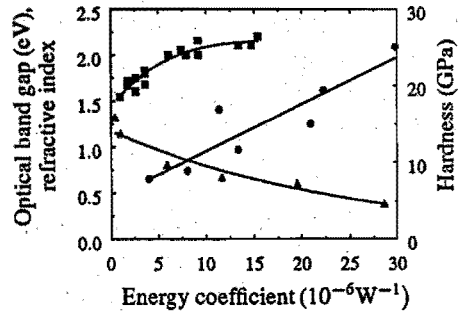


Figure 2.4: Optical band gap \blacktriangle , hardness \bullet , and refractive index \blacksquare of a-C:H films as a function of the inverse power factor Q . (Adapted from [2].)

The reactor settings for some specific deposits are summarized in Table 2.1. The values for graphite should be considered as indications based on experiences acquired during the diamond deposition experiments [4].

Table 2.1: Typical Parameter Settings for a-C:H, Diamond, and Graphite Deposition

	a-C:H		diamond	graphite
Argon flow rate	(cm^3s^{-1})	100.	20.	100-150
Monomer flow rate	(cm^3s^{-1})	1.8	0.2	1-8
Molecular hydrogen flow rate	(cm^3s^{-1})	0.	20.	0-15
Arc current	(A)	50.	35.	35-50
Arc voltage	(V)	88.	110.	74-100
Arc power	(kW)	4.4	3.85	2.5-5
Q	(10^{-6}W^{-1})	4.1	2.6	> 4
H/C	ratio	0.	100.	< 5
T_s	($^{\circ}\text{C}$)	20.	1000.	400-800
d_{n-s}	(cm)	80.	5.	20-40
p_c	(Pa)	10^2 .	$6 \cdot 10^3$.	10^2 - 10^3

2.3.1 a-C:H films

In Fig. 2.4 some of the properties of a-C:H films, obtained at room temperature, are shown as a function of Q . Steel samples with a thin ($2 \mu\text{m}$) gold layer

were used as a substrate. This facilitates monitoring of the refractive index and the film thickness by *in situ* He-Ne ellipsometry [5]. The optical band gap was determined using spectroscopic ellipsometry determined by way of a Tauc plot [2]. Furthermore, the presence of hydrogen in CH₂ and CH₃ binding forms was also observed from the carbon-hydrogen absorption bands. The total hydrogen content was estimated to be in the 10 to 60% range for films with refractive indexes ranging from 1.3 to 2.2. The hardness of the films increases strongly with an increasing value of Q , from 400 Vickers for polymer-like- to 5000 for diamond-like films [11]. It can be noted that for graphite deposition (band gap 0 eV, refractive index 2.18) the Q factor may have to be high.

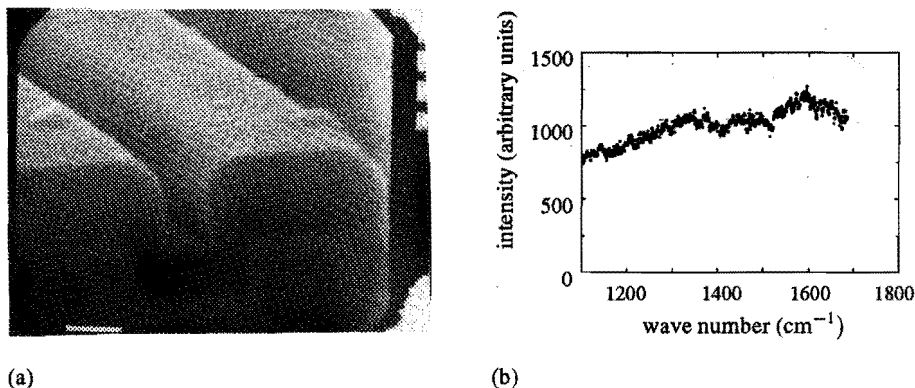


Figure 2.5: (a) SEM image of trenches filled with an a-C:H film (1 bar corresponds to 1 μm) and (b) Raman spectrum of the film.

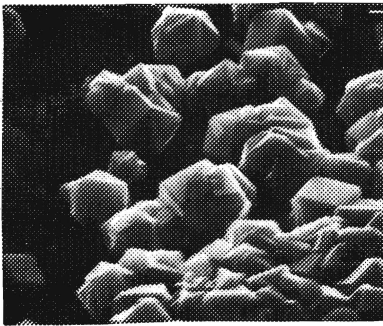
The maximum deposition rate achieved is 200 nm s⁻¹ on an area of ~ 100 cm². The film morphology as shown in Fig. 2.5 (a) does not reveal any distinct features. The Raman spectrum (Fig. 2.5 (b)) exhibits the typical continuous bulk signal for a film of non-crystalline nature [12].

2.3.2 Diamond

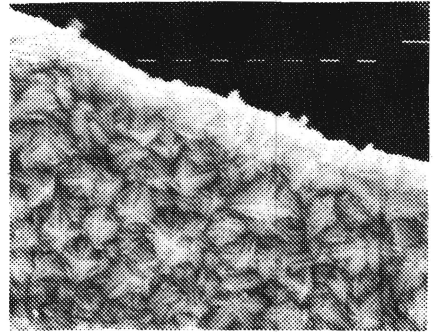
In the past, diamond single crystals and films were produced in a collaborative effort with Philips Aachen [4]. The deposition conditions used are given in Table 2.1. Three-inch silicon wafers were used as the substrate. The substrate was heated by the plasma beam itself. The substrate temperature was monitored with an optical pyrometer. Without special pretreatment of the surface faceted individual crystals of 15 to 25 μm , (up to a maximum of 65 μm) were deposited

within 1 h (Fig. 2.6 (a)). If the substrate surface is pretreated by scratching with diamond powder ($1\ \mu\text{m}$ particles) continuous diamond films were grown on an area of about $3\ \text{cm}^2$ (Fig. 2.6 (b)). The number of nucleation sites is strongly increased in this case as a consequence of surface roughness.

For the individual crystals as well as for the continuous film, the structures are well faceted only in the center of the deposit. Raman spectroscopy reveals that, in both cases, the morphology changes from diamond to graphitic ball-shaped and amorphous structures towards the edges of the substrate. This is caused by a combination of three factors: a reduced substrate temperature near the edge, a different effective pressure as a consequence of the flow pattern and a change in particle densities. In Fig. 2.7 some Raman spectra are shown. It is clearly demonstrated that moderate chamber pressures can lead to the deposition of graphitic material.



(a)



(b)

Figure 2.6: SEM image of (a) individual diamond particles (1 bar represents $10\ \mu\text{m}$) and (b) a continuous diamond film (1 bar corresponds to $1\ \mu\text{m}$)

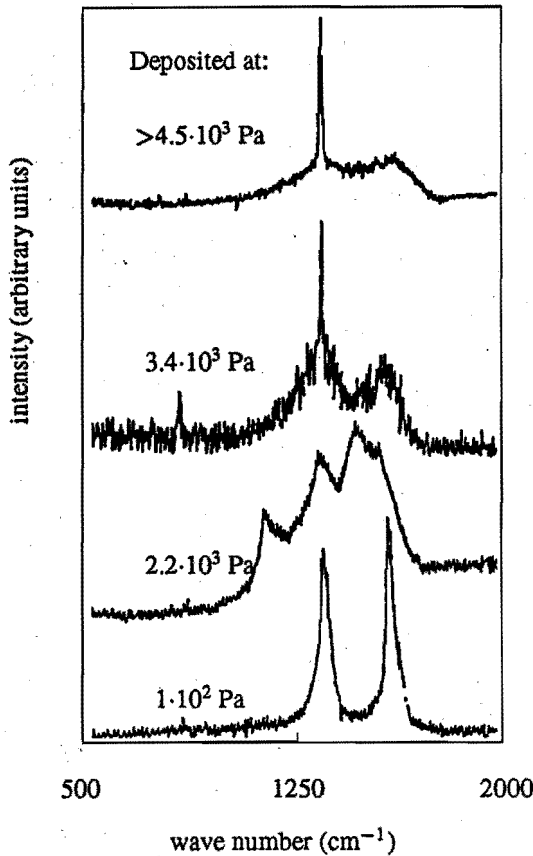


Figure 2.7: Raman spectra of deposits obtained under the diamond conditions (cf. Table 2.1), with variable chamber pressure. At 10^2 Pa, only the peaks associated with graphitic material can be observed. From $2.2 \cdot 10^3$ Pa on, the diamond precursor peaks at ~ 1150 and ~ 1470 cm^{-1} appear, and then the single crystal diamond peak at 1332 cm^{-1} becomes predominant. (adopted from [8])

2.4 Graphite deposition

In the next-step fusion device NET/International Thermonuclear Experimental Reactor (ITER) the materials for the plasma-facing components are a critical issue. Of most concern is the design of the divertor, which will receive a peak heat flux of 15 MW m^{-2} during normal operation. The divertor surface will reach temperatures up to 1000°C , and suffer from the effects of severe disruptions with peak energy dumps of 20 MJ m^{-2} in milliseconds [6]. Disruption erosion is a primary lifetime-determining factor. Covering the divertor plates with either

pyrolytic carbon (PyC) or carbon-fiber composite (CFC) is considered one of the best engineering solutions. Recent estimates for the erosion of a carbon divertor indicate values of 0.5 to 1 mm material loss per disruption event [13]. Avoiding frequent shutdown of the machine for replacement of the plates is a major problem.

Graphitic or diamond-like carbon deposition by cascaded arc gun is an option for *in situ* repair of erosion damage. The primary requirements for the coating to be deposited are that it should be crystalline (good thermomechanical performance) and that the deposition rate should be high [thick (several millimetres) layers within acceptable periods of time]. As a first research stage, a program of reactor settings, starting from the graphite values of Table 2.1, has been attempted in which increasing the growth rate is emphasized.

2.4.1 Specific experimental data

All experiments were performed with the setup shown in Fig. 2.2. The desired deposition temperature was attained by direct heating of the substrate by the plasma beam itself. The sample holder consisted of a stainless steel hollow cylinder with an auxiliary heating facility up to 500 °C. A stainless steel (type AISI 316 Ti) pedestal with a sample support was mounted on this. The head could be screwed on the pillar. The dimensions of this pedestal were chosen such that an extensive range of substrate temperatures from 400 to 1200 °C could be covered on different substrate-to-sample distances. The cross section of the top disc was 6 cm; the 1-cm long pillar had a 1.5-cm cross section. A Chromel-Alumel thermocouple for temperature measurements was mounted right next to the sample. Surface temperatures were also measured by an optical pyrometer (type Chino IR-AHIS). A water cooled sample holder was used for deposition experiments at 100 °C. As substrates, 10-mm discs (5 mm thick) of CFC (Dunlop DMS 678) were used. Experiments with the fiber planes parallel and perpendicular to the surface normal were carried out. As a reference for weight gain determination and for morphology considerations experiments were also executed with samples of commercial graphite and of stainless steel (AISI 316 Ti).

The graphitic samples were baked on a temperature of 200 °C for 24 hours. They were preheated up to a temperature of 600 °C by an Ar/H₂ plasma (100 : 5 ratio) in 20 minutes in the deposition reactor. As feed gases, CH₄ and C₂H₂ were used. To encourage the deposition of a crystalline layer rather than an amorphous hydrogen-containing layer, several experiments were done with different amounts of hydrogen addition. Observations for morphology were done by SEM. The crystallinity of the layer was determined by Raman spectroscopy. Film thickness

and growth rate were determined by weight change measurements.

2.4.2 Results and discussion

For convenience, we introduce the following quantities and notations:

- P' = normalized power product: $P' = P/P_s$, where P_s is the power product at the following standard settings: $I_{\text{arc}} = 35$ A, $V_{\text{arc}} = 74$ V, argon flow = $100 \text{ cm}^3 \text{ s}^{-1}$. It follows that $P_s = 2.59 \cdot 10^5 \text{ cm}^3 \text{ kW s}^{-1}$.
- Q' = normalized inverse power coefficient: $Q' = Q/Q_s$, where Q_s is the Q -factor for a flow of $1 \text{ cm}^3 \text{ s}^{-1}$ CH_4 . At the standard power product P_s , Q_s has the value $3.86 \cdot 10^{-6} \text{ W}^{-1}$.
- R_d = growth rate, determined from weight measurements, assuming a density of 1 g cm^{-3} . Inaccuracy in R_d by this way of determination is generally $< 1 \text{ nm s}^{-1}$.
- $\{\text{C}_x\text{H}_y\} = z =$ monomer flow of $z \text{ cm}^3 \text{ s}^{-1}$.

Note that in this experimental configuration, T_s is a function of d_{n-s} , P , p_c and, to a minor extent, of the monomer admixture. The growth rate is a function of substrate temperature [3]. This should be taken into account when considering the results presented below. The main tendencies, however, are not disturbed by this temperature dependence. Furthermore, no definite distinctions between the growth rate results for the parallel and perpendicular CFC samples were observed.

The following results are for films produced at a nozzle-to-sample distance of 20 cm, substrate temperatures between 600 and 1000 °C (determined by pyrometry), and with $\text{H/C} = 0$ (no H_2 admixture) unless otherwise indicated. In the SEM pictures one bar represents 100 μm unless otherwise indicated.

Growth rate

Figures 2.8 through 2.11 show the dependence of the growth rate as a function of the relevant deposition parameters.

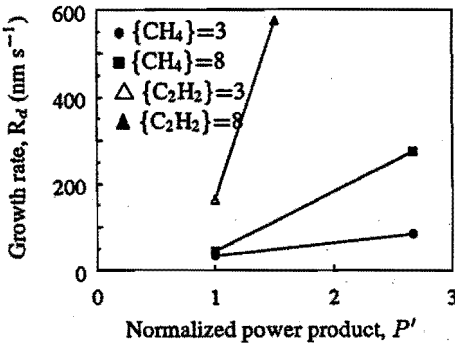


Figure 2.8: Deposition rate R_d as a function of normalized power product; $p_c = \frac{1}{3} \cdot 10^2$ Pa.

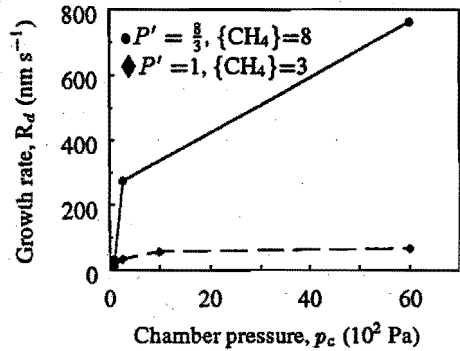


Figure 2.9: Deposition rate R_d as a function of chamber pressure.

For the initial standard power product ($P' = 1$) saturation arises readily at low CH_4 flow rates ($< 1 \text{ cm}^3 \text{ s}^{-1}$). The energy available for dissociation to CH radicals and excited carbon species is totally consumed. Consequently, by increasing the power product and the monomer flow, the growth rate can be upgraded (Fig. 2.8). In addition, a further improvement has been achieved by using C_2H_2 instead of CH_4 . This is a consequence of the smaller amount of energy necessary for complete dissociation and ionization of the monomer.

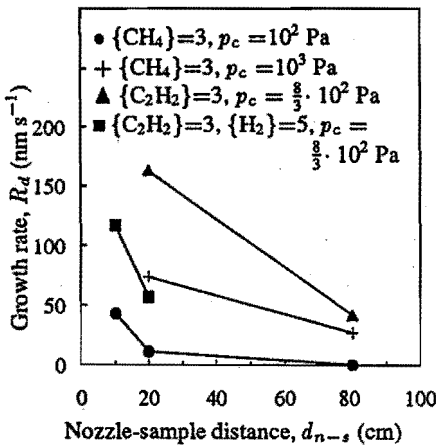


Figure 2.10: Deposition rate R_d as a function of nozzle-sample distance; $P' = 1$. (At $d_{n-s} = 80 \text{ cm}$, $T_s \approx 100^\circ \text{ C}$)

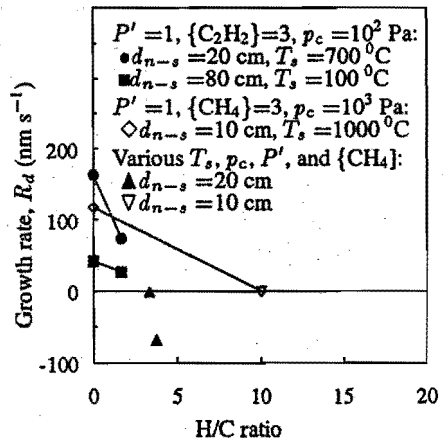


Figure 2.11: Deposition rate R_d as a function of H/C ratio in the beam.

By increasing the chamber pressure, R_d can be upgraded almost linearly (Fig. 2.9), but there are a few drawbacks. At high p_c ($>10^3$ Pa) the radial diffusion of the plasma beam particles is severely restricted, and the beam cross section is reduced to ~ 1 cm², decreasing the exposed substrate area. Consequently the substrate temperature is higher, but the beam is unstable. From Fig. 2.10, it follows that closer to the nozzle, within practical limitations, even higher growth rates may be achieved. With the addition of hydrogen (Fig. 2.11), the growth rates are greatly reduced. Appreciable growth rates can be achieved with small amounts of added H₂ only with C₂H₂ as the feed gas. Because hydrogen addition is necessary to improve the film quality, other parameter settings will have to be studied in the future. The most relevant results on the growth rate are summarized in Table 2.2.

Table 2.2: Survey of deposition time (t_d), film thickness (d_d), growth rate (R_d) and deposited area (A_d) for the most relevant trials

Trial	Setting	t_d (min)	d_d (μm)	R_d (nm s^{-1})	A_d (cm^2)
1	{CH ₄ }=1, $p_c = 10^2$ Pa, $P' = 1$	110	75	11.6	30
2	+{CH ₄ }=8	30	30	16.7	30
3	+ $p_c = \frac{8}{3} \cdot 10^2$ Pa, $P' = \frac{8}{3}$	7	115	274.	12
4	+ $p_c = 6 \cdot 10^3$ Pa	4	183	762.	1
5	{C ₂ H ₂ }=8, $p_c = \frac{8}{3} \cdot 10^2$ Pa, $P' = \frac{3}{2}$	7	241	574.	12
6	{C ₂ H ₂ }=3, {H ₂ }=5, $p_c = \frac{8}{3} \cdot 10^2$ Pa, $P' = 1$	30	133	74.	12

Morphology and type of the film

Figures 2.12 and 2.13 show SEM micrographs and Raman spectra of films deposited under the divergent conditions of trials 4 and 6 (cf. Table 2.2).

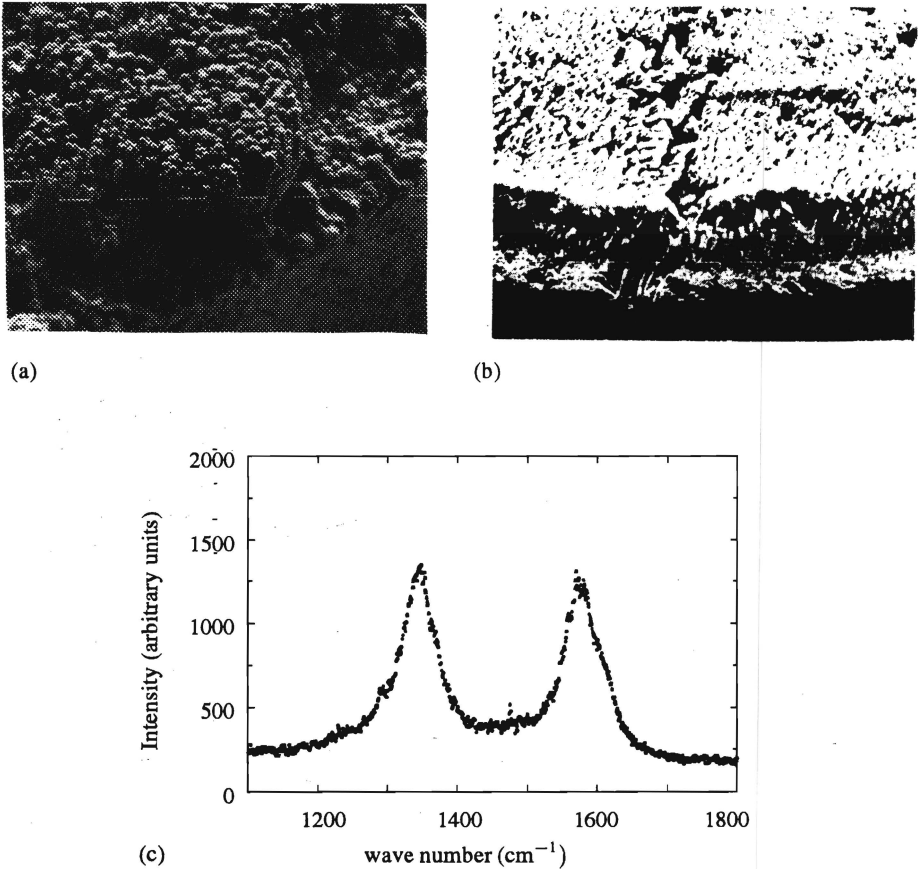


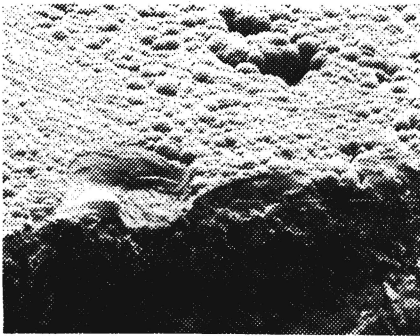
Figure 2.12: Film deposited on (a) perpendicular and (b) parallel CFC ($1 \text{ bar} = 10 \mu\text{m}$) and (c) associated Raman spectrum for the perpendicular CFC film: $\{\text{CH}_4\}=8$, $T_s = 1200^\circ\text{C}$, $p_c = 6 \cdot 10^3 \text{ Pa}$, $P' = \frac{8}{3}$, $Q' = 3$.

Figure 2.14 shows some interesting pictures of a film obtained under the conditions of trial 2.

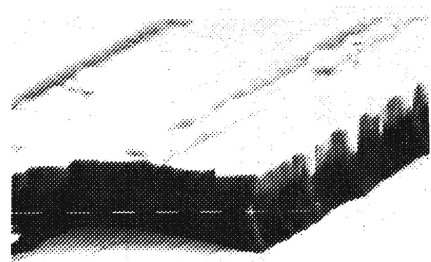
Most of the deposits exhibit a cauliflower morphology, which is similar to that of conventional pyrolytic carbon (PyC). In this case the basal planes of the graphite packets are parallel to the substrate surface [14]. A characterization of the deposits in terms of the random fractal-like structure model as described by Messier and Yehoda [15] is appropriate. The main features of this model are low mobility ($T_{\text{depo}} < 0.5 \cdot T_{\text{melt}}$), competitive cone growth, and self-similarity on

every dimension of scale. The layers are more continuous on the steel substrate. This may be caused by the lack of preferential sites for nucleation. The sharp edges that can be observed are an indication of the crystalline nature of the deposit.

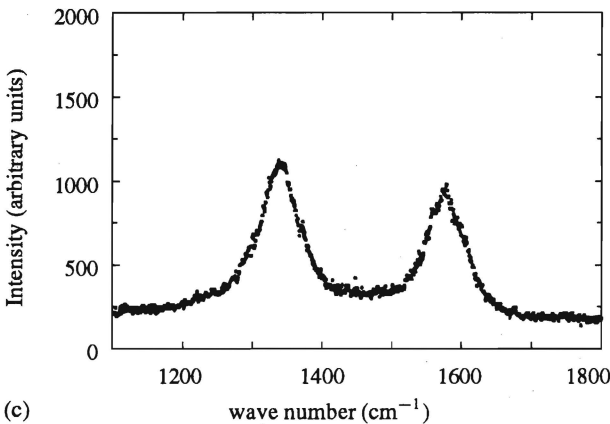
In all Raman spectra both the first order graphite (1581 cm^{-1}) and defective graphite peak (1355 cm^{-1}) are prominently present. From the intensity ratio of these peaks, a measure for the crystallite size can be estimated [16]. When the peaks are equal in intensity, this size is $\sim 3\text{ nm}$.



(a)



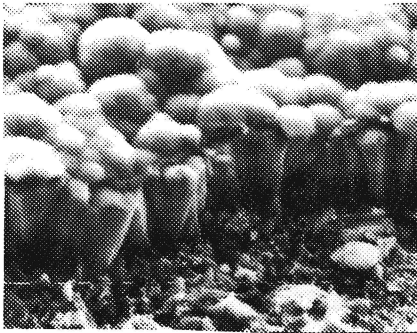
(b)



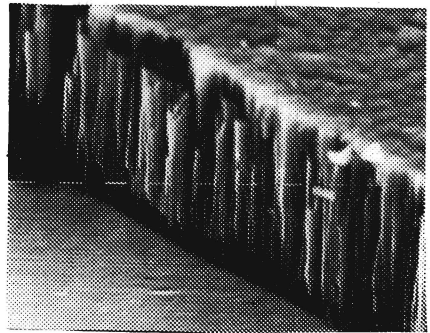
(c)

Figure 2.13: Film deposited on (a) parallel CFC and (b) steel (1 bar = $10\ \mu\text{m}$) and (c) associated Raman spectrum for the parallel CFC film: $\{C_2H_2\}=3$, $\{H_2\}=5$, $H/C = 10/6$, $T_s = 700\ ^\circ\text{C}$, $p_c = \frac{8}{3} \cdot 10^2\ \text{Pa}$, $P' = 1$ and $Q' = 6$.

Unfortunately, however, as demonstrated in Figs. 2.12 (c) and 2.13 (c), this is the case for almost all of our films, regardless of the deposition settings. Also no substantial change in Raman spectrum could be observed for the films produced with admixture of low amounts of hydrogen. A broadening of the Raman graphite peaks was observed only for the films deposited at 100 °C, indicating a more amorphous film character. Furthermore, the Raman spectra of the films on the steel substrates are very similar to those of the associated films on the CFC substrates. For the films of Fig. 2.14 on the graphite and the steel substrate, the intensity ratios I_{1355}/I_{1581} amount to 1.30 and 1.25, respectively. Consequently, a more sophisticated analysis of the spectra will be performed in future. The width of the peaks and their shift with respect to the ideal single crystal values and analysis of the second order peaks will provide additional information [16].



(a)



(b)

Figure 2.14: Films deposited on (a) commercial graphite and (b) steel: $1 \text{ bar} = 10 \mu\text{m}$, $\{CH_4\}=8$, $T_s \simeq 700 \text{ }^\circ\text{C}$, $p_c = 10^2 \text{ Pa}$, $P' = 1$, $Q' = 8$.

Conclusions

The growth rates obtained without added H_2 offer a perspective for further research. Layers that are hundreds of microns thick on an area of $\sim 12 \text{ cm}^2$ have been deposited within <30 minutes. The production of very thick (several millimetres) carbon films within an acceptable period of time (hours) seems to be within the range of possibilities.

The morphology and crystallinity of the deposited film seem to be not very dependent on the deposition parameters, at least in the range used up to now.

Most of the films consist of pyrolytic graphite with a crystallite size of ~ 3 nm and with the basal planes parallel to the substrate surface. In view of the desired thermomechanical qualities of the film, a method for growing films with the basal planes perpendicular to the substrate surface will be sought.

Up to now, the effect of H₂ admixture on the film quality could not properly be investigated. With a minor H₂ content (<5%) in the flow, no change in crystallite size could be observed.

Addition of a substantial amount of hydrogen leads to etching of the graphitic substrates; this shows that deposition is in fact a balance between deposition and etching. The amount of H₂ admixture against the arc power may need a very delicate balance in view of optimal ionization and dissociation.

Acknowledgement

The authors would like to thank D.J. Stufkens and T.L. Snoeck of the University of Amsterdam for measuring the Raman spectra.

The work reported in the section of graphite deposition in this paper forms part of the NET-ECN Petten- Eindhoven University of Technology research agreement on Investigation of Plasma-Deposited Carbon Films as Possible Means of Divertor Repair, as established in NET contract 90-237 between The European Atomic Energy Community and Euratom/FOM Association. It is funded by the Commission of the European Communities, which represents the European Atomic Energy Community.

Bibliography

- [1] H. Borning, *Plasma News Report*, Research Institute of Plasma Chemistry and Technology, Carlsbad, (1986).
- [2] G.M.W. Kroesen, *Ph.D. Thesis*, Eindhoven University of Technology, (1988).
- [3] H. Kersten and G.M.W. Kroesen, *J. Vac. Sci. Technol.*, **A8**, (1), 38, (1990).
- [4] P.K. Bachmann, H. Lydtin, D.U. Wiechert, J.J. Beulens, G.M.W. Kroesen, and D.C. Schram, *Proc. 3rd Int. Conf. on Surface Modification*, T.S. Sudarshan and D.G. Bhat (eds.), Surface Modification Technologies III, The Minerals, Metals and Materials Society, Warrendale (PA), 69, (1990).
- [5] A.T.M. Wilbers, J.J. Beulens, and D.C. Schram, *J. Quant. Spectrosc. Radiat. Transfer*, **46** (5), 385, (1991).

- [6] T. Kuroda and G. Vieider, eds., *ITER Plasma Facing Components*, ITER Documentation series, No. 30, International Atomic Energy Agency, Vienna, (1990).
- [7] J.J. Beulens, M. de Graaf, G.M.W. Kroesen, and D.C. Schram, *Proc. Materials Research Society Spring Meet., San Francisco (CA), April 1990*, D. Apelian and J. Szekely (eds.), Materials Research Society Pittsburgh (PA), A331, (1991).
- [8] J.J. Beulens, *Ph. D. thesis*, Eindhoven University of Technology, (1991).
- [9] M.C.M. van der Sanden, *Ph. D. thesis*, Eindhoven University of Technology, (1991).
- [10] G.M.W. Kroesen, D.C. Schram, A.T.M. Wilbers, and G.J. Meeusen, *Contrib. Plasma Phys.*, **31** (1), 27, (1991).
- [11] G.M.W. Kroesen, D.C. Schram, and M.J.F. van de Sande, *Plasma Chem. Plasma Proc.*, **10** (1), 49, (1990).
- [12] J. Robertson, *Adv. Phys.*, **35** (4), 317, (1986).
- [13] R.D. Watson, ed., *ITER Divertor Engineering Design, ITER-TN-PC-8-9-1*, Max-Planck-Institut fur Plasmaphysik, Garching-bei-Munchen, (1989).
- [14] P.L. Walker and P.A. Thrower, eds., *Chemistry and Physics of Carbon; A Series of Advances, Vol. 11*, Marcel Dekker, New York, (1984).
- [15] R. Messier and J.E. Yehoda, *J. Appl. Phys.*, **58** (10), 3739, (1985).
- [16] N.B. Brandt, S.M. Chudinov, and Ya. G. Ponomarev, *Semimetals; I. Graphite and its compounds*, 388, North-Holland, Amsterdam, (1988).

Chapter 3

Plasma deposited carbon films as a possible means for divertor repair¹

A. J. M. Buuron, J. J. Beulens and D. C. Schram
*Dept. of Physics, Eindhoven University of Technology
P.O. Box 513, 5600 MB Eindhoven, The Netherlands*

P. Groot and J. Bakker
*Netherlands Energy Research Foundation, ECN,
P.O. Box 1, 1755 ZG Petten, The Netherlands*

abstract

Fast deposition of graphitic carbon layers by an expanding cascaded arc plasma was studied as a means for *in situ* repair of graphite erosion damage in the next step fusion reactor NET/ITER. Amorphous graphite was produced at rates of hundreds of nanometers per second on several square centimeters with an argon-hydrocarbon plasma. Crystalline graphite was produced at rates of 10-50 nm s⁻¹ on several square centimeters by means of an argon-hydrogen-hydrocarbon plasma. Relations between the deposition parameters, morphology (from scanning electron microscopy) and Raman spectra were determined. Using laser thermal shock testing, the erosion resistances of the best crystalline coatings were determined at about 2 MJ m⁻² (in a 10 ms pulse).

¹This article has been published in *Thin Solid Films* 212 (1992) 282

3.1 Introduction

In the next step fusion device NET/ITER the surface armor for the plasma-facing components is a critical issue. Disruption erosion, particularly on the divertor plates, is a primary lifetime determining factor. One of the best engineering solutions is coating the divertor plates with carbon-based materials, either with highly oriented pyrolytic graphite (HOPG) or carbon fiber composite (CFC). The erosion of a carbon divertor is estimated as a total of 50 kg material loss per disruption event [1]. This would necessitate frequent shutdown of the machine for replacement of the plates. Performing this by remote handling techniques would require months. *In situ* repair methods are under investigation as an alternative solution.

Eindhoven University of Technology, The Netherlands, Energy Research Foundation (Petten ECN) and the Next European Torus (NET) team are cooperating in the study of fast carbon deposition by an expanding cascaded arc as an option for *in situ* repair of erosion damage. With this particular deposition method, in the past deposition rates of up to 200 nm s^{-1} for a-C:H (amorphous hydrogenated carbon) [2] and of up to 10 nm s^{-1} for diamond films [3] have been obtained. These rates are an order of magnitude higher than those with the conventional RF or DC glow discharge methods.

For the present purpose, attention was focused on the deposition of graphitic carbon. In a feasibility study the possibility of very fast deposition of nanocrystalline ("amorphous") graphite at hundreds of nanometers per second by an argon-hydrocarbon plasma has been demonstrated (cf. Chapter II). The microstructure of the coatings was analyzed by scanning electron microscopy (SEM) and Raman spectroscopy. At the Netherlands Energy Research Foundation, ECN, disruption simulation experiments with a laser thermal shock set-up [4] were carried out. It appeared that the amorphous graphite coatings cannot sustain a thermal shock of 4 MJ m^{-2} in 10 ms (a lower limit for the disruption energy dump).

In an extensive second stage of the project the crystallinity of the graphite was optimized. To this end hydrogen was admixed in the argon-hydrocarbon plasma while other parameters were also varied. In this study direct relations between morphology (from SEM), Raman spectra and thermal shock (erosion) resistance of the coatings on the one hand and the reactor parameters during deposition on the other hand are demonstrated. Interrelations between the results of the three diagnostics are also shown.

3.2 Design of the next step fusion reactors

In Fig. 3.1 an outline of the design of ITER, the International Thermonuclear Experimental Reactor, is shown [5]. It is designed to operate in a double null separatrix configuration with divertor plates. By virtual crossings of the magnetic field lines (the X-points), the fusion product helium, impurities and thermal power are diverted from the plasma edge toward the plates. After neutralization the particles are abducted by the torus vacuum pumping system. A relevant feature of the machine with respect to maintenance are the giant dimensions. The torus center radius is 5.8 m. The required divertor plate area is about 200 m².

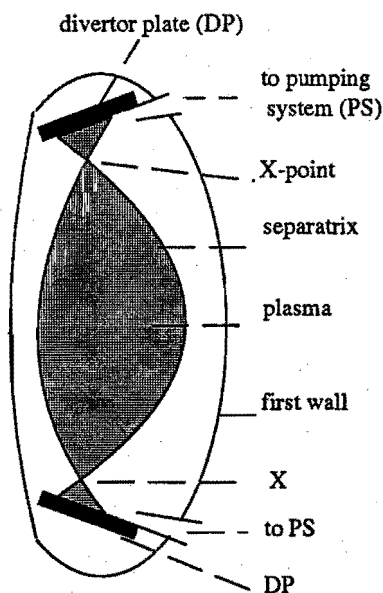


Figure 3.1: Outline of ITER design with the divertor plates

The choice of materials for the plasma-facing components, divertor plates and first wall, is a critical issue. Particularly the divertor plates are subjected to high heat loads and particles fluxes. The principal requirements for surface armor material can be summarized as follows: a low atomic number Z , a high thermal conductivity and a high thermal shock resistance, and, a dense structure to minimize the tritium retention.

We will summarize the estimated performance data of carbon as a surface armor material [1, 4, 5]. Compression annealed pyrolytic graphite (CAPG) and carbon fiber composites (CFC) in particular are considered as suitable materials.

In the most recent design [5] the latter were selected primarily because of their unique thermal shock resistance and the potential for tailoring them to specific other requirements such as a high thermal conductivity.

During normal operation the divertor plates will have to accommodate an average heat flux of 0.6 MW m^{-2} , with static peak surface heat fluxes of $15\text{-}30 \text{ MW m}^{-2}$. In addition the surface will suffer from an average neutron wall load of 0.5 MW m^{-2} , and a DT-ion peak flux of $4 \cdot 10^{23} \text{ m}^{-2}\text{s}^{-1}$ (energy $50\text{-}100 \text{ eV}$). The surface temperature of the carbon divertor armor has to be controlled to maximally $\sim 1000^\circ\text{C}$ in order to limit "run-away" erosion by self sputtering.

Estimates for the energy deposition on the divertor plates in a disruption are $10\text{-}20 \text{ MJ m}^{-2}$ in $0.1\text{-}3 \text{ ms}$ (in the thermal quench) and 2 MJ m^{-2} in $5\text{-}50 \text{ ms}$ (in the consequent current quench).

In one of the main design options [1] the divertor armor will consist of $5 \cdot 10^5$ replaceable carbon tiles brazed to a metallic alloy as a heat sink. In the case of a full power disruption, the material loss is predicted to be 50 kg of carbon, equivalent with a damage track of $\sim 0.7 \text{ mm}$ depth on a total area of $\sim 3.6 \text{ m}^2$. The thickness of the armor is limited by its maximally allowable surface temperature of 1000°C , and thus by its thermal conductivity. For CFC/graphite the maximum is $\sim 1 \text{ cm}$, which limits the the allowable number of disruptions per plate to $8\text{-}12$. The local erosion can be reduced by sweeping the X-points of the separatrix (by values in the order of $\pm 10 \text{ cm}$ and at 0.1 Hz), reducing the number of necessary replacements. An estimated minimum of 100 disruptions in the first operation phase ('physics' phase) would still imply a number of divertor plates replacements of $6\text{-}10$. In an alternative calculation [5] a number of $9\text{-}17$ replacements is obtained (see also [4] on this issue). Considering the estimate that each replacement will require $3\text{-}6$ months, the need for an effective *in situ* repair method is obvious. The *in situ* deposited material should approach the specifications summarized above. An additional requirement is an adequately high deposition rate. The feasibility of achieving high carbon deposition rates with the expanding cascaded arc technique has already been reported in (Chapter II). The present study was primarily focused on depositing (crystalline) coatings with good thermal shock resistance, while retaining a reasonably high growth rate.

3.3 Carbon deposition by an expanding cascaded arc plasma

3.3.1 The expanding cascaded arc set-up

In Fig. 3.2 an outline of the expanding cascaded arc set-up for carbon deposition is shown. The main feature of the method is the separation of the three functions

production, transport, and deposition. The principal advantages of this method compared to conventional methods are high growth rates by the active particle transport towards the substrate, and flexibility in handling arc and substrate parameters. A cascaded arc plasma (4 mm diameter, 6 cm length), expanding in a vacuum chamber is used as a particle source. Specific features of this source are a high power dissipation (~ 5 kW), a thermal plasma (temperatures of ~ 1 eV) and, very long times of continuous operation (days). The carrier gas argon is injected at the beginning of the arc channel at a flow rate of 100 scc/s, which means a flow rate of $100 \text{ cm}^3 \text{ s}^{-1}$ normalized on a pressure of 10^5 Pa. The inlet pressure is in the order of $5 \cdot 10^4$ Pa. The ionization degree is typically about 10%, rendering an electron density in the order of 10^{22} m^{-3} . As a consequence the arc plasma is close to local thermal equilibrium (LTE). A hydrocarbon (CH_4 or C_2H_2) can be injected (at rates of 0 to 10 standard $\text{cm}^3 \text{ s}^{-1}$ at the end of the arc channel. Hydrogen can be admixed as an etching agent in the middle of the channel. By dissociation and charge exchange a beam of excited species, radicals and ions (Ar , C , H , C_xH_y) is created, expanding out of the end of the arc channel (the nozzle). The particles are accelerated to supersonic velocities of up to $\sim 4000 \text{ m s}^{-1}$, pass through a shock and are transported further towards a substrate at subsonic velocities, decreasing down to a few hundreds of meters per second. A typical value for the chamber pressure is 10^2 Pa (for a-C:H deposition); in this case the shock can be observed at about 4 cm from the nozzle. Beyond the shock, the total energy of the species decreases to typically about 0.5 eV. A typical value for the carbon ion flux is 10^{19} s^{-1} . The total transport time of all particles is relatively small (of the order of 10^{-4} to 10^{-3} s), the radiative recombination is negligible, the loss of ionization by three particle recombination is less than 1% [6].

An important aspect in the present framework is the radial expansion of the beam, which is governed by diffusion. From Fig. 3.3 we can deduce that the beam cross section area A_b is approximately linearly proportional to the distance to the nozzle d_{n-s} , and reciprocal to the chamber pressure p_c . For instance, for a-C:H deposition with $d_{n-s}=80$ cm and $p_c=20$ Pa, A_b is $\sim 120 \text{ cm}^2$. Extrapolating, for all values of chamber pressures, we can calculate the beam cross-section area by dividing the area at $p_c = 1$ mbar (10^2 Pa) by p_c (expressed in mbars). In a similar way the beam cross-section areas for various nozzle to substrate distances can be deduced linearly from the value at one specific d_{n-s} . We define a normalized deposition rate R_n as a measure for the volume deposition rate by dividing the linear deposition rates by p_c : $R_n := R_d/p_c$. More details on the reactor and the cascaded arc can be found elsewhere [2, 7, 8, 3, 8, 9].

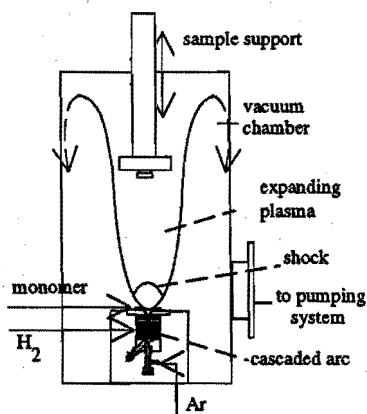


Figure 3.2: The expanding cascaded arc set-up for deposition

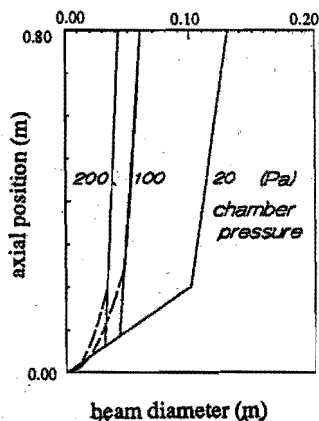


Figure 3.3: Measured (---) and calculated (—) beam profiles in the expansion (from [2]).

3.3.2 Deposition conditions and materials

By variation of the reactor parameters, the type, quality and growth rate of the films can be modified. As reported in Chapter II, the (linear) deposition rate R_d is a function of all reactor parameters: the arc power (P_{arc}), the gas flow rates ($\{\text{argon}\}$, $\{\text{hydrocarbon}\}$, $\{\text{hydrogen}\}$), the type of hydrocarbon (monomer) feed gas, the number of carbon atoms in relation to the arc power (expressed by an inverse power factor Q), the chamber pressure p_c , the deposition temperature T_s and the nozzle to substrate distance d_{n-s} . In Chapter II a survey of reactor settings for different materials was given. For the actual goal of crystalline graphite deposition the following considerations have been taken into account:

- 1 For the specified purpose, a coating without hydrogen and weakly bonded carbon is required. This can be done by increasing the hydrogen admixture in the plasma while reducing the nozzle to substrate distance and increasing the chamber pressure. At a nozzle-substrate distance of 20 cm the addition of a moderate amounts of hydrogen in the plasma leads to etching of the CFC substrates (Chapter II). Currently, for most trials a nozzle-sample distance of 5 cm has been applied (unless indicated otherwise).
- 2 A high deposition temperature, of at least 600°C , to avoid hydrogen incorporation [10], and probably even $>900^\circ\text{C}$ [11] to favor crystallization, is required.

- 3 For high rate graphite deposition acetylene (C_2H_2) is more efficient than methane (CH_4), with and without hydrogen addition (Chapter II). This choice is also indicated by others. The C_2 radicals play an important role [12].

Taking into account these data, the properties of the deposited graphite have been studied primarily in relation to the following three main deposition conditions:

- 1 The hydrogen admixture flow rate $\{H\}$; the effect of hydrogen in the plasma beam may also be expressed as the ratio of the total hydrogen flux (including the hydrogen from the hydrocarbons) and the carbon flux in the expanding beam:

$$\{H_{tot}\}/\{C\}$$
- 2 The hydrocarbon injection rate $\{C_xH_y\}$, expressed in an inverse power factor Q (W^{-1})

$$Q = \{C\}/(\{Ar\} \cdot P_{arc})$$
- 3 The substrate temperature
 T_s ($^{\circ}C$)

For the actual purpose, the relation of layer quality with growth rate and layer thickness and the influence of the substrate type and feed gas (methane or acetylene) has also been studied.

In the present experimental configuration the desired deposition temperature is obtained by direct heating of the substrate by the plasma beam itself. It is a function of d_{n-s} , P_{arc} , p_c and, to a minor extent, of the hydrogen and monomer admixture.

In order to achieve high substrate temperatures, on the movable sample support an extra pedestal with 5 substrate supports is mounted (Fig. 3.4 (a), (b)). One of the substrate supports is centered because of the reduced deposition area ($\sim 1 \text{ cm}^2$) at high chamber pressures. An extensive range of substrate temperatures from 400 to 1400 $^{\circ}C$ can be covered on different nozzle to substrate distances. Right underneath the center sample a chromel-alumel thermocouple for temperature checking is mounted. As actual deposition temperatures, the surface temperatures T_{py} as measured with an optical pyrometer (type Chino IR-AHIS) were adapted.

As substrates, 10 mm discs (thickness 5 mm) of carbon fiber composite (CFC, Dunlop DMS 678) and stainless steel (type AISI 316 Ti) were used. The composite consists of plane matrices of carbon fibers, with pyrolytic graphite in between. CFC can be applied in two orientations: as a CFC or as CFC \perp substrate. The most useful orientation is CFC, with the fiber planes parallel to the surface normal. In this case the direction of highest thermal conductivity

is perpendicular to the surface. In Fig. 3.4(c), a schematic view of the CFC surface is shown in the two orientations. As a pretreatment substrates can be polished, for equal reference conditions. The substrates were baked in vacuum on a temperature of 200 °C during 24 hours, in order to dehydrate them. In most trials, a batch of several substrates was installed consisting of polished and unpolished CFC and CFC \perp substrates. Furthermore, a substrate of stainless steel (AISI 316 Ti) was mounted as an extra facility for weight gain determinations. In this way the influence of substrate material on morphology and Raman spectrum could be studied. Deposition times were on the order of 20 minutes. Thicknesses and growth rates were estimated by weight change measurements, normalized to a density of 1 g cm $^{-3}$. In general growth rates on the center substrate are higher than on the sideways placed substrates, particularly at high chamber pressures.

Some experiments with a modified substrate geometry were also performed. After finding the estimated optimal settings (trial B40, 47 or 54) these trials were repeated with oblique incidence of the beam on the sample, and, with a recirculation cup (resp. B56+59 and B57). The aim of the former was trying to influence the orientation of the deposited graphite. In the latter trial the purpose was to create small convective cells over the substrate, in order to achieve an enhanced carbon deposition efficiency.

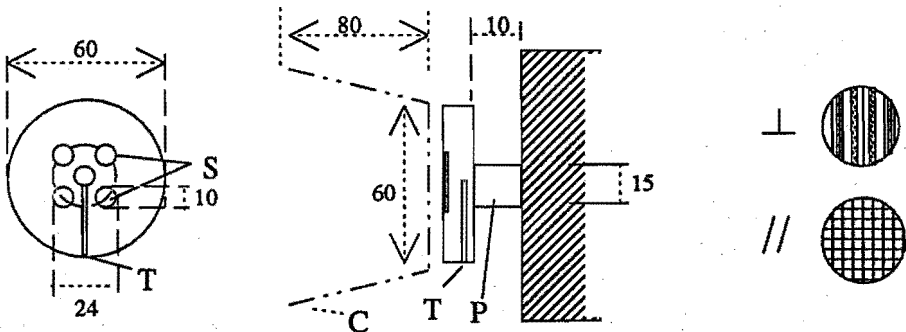


Figure 3.4: (a) Front and (b) side view of the pedestal with the 5 substrate supports. T: thermocouple insert hole; C: optional recirculation cup (dimensions in mm). (c) (adapted from [4]) top view of CFC substrates in the two orientations.

3.4 Diagnostics

3.4.1 Raman spectroscopy set-up

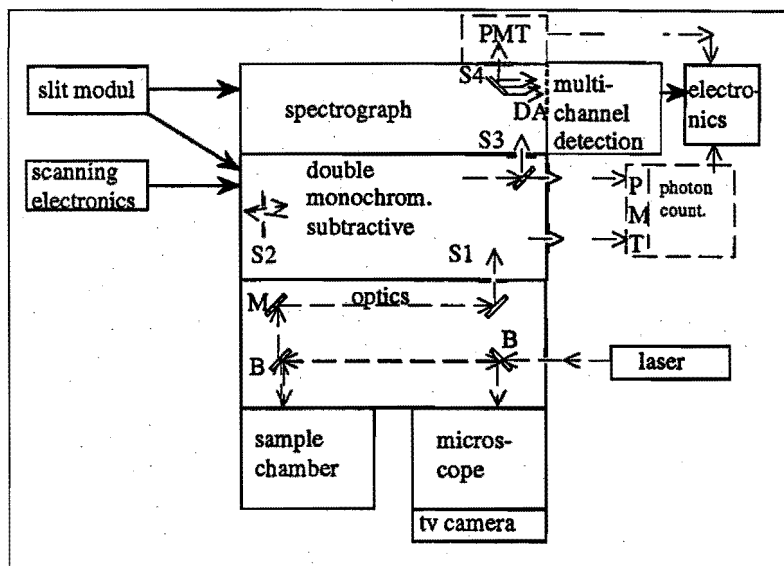


Figure 3.5: Outline of the micro-Raman set up with DA, the diode array for multichannel analysis; PMT, photo multiplier tubes for optional photon counting; B, beam splitters; M, mirrors; S1-4, slits.

Spectra were recorded with the micro-Raman set up (Dilor) of the Department of Inorganic Chemistry of the University of Amsterdam (Fig. 3.5). This arrangement enables accurate laser spot adjustment and direct sample inspection. The spectra were measured in a 180° back scattering geometry. As a source the 514.5 nm line of an argon ion laser was used. In general the power was 100 mW and the area of cross section $4 \mu\text{m}^2$. Signal detection was done by means of a double monochromator (in the subtractive mode for straylight rejection) and a diode array with signal accumulation ($20 \times$). The width of the apparatus profile was 6.6 cm^{-1} . As this is still much smaller than the relevant peak widths, no deconvolution was performed.

3.4.2 Set-up for thermal shock experiments

In Fig. 3.6 an outline of the set-up for thermal shock tests is given. As a source a pulsed Nd-YAG laser (LASAG KLS-321) is used. The laser is equipped with a

plan-parallel resonator with a length of 500 mm and a diaphragm with a diameter of 5.8 mm. Experimental conditions of the laser and the shape of the pulse are given in the inset of Fig. 3.6.

The laser beam is transmitted to the specimen by an optical system. The beam is expanded to a diameter of 13 mm and then focused on the specimen by a lens (focal distance 100 mm). The minimal spot diameter is 0.5 mm in the focal plane. The specimen is placed in a vacuum chamber with a pressure of less than 10^{-2} Pa. By positioning the specimen out of focus, the spot diameter and the energy density on its surface can be varied. Assuming a homogeneous distribution of the intensity over the laser beam, the spot diameter c in mm at the defocus distance x (in mm) can simply be calculated according to the following formula:

$$c = (x + 4)/(100 + 4) \cdot 13 \quad (3.1)$$

For example with a defocus distance of 30 mm, the energy density is 2.82 MJ m^{-2} . For the actual values of x the relative inaccuracy in the energy density is about two times the relative inaccuracy in x , which means only about 2%.

For an inhomogeneous distribution of the intensity over the laser beam all of the energy density values used in this investigation should be corrected to a peak energy density of 1.3 times the given values [13, 14]. More details on the facility can be found elsewhere [15].

The results of the thermal shock testing, were primarily quantified by the parameter erosion threshold, *i.e.* the lower limit of the laser pulse power at which erosion starts to occur. Secondly, a qualitative study of the damage by a 3 MJ m^{-2} energy dump (in 10 ms) was performed.

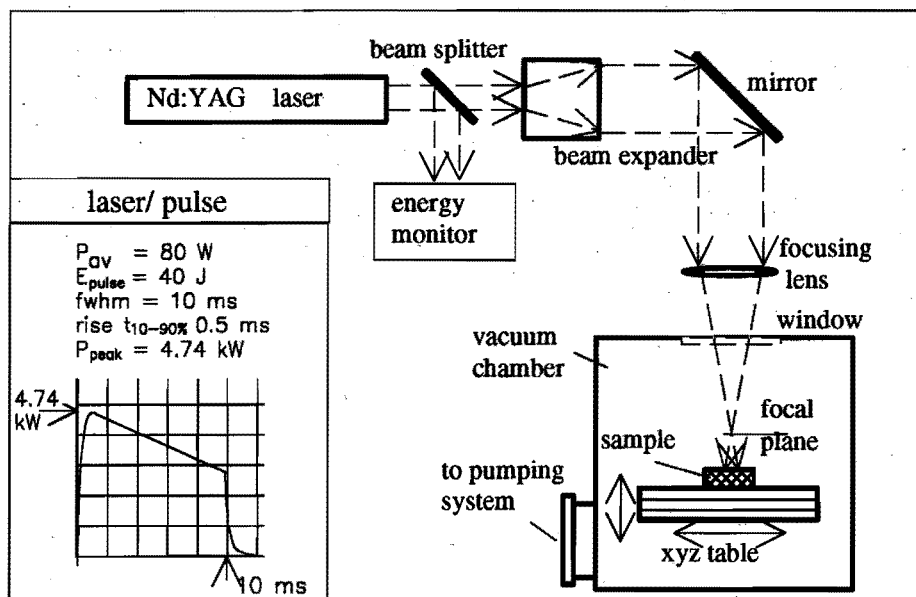


Figure 3.6: Set-up for laser thermal shock tests (from [15]); in the inset some specific experimental data and the shape of the 10 ms pulse are given.

3.5 Results and discussion

3.5.1 Introduction

In this section, the morphology and Raman spectra of the films, their macroscopic properties, the relations between Raman spectrum parameters and the erosion resistance of the coatings on the one hand and the reactor parameters during deposition on the other hand, growth rates and efficiency, the qualitative damage study, and some particular deposition results are presented.

3.5.2 Morphology and crystallinity of the coatings; hydrogen admixture, the principal determining factor.

In Fig. 3.7(a) an example of the typical morphology of a graphitic film grown without or with a small amount of hydrogen admixture is shown. A cauliflower or ball-like morphology with a columnar growth mechanism can be observed. Its appearance is similar to that of conventional pyrolytic carbon [16]. In pyrolytic carbon the basal planes are quasi-parallel to the substrate surface. It is not sure whether this was the case for our deposits too. Possibly there is no two-

dimensional ordering of the basal planes at all, and that we are dealing with isotropically distributed nanocrystallites of graphite. In Fig. 3.7(b) the Raman spectrum of the film is shown. It is typical for nanocrystalline graphite without long range order [17, 18]. All of the films deposited in the previous research stage (Chapter II) had a similar spectrum. The following features are present, denoted by their specific character: The single crystal graphite peak G (sp^2 bonding), shifted with respect to its ideal position at 1581 cm^{-1} ; a defective graphite peak D at about 1355 cm^{-1} and a shoulder S at about 1621 cm^{-1} , originating by edge effects of the finite microcrystals. A component A at approximately 1500 cm^{-1} , which is often observed in a-C:H [17]; a fluorescence background F. In the following we refer to this material as “amorphous graphite”, and denote it as AG.

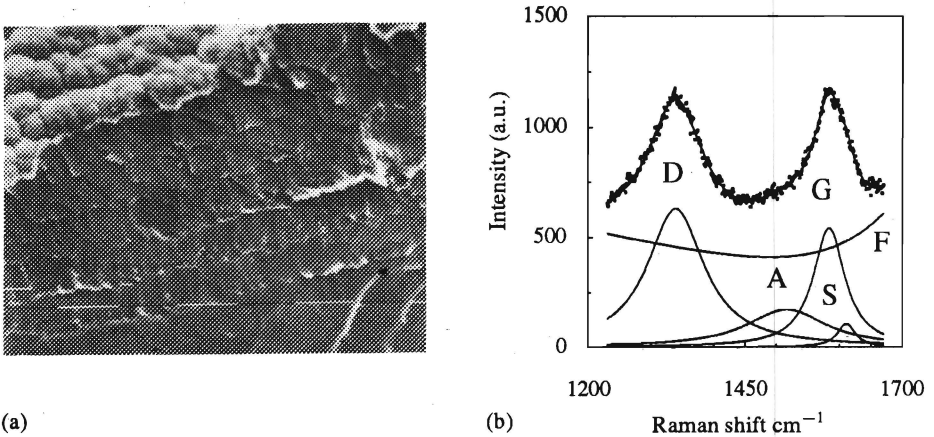


Figure 3.7: (a) SEM image (side view, 1 bar= $100\mu\text{m}$) and (b) Raman spectrum of a typically amorphous graphite film (B19): substrate steel; $d_{n-s}=10\text{ cm}$; $\{C_2H_2\}=8$, $\{H_2\}=8$; $T_{py} = 860\text{ }^\circ\text{C}$; $p_c = 10^2\text{ Pa}$; $P_{arc}=3.12\text{ kW}$; $Q=51\cdot 10^{-6}\text{ W}^{-1}$; $d=359\text{ }\mu\text{m}$, $R_d=99\text{ nm s}^{-1}$

The spectra were resolved in their components by a least squares fitting program [19]. It appears that they are best fitted by Lorentzian distributions, in accordance with [20], on top of the background. In the case of highly crystalline graphite *e.g.* HOPG, only a sharp G-peak would be present [21]. Several methods for deducing information on the quality of the material are given in literature: A measure for the crystallite size of the graphite can be deduced from the intensity ratio of the D and the G peak I_d/I_g [21] and from the shift of the G peak with respect to its ideal value [18]. From the widths of the D and the G peaks an impression of the degree of amorphization can be obtained [22]. A study of the

shoulder S gives an indication of quality [23]. We will mainly use the I_d/I_g intensity ratio as a quality indication; in Section 3.5.4 the use of the other Raman parameters is briefly discussed.

The crystallinity of our deposited materials was improved by increasing the hydrogen addition. In the sequence of Fig. 3.8(a)-(c) the gradual structural transition with increasing hydrogen admixture is illustrated. All other reactor parameters were kept approximately the same. The defective graphite 1355 cm^{-1} D peak decreases strongly with respect to the 1581 cm^{-1} G peak. In comparison with Fig.3.7(b) the amorphous component could not be resolved significantly. In Fig.3.8(d) the morphology of the film of Fig. 3.8(c) is shown. Distinct foliates can be observed, with dimensions of several micrometers, obviously separated by pores. Most likely, the foliates are actually oriented graphite single crystals. Estimating the crystallite size from the ratio I_d/I_g according to Tuinstra and König [21] in the sequence of Fig. 3.8(a) to (c), we get an increase from approximately 3 to 30 nm. The discrepancy with the dimensions observed in the SEM image of Fig. 3.8(d) may be caused by the presence of minor misorientations of the basal planes within the crystals [24].

3.5.3 Macroscopic properties of the films: appearance, cohesion and adhesion, density

Macroscopically all of the materials which were produced with CH_4 , or with low amounts of C_2H_2 admixtures (less than $1\text{ standard cm}^3\text{s}^{-1}$), consist of a black, sooty material with poor coherence. As a consequence the adhesion of these layers as a whole to the substrates was weak. It was found that the principal requirement for obtaining coherent and hard films is the use of C_2H_2 at high flow rates ($8\text{ standard cm}^3\text{s}^{-1}$). An additional advantage of the high flow rate are high growth rates, tens to hundreds of nanometers per second on several square centimetres, for crystalline graphite (CG) and AG coatings respectively. In the thick ($\sim 1\text{ mm}$) AG films the cauliflower structure could even be observed visibly. The CG films are smoother. Most likely the materials are a kind of hard carbon without hydrogen (i-C), with predominantly (in AG) or exclusively (in CG) sp^2 bondings. A similarity with the sooty and the hard materials (re)deposited on the walls of a tokamak during operation can be noted [10].

In general the adhesion of the layers depends on the type of substrate; for all graphitic films adhesion to steel substrates is poor; the adhesion to CFC substrates is rather good for the AG films, and excellent for the CG films (film coalesced to substrate).

A well known feature of amorphous films grown by various methods is the existence of large voids between columnar growth structures, leading to a very

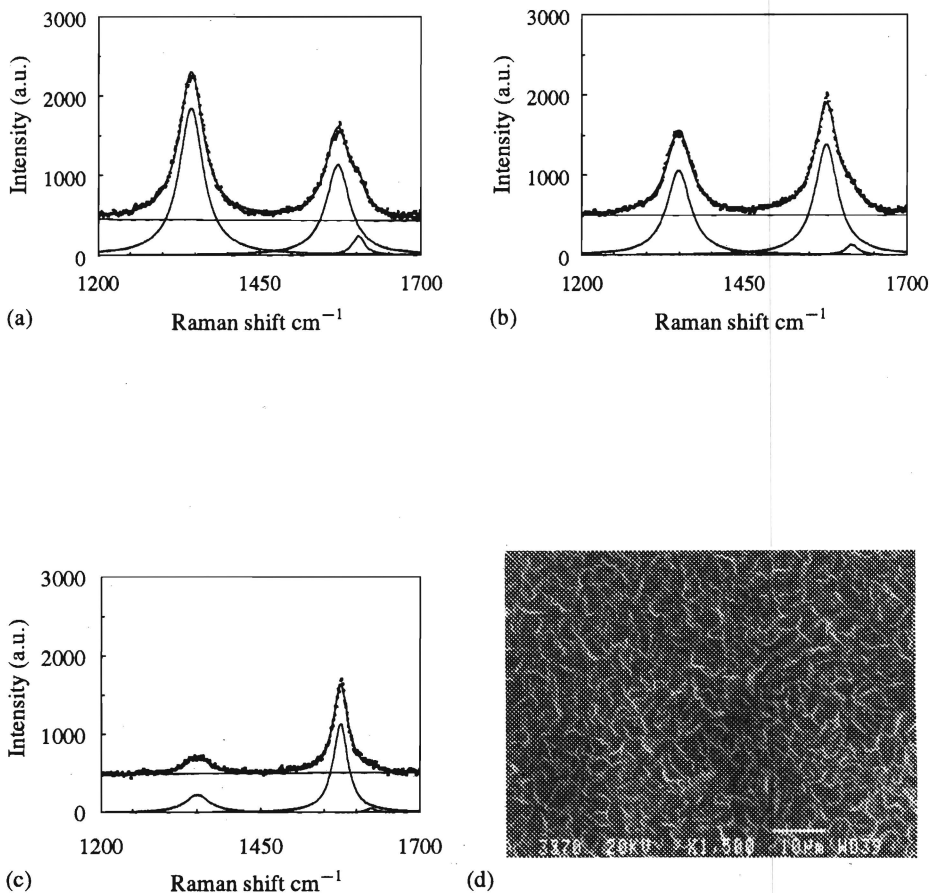


Figure 3.8: (a)-(c) Effect of increasing H_2 admixture on the Raman spectrum, with other reactor settings constant: $\{\text{C}_2\text{H}_2\}=1$; $P_{\text{arc}} \simeq 2.6 \text{ kW}$; $Q \simeq 7.10^{-6} \text{ W}^{-1}$; $p_c=10^2 \text{ Pa}$; $T_{\text{py}} \simeq 840^\circ\text{C}$; increasing H_2 addition, 5, 10 and 20 standard $\text{cm}^3 \text{ s}^{-1}$ respectively. (d) Micrograph of the film of (c).

porous material [16, 25]. Comparing thickness estimates from SEM images and from weight change measurements, it appears that both our AG and CG coatings

have a low density: ~ 0.5 to 1 g cm^{-3} , compared to a value of 2.27 g cm^{-3} for HOPG [24]. It is expected that by optimizing the substrate geometry and chamber pressure higher densities can be achieved in future.

3.5.4 Relations of the Raman spectra parameters and the thermal shock resistance with the deposition conditions.

Similar to Tuinstra and König [21], we studied the intensity (peak height) ratio of the D and G peaks I_d/I_g as a suitable parameter for describing the crystallinity of the materials. For our materials we found a direct linear relation with the integrated intensity (peak area) ratio A_d/A_g . Furthermore, globally, linear relations of this ratio with the full widths at half maximum (FWHM) of D, G and S peaks (d_d , d_g , d_s), and with the intensity ratios of the A and the S peak with the G peak exist (A_a/A_g and A_s/A_g), so these do not render much extra information. As an example this is illustrated in Fig. 3.9 for the trial sequence of Fig. 3.8. For this specific trial sequence the width d_d of the D peak does not decrease. In general however, we obtained an approximately constant ratio for the width of the D and the G peaks. As a second example in Fig. 3.10 an almost linear relation exists between the intensity ratio I_s/I_g of the shoulder S and the G peak, and the intensity ratio I_d/I_g , in agreement with [23].

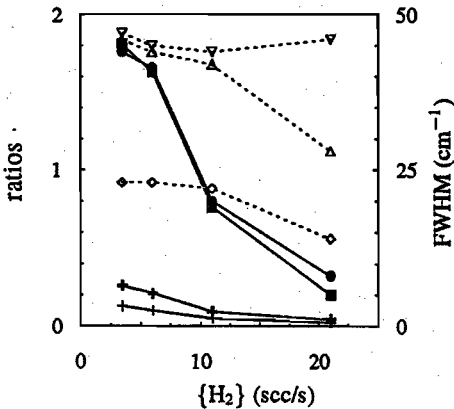


Figure 3.9: Covariation of various Raman fit parameters: $\blacksquare I_d/I_g$, $\bullet A_d/A_g$, $+ I_s/I_g$, $+ A_s/A_g$ (left axis), ∇d_d , $\triangle d_g$, $\diamond d_s$ (right axis).

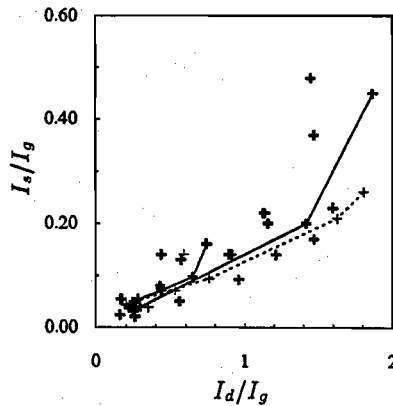


Figure 3.10: Relation between Raman fit parameters I_d/I_g and I_s/I_g . (cf. Table 3.1 for legend.)

Table 3.1: Legend for Figs. 3.10, 3.11 (a), 3.12 (a), 3.15 and 3.16

Lines of constant Q -factor		
+	CFC	various Q
+	Steel	various Q
—+	CFC	$Q \approx 3 \cdot 10^{-6}$
---+---	CFC	$Q \approx 60 \cdot 10^{-6}$
-+-	CFC	$Q \approx 7 \cdot 10^{-6}$

Table 3.2: Legend for Figs. 3.11 (b), 3.12 (b), 3.13, 3.14 and 3.15

CG	AG	Substrate
•	◦	CFC
▲	△	Steel
■	□	CFC special trial
▼	▽	Steel special trial

In the following the results of Raman spectroscopy and of the laser heat shock tests are treated quantitatively as a function of the most relevant parameters hydrogen admixture, growth rate, inverse power factor Q and deposition temperature by pyrometry T_{py} . The Raman measurements served as a direct feedback diagnostic medium on a selected number of samples for finding trends during the project. It appeared that the Raman intensity ratio (I_d/I_g) was only a function of the hydrogen addition, and the growth rate. These relations are shown in Fig. 3.11(a) and 3.12(a). No definite functional relationship between the Raman intensity ratio and Q or T_{py} could be found, so these graphs are not shown.

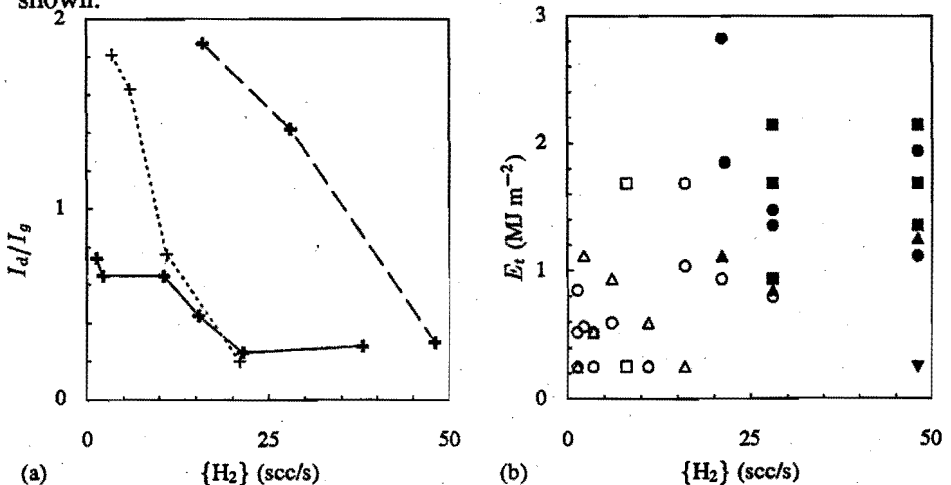


Figure 3.11 (a) Raman intensity ratio (cf. Table 3.1 for legend) and (b) erosion threshold vs. total H_2 input $\{H_2\}$ (cf. Table 3.2 for legend).

The erosion threshold values E_t were determined afterwards. In the graphs of the erosion thresholds all available data have been displayed in order to find

global trends. All the results are for layers deposited onto polished CFC or steel substrates. Furthermore, all erosion threshold measurements were accompanied by SEM observations. The results of these observations are included in the figures: whenever the coating exhibited the foliate structure of CG, a solid symbol is used. When the coating had the cauliflower-like structure of AG an open symbol is used. Furthermore, the results of the modified-geometry trials are denoted by a specific symbol.

In Fig. 3.11(a) and (b) the role of the H_2 admixture is clearly illustrated. In Fig. 3.11(b) it can be observed that both the erosion threshold and the crystallinity increase with an increasing hydrogen admixture, consistent with the decrease of the Raman intensity ratio in Fig. 3.11(a). In Fig. 3.12(b) it can be observed that the layers with the top values of erosion threshold have been obtained for the lowest growth rates. These low growth rates are a direct consequence of high hydrogen admixtures. The large scatter in Fig. 12(b) however shows that for the medium E_t values the relation of coating quality with growth rate is certainly not strict. A few of the fast grown amorphous coatings (B34 and B39) have a relatively high E_t of 1.68 MJ m^{-2} . Crystalline graphite (low Raman intensity ratios) with high E_t of up to 1.94 MJ m^{-2} were also produced at reasonably high rates (tens of nanometers per second), *e.g.* in trials B47 and B54 and B55 (cf. Table 3.3).

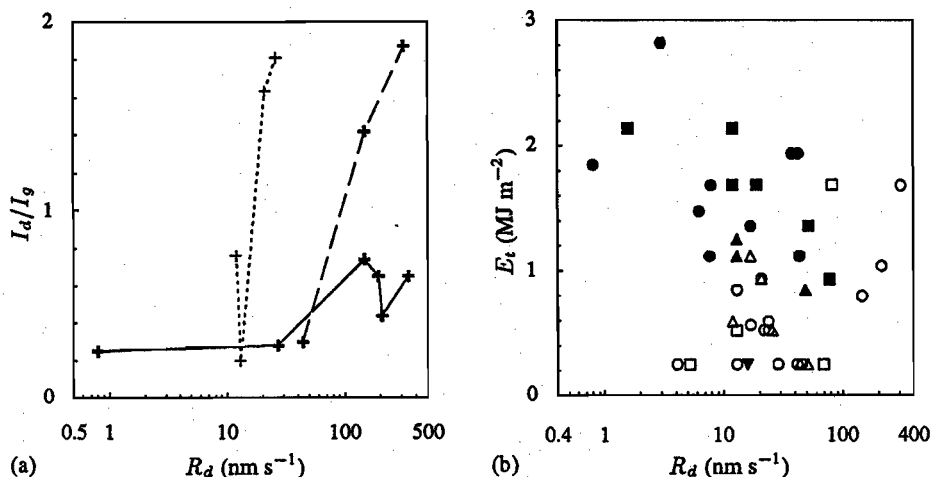


Figure 3.12: (a) Raman intensity ratio (cf. Table 3.1 for legend) and (b) erosion threshold it vs. growth rate R_d (cf. Table 3.2 for legend)

In Fig. 3.13 and 3.14 erosion thresholds are given in relation to Q and T_{py} respectively. In Fig. 3.13 it can be observed that particularly for high values of Q ($\sim 60 \cdot 10^{-6} \text{ W}^{-1}$) the higher values of erosion thresholds were measured.

These Q values are equivalent with an acetylene flow rate of $8 \text{ standard cm}^3\text{s}^{-1}$. This result confirms the observation (not shown here) that E_t does not explicitly depend on the $\{H\}/\{C\}$ ratio but rather on the absolute hydrogen admixture (Fig. 3.11(b)). High absolute hydrogen admixtures together with high Q -values give a low $\{H\}/\{C\}$ value, but a high E_t . In Fig. 3.14 two tendencies seem to be present. For the CG materials (full symbols) the erosion thresholds E_t tends to decrease, and for the AG coatings (open symbols) E_t tends to increase with increasing deposition temperatures. The first effect is caused by the fact that the large hydrogen admixtures used for the deposition of crystalline coatings quench the plasma, and so reduce the plasma heating of the substrate. For the second effect no explanation is available yet.

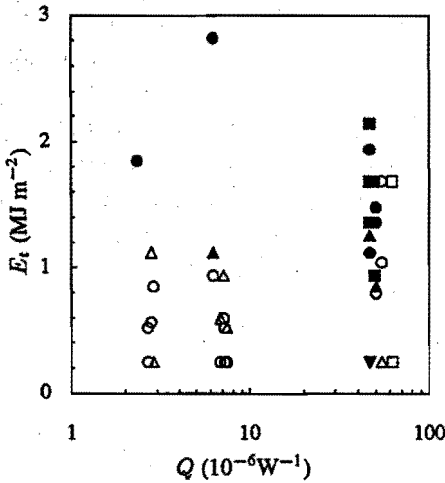


Figure 3.13: Erosion threshold E_t vs. inverse power factor Q (See Table 3.2 for legend).

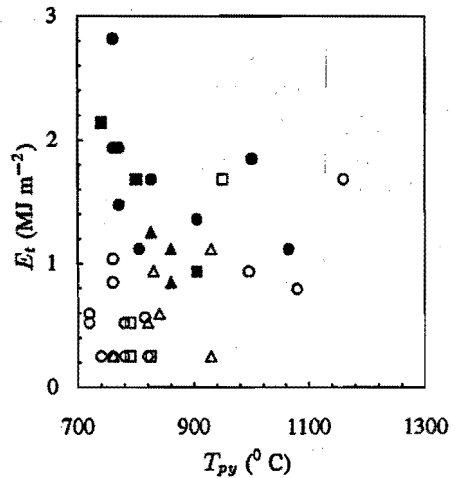


Figure 3.14: Erosion threshold E_t vs. deposition temperature by pyrometry T_{py} (See Table 3.2 for legend).

Concerning the erosion threshold as a function of coating thickness a distribution similar to that of Fig. 3.12(b) is obtained, because of the direct coupling of thickness with growth rate. This implies that as a function of thickness only, taking into account the influence of the growth rate, no real deterioration of the erosion resistance is present.

Regarding the influence of the substrate type it has been observed that, comparing the erosion thresholds for coatings on steel and on CFC that have been deposited under the same conditions, in general the erosion thresholds on steel are lower.

3.5.5 Summary and evaluation of the results of the diagnostics

The best results of Raman intensity ratio and erosion threshold are summarized in Table 3.3. In interesting cases the result for more samples of the same batch are also given. The reduction in deposition area at high chamber pressures p_c is taken into account by dividing the estimated area of deposition for 1 mbar by p_c (in millibars).

The best coating B38 shows slight erosion at an energy density of 2.82 MJ m^{-2} . (For comparison, the CFC substrate begins to show erosion at about 2.8 MJ m^{-2} [4]). According to SEM observations this is a crystalline coating. However, the coating thickness is only $4 \mu\text{m}$. The second best coatings are B8 and B57 with a threshold of 2.14 MJ m^{-2} . These are all crystalline coatings on a substrate of CFC. Coating numbers B57 were made by means of a cup to control the mass flow towards the substrate better. The result for coating B39c is striking. It concerns an amorphous graphite coating, with a very high deposition rate and a relatively high erosion threshold. The coatings of B40 and #B56 were deposited at somewhat less favorable, equal settings. In trial 56 the substrate had been tilted with respect to the plasma beam. It can be noticed that this may improve the thermal shock resistance. The best coating on steel is sample B47St with a threshold of 1.25 MJ m^{-2} . The coating is also crystalline. The conditions of trial B47 ($T_{py} = 825^\circ\text{C}$, $p_c = 10^2 \text{ Pa}$) are considered as representing the optimal reactor settings for crystalline graphite

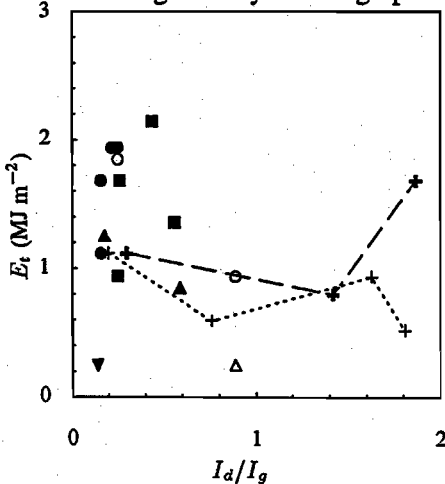


Figure 3.15: Erosion threshold e_t vs. Raman intensity ratio (See Tables 3.1 and 3.2 for legend).

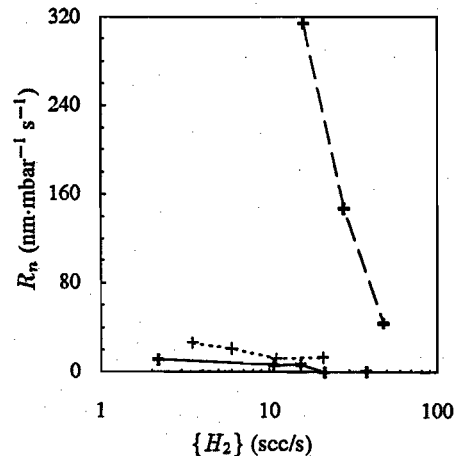


Figure 3.16: Normalized growth rate r_n vs. total hydrogen input (See Table 3.1 for legend).

Table 3.3: Trials with lowest Raman intensity ratios I_d/I_g and highest erosion thresholds E_t , in relation to reactor parameters $\{C_2H_2\}$ and $\{H_2\}$, film thickness d , growth rate R_d , and approximated deposited area A_d : $d_{n-s} = 5$ cm and $p_c = 10^2$ Pa unless indicated otherwise. Flow rates in sccs, = standard $cm^3 s^{-1}$.

Sample	$\{C_2H_2\}$ (sccs)	$\{H_2\}$ (sccs)	d (μm)	R_d ($nm s^{-1}$)	A_d (cm^2)	I_d/I_g	E_t ($MJ m^{-2}$)	Remarks
B38c	1	21	4.	3.	7.5	---	2.82	
B57c	8	40	57.	12.	7.5	---	2.14	Recirculation cup, $d_{n-s} = 8$ cm
B57St			76.	16.	12.	0.14	<0.5	
B47	8	40	39.	7.9	7.5	0.16	1.68	Optimum
B47c			212.	44.	7.5	0.30	1.12	
B54	8	40	204.	43.	0.75	0.22	1.94	Optimum, but $p_c \uparrow 10^3$ Pa repetition of B54
B54c			~1900.	~400.	0.75	1.66	---	
B55			193.	38.	0.75	0.25	1.94	
B52c	$\frac{3}{8}$	21	2.	0.8	0.75	0.25	1.85	$p_c = 10^3$ Pa
B40c	8	20	265.	147.	7.5	1.42	0.80	
B56c			69.	19.	7.5	0.26	1.68	oblique incidence
B59c			282.	78.	0.75	0.25	0.94	oblique incidence,
B46c	8	40	~2300.	~2600.	0.13	0.43	---	$p_c = 6.10^3$ Pa
B8c	8	20	5.9	1.6	30.	0.44	2.14	$d_{n-s}=20$ cm
B39c	8	8	377.	314.	7.5	1.87	1.68	AG
B34	8	0	42.	83.	15.	---	1.68	AG, $d_{n-s}=10$ cm, bias-261 V

c, sample in center position of pedestal; St, steel.

deposition so far, and equally B54 and B55 with a higher p_c . All three trials yield coatings with a high erosion threshold.

Considering the equal results of trials B54 and B55 it can be deduced that the reproducibility of both the deposition process and the erosion threshold measurement is good.

In Fig. 3.15 the results of Raman spectroscopy and erosion threshold are combined. In general the highest E_t values coincide with the most crystalline coatings according to the Raman spectrum. This means that Raman spectroscopy

is a suitable means for a first fast prediction on the thermomechanical properties of the coating. There are exceptions, *e.g.* B39, an amorphous coating with a high erosion threshold. Other properties (*e.g.* density) of the coating play an important part in determining the thermomechanical qualities.

3.5.6 Growth rate and efficiency considerations.

In Fig. 3.16 the normalized growth rates as a measure for the volume deposition rates are shown as a function the hydrogen admixtures. The deposition rates decrease with increasing hydrogen admixtures generally. In order to control the relative etching effect by the hydrogen radicals, the use of a small nozzle to substrate distance of 5 cm was necessary. The area of deposition was measured directly on the sample pedestal. It appears that this area is somewhat larger than the cross section area of the actual (light emitting) plasma beam as shown in Fig. 3.3. This is caused by the stagnation by the pedestal causing a sideways expanding flow of plasma over the pedestal. For $d_{n-s} = 5$ cm and $p_c = 10^2$ Pa the area of deposition A_d is ~ 7.5 cm². This value is used as the standard value, and can be linearly adjusted for d_{n-s} and reciprocally for p_c . Again the three lines for constant Q are drawn. The two dashed lines are for trials with chamber pressure of 1 mbar. The solid line represents a trial sequence with various high chamber pressures. In this view mostly the results for the high Q values ($Q \simeq 60 \cdot 10^{-6}$ W⁻¹), *i.e.* a high acetylene flow of 8 standard cm³s⁻¹ are practically useful. For smaller deposition areas, with these high Q values, CG can be obtained with much higher (linear) growth rates, *e.g.* B46 (more than 2000 nm s⁻¹!).

A way of describing the efficiency of the deposition proces is the following. A monomer flow rate of 1 standard cm³s⁻¹ (at room temperature) means a carbon injection rate of 0.488 mg s⁻¹ for each carbon atom in the monomer. When every carbon particle is deposited at the substrate we get the following equivalent deposition rate (in nanometers per second)

$$R_{eq} = 4.88 \cdot 10^3 \Phi n / \rho A_d \quad (3.2)$$

with n the number of carbon atoms in the monomer, Φ (standard cm³s⁻¹) the monomer flow rate, ρ (g cm⁻³) the density of the deposit, A_d (cm²) the estimated area of deposition. We define an efficiency factor F as the ratio of the observed and of the equivalent deposition rate, $F = R_d / R_{eq}$. In Table 3.4 the most interesting results are given (for AG and CG calculated with $\rho = 1$ g cm⁻³). In the calculations the inhomogeneity of the growth rate over the area was not taken into account.

It can easily be calculated that, with a flow rate of 1 standard cm³s⁻¹ and a deposition efficiency F of 1, it would take ~ 1200 days to repair a typical

Table 3.4: Summary of deposited areas, equivalent deposition rates, observed deposition rates and deduced deposition efficiency factor F

A_d (cm^2)	R_{eq} (nm s^{-1})	R_d (nm s^{-1})	F	type	reference or sample	remarks
3.	93	10	0.11	diamond	[3]	{ CH_4 }=0.2
7.5	10410	44	0.004	CG	B47	{ C_2H_2 }=8
7.5	1301	21	0.016	CG	B38	{ C_2H_2 }=1
7.5	10410	314	0.03	AG	B39	{ C_2H_2 }=8
7.5	1301	196	0.15	AG	B35	{ C_2H_2 }=1
30.	2603	383	0.15	AG	B5	{ C_2H_2 }=8
120.	239	200	$\sim 1.$	a-C:H	[2]	{ C_2H_2 }=6.7

disruption erosion damage. For AG with a F of 0.1 and with the application of 10 arcs with a flow rate { C_2H_2 }= 10 standard cm^3s^{-1} (essential to keep the number of arcs limited!) a value of about 120 days is obtained. With the application of more arcs this period could be reduced further, or CG (F typically ~ 0.01) could be applied. Covering the total divertor plate area of 200 m^2 would take about 50 times as long, so this is problematic.

The calculations for diamond and a:C-H ([2, 3]), although unsuited for the present purpose, are interesting. For diamond we obtain a surprisingly high F of ~ 0.11 . However, because of the low flow rate { CH_4 }=0.2 standard cm^3s^{-1} only a very low part of the actual arc capacity is used. For a:C-H we obtain $F \sim 1$.

3.5.7 Qualitative study of thermal shock damage

In a second heat shock test sequence the best erosion resistant coatings were subjected to a 3 MJ m^{-2} (in 10 ms) thermal shock. Erosion depths were measured with a light microscope by focusing on the highest and lowest point of the erosion crater respectively. The light microscope is equipped with a nonius, so the depth can be measured in microns. However, this method is not accurate and the error may be tens of percents. SEM analysis yields more detailed information of the surface damage of the coatings. The most interesting results of tests of the CG coatings are given in the Figs. 17-19. The structure of all these coatings is well

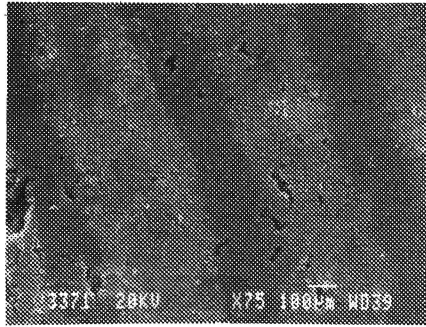


Figure 3.17: B38c; highest $E_t = 2.82 \text{ MJ m}^{-2}$; $d = 4 \text{ }\mu\text{m}$; partly eroded and cracks

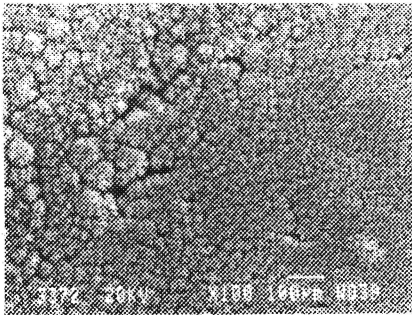


Figure 3.18: B57c; "recirculation" trial; $d = 57 \text{ }\mu\text{m}$; lowest $E_d = 32 \text{ }\mu\text{m}$; layer modification

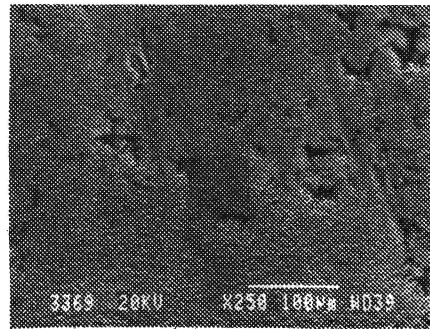


Figure 3.19: B47; lowest $I_d/I_g = 0.16$ on CFC; crystallinity optimum; $d = 39 \text{ }\mu\text{m}$; partly eroded, small cracks.

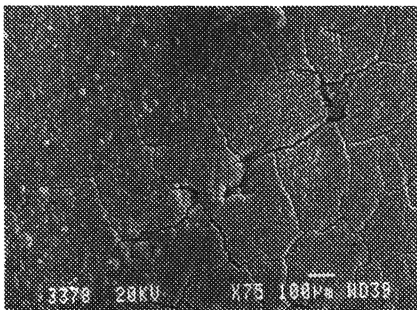


Figure 3.20: B34; bias -261 V d.c. ; $d = 43 \text{ }\mu\text{m}$; $R_d = 83 \text{ nm s}^{-1}$; high $E_t = 1.68 \text{ MJ m}^{-2}$; eroded and large cracks.

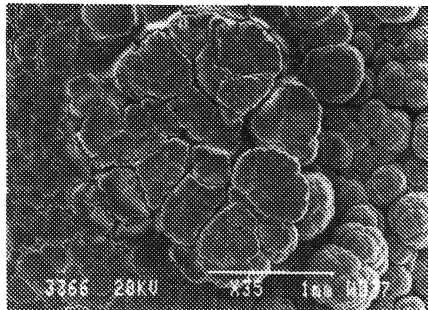


Figure 3.21: B39c; $d = 377 \text{ }\mu\text{m}$; high $R_d = 314 \text{ nm s}^{-1}$; high $E_t = 1.68 \text{ MJ m}^{-2}$; eroded depth $145 \text{ }\mu\text{m}$; flattened cauliflowerers.

represented by the typical foliate structure shown in Fig. 3.7, with only minor variations. In Fig. 3.17 a micrograph of the thin coating of substrate B38c, with the highest erosion threshold is shown. The Raman spectrum of this sample is not available, but the spectrum of B38St out of the same batch (cf. Fig. 3.8(c)) indicates a highly crystalline material. It can be observed that on thermal shock testing the layer remains in place but has been partly eroded. In the residue cracks protruding in the CFC substrate are present. In Fig. 3.17 the result for the specific batch B57 (the "recirculation trial") is shown. The center sample of this batch (B57c) appeared to have the smallest erosion depth. It can be noted that the layer has remained in its place. The foliates have changed in structure somewhat, but are still clearly observable. The loss of thickness can be explained by erosion, but also by layer modification due to a kind of annealing effect. In Fig. 3.19 the micrograph for the interesting trial of B47 is shown. This coating is highly crystalline (Table 3.3). Under the 3 MJ m^{-2} thermal shock the layer suffered by erosion but remained largely intact. As for trial B57, some modification of the foliate structure has occurred. In Figs. 3.20 and 3.21 the micrographs of two typical AG coatings after thermal shock testing are shown. It concerns B34 and B39c. Both had a rather high E_t of 1.68 MJ m^{-2} and were produced at high growth rates (Table 3.3). Upon thermal shock testing they appear to remain in their place. The former shows extensive cracks, while the latter suffers by erosion, resulting in a crater of flattened cauliflowers.

3.5.8 Diamond conditions

Applying hydrogen admixtures suitable for diamond deposition onto silicon [3], on CFC substrates etching becomes predominant. Only in one trial on the center CFC substrate a small peak of CG was deposited. On the accompanying steel substrate diamond was formed. Images of these deposits are shown in Figs. 3.22 and 3.23. In Fig. 3.22 it can be observed that underneath the diamond crystals an amorphous carbon sublayer has first been formed on the steel. As direct diamond formation on steel is theoretically impossible, this has been a necessary condition. The influence of the substrate type in the deposition process is once more stressed. The present finding is in agreement with the assumption [26] that diamond deposition on graphite is impossible. Recently however Angus has reported the growth of diamond on graphite [27].

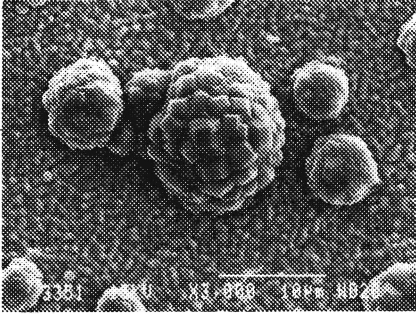


Figure 3.22: SEM image of diamond (precursor) deposited onto steel, top view, B45; $\{C_2H_2\}=3/8$; $\{H_2\}=37.5$; $\{H\}/\{C\}=101$; $T_{py} \approx 810^\circ C$ $p_c = 6.0 \cdot 10^3 Pa$; $P_{arc} = 3.19 kW$; $Q = 2.3 \cdot 10^{-6} W^{-1}$; $d \approx 7 \mu m$, $R_d \approx 2.0 nm s^{-1}$.

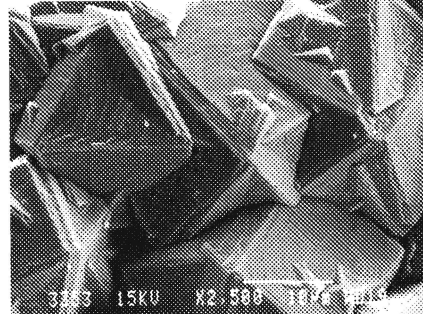


Figure 3.23: SEM image of diamond film deposited onto steel, top view, B49; $\{C_2H_2\}=0.25$; $\{H_2\}=50$; $\{H\}/\{C\}=201$; $T_{py} \approx 900^\circ C$ $p_c = 6.4 \cdot 10^3 Pa$; $P_{arc} = 4.17 kW$; $Q = 1.2 \cdot 10^{-6} W^{-1}$; $d \approx 17 \mu m$, $R_d \approx 4.7 nm s^{-1}$.

3.6 Conclusions

- A diverse range from amorphous to highly crystalline graphite was deposited. Amorphous graphite shows a typical cauliflower structure. In crystalline graphite distinct foliates with dimensions of several micrometers can be observed. The Raman spectrum of the most crystalline materials is comparable with that of the substrate CFC, *i.e.* of conventional CVD pyrolytic graphite. For the deposition of crystalline materials the addition of an etching medium such as hydrogen is essential. Growth rates were on the order of hundreds of nanometers per second for the amorphous graphites and tens of nanometers per second for the crystalline graphites, both on areas of several square centimeters.
- For an application as a plasma-facing material processing of the coating material still needs improvement. Upon laser thermal shock tests the best crystalline coatings have an acceptable erosion threshold of about $2 MJ m^{-2}$ (in 10 ms). Of the amorphous coatings only one (B39) showed a reasonable thermomechanical behavior, with a threshold of $1.7 MJ m^{-2}$. This coating could be produced with an adequate growth rate of hundreds of nanometers per second. Under the $3 MJ m^{-2}$ pulse most coatings suffered from substantial damage. The adhesion of most coatings to the

CFC substrates is good, to steel it is poor. The mechanical strength of the material is moderate. It is porous. This may be an advantage in resisting heat shocks as it may prevent cracking. In view of tritium retention it is an undesired property.

- Relations between deposited material and the deposition conditions were found. The three diagnostics SEM, Raman spectroscopy and laser thermal shock testing give consistent results: hydrogen addition, growth rate and possibly the Q -factor play a major role in determining the quality of the graphite. The correlation between the results of the diagnostics implies that SEM and Raman spectroscopy are suitable and fast methods to obtain a prediction of the coating quality, and in particular its thermomechanical qualities.
- The type of substrate is a principal factor in the deposition process. It appeared that the general condition of a large hydrogen admixture (to obtain a hydrogen-free crystalline layer), on CFC results in etching. With the hydrogen concentrations necessary for the deposition of pure diamond (on silicon [3]), crystalline graphite was deposited onto the center CFC substrate. On a steel substrate diamond was deposited onto an amorphous sublayer, once more indicating the influence of the substrate.

Concerning optimization of the deposition process, recent investigations indicate that with the use of another etching medium, *e.g.* oxygen, crystalline materials can be produced at much higher growth rates [28]. An issue is to verify that no incorporation of oxygen in the layer occurs.

The best coatings appear to have been produced with the aid of a recirculation cup (B57). Also a coating with oblique incidence of the beam (B56) gave a good result, as well as one with bias (B34). Optimization of other aspects of the deposition technique, such as substrate geometry, is promising.

The optimum between (volume) growth rate and crystallinity is most probably not yet reached. At present, it is approximated best by the conditions of B47. It is expected that with independent control of the various reactor parameters, *e.g.* substrate temperature and nozzle to sample distance, the results can still be improved.

Acknowledgements

This paper reports the main results of the NET Garching - ECN Petten - TU Eindhoven research agreement *Investigation of Plasma-deposited Carbon Films as Possible Means of Divertor Repair*, as established in the NET contract 90-237

between The European Atomic Energy Community and Euratom/FOM Association. It is funded by the Commission of the European Communities, which is representing the European Atomic Energy Community.

The authors would like to thank M.J.F. van de Sande for solid technical support, and G.M. Janssen and M.C.M. van de Sanden for the computational support. Further the authors would like to thank Dr. Stufkens and Mr. Snoeck of the University of Amsterdam for measuring the Raman spectra.

Bibliography

- [1] R.D. Watson, ed., *ITER Divertor Engineering Design, ITER-TN-PC-8-9-1*, Max-Planck-Institut für Plasmaphysik, Garching-bei-München, (1989).
- [2] G.M.W. Kroesen, *Ph.D. Thesis*, Eindhoven University of Technology, (1988).
- [3] P.K. Bachmann, H. Lydtin, D.U. Wiechert, J.J. Beulens, G.M.W. Kroesen, and D.C. Schram, *Proc. 3rd Int. Conf. on Surface Modification*, T.S. Sudarshan and D.G. Bhat (eds.), Surface Modification Technologies III, The Minerals, Metals and Materials Society, Warrendale (PA), 69, (1990).
- [4] J.G. van der Laan, H.T. Klippel, R.C.L. van der Stad, and J. Bakker, *Fusion Technol.*, **19**, 2070, (1991).
- [5] T. Kuroda and G. Vieider, eds., *ITER Plasma Facing Components*, ITER Documentation series, No. 30, International Atomic Energy Agency, Vienna, (1990).
- [6] M.C.M. van der Sanden, *Ph. D. thesis*, Eindhoven University of Technology, (1991).
- [7] J.J. Beulens, *Ph. D. thesis*, Eindhoven University of Technology, (1991).
- [8] A.J.M. Buuron, J.J. Beulens, M.J.F. van de Sande, and D.C. Schram, *Fusion Technol.*, **19**, 2049, (1991).
- [9] G.M.W. Kroesen, D.C. Schram, A.T.M. Wilbers, and G.J. Meeusen, *Contrib. Plasma Phys.*, **31** (1), 27, (1991).
- [10] D.L. Smith *et al.* and (US ITER Team), *U.S. Technical Report for the ITER Plasma Facing Components, ITER-TN-PC-1-0-4-2*, Max-Planck-Institut für Plasmaphysik, Garching-bei-München, (1990).
- [11] W. Zhu, C.A. Randall, A.R. Badzian, and R. Messier, *J. Vac. Sci. Technol. A*, **7** (3), 2315, (1989).
- [12] Y. Mitsuda, Y. Kojima, T. Yoshida, and K. Akashi, *J. Mat. Sci.*, **22**, 1557, (1987).
- [13] J.G. van der Laan and J. Bakker (Petten ECN), *private communication*, (1990).

- [14] J.G. van der Laan, J. Bakker, R.C.L. van der Stad, and H.T. Klippel, *Proc. 16th Symp. on Fusion Technology, London, September 3-7, 1990*, Elsevier, Amsterdam, 438, (1991).
- [15] J.G. van der Laan, H.T. Klippel, J. Bakker, and R.C.L. van der Stad, *Proc. 4th Int. Conf. Fusion Reactor Materials, Kyoto, Japan, 1989*, in *J. Nucl. Mater.*, **179-181**, 270, (1990).
- [16] R. Messier and J.E. Yehoda, *J. Appl. Phys.*, **58** (10), 3739, (1985).
- [17] J. Robertson, *Adv. Phys.*, **35** (4), 317, (1986).
- [18] N.B. Brandt, S.M. Chudinov, and Ya. G. Ponomarev, *Semimetals; 1. Graphite and its compounds*, 388, North-Holland, Amsterdam, (1988).
- [19] G. M. Janssen, *Master's Thesis*, Eindhoven University of Technology, (1991).
- [20] R.J. Nemanich and S.A. Solin, *Phys. Rev. B*, **20**, 392, (1979).
- [21] F. Tuinstra and J.L. Koenig, *J. Chem. Phys.*, **53**, 1126, (1970).
- [22] K. Niwase, K. Nakamura, I. Tanaka, Y. Miyamoto, and T. Tanabe, *Proc. 4th Int. Conf. on Fusion Reactor Materials, Kyoto, Japan, 1989*, in *J. Nucl. Mater.*, **179-181**, 214, (1990).
- [23] K. Ashida, K. Kanamori, and K. Watanabe, *J. Vac. Sci. Technol. A*, **6** (4), 2232, (1989).
- [24] P.L. Walker and P.A. Thrower, eds., *Chemistry and Physics of Carbon; A Series of Advances, Vol. 11*, Marcel Dekker, New York, (1984).
- [25] A. Staudinger and S. Nakahara, *Thin Solid Films*, **45**, 125, (1977).
- [26] S. P. Chauhan, J.C. Angus, and N.C. Gardner, *J. Appl. Phys.*, **47** (11), 4746, (1976).
- [27] J.C. Angus, Oral contribution to *Proc. 2nd Eur. Conf on Diamond, Diamond-like and Related Materials, Nice, September 2-6, 1991*.
- [28] D.C. Schram and J.J. Beulens, *private communication*, Eindhoven University of Technology, (1991).

Chapter 4

Absorption spectroscopy on the expanding cascaded arc plasma jet

abstract

An expanding cascaded arc plasma jet is used for the deposition of amorphous and crystalline carbon films. In the expanding jet, an important radicalization process is the charge exchange between the argon ions of the carrier plasma and the injected hydrogen and deposition monomers, followed by dissociative recombination. Besides this process, excitation transfer from argon metastables to the admixed species may occur. In order to investigate the order of magnitude of the latter effect, the densities of argon- and hydrogen metastable states were determined by means of absorption spectroscopy. An experimental set up using a cascaded arc as a continuum light source with optical multichannel detection is presented. Some specific aspects in employing these components for absorption spectroscopy are treated. Measurements were done on strong argon lines in the range between 790 and 860 nm, and on the 656.3 nm H_{α} line. Analyzing the experimental data using a common Abel inversion technique resulted in radial density profiles obscured by oscillations due to the noise in the data. Therefore, an efficient numerical method for obtaining radial density and temperature profiles, using Abel integration in stead of Abel inversion was developed. For a pure argon plasma the $Ar(3p^54s)$ metastable and resonance state densities lay in the range of 10^{18} to 10^{16} m^{-3} at a chamber pressure of 40 Pa. The decay of the metastables and resonance states densities in axial direction were also calculated using a local quasi steady state model. It appears that the (re)capture of resonance radiation is keeping up the population density of the argon $4s$ states. The effect of the admixture of various gases used in deposition experiments, such as hydrogen, oxygen and methane on the $Ar(3p^54s)$ metastable and resonant states was investigated. The addition of hydrogen to the argon plasma leads to a rapid disappearance of the argon $4s$ states. Possible explanations are the excitation energy transfer with the $H^*(n=2,3)$ levels, and a lowering of the argon ion density by dissociative recombination. Densities of

the hydrogen H(2s) metastable state could only be measured at a relatively high chamber pressure and a high hydrogen partial pressure. For a pressure of $1.1 \cdot 10^3$ Pa in a 1:4 hydrogen/argon plasma, at the plasma axis at a distance of 20 mm from the nozzle, the densities are of the order of 10^{16} m^{-3} .

4.1 Introduction

With the expanding cascaded arc method layers of all types of carbon from amorphous hydrogenated carbon to the crystalline forms graphite and diamond are deposited at high rates. To this end, hydrocarbons, and hydrogen and/or oxygen are admixed in the argon carrier gas. In the past, the expanding cascaded arc plasma jet has been subject of extensive studies already [1, 2, 3]. It has been postulated [2], that carbon ions, hydrocarbon radicals and excited carbon species are created through multiple charge transfers from the argon to the hydrocarbon radicals, followed by dissociative recombinations of the radicals. The question has risen whether the argon Ar($3p^5 4s$) metastable states (in the following denoted as argon 4s states) can also play an important role through excitation energy transfer to other species, since the rate coefficients for charge transfer from argon ions and excitation transfer from argon 4s metastables are often of the same order. *E.g.* for methane these rate coefficients are both of the order of $1 \cdot 10^{-15} \text{ m}^3 \text{ s}^{-1}$ [4, 5]. Ion densities in argon/methane plasmas have been determined in the past [2] using emission spectroscopy and, recently, by probe measurements [6]. Absorption spectroscopy enables the determination of densities and temperatures of metastable states, which are not observable in emission spectroscopy. The influence of the admixture of various gases used in deposition experiments like hydrogen, oxygen and hydrocarbons on the density of the argon 4s states was studied on various positions in the expanding plasma jet. In [7] a method was presented for solving radial profiles of the species densities, using a conventional deconvoluting Abel inversion method in combination with the common correction procedure for nonlinearity in the case of strong absorptions [8]. An important restriction in applying this method is that one has to assume that the absorption line profile does not change significantly over the line of sight. In other words the gradients of the temperatures and the densities in radial direction are assumed to be small. This assumption only holds in the subsonic part of the expansion. In the supersonic part and the shock interesting features are averaged out by applying this simplification. Furthermore, by employing a deconvolution technique like Abel inversion, results are obscured by the noise amplifying character of these techniques. In the present study an efficient numerical method is developed, based on a reverse approach using Abel integration over a line of sight. This

method enables the implication of radial variations of the absorption line profile and leads to a noise diminishing convolution technique.

Practically, the present study also serves as a prestudy of future absorption spectroscopy on the species which may be important for the deposition of the crystalline forms. The abundance of carbon ions in a plasma used for the deposition of amorphous hydrogenated carbon layers has already been proven with other methods [2, 1]. Absorption spectroscopy supplies a means to study whether also hydrocarbon radicals in the ground states play a role in the deposition of diamondlike carbon, graphite and diamond. It is generally accepted that for graphite deposition the C_2 radical is beneficial (cf. Chapter III). Concerning the species prevalent for the deposition of diamondlike and diamond materials, no unanimity exists in the literature. Generally it is assumed that hydrocarbon radicals are relevant. Various hydrocarbon radicals have been postulated, such as CH_3 [9, 10, 11], C_2H_2 [12, 13], CH [14] and many others [15, 9, 16]. We believe that in our method, using a thermal plasma with a high ionization degree as a source, the role of the complex radicals will be limited and future absorption studies will be directed to the simple radicals CH and C_2 and the C atoms and ions. Up to now, with the present experimental arrangement, no absorption on these species could be measured. Probably a multipass optical system is required for this purpose; in a comparable situation a system of 30 passes was needed to obtain a measurable absorption (a few percent) on the molecular radicals [17]. This is due to the distribution of the signal over the rotational bands.

In this chapter, firstly a brief survey of techniques, theory and data analysis methods of absorption spectroscopy will be given. Subsequently the experimental set up will be described and some specific aspects of the absorption technique using a continuum light source will be discussed. The convolution method for elaborating the experimental data will be treated. In Sec. 4.4.1 the results for the purely argon plasma will be presented, recapitulating firstly the results of [18]. Then the more accurate results as obtained by the actual convolution method will be given and compared with theoretical values as calculated with a local quasi steady state approximation. Finally, the results of the effect on the argon $4s$ densities of admixing various gases in the argon plasma and a preliminary result on the hydrogen $2s$ metastables will be discussed.

4.2 General description of absorption spectroscopy

4.2.1 Techniques of absorption spectroscopy

Techniques of optical absorption are frequently used for the determination of the absolute concentrations in a plasma of atoms and molecules in ground and excited

states. Nowadays, the sensitivity of spectroscopic instruments is adequate for the measurement of the absorption on the metastable and resonant levels of various radicals and stable particles, even in the case of a low pressure plasma.

Different methods have been used for the quantitative determination of the absorption in a medium. Line reversal and reabsorption methods do not require [19, 20, 21] the application of an independent light source, and the results can easily be interpreted if the spectral lines emitted and absorbed by the medium have a Gaussian profile owing to the Doppler effect. In that case one must also know the temperature of the heavy particles in the plasma. The interpretation of the results of reabsorption measurements may be more complicated in the case of additional van der Waals [22] and Stark broadenings and shifts of the spectral lines [23]. But serious complications arise when the medium is inhomogeneous and at the same time both emission and absorption of radiation occur [19].

Another method, developed in [24] and [25] uses a mirror placed at the end of the absorbing medium in order to reflect the light towards the photon detector placed at the other end. One can determine the absorption by comparing the intensities obtained with and without the mirror. The main difficulty of this method consists of determining the intensity of the reflected component, taking into account the reflectivity of the mirror and the transmission efficiencies of the windows (which may change in time).

Many authors use for the determination of the absorption coefficient an independent light source, which radiates either spectral lines, or continuum [26, 27]. The recently developed cascaded arc plasma source [28] has already proven to be a very versatile continuum light source. It has a high intensity in the ultraviolet, visible and near infrared wavelength range (with spectral line emission approximately according to Planck's law (with $T = 15\ 000\ \text{K}$)). The source fulfills the requirement of emitting a narrow beam of sufficiently high intensity. On the other hand, it has to be checked that perturbation of the plasma under observation by the strong radiation does not occur.

If the absorbing medium emits the same lines as for which one measures the absorption, then the application of a modulated source and phase-sensitive detection are indicative. Another method is to measure the pure emission of the absorbing medium without the light source, and subtract it from the measurement with the light source on.

Currently, the method with a cascaded arc as a light source is used for the measurement of metastable particles in the expanding cascaded arc plasma, a nonequilibrium low-pressure atomic and molecular plasma.

4.2.2 Absorption coefficient of spectral lines

The general case of the transport of radiation through inhomogeneous, radiating plasmas is very complicated, and has been solved only for some particular examples [19]. Significant simplification is obtained in our case where the emission of the absorbing medium is small compared to the intensity of the light source. Consider a beam of parallel light from a source emitting a continuum spectrum with constant spectral intensity I_0 , passing through an (in)homogeneous absorbing medium (cf. [26].)

The attenuation of the intensity on passing through a slab of thickness dx of a medium is then:

$$\frac{dI_0}{dx} = -k(\nu, x)I_0, \quad (4.1)$$

where $k(\nu, x)$ is the frequency and spatially dependent absorption coefficient of the medium. If the medium is homogeneous then the spectral intensity of the transmitted light I_ν shows an exponential dependence:

$$I_\nu = I_0 \exp(-k_\nu l), \quad (4.2)$$

where k_ν is the frequency dependent absorption coefficient of the medium, l is the thickness of the absorbing layer. (As common, frequency dependence or definition per unit of frequency of a quantity will be expressed with ν as a subscript, so $k_\nu = k(\nu)$ etc.) Eqs. (4.1) and (4.2) express the Beer-Lambert relationship in its differential and integral forms respectively. The first has to be used in the case of inhomogeneous media.

The dependence of the absorption coefficient k_ν on the frequency ν can be described by a line profile P_ν , which, as a rule, is normalized on unity area:

$$\int_0^\infty P_\nu d\nu = 1. \quad (4.3)$$

The integration up to infinity implies the integration over the line profile as a whole.

If it is assumed, that the upper quantum level k of the optical transition $i \rightarrow k$ is not significantly populated from the quantum level i , then the absolute value of k_ν results from the relationship [29]:

$$\int_0^\infty k_\nu d\nu = \frac{h\nu}{c} N_i B_{ik}, \quad (4.4)$$

with N_i the total number of absorbing particles per unit volume, h Planck's constant, c the speed of light and B_{ik} the Einstein coefficient (transition probability) for absorption. B_{ik} is related to the Einstein coefficient for spontaneous emission A_{ki} by

$$A_{ki} = \frac{g_i}{g_k} B_{ik} \frac{8\pi h\nu^3}{c^3}, \quad (4.5)$$

with g_i and g_k the statistical weights of lower and upper level respectively. By this equation the Einstein B coefficient is defined in terms of radiation density (cf. [26] where a definition in terms of isotropic radiation is used). From (4.3) and (4.4) one immediately obtains the line absorption coefficient:

$$k_\nu = \frac{h\nu}{c} N_i B_{ik} P_\nu = \frac{h\nu}{c} N_{i\nu} B_{ik} \quad (4.6)$$

with $N_{i\nu}$ the number of absorbing particles per frequency interval and per unit volume. If the upper level of the transition is being populated from the lower level i , then induced emission occurs. Usually the contribution of the induced emission is included in the absorption coefficient. This is convenient, since the induced emission has the same frequency and direction as the incident radiation, and thus may be considered as negative absorption. Assuming that the line profiles for emission and absorption are the same, then the absorption coefficient k'_ν , with a correction for induced emission has the following form:

$$\begin{aligned} k'_\nu &= \frac{h\nu}{c} (N_{i\nu} B_{ik} - N_{k\nu} B_{ki}) \\ &= k_\nu \left(1 - \frac{N_{k\nu} B_{ki}}{N_{i\nu} B_{ik}}\right). \end{aligned} \quad (4.7)$$

Taking into account that $g_k B_{ki} = g_i B_{ik}$, one can obtain the integrated absorption coefficient in general form:

$$\int_0^\infty k'_\nu d\nu = \frac{h\nu}{c} B_{ik} N_i \left(1 - \frac{g_i N_k}{g_k N_i}\right), \quad (4.8)$$

with N_i and N_k the total number of absorbing particles per unit volume in the lower and the upper level respectively. Often the ratio N_k/N_i is very small and using Eq. (4.5) we can write the frequency integrated absorption coefficient in a more convenient way as:

$$\int_0^\infty k_\nu d\nu = \frac{\lambda_0^2 g_k}{8\pi g_i} N_k A_{ki}. \quad (4.9)$$

For the description of absorption processes often the oscillator strength f_{ki} is used in stead of the Einstein transition probabilities. This concept was introduced by Ladenburg [29]. Classical theory yields for the integrated absorption:

$$\int_0^{\infty} k_{\nu} d\nu = \frac{e^2}{\epsilon_0 m_e c} N_i f_{ki}, \quad (4.10)$$

where e and m_e are the electron elementary charge and mass and ϵ_0 is the dielectric permittivity of vacuum. The oscillator strength f_{ki} is directly proportional to the Einstein A_{ki} coefficient.

Furthermore, the degeneracies of the states i and k have to be taken into account leading to a different absorption f_{ik} and emission oscillator strength f_{ki} :

$$g_i f_{ik} = g_k f_{ki}. \quad (4.11)$$

Now combining Eqs. (4.9) and (4.10), f_{ik} is related to A_{ki} in the following way:

$$f_{ik} = \frac{4\epsilon_0 m_e c \lambda^2}{2\pi e^2} \cdot \frac{g_k}{g_i} \cdot A_{ki}. \quad (4.12)$$

The Einstein A_{ki} coefficient is related to the radiative lifetime τ of a state by:

$$\tau = \frac{1}{\sum_i A_{ki}}. \quad (4.13)$$

So in the case of one distinct transition (e.g. a resonance line), A_{ki} is inversely proportional to the lifetime of the upper state.

4.2.3 Spectral line shapes and broadening mechanisms

The particular shape of the profile of the absorption coefficient depends on the mechanisms of spectral line broadening in the plasma. For this purpose one can consider three types of lines profiles [26, 30].

1 The Gaussian profile:

$$k_{\nu} = k_0 \exp \left\{ - \left[2\sqrt{\ln 2} \frac{(\nu - \nu_0)}{\Delta\nu_D} \right]^2 \right\}, \quad (4.14)$$

with $\Delta\nu_D$ the full width at half-height. The value of $\Delta\nu_D$ depends only on the temperature T , and on the atomic weight M of the absorbing (emitting) particles:

$$\frac{\Delta\nu_D}{\nu_0} = \frac{2\sqrt{\ln 2}}{c} \sqrt{2k_B T/M}, \quad (4.15)$$

with k_B the Boltzmann constant.

By integrating Eqs. (4.14) and using (4.9) the value of the absorption coefficient at the center of the line, k_0 , is expressed as a function of the density of the absorbing particles N_i as follows:

$$k_0 = \frac{2\sqrt{\ln 2}}{\Delta\nu_D} \frac{\lambda_0^2 N_i A_{ki} g_k}{8\pi^3/2g_i}. \quad (4.16)$$

2 The Lorentzian profile:

$$k_\nu = k_0 \frac{\Delta\nu_L/2}{(\Delta\nu_L/2)^2 + (\nu - \nu_0)^2}, \quad (4.17)$$

where $\Delta\nu_L$ is the full width at half-height. This profile results from the finite lifetime of the states (natural broadening), collisions (homogeneous broadening) and influences of charged particles (Stark broadening). The absorption coefficient at the center of the line is in this case:

$$k_0 = \frac{2\pi}{\Delta\nu_L} \frac{\lambda_0^2 N_i A_{ki} g_k}{8\pi^3/2g_i}. \quad (4.18)$$

In Sec. 4.4.1 the specific case of only natural broadening is adressed in more detail.

3 The Voigt profile, resulting from the convolution of Gaussian and Lorentzian profiles

$$k_\nu = k_0 \frac{a}{\pi} \int_{-\infty}^{+\infty} \frac{\exp(-y^2) dy}{a^2 + (\omega - y)^2}, \quad (4.19)$$

with $a = \sqrt{\ln 2} \Delta\nu_L / \Delta\nu_D$, $\omega = 2\sqrt{\ln 2}(\nu - \nu_0) / \Delta\nu_D$ and $y = \delta \cdot 2\sqrt{\ln 2} / \Delta\nu_D$; δ expresses the variable distance to a point $\nu - \nu_0$ of the Lorentz profile (which is centered at ν_0). The Lorentz profile (with parameter $\nu - \nu_0$) is folded with a Gaussian profile (with parameter δ). In this case k_0 is defined by expression (4.16), but it should be emphasized, that this value of k_0 does not correspond to the absorption coefficient at the center of the line. The Voigt profile can only be approximated numerically (cf. e.g. [31]).

4.2.4 Total absorption of spectral lines

Frequently, one is interested more in the integrated (total line) intensity and in the integrated line absorption than in the spectral line intensity I_ν . For example, one wants to determine the density of the absorbing species from the absorption of continuum radiation. If the intensity of the transmitted radiation is plotted against the frequency in the vicinity of an absorption line, the obtained dependences may appear as the solid and dashed curves in Fig. 4.1.

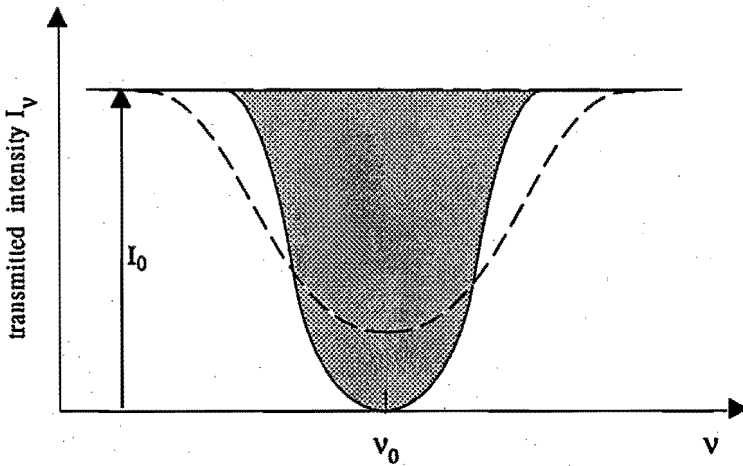


Figure 4.1: Typical profiles obtained in an absorption experiment. The shaded area indicates the integrated absorption A_g for the solid line profile (adopted from [26]).

The total absorption A_g is defined as ratio of the absorbed energy (shaded area in Fig. 4.1) and the incident intensity [26]). If the incident intensity is I_0 , the absorbed fraction will be $I_0 \int_0^\infty [1 - \exp(-k_\nu l)] d\nu$, and:

$$A_g = \int_0^\infty [1 - \exp(-k_\nu l)] d\nu = \Delta\nu_c \frac{I_0 - I_\nu}{I_0}, \quad (4.20)$$

with $\Delta\nu_c$ the spectral width of the detection device and l the optical pathlength. The total absorption of the line depends on the absorption coefficient and the thickness of the layer, that is on the product $N_i f_{ik} l$. It follows from (4.20) that, in general, the relation between measured total absorption A_g and density N_i of the absorbing particles is non-linear. A graph which represents the relation between A_g and the product $N_i f_{ik} l$ is called "curve of growth". The calculation of these curves is very laborious [31] for the general case of a Voigt profile. In the literature many different methods of calculation and representation can be

found (cf. e.g. [8, 19, 31, 32, 33, 34]). In [18] the reproduction of the exact curve for the specific case of a purely Gaussian profile was given, as obtained by a simple numerical algorithm. Generally the curves are presented as a function of parameter $a = \sqrt{\ln 2} \Delta\nu_L / \Delta\nu_D$. In Fig. 4.2 they are shown in their most common representation.

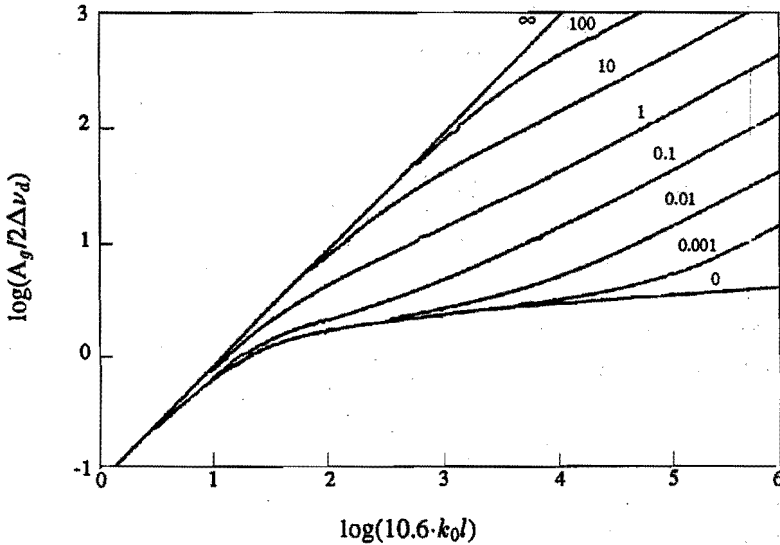


Figure 4.2: The curves of growth for various ratios a of the Lorentz and the Gauss fraction of the line (adopted from [19]).

In the linear part the optical thickness is small ($k_\nu l < 1$), and the curves with different values of a fall together. The measured total absorption is proportional to the density of the absorbing species. For $k_\nu l \rightarrow \infty$ all curves (for $a > 0$) converge into straight line of equal slope which means that the total absorption increases proportionally to the square root of the product $N_i f_{ik} l$. For the case of strong absorption this situation can be explained by the $1/\omega^2$ dependence of the Lorentzian profile on the line wings. In the limit of $a \rightarrow 0$ (only Doppler broadening of the spectral lines) and/or strong absorptions, the curve of growth shows an almost flat part, reflecting that a large part of the line is optically thick (the solid curve in Fig. 4.1).

So by measuring the total line absorption A_g , it is possible to obtain the product $N_i f_{ik} l$ from the "curves of growth" and to calculate the concentration of the absorbing particles. To this end values for the parameter a and f_{ik} and l have to be known.

A special case is the case of weak absorption, when $k_\nu l \ll 1$. The general expression (4.20) can then be simplified:

$$A_g = \int_0^\infty [1 - \exp(-k_\nu l)] d\nu \cong l \int_0^\infty k_\nu d\nu. \quad (4.21)$$

Therefore, using Eqs. (4.9) and (4.20) one can obtain:

$$\Delta\nu_c \frac{I_0 - I_\nu}{I_0} = \frac{\lambda^2 g_k}{8\pi g_i} N_i A_{ki} l, \quad (4.22)$$

and for the determination of the product $N_i f_{ik} l$, it suffices to measure only the value of the relative absorption $(I_0 - I_\nu)/I_0$, and the spectral width of the detection device $\Delta\nu_c$. Thus, for the case of weak absorption it is not necessary to determine the detailed profile of the spectral line, which is a complicated and time-consuming procedure. Only the frequency integrated relative absorption is required.

4.2.5 Measurement and data analysis techniques in the case of spatially inhomogeneous absorbing media

In many experimental situations one can suppose that the analysed absorbing medium has cylindrical symmetry and that the observation occurs perpendicularly to the axis of symmetry. As in emission, the radial dependence of the absorption can then be obtained by making a number of measurements in lateral direction and by Abel inverting the measured values. Strictly speaking, for the optically inhomogeneous medium one has to introduce an absorption coefficient $k(\nu, x)$, depending on frequency and location. A simplified case occurs when one can assume that along the observation path, the profiles of the spectral lines do not change. The latter requirement will be fulfilled if the radial gradient of the heavy particles temperature (for Doppler broadening) and the radial gradients of the electron temperature and density (for Stark broadening), are small enough. In that case the only parameter is the density of the absorbing particles, and a straightforward Abel inversion technique [3] can be used. However, care should be taken still; it is not allowed to Abel invert the measured values of the total absorption immediately; at each lateral position the profile of the total absorption is different, as a result of the non-linearity as a function of the density of the absorbing species. This implies that first one has to calculate the k_0 value associated with the measured value of A_g , by using the curves of Fig. 4.2. The value obtained for $k_0 l$ can now be Abel inverted in a straightforward manner. In

the following we will refer to this method as the deconvolution method. This method was applied in [18].

When the profiles of the spectral lines change along the observation path a straight forward Abel inversion is no longer adequate. In that case one obtains a set of equations for the different lateral positions, with parameters N_i (absorbing particles density), T_h (heavy particles temperature), and additionally n_e (in the case of a Lorentz Stark fraction in the profile). These can be solved by sophisticated numerical techniques ([35] and references therein). A method to circumvent these complicated procedures and still implement a variation of the spectral line profile over the line of sight is the following. One may adapt a profile for the densities and temperatures in the plasma beam, and calculate the expected values of the total absorption over a line of sight. Consequently, by fitting the calculated values to the measured values in a least squares procedure, the parameters of the profiles can be determined. For the expanding cascaded arc jet radial density profiles may be approximated by (combinations of) Gaussian profiles (cf. [1]). In section 4.3.4 this method will be addressed in more detail.

Another important aspect is the shape of the absorption line profile. Close to the exit of the arc, the electron density is high and besides Doppler broadening, Stark broadening may become significant too. The resulting line profile is a Voigt function. In principle the present method can cope with all types of absorption line profiles, using appropriate initial assumptions. In Sec. 4.3.3 it will be shown that in our case the absorption line profile is predominantly Doppler broadened and that a Gaussian shape may be adapted for the absorption line profile.

4.3 Experimental

4.3.1 The cascaded arc set-up for deposition

The plasma is generated in a cascaded arc (Fig. 4.3). The arc consists of three tungsten thorium cathodes, with a diameter of 1 mm and a maximum current of 30 A, a stack of ten insulated copper plates, and an annular copper anode. The cascade plates have an inner bore of 4 mm and a thickness of 5 mm. They are insulated from each other by boron-nitride spacers (thickness 1 mm). Together they build up a plasma channel with a length of 60 mm. Argon is injected in the cathode space as a carrier gas, at flow rates adjustable over a wide range of about 10 to 400 standard cm^3s^{-1} , and a pressure of the order of 0.5 bar ($0.5 \cdot 10^5$ Pa). The total current can be adjusted from 30 to 100 A, with a voltage of the order of 50 -150 V. So the power density in the arc is very high, of the order of 10 kWcm^{-3} . A plasma is generated with temperatures of the order of 1 eV, an electron density of the order of 10^{22}m^{-3} , and an ionization degree of $\sim 10\%$.

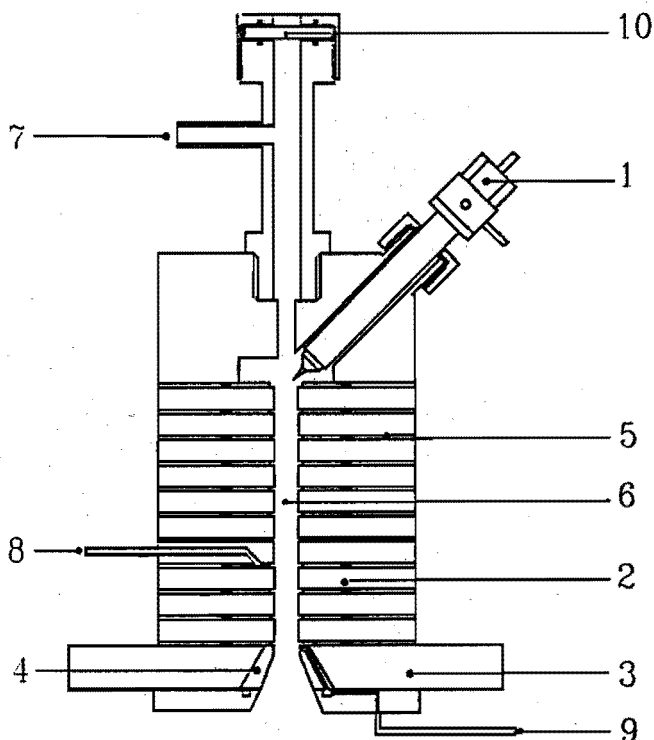


Figure 4.3: Schematic of the cascaded arc: (1) cathode, (2) copper plate, (3) end plate, (4) nozzle, (5) insulation plate, (6) plasma channel, (7) argon injection site, (8) hydrogen injection site, (9) monomer injection site, and (10) viewing port.

In Fig. 4.4 the position of the arc in the deposition and spectroscopy set-up is shown. The deposition vacuum chamber is evacuated to pressures of $\sim 10^2$ Pa by two roots blowers and a rotating piston pump with a total capacity of $2600 \text{ m}^3\text{hr}^{-1}$. Using a stepper motor controlled valve the pumping speed can be modified, and in this way the chamber pressure can be adjusted, independently of the gas flow rate. The plasma expands supersonically through a ring shaped anode, the nozzle, into the vacuum chamber. In the nozzle a hydrocarbon gas can be injected, and by charge exchange from the argon to the hydrocarbon radicals, followed by dissociative recombination of the hydrocarbons, a beam of active carbon containing species is created. The active particles are accelerated into the vacuum chamber, pass through a shock, and are transported subsonically toward the substrate where the deposition takes place. Specific features of this method are that the three functions, production, transport and deposition can be optimized independently, and that there is convective transport of the active

particles. Consequently the deposition rates are orders of magnitude higher than in diffusion governed plasmas. More information on this technique can be found elsewhere ([1, 2, 3]).

4.3.2 The spectroscopic set-up

The light source

In Fig. 4.4 the optical set up for performing emission- end absorption spectroscopy on the expanding plasma beam is shown. As a light source, a stagnant cascaded arc is employed [28]. This arc is specifically tailored for the purpose of emitting high intensity radiation from the near infrared, through the visible, to the ultraviolet range. The arc is similar to the arc for deposition, but consists of a stack of only six plates. The length of the arc is 42 mm, and the diameter of the channel 2 mm. The aperture is $\sim 3 \cdot 10^{-3}$ sr. The arc operates on argon, at a pressure of the order of 2 to 5 bars; the argon is flushed at a low rate of only $3 \text{ cm}^3 \text{ min}^{-1}$. The current can be adjusted from ~ 20 to 50 A, at a voltage ranging from ~ 60 to 110 V. The temperature in the arc is of the order of 1.5 eV. The intensity of the continuum radiation is only a factor of ~ 10 lower than according to Planck. In the spectral lines, the intensity approaches the value according to Planck's law and is of the order of $10^{14} \text{ W m}^{-3} \text{ sr}^{-1}$. The Stark broadening of the argon lines is very large (several tenths of nanometers), compared to the widths of the lines under investigation, and we can consider the source as a continuum source in the vicinity of the studied line. Besides for absorption spectroscopy the source can be used for spectroscopic ellipsometry [28] and infrared absorption measurements [36].

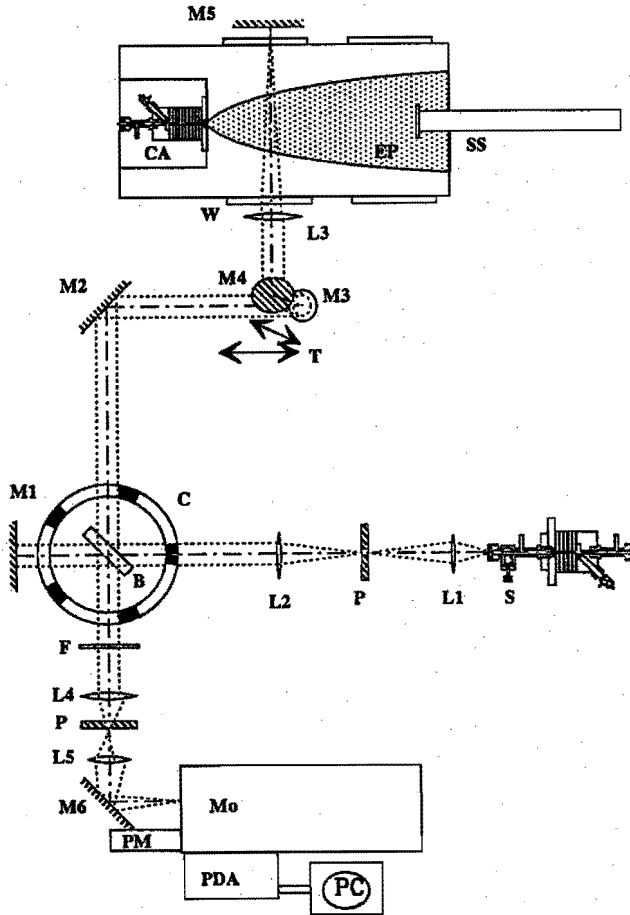


Figure 4.4: Outline of the spectroscopic set-up; S: cascaded arc light source; M: mirrors; L: lenses; P: pinholes; B: beam splitter; C: chopper; T: translator; CA: cascaded arc; EP: expanding plasma; SS: movable substrate support; W: quartz window; F: order filter; Mp: monochromator; PDA: photo diode array; (PM: photo multiplier;) PC: personal computer

Influence of the photoabsorption of external source radiation on the plasma parameters

It should be checked if the high intensity cascaded arc light source does not influence the plasma under investigation. Based on the experimental data on the cascaded arc light source given in [28], it is not difficult to estimate quantitatively the rate of the photoexcitation of $4s$ atoms in the analysed plasmas. Let us restrict the analysis to the spectral range between 750 and 850 nm, where the strongest

argon lines are situated. The lower quantum levels (configuration $\text{Ar}(3p^5 4s)$) of this transition are, as a rule, significantly populated in low-temperature plasmas. Then it follows, that for the cascaded arc (radius to length ratio $\approx 1/21$) with a pressure of 4 bar, and a current of 40 A, the intensity of the continuum radiation will be $\approx 10^{13} \text{ Wm}^{-3} \text{ sr}^{-1}$ and the intensity at spectral lines $\approx 10^{14} \text{ Wm}^{-3} \text{ sr}^{-1}$. One can estimate that the maximum number of atoms ΔN_{ik} , photoexcited per unit of time and per unit of volume as consequence of light absorption. In a transition with an oscillator strength $f=0.01$ ΔN_{ik} is equal to $\approx 2 \cdot 10^1 N_i$ for the photoexcitation by continuum radiation, and $2 \cdot 10^2 N_i$ for the photoexcitation by spectral lines. N_i is the concentration of the absorbing atoms.

It is interesting to compare these photoexcitation rates with the same atom excitation rates by collisional processes in plasma. For the typical conditions in the expanding cascaded arc argon plasmas: $n_e \approx 10^{19} \text{ m}^{-3}$, $T_e \approx 2 \cdot 3 \cdot 10^3 \text{ K}$ [3], and for the rate constants $\langle \sigma v \rangle$ of direct electron excitation of argon atoms $\text{Ar}(4s \rightarrow 4p)$ [33], it is easy to find, that $\Delta N_{ik} = N_i n_e \langle \sigma v \rangle \approx 10^5 N_i$. Thus, the estimations shows that the efficiency of photoexcitation of the argon atoms in expanded arc plasmas, is of much lower order than the electron excitation of the atoms in the plasma. So, in this case, the influence of the external source radiation on the properties of the plasma under investigation can be neglected and the use of filters is not necessary.

The optical system and the detection section

By the lenses L1 and L2 (focal lengths 75 and 400 mm respectively) a beam of parallel light is created, and passed on by the beam splitter (B). Rotating the chopper (C) now makes it possible to image a selected signal on the detection system. By using the mirror M1 a reference measurement of the source signal (I_s) can be obtained. By blocking *e.g.* the source, the plasma emission (I_e) is transmitted to the detection elements. In a similar way the dark current of the detection system (I_d) can be measured. The transmission of the light beam through the plasma (I_t) is measured in the following way: The beam is passed on by the mirror M2, M3 and M4 and focused by a lens L3 (focal length 700 mm), through the plasma, on the mirror M5. The mirror M3, and mirror M4 together with lens L3 are translatable, which enables axial and lateral scanning. The light is reflected, passing the plasma once again, and is transmitted, through the order filter F, to the detection section. Simultaneously the plasma emission I_e of the beam itself is collected by an additional measurement and is subtracted. The beam is focused on the entrance slit of the monochromator by the optical system, consisting of the lenses L4 and L5; the focal lengths of these lenses are 400 and 75 mm respectively. The pinhole P (diameter 1 mm) limits (by backprojection)

the actual detection volume in the plasma. The detection volume is a cone with a top diameter of 2 cm on lens L5, and the pinhole diameter on mirror M5; so on the plasma axis the diameter of the detection volume is ≈ 1 cm.

The detection section consists of a Czerny-Turner high resolution monochromator (THR-1000 of Jobin-Yvon), with a focal length of 1 m. The entrance angle of the light beam is 1/10 rad, the entrance slit width is 25 μm , and optimum filling of the diffraction grating (1200 lines/mm) is obtained. The dispersion of the monochromator is 0.8 nm/mm (at a wavelength of 500 nm). On the exit plane a Peltier cooled (-14 $^{\circ}\text{C}$) photodiode array (Reticon RL 1024S) is placed [3]. It consists of 1024 elements with a width of 25 μm per diode and a height of 2.5 mm. With this element a spectral range of 17 nm (at 800 nm) can be recorded in one time. After AD conversion, by a PLC718 lab-card (4096 bits), the signal of the photodiode array is recorded by a personal computer.

Deconvolution of the measured absorption to the desired integrated absorption

Here we want to discuss briefly some details of the application of photodiode arrays for absorption spectroscopy experiments, in view of lack of discussion of that problem in the literature. The measured integrated absorption \mathcal{A}_m is given by:

$$1 - \mathcal{A}_m = \frac{\int_{\text{app}} (I_t + I_e) - \int_{\text{app}} I_e}{\int_{\text{app}} (I_s + I_d) - \int_{\text{app}} I_d} \quad (4.23)$$

\int_{app} denotes convolution of the intensities with the apparatus profile of the detection system, that is the monochromator and the diode array. The following reasoning now applies:

The measured source intensity per pixel is

$$\int_{\text{pixel}} \left(\int_{\text{app}} M(\nu) I_0 d\nu \right) d\nu \quad (4.24)$$

$M(\nu)$ expresses the apparatus profile. As usual the profile is normalized to unity:

$$\int_{\text{app}} M(\nu) d(\nu) = 1. \quad (4.25)$$

As the source is a continuum source, Eq. (4.24) is true for every pixel in the array. Considering that the width of the absorption line (~ 4 pm) is much smaller

than the spectral width of one pixel (~ 17 pm), the measured absorbed source intensity per pixel is the integrated absorption area $\int_{\text{line}} I_{\text{abs}}(\nu) d\nu$ and the measured absorbed source intensity per pixel A_p can be written as:

$$A_p = \int_{\text{pixel}} M(\nu) \left(\int_{\text{line}} I_{\text{abs}}(\nu) d\nu \right) d\nu. \quad (4.26)$$

This equation is similar to the one for an emission line. Some care should be taken in applying Eq. (4.26). In general it is not allowed to apply this equation for each pixel separately; only in the case of a large entrance slit width, a rectangular profile arises and the value of Eq. (4.23) is equal for each pixel. So it is more convenient to integrate the intensities over the entire apparatus profile (N pixels). By using Eq. (4.25), we can write equation Eq. (4.23) as:

$$A_m = - \frac{\int_{\text{app}} A_p d\nu}{\int_{\text{app}} I_0 d\nu} = - \frac{1}{N \Delta\nu_{\text{pixel}}} \frac{\int_{\text{line}} I_{\text{abs}}(\nu) d\nu}{I_0} = - \frac{1}{N \Delta\nu_{\text{pixel}}} \cdot A_g, \quad (4.27)$$

with A_g the total absorption as defined in Sec. 4.2.4 and $N \times \Delta\nu_{\text{pixel}} = \Delta\nu_{\text{mono}}$. Eq. (4.27) is equal to Eq. (4.20). It should be noted that increasing the entrance slit width of the monochromator does not change the surface area of the total absorption (Fig. 4.1) at all. The slit width enters the calculation only, because a modified total source intensity is measured. It should be stressed that N is the number of pixels over which the apparatus profile spreads the absorption, and it is clear that this number should be taken not too small. However, the exact value of N is not clear. Fortunately Eq. (4.27) remains valid if the number of pixels N is taken larger than the number over which the apparatus profile is spread, and this supplies us the following method of determining A_g without determining N exactly. By numerically integrating the last term of (4.27) over a variety of values N , A_g can be determined from the slope in a graph of measured absorption $A_m \cdot \Delta\nu_{\text{pixel}}$ vs. $1/N$. This procedure was applied on every measured absorption.

4.3.3 Measurement conditions

In Fig. 4.5 the studied section of the argon system and the selected spectral transitions are shown. The four argon $3p^5 4s$ states under investigation can be distinguished in two metastable states (3P_0 and 3P_2 , also denoted as s_3 and s_5) and two resonant states (1P_1 and 3P_1 , s_2 and s_4).

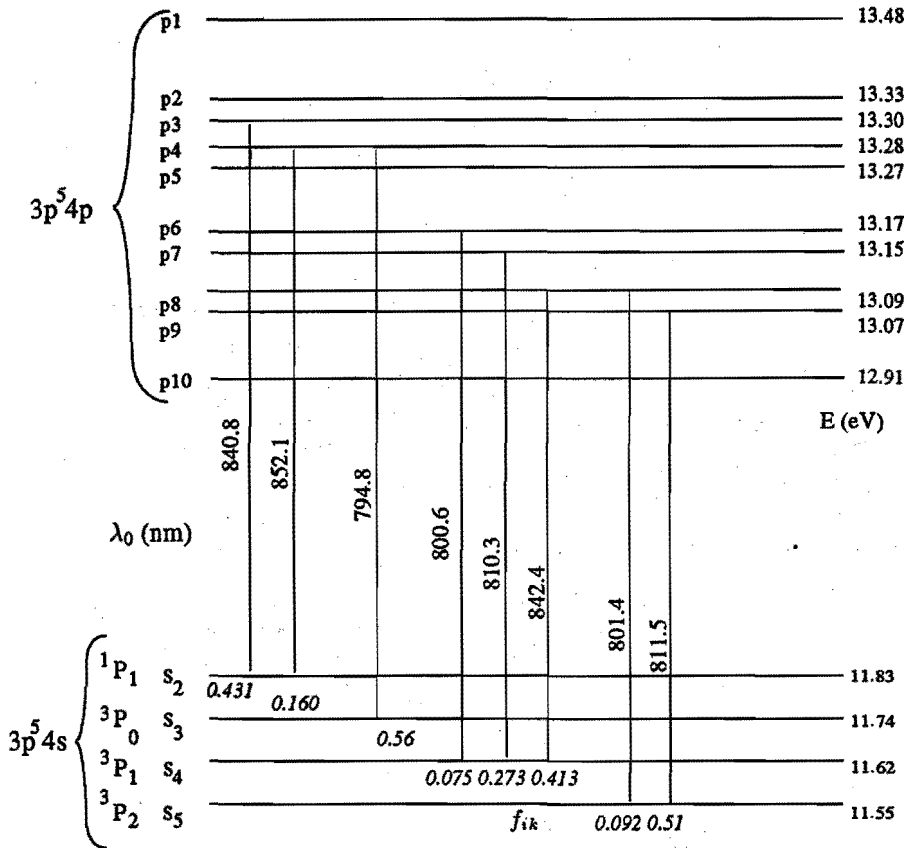


Figure 4.5: The four argon 3p⁵4s states and the spectral transitions under investigation. In italics the absorption oscillator strengths f_{ik} are given.

By means of the photodiode array absorption measurements could be performed simultaneously on the eight spectral transitions depicted in Fig. 4.5. These lines were covered by selecting only two monochromator positions. In Table 4.1 the specific parameters of the studied spectral transitions are given (adopted from [37]). Using Eq. (4.12) the relationship between the absorption oscillator strength f_{ik} and the transition probability A_{ki} of these transitions is given by:

$$f_{ik} \simeq 9.56 \cdot 10^{-9} \frac{g_k}{g_i} A_{ki} \tag{4.28}$$

Most of the lines have large oscillator strenghts. They were selected to obtain

Table 4.1: The transitions from the 4s-states under investigation

transition	Paschen notation	λ (nm)	g_i	g_k	A_{ki} 10^8 s^{-1}
$4s'[\frac{1}{2}]^o - 4p'[\frac{3}{2}]$	$1s_3 - 2p_4$	794.8	1	3	0.196
$4s[\frac{3}{2}]^o - 4p[\frac{3}{2}]$	$1s_4 - 2p_6$	800.6	3	5	0.0468
$4s[\frac{3}{2}]^o - 4p[\frac{5}{2}]$	$1s_5 - 2p_8$	801.4	5	5	0.096
$4s[\frac{1}{2}]^o - 4p[\frac{3}{2}]$	$1s_4 - 2p_7$	810.3	3	3	0.277
$4s[\frac{3}{2}]^o - 4p[\frac{5}{2}]$	$1s_5 - 2p_9$	811.5	5	7	0.366
$4s'[\frac{1}{2}]^o - 4p'[\frac{3}{2}]$	$1s_2 - 2p_3$	840.8	3	5	0.244
$4s[\frac{1}{2}]^o - 4p'[\frac{5}{2}]$	$1s_4 - 2p_8$	842.4	3	5	0.233
$4s'[\frac{1}{2}]^o - 4p'[\frac{3}{2}]$	$1s_2 - 2p_4$	852.1	3	3	0.147

strong absorption, leading to an acceptable signal-to-noise ratio. We can easily estimate the detection limit for the various transitions, because in this case it is allowed to use Eq. (4.21) for weak absorptions (and applying Eq. (4.27)). For the measured total absorption A_m we find, with $\Delta\nu_c = 8 \cdot 10^9 \text{ s}^{-1}$:

$$A_m = 6.4 \cdot 10^{-3} \frac{g_k}{g_i} \hat{N}_i \hat{A}_{ki} \hat{l}, \quad (4.29)$$

with \hat{N}_i expressed in units of 10^{15} m^{-3} , \hat{A}_{ki} in units of 10^8 s^{-1} , \hat{l} in cm (and the coefficient multiplied by 2 for the double pass). As an example, taking a density of 10^{15} m^{-3} and for the length l the diameter of the chamber (50 cm), for the three transitions coming from the s_4 substate, we will find measured absorptions of 0.025, 0.089 and 0.124 respectively. The error in one measured lateral absorption value is of the order of 0.05. However because many lateral data are available, this error will be averaged out by the fit procedure and the real error is of the order of 0.01. This implies that using the strong lines, the lower limit of the detection is of the order of a density of 10^{15} m^{-3} over a length of 5 cm, that is the plasma core. This means also, that when the optical pathlength is longer *e.g.* for the background gas, also lower densities will give significant absorption data. An illustration of this sensitivity can be found in Sec. 4.4.3.

Measurements on the densities of the argon 4s-states were done for the reactor settings given in Table 4.2. These are the standard settings also used in Thomson scattering experiments [3] and Fabry-Pérot line profile measurements [3, 23]. At six axial positions, 20, 40, 60, 80, 100 and 120 mm from the center of the nozzle, 45 lateral measurements were made, 2 mm apart from each other.

Table 4.2: The standard reactor settings for the argon plasma

I_{arc}	45 A
V_{arc}	85 V
Φ_{Ar}	$58 \text{ cm}^3\text{s}^{-1}$
$p_{chamber}$ (spectrosc.)	40 Pa

On these measurement positions the Lorentz fraction of the absorption line profiles can be neglected compared to the Gauss fraction. This is justified as follows: The Doppler broadening in the expansion, with an argon heavy particle temperature of ~ 3000 K is ~ 4 pm (picometer). The Stark broadening for the observed 4s-4p transitions, assuming a typical electron density of 10^{19} m^{-3} , is of the order of $5 \cdot 10^{-3}$ pm [33]. The natural widths of the resonant 4s lines (with $A_{ki} = 1.2 \cdot 10^8 \text{ s}^{-1}$ and $5.1 \cdot 10^8 \text{ s}^{-1}$) are about $5 \cdot 10^{-4}$ and $2.5 \cdot 10^{-3}$ pm. Resonance broadening (including homogeneous broadening) at 40 Pa and 3000 K is $O(10^{-4})$ pm. Consequently the ratios of the Lorentz and Gauss fraction of the line profiles are less than 0.01, in which case the effect of the Lorentz fraction is very small (cf. Fig. 4.2) for optical depths $k_0 l \leq 100$. So in the data analysis we can adopt a pure Gaussian line profile.

4.3.4 Treatment of experimental data

Convolution method for determining the absorption in inhomogeneous media

As mentioned already in Sec. 4.4.1 sophisticated numerical methods are necessary to obtain an exact solution (cf. [35] and references therein) if the absorption line shape is not constant over the line of sight. In the actual case of a Gaussian absorption line profile, with Doppler broadening as the predominant broadening mechanism, the following efficient numerical method can be applied. On the basis of known experimental data [1], [3] we may adapt also a Gaussian radial profile of the density and the temperatures of the absorbing species in the following way:

$$N_i(r) = N_i(0) \exp\left[-\left(\frac{r-r_0}{\Delta r}\right)^2\right] \quad (4.30)$$

with $N_i(0)$ the density at the axis of the plasma, Δr is the width of the Gaussian distribution ($1/e$ width), and r the radial coordinate, $r = \sqrt{x^2 + y^2}$, with x the coordinate along the line of sight which is taken at a height y (the lateral

coordinate). In the present case r_0 is taken equal to 0. For the temperature a similar Gaussian profile can be adapted. An issue is the physically reasonable combination of profiles. From experimental data on the expanding cascaded arc plasma jet [1], [3], it is plausible to take for the density a combination of a narrow Gauss (the plasma core) on top of a wide Gauss as a background (metastables in the recirculating background gas, created by capture of resonance radiation). For the temperature we adopt a narrow Gauss (with the same width as the narrow density Gauss) on top of a constant low background temperature. In Fig. 4.6 (a) and (b) the geometry and the adapted profiles are illustrated.

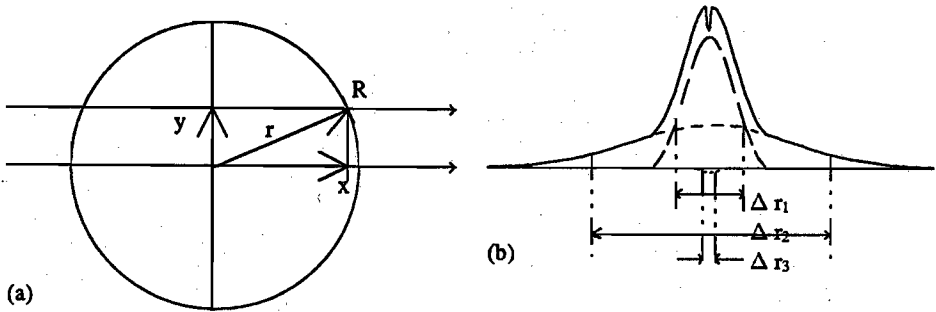


Figure 4.6: (a) Geometry of a line of sight at height y through the expanding plasma beam and (b) adapted density and temperature profiles over a line of sight.

This leads to the six parameters given in Table 4.3 in the fit procedure:

Table 4.3: Fit parameters

Parameter	Notation
top value of the plasma core density profile	n_1
width of this profile	Δr_1
top value of the density profile of the background gas	n_2
width of this profile	Δr_2
the top value of the temperature profile	T_0
width of the temperature profile	Δr_1
basis temperature of the background gas	T_B

A dip in the center of the density profiles, which is often observed in emission profiles for other levels [3], can be simulated by subtracting a third Gaussian in the total density profile, leading to two more parameters, given in Table 4.4.

Table 4.4: *Additional fit parameters*

Parameter	Notation
top value of the 'negative' Gaussian density profile	n_3
width of this profile	Δr_3

Using the prescribed temperature and density profiles, at each point (x, y) the Gaussian profiles of $k(\nu, r(x, y))$ and the density $N_i(x, y)$ are defined. Eqs. (4.2) and (4.14) can now be integrated over the line of sight and per frequency channel using (4.16). To this end, the line of sight has to be divided in a large number of small steps (250 steps of 2 mm), giving sufficient resolution of the density and temperature profiles. The integrated absorption area, which expresses the line integrated absorption in traversing (in our case two times) the plasma, can now be obtained by integrating over all frequency channels. It appears that 30 channels of 1/10 of the Doppler line width, covering the profile over three times this width, is sufficient to keep the error in the integrated area less than 1%. Numerically, the most convenient way for obtaining the integrated absorption is to determine the frequency step by the smallest Doppler width (at the plasma edge), and then, going to the center, increase the number of steps proportionally with the Doppler width, illustrated in Fig. 4.7.

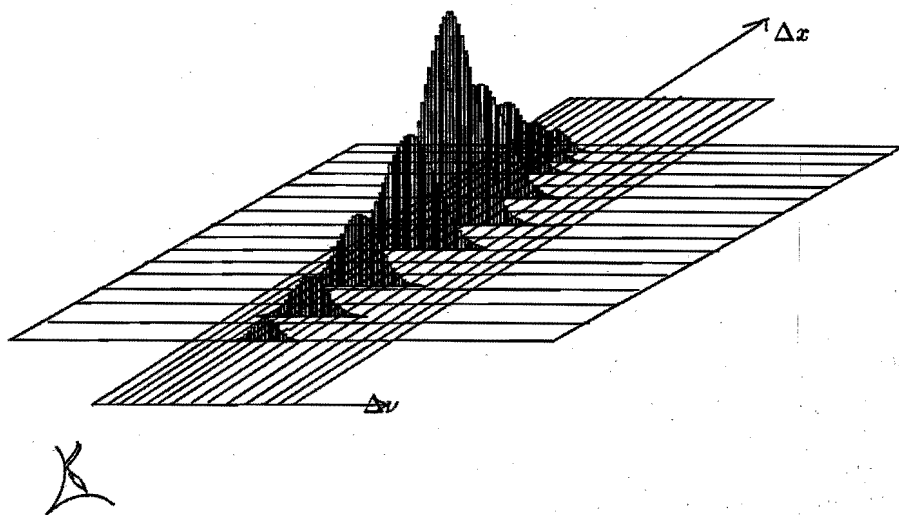


Figure 4.7: Numerical step procedure for calculating the integrated absorption.

This procedure was carried out for each lateral position, and the calculated values can be fitted to the measured integrated absorption values using a least-squares parameter fit method. In this way optimum values for the parameters of the densities and temperatures profiles can be obtained. As a measure for the fit quality the following least-squares error function was used:

$$\chi^2 = \frac{1}{N_y} \sum_1^{N_y} (\mathcal{A}_{m,y} - \mathcal{A}_{f,y})^2, \quad (4.31)$$

with $\mathcal{A}_{m,y}$ and $\mathcal{A}_{f,y}$ the measured and fitted total absorption respectively on lateral position y , and N_y the number of lateral data points. No weighing was applied because the (absolute) detection device noise was the predominant noise source.

Approximation of the temperature profiles and their effect on the density determinations

In Ref. [18] it was already demonstrated that, despite a large difference in oscillator strength, the use of different spectral lines leads to roughly to the same densities if the correct heavy particle temperatures are used. In the present method, following the reverse way, temperature profiles can actually be determined, making use of the non-linear behavior of the absorption. Because the Doppler width

appears in (4.14), the temperature has effect on the density determination in the case when lines with strong absorptions are used. This fact is illustrated by the curve of growth for the purely Gaussian profile ($a=0$ in Fig. 4.2). For weak absorptions the region of linear relation between measured absorption and optical depth, is entered, as described by Eq. (4.21). In this case the effect of temperature becomes negligible, because of the fact that the area of the absorption profile, in the Gaussian case $k_0 \Delta \nu_d \sqrt{\pi}$, is proportional to the density, independent of the broadening mechanisms in the plasma [26]. For strong absorptions the flat part on the right hand side of the curve is entered, and the line width determines the amount of loss in measured absorption due to saturation in the top of the profile.

As an example the absorption data for the three lines from level s_4 were used. The optical depths $k_0 l$ for these three lines differ widely. For the weak 800.6 nm line ($f=0.092$) the measured values of $k_0 l$ are of the order of unity, and the measured absorption is about linear with the density. For the two strong lines (810.3 nm, 842.4 nm) values of $k_0 l$ of up to ~ 20 are obtained, and the measured absorption is non-linear with the density. Making use of the difference in non-linearity in measured absorption a determination of the parameters of the temperature profile is possible by fitting the measured absorption values for these three lines simultaneously with the same density and temperature profiles. All seven parameters of Table 4.3 were used. In Fig. 4.8 the temperatures profiles obtained from this procedure are shown. It can be observed that for the axial positions 20, 40, 60 and 80 mm from the nozzle realistic values of the temperatures were obtained, roughly in agreement with the ones of Ref. [23] and [2]. With the present method, temperature determinations for the positions $z=100$ and $z=120$ mm were not possible, as the non-linearity in the absorption is small.

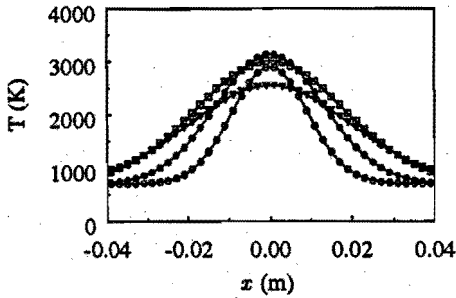


Figure 4.8: Heavy particles temperature profiles as obtained in the optimal six-parameter fit for the three lines simultaneously; \circ , \bullet , \square , ∇ , axial positions $z=20$, 40, 60 and 80 respectively. (Here the symbols only serve to clarify the lines.)

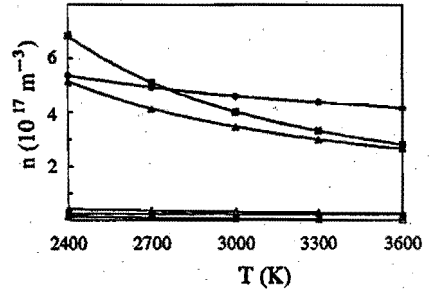


Figure 4.9: Analysis of the top values of the radial density profiles for the three s_4 spectral lines, \bullet , \blacktriangle , \blacksquare : $\lambda=800.6$, 810.3 and 842.4 nm respectively, and for two axial positions: $z=20$ mm: solid symbols, $z=120$ mm, open symbols

In Fig. 4.9 this is illustrated. The variation of this best-fit density with the top value of the temperature profile (on the plasma axis) for the three lines of level s_4 is shown, for the two axial positions $z=20$ (solid symbols) and $z=120$ mm (open symbols). Regarding the position close to the nozzle, it can be observed that for the two strong lines 810.3 and 842.4 nm the variations can be substantial (for the 842.4 nm line even $>100\%$), while for the weak line (800.6 nm) the effect is still small. For the location ($z=120$ mm) where the densities are much lower the variation is small even for the strong lines, of the order of 10%. It becomes clear now why the numerical algorithm could do a temperature determination for the locations close to the nozzle, using the three lines simultaneously. The numerically optimum density determination is laying somewhere in the triangle crossing of the lines at about 2800 K. For $z=120$ mm the three lines vary smoothly with temperature in an almost parallel fashion. This implies that for weak absorptions ($k_0 l < 1$) an accurate temperature determination is not possible, but also not necessary. For large values of $k_0 l$ a temperature estimation is desired and on the other hand, feasible.

For the first four axial positions the determined temperatures agree reasonably well with determinations of other experiments. Heavy particle temperatures and rotational temperatures were determined to be around 3000 K [2, 23] at all of the six axial positions. So for the elaboration of all other measurements the following procedure was followed. A standard Gaussian temperature profile with a top temperature of 2300 K on top of an (averaged, non-critical) background temperature of 700 K was adopted. The population densities for the four $4s$ -states

were fitted to the measured absorption for the available lines on each state: the three lines for the s_4 state, two lines for the states s_2 and s_5 and one line for the s_3 state. Because of the above reasoning, the errors in density will be small on all positions. The result of the density profiles obtained by fitting of the s_4 three lines simultaneously for these temperature profiles is treated in Sec. 4.4.1 (Fig. 4.11 (a)).

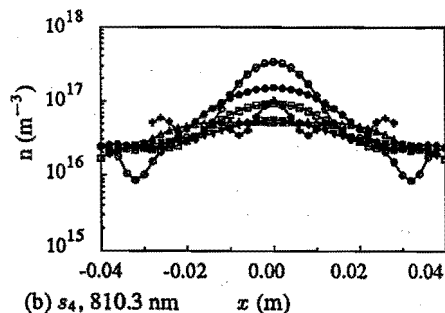
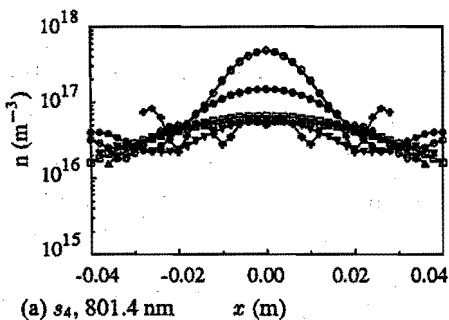
4.4 Results and discussion

In the following figures, radial density or temperature profiles at the six axial positions of measurement will always be depicted by the following symbols: \circ , \bullet , \square , \blacktriangledown , \triangle , $+$, at axial positions $z=20, 40, 60, 80, 100$ and 120 mm respectively. It should be noted that these profiles are calculated and do not show fits, the symbols only serve to clarify the lines for the various axial positions. Only in figures showing fit qualities the symbols depict measured absorption values on these positions.

4.4.1 Absolute density of the $\text{Ar}(3p^54s)$ states in a pure argon plasma

Density profiles obtained with the conventional deconvolution method (adopted from [18])

As an example, in Fig. 4.10 (a) through (c) the results for the three transitions from the s_4 substate, with various oscillator strengths, are given. These results were obtained with the Abel inversion method [3, 38]. The figures show that the reproducibility of the obtained densities using three lines of varying strengths is reasonably well, indicating that the method for analyzing the non-linear absorption is adequate. For most axial positions the values vary within 20%.



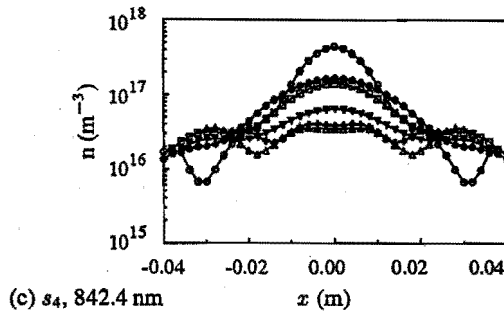


Figure 4.10: (a)-(c) Radial density profiles of the argon s_4 -substate, using various lines, as obtained using Abel inversion. x is the lateral coordinate, z the distance from the nozzle, \circ , \bullet , \square , ∇ , \triangle , $+$ 20, 40, 60, 80, 100 and 120 mm respectively.

However, the use of this method implied several severe restrictions:

- As explained in Sec. 4.2.5, the heavy particle temperature had to be taken constant over a line of sight through the plasma.
- the heavy particles temperatures have to be obtained by other measurement techniques. Based on the results obtained by Fabry-Pérot line profile measurements on a similar cascaded arc set up [23], with the same standard conditions, values of the order of 3000 K were applied.
- It can be observed that the profiles are obscured by oscillations due to the Abel inversion of the noise in the measured lateral profiles. Due to these oscillations, the exact shape of the profiles in the supersonic expansion and the shock region (at $z \simeq 60$ mm) could not be resolved properly. The typical central dip in the density profiles (as observed for other species in the supersonic expansion [3]) can not be observed. It is not clear whether the dip is actually absent, or whether it is obscured by the oscillations.

Density profiles obtained with the convolution method and accuracy of the results

The main goal of the actual method is to obtain a more accurate density determination on the plasma axis. This method now enables to establish whether the absence of the central dip is a real physical phenomenon. To this end, firstly it was investigated what combinations of Gaussian density functions describe the measured absorption adequately. It appeared that applying only one Gaussian yielded values which were too low in the center of the plasma. This implied that

a second broad profile was needed, representing metastables which were apparently also present in the background gas. In Fig. 4.11 (a) density profiles in the expansion for the s_4 sublevel are shown as obtained in the combined 4-parameter fit for the three s_4 -lines simultaneously in a pure argon plasma, using a combination of two Gaussian profiles. The temperature profiles were fixed, following the reasoning of Sec. 4.3.4. A dip in the central densities was simulated by fitting the measured data with an extra 'negative' Gaussian density profile in the center. As an example the result of this fit is given for the s_4 -substate, for the first four axial positions in Fig. 4.11 (b). The temperature profile was again a centralized Gaussian on top of a constant background. Only insignificant central dips can be observed for the positions $z=40$ and 60 mm, so it is reasonable to limit the modelling to two centralized Gaussian profiles.

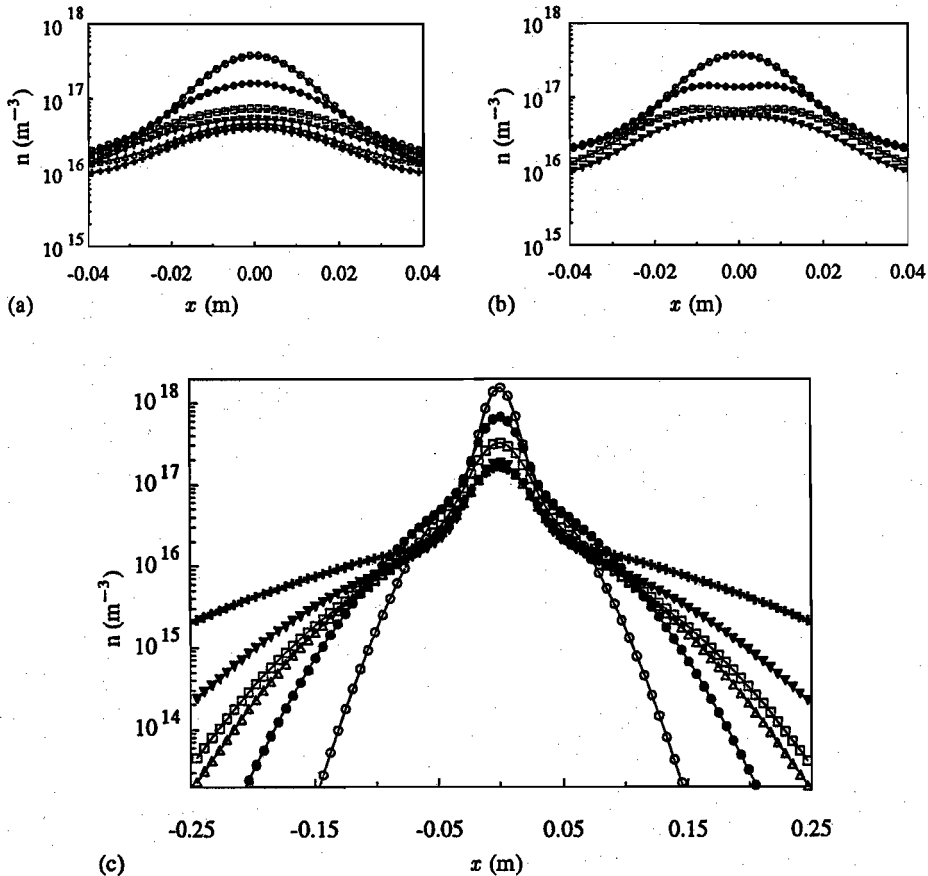
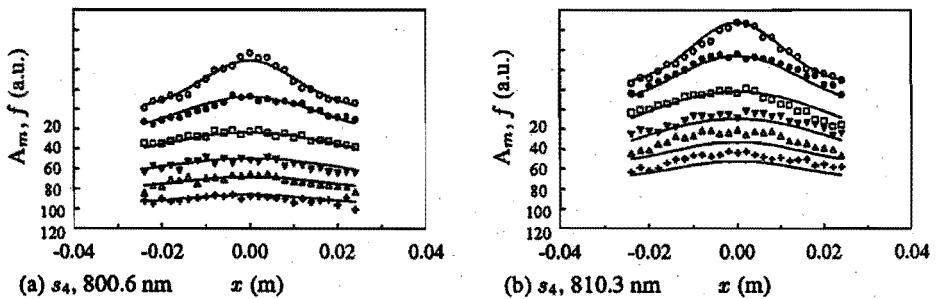


Figure 4.11: (a) s_4 radial density profiles obtained by fitting with two Gaussians. (b) s_4 radial density profiles obtained by fitting with three Gaussians (one negative). (c) s_4 radial density profiles of Fig. (a) throughout the chamber, showing the summation of the narrow and the broad Gaussian profiles. $\circ, \bullet, \square, \blacktriangledown, \triangle, +$, axial positions $z=20, 40, 60, 80, 100$ and 120 mm respectively. (Note that here the symbols only serve to clarify the lines for the various axial positions.)

Its interesting to observe the extension of the profiles throughout the vacuum chamber in Fig. 4.11 (c). Although the lateral scan range was only 9 cm, the representation with two Gaussians renders a physically very reasonable picture of an expanding beam of $4s$ states, extending throughout the chamber on position $z=120$ mm.

In Fig. 4.12 (a) through (c) the fit quality for the three lines separately is shown, using the combination of two Gaussian profiles. It can be observed that for the first four positions the fits are indeed reasonably good. For $z=100$ and 120 mm however, significant deviations for the expected absorption for the three lines can be observed. Systematic deviations of the whole profiles from their expectation value for the optimized density, can be observed. The reason for this is that the signal-to-noise ratio for these weak absorptions was moderate. The pixel blurring of the array may give rise to an artificial positive or negative total absorption area, depending on the position of the line on the array.



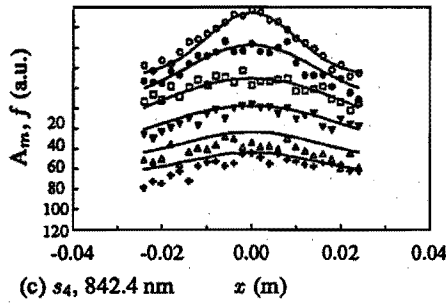


Figure 4.12: Fit quality for the three s_4 lines obtained in the simultaneous fit (with fixed Gaussian temperature profiles). The zero axis for the various positions has been shifted to get a clearer image; the small figures on the left hand axis indicate the zero axis for the respective axial position. (Note that here symbols depict actual measured absorption values.)

The results of the $4s$ densities for the four substates s_2 , s_3 , s_4 and s_5 as determined with application of the standard Gaussian temperature profile of Sec. 4.3.4 are shown in Fig. 4.13 (a) through (d). So only the four density parameters of Table 4.3 were included in the fit procedure.

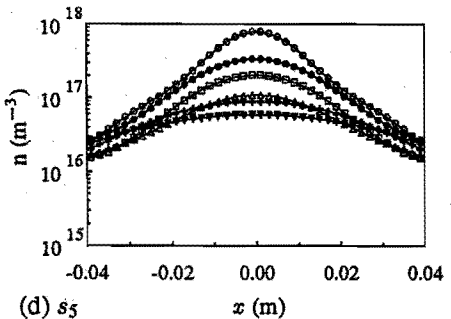
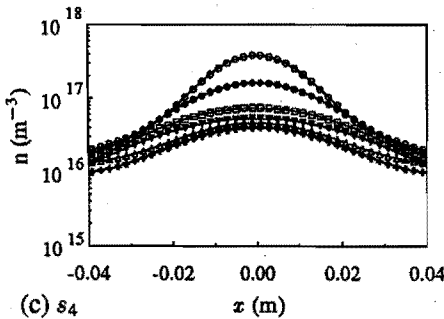
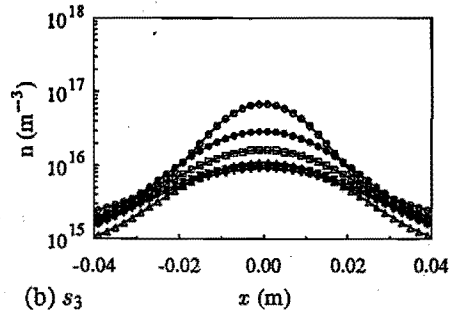
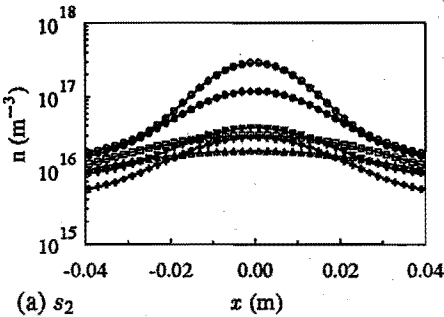


Figure 4.13: *Radial density profiles of the four argon 4s substates in a pure argon plasma.*

The accordance with the results of the deconvolution method in [18], shown in Sec. 4.4.1, is very well. But a major improvement obtained by the present method is that the results are not obscured by oscillations arising from the Fourier transform in the Abel inversion procedure. Now a more detailed image of the decay of the argon 4s-metastable and resonant states in axial direction has been obtained.

In Fig. 4.14 the axial profile of the four 4s substates is elucidated for two radial positions, at the plasma axis, and at 4 cm from the axis (which is approximately the limit of the plasma core at this chamber pressure). The triangles depict the resonant states. It appears that the densities of the four states per statistical weights g_i (3, 1, 3, 5 respectively) are approximately equal, indicating a strong collisional coupling between the four states (cf. [33, 39]). The densities of the upper levels are slightly less populated. This leads us to simplify the analysis further, by just considering the sum of the densities of the 4s states. In Fig. 4.15 the radial profiles of this total density of 4s states is given.

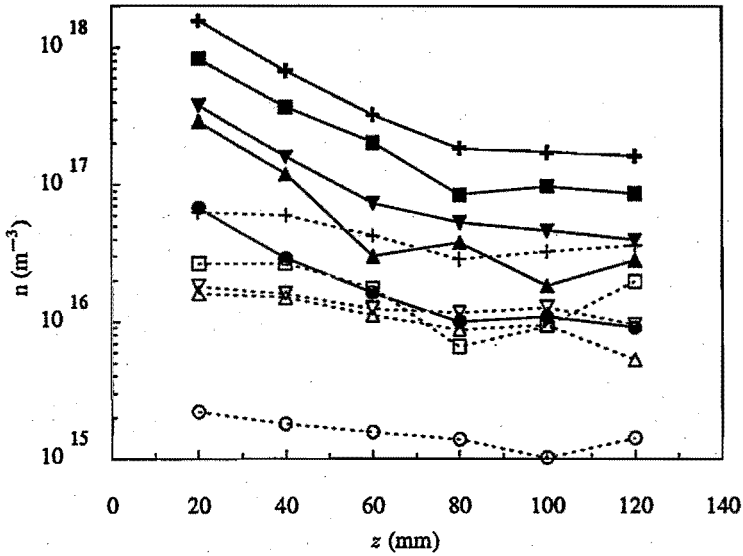


Figure 4.14: Axial profiles of the densities of the 4s states; ▲, ●, ▼, ■, +, s₂, s₃, s₄, s₅ and sum respectively, solid symbols, solid lines, at the plasma axis. The same open symbols and the dashed lines depict the densities at radial position x=40 mm.

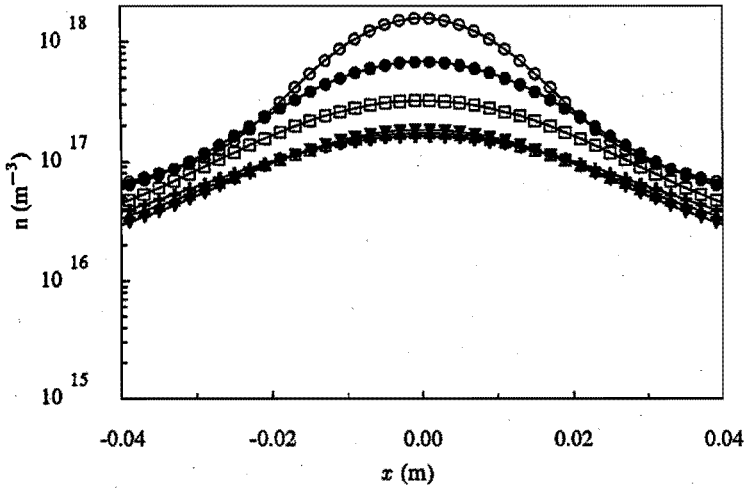


Figure 4.15: Radial profiles of the total density the argon 4s-state x is the lateral coordinate, z the distance from the nozzle, $\circ, \bullet, \square, \blacktriangledown, \triangle, +$, axial positions $z=20, 40, 60, 80, 100$ and 120 mm respectively.

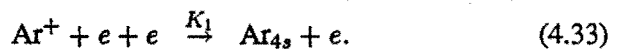
Estimate of the population densities of the Ar ($3p^54s$) states

The measured argon 4s densities can be explained using a simple model. In the expansion the situation is quasi-stationary and we can use the time-independent mass balance equation

$$\nabla \cdot (nw) = \left(\frac{\partial n}{\partial t} \right)_s, \quad (4.32)$$

with n and w the density and the velocity of the species concerned. The source term on the right hand side is built up by several contributions. The most important in the case of pure argon plasma are:

- 1 For the production, the three-particle recombination:



Here it is assumed that all three particle recombinations cascade down to the $4s$ states (supported by the findings of Benoy [40]).

- 2 For destruction, radiative decay (after $4s$ -mixing) through the resonant states, followed by production by capture of the radiation:



The contributions of other reactions to production and destruction appear to be negligible:

• Production:

- Formation of Ar_2^+ , followed by dissociative recombination [41, 42].
- Three-body recombination ($\text{Ar}^+ + e + \text{Ar}$) (a factor $\sqrt{M_{\text{Ar}}/m_e}$ slower than reaction (4.33)).
- Radiative recombination [3].

• Destruction:

- Quenching of metastables by electronic collisions [33].
- Association to Ar_2^* [43, 44]
- Diffusion to the walls [45].

Eq. 4.32 now becomes:

$$\frac{\partial}{\partial z}(n_{4s}w_z) + \frac{1}{r}\frac{\partial}{\partial r}(rn_{4s}w_r) = K_1 \cdot n_e^3 - n_{4s}A_{4s \rightarrow 3p}\Lambda, \quad (4.35)$$

with Λ the escape factor for resonance radiation and w_z and w_r the axial and radial components of the velocity of the particles respectively. For the three particle recombination we adopt the following expression given by Biberman [3, 46]:

$$K_1 = 1.1 \cdot 10^{-20} T_e^{-9/2} \text{m}^6 \text{s}^{-1}, \quad (4.36)$$

with $n_e = 10^{20} \text{m}^{-3}$, $T_e = 3000 \text{K}$ and $n_0 = \text{O}(10^{21}) \text{m}^{-3}$, $K_1 = 2.5 \cdot 10^{-36} \text{m}^6 \text{s}^{-1}$. Furthermore, $A_{4s \rightarrow 3p} = 1.57 \cdot 10^8 \text{s}^{-1}$ and $\Lambda = \text{O}(10^{-3})$ [33].

An exact solution of Eq. (4.32) is readily obtained only in the subsonic expansion region. Here the gradients are small and the entire left hand side of Eq. (4.32) can be neglected. So in this region we can apply the following local balance between production and destruction:

$$K_1 n_e^3 = n_{4s} A_{4s \rightarrow 3p} A. \quad (4.37)$$

The escape factor A now appears to be the determining factor on the $4s$ -density. It is related to the optical depth $k\bar{R}$ [33], given by:

$$k\bar{R} = \frac{\sqrt{\ln 2}}{4\pi\sqrt{\pi}} \frac{\lambda_{qp}^4}{c\Delta\lambda_{qp}} \frac{g_q}{g_p} A_{qp} n_p \mu R, \quad (4.38)$$

with μ a geometrical factor ($\mu=1.2$) and R the radius of the plasma beam. The escape factor A is then given by:

$$A(k\bar{R}) = \frac{\sqrt{\ln 2}}{k_L R \sqrt{\pi}} = \sqrt{\frac{4\pi c g_p \Delta\lambda_L}{g_q A_{qp} n_p \lambda_{qp}^4 \mu R}}. \quad (4.39)$$

Here k_L and $\Delta\lambda_L$ are the quantities taking only the Lorentzian part of the line into account, which is valid as $\frac{\Delta\lambda_L}{\Delta\lambda_D} \leq \frac{100}{k\bar{R}}$.

The Lorentzian broadening mechanisms in the expansion which we should consider are natural broadening, Stark broadening and resonance broadening. The first has values of $\Delta\lambda_{\text{nat}}=5 \cdot 10^{-7}$ nm and $2.5 \cdot 10^{-6}$ nm respectively for the two lines. The Stark broadening is of the order of $\Delta\lambda_{\text{Stark}} = 5 \cdot 10^{-27} n_e$ nm [33], so in the subsonic part of the expansion, with $n_e = O(10^{19}) \text{ m}^{-3}$, $\Delta\lambda_{\text{Stark}} < 10^{-7}$ nm and we may neglect it in first order approximation. Resonance broadening of the two resonant lines can be estimated at $4 \cdot 10^{-8}$ and $1.5 \cdot 10^{-7}$ nm [47], [48], [49] (with $n_0 \sim 10^{21} \text{ m}^{-3}$) and can also be neglected. So in the subsonic part of the expansion, natural broadening is the most important Lorentzian broadening mechanism. Now using $\Delta\nu_L = \frac{1}{2\pi\tau} = \frac{A}{2\pi\nu}$ (for a resonance line) and $\frac{\Delta\lambda_L}{\lambda} = \frac{\Delta\nu_L}{\nu}$, equation (4.39) becomes

$$A(k\bar{R}) = \sqrt{\frac{2g_p}{g_q n_p \lambda_{qp}^2} \mu R}. \quad (4.40)$$

It appears that the escape factor for the resonant lines is independent of the transition probability A , caused by the proportionality of the Lorentzian width with the A -value. Furthermore it implies that the effective transition probabilities $A \cdot A$ of the levels s_2 and s_4 remain linear in A , and that the level with the largest transition probability A ($5.1 \cdot 10^8 \text{ s}^{-1}$) represents the most important loss channel for the argon $4s$ -states. Furthermore, because of the strong coupling between the four $4s$ -sublevels, the radiative decay through the resonant lines is also indirectly providing a rapid depopulation of the metastable levels. Now for calculating the decay rates of the $4s$ -states first one has to calculate the effective transition

probability $\Lambda \cdot A$ per line and average it over the entire 4s-group [33]. This leads to an average effective 4s transition probability of

$$A_{4s \rightarrow 3p}^{av} = \frac{\sum_{k=1}^4 g_k A_{k \rightarrow 0} \Lambda_{k \rightarrow 0}}{\sum_{k=1}^4 g_k} = \Lambda \cdot 1.57 \cdot 10^8 \text{s}^{-1} \quad (4.41)$$

Using the values for n_e , T_e and n_0 as obtained with Thomson scattering, and values of R from a quasi one-dimensional model [3], an axial dependence of the total 4s-density in the subsonic expansion region is obtained (cf. Fig. 4.16). In the supersonic part the situation is much more complicated. First of all, axial transport and radial diffusion cannot be neglected. Moreover the production of 4s-states by three particle recombination in the first millimeters of the expansion is large, because of the high electron density and the relatively rapidly dropping electron temperature. In other words, the plasma is recombining. Furthermore the escape factor cannot easily be calculated, because several line broadening mechanisms come into play. An exact solution in this region is out of the scope of this thesis. An indication for the 4s densities at the point $z=0$ can be obtained in the following way: In the arc the plasma is approximately in Partial Local Thermal Equilibrium (PLTE). Using the Saha equation with $n_e=10^{22} \text{ m}^{-3}$ and $T_e=1 \text{ eV}$ the 4s-density can be calculated to be $\approx 1.5 \cdot 10^{18} \text{ m}^{-3}$. Now for the missing part in the graph, the supersonic expansion, it is reasonable to assume that the production of 4s compensates for the density decrease by the expansion, and the actual profile in this region can be approximated by a gradual density decrease. The assumption that there is a large net production of 4s-states in the supersonic expansion is justified by considering the increase in the 4s-fluence. The diameter of the nozzle ($z=0$) is only 4 mm, the diameter of the plasma beam in the subsonic expansion is $\sim 5 \text{ cm}$, while the velocities and the densities are in the same order.

The specific features of the results of Fig. 4.13 (a) through (d) can now be explained:

- As already noted in Sec. 4.4.1, the densities per statistical weight of the four substates are approximately equal. The explanation for this is the strong collisional coupling by electrons and by neutrals between the sublevels [33, 39].
- Compared to the densities for the electrons and the neutrals, the 4s density is relatively low in the first millimeters of the supersonic expansion. The absolute values of the densities are in the same order as the ones obtained in [23]. With respect to the argon ion level, these 4s densities imply an

underpopulation factor of about $3.5 \cdot 10^{-4}$ [3], indicating the recombining character of the plasma.

- the supersonic density drop appears to be absent for the $4s$ -densities. There is a production by recombination and a large transport of $4s$ states in the supersonic region. Also transport of radiation from the arc into the expansion may increase the $4s$ densities. Furthermore, it should be noted that the results are somewhat averaged spatially, due to the relatively large beam diameter (about 1 cm) of the light source. So, for future measurements a smaller light beam is recommendable.
- In the subsonic part ($z > 60$ mm) the $4s$ densities remain approximately constant. This is confirmed by the local balance model. Only a quantitative difference is present. This is caused by the discrepancies for the three-particle recombination formulae found in the literature [3, 40, 50, 51]. Using the values of [3], which are a factor of 6 lower than those of Biberman, the estimated densities come out lower than the measured ones. So, on the average, the agreement of the measurements with the simple model is quite good. Another possible cause for the deviation is the sensitivity of Eq. (4.36) to the inaccuracy in the determination of T_e .

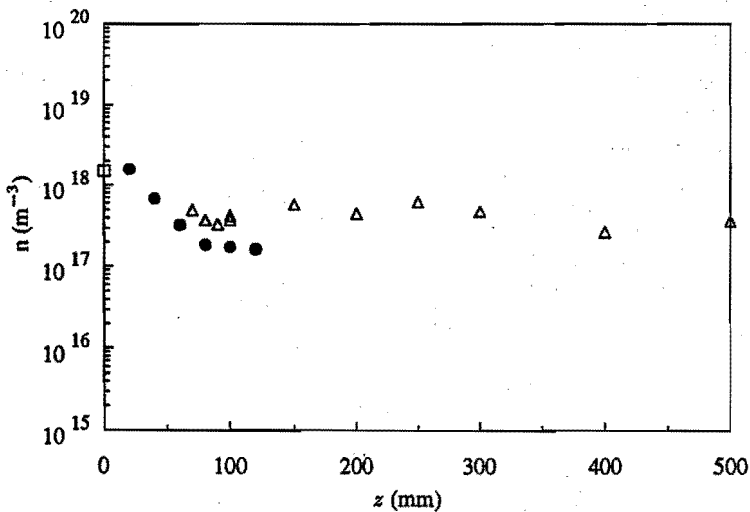


Figure 4.16: Total density of $4s$ -states n_{4s} as a function of axial position z ; Δ , as calculated by the model of Eq. (4.37), and, \bullet , measured values. The symbol \square on position $z=0$ denotes the value of the $4s$ -density, obtained using the Saha equation.

4.4.2 Absolute density of Ar($3p^54s$) states in plasmas used for carbon deposition

The effect of the addition of hydrogen, methane and oxygen on the argon $4s$ metastables has been investigated. When only methane is added and the chamber pressure is low ($O(10-100$ Pa), a plasma suited for amorphous hydrogenated carbon (a-C:H) is obtained. The combination of the three admixtures yields a plasma which is used for diamond deposition. The reactor parameters for crystalline diamond deposition are given in Table 4.5. Typical is the high chamber pressure of $6 \cdot 10^3$ Pa, needed for this type of deposition. Due to the lack of line profile data for these settings, the analysis of absorption data at this pressure would be very cumbersome. Therefore we reduced the chamber pressure to 40 Pa, and obtained standard reactor settings for which the necessary data have been determined ([2, 3, 23]).

Table 4.5: *The additional reactor parameters for diamond deposition using the standard argon plasma. (The basic settings were already given in Table 4.2.)*

Φ_{H_2}	$3.2 \text{ cm}^3\text{s}^{-1}$
Φ_{CH_4}	$0.8 \text{ cm}^3\text{s}^{-1}$
Φ_{O_2}	$0.4 \text{ cm}^3\text{s}^{-1}$
p_{chamber} (diamond depo)	$6 \cdot 10^3$ Pa
p_{chamber} (spectrosc.)	40 Pa
d_{n-s}	120 mm

First of all the effect of each gas admixture separately was investigated. As data on the heavy particles temperatures for these mixed plasmas are not available yet, the temperatures were estimated based on experiences in emission spectroscopy [2] and deposition experiments. For the argon/methane plasma an axial temperature of 2500 K, for the argon/oxygen a temperature of 3000 K, and for the argon/hydrogen plasma and the argon/hydrogen/methane/oxygen an axial temperature of 2000 K was adopted. It should be noted that for all the admixtures, no central dips were observed in the measured absorption data. It appeared that applying again the two centralized Gaussian density profiles yielded adequate fits. Two interesting axial positions were chosen, close to the nozzle ($z=20$ mm) and at the substrate location ($z=120$ mm).

In order to discuss the result for each admixture separately in more detail, the main results are summarized in the following figures. In Fig. 4.17 (a) through (d) the radial profiles of the total density of the $4s$ states are given for the various gas admixtures. In Fig. 4.18 (a) through (d) the axial decay of the densities of

the four $4s$ substates are given separately for the various gas admixtures. Again the results for the two radial positions are shown. In Fig. 4.18 (c) and (d) the lower limit of the displayed densities had to be decreased to 10^{14} m^{-3} , in order to observe still some trends. It Sec. 4.3.3 it was argued that these data may still be realistic.

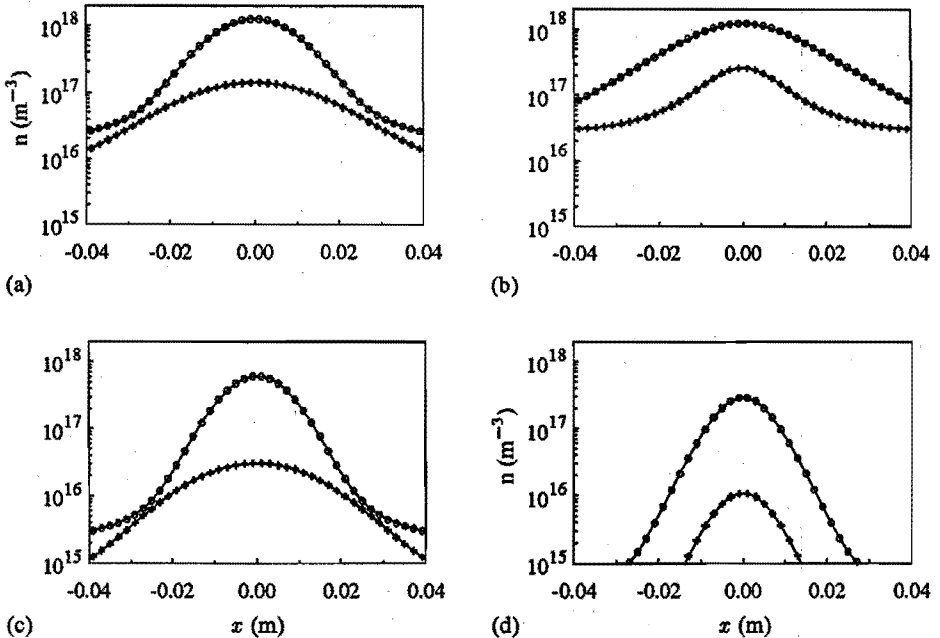


Figure 4.17: Radial profiles of the total density of the argon $4s$ state upon the addition of various gases: (a) $0.8 \text{ cm}^3 \text{ s}^{-1} \text{ CH}_4$ in the nozzle. (b) $0.4 \text{ cm}^3 \text{ s}^{-1} \text{ O}_2$ in the nozzle. (c) $3.2 \text{ cm}^3 \text{ s}^{-1} \text{ H}_2$ in the middle of the arc. (d) combination of the gas admixtures (a)-(c). \circ , $+$ $z=20, 120 \text{ mm}$ respectively;

Comparing the profiles of Figs. 4.17 and 4.18 (a) through (d) with those for the pure argon plasma, Figs. 4.14 and 4.15 generally the following features can be noted:

- The shape and the values of the radial profiles are only slightly affected by the admixture of oxygen and methane in the nozzle. The admixture of hydrogen (in the arc), both separately, Figs. (c) and the admixture of the three gases simultaneously (the combination used for diamond deposition), Figs. (d), leads to narrower profiles, and substantially lower density values.
- The densities per statistical weight are no longer approximately equal for most of the positions. Particularly for the off-axis positions (the open

symbols) the electronic coupling appears to be bad. This may be due to a lower electron density caused by the admixture. Particularly the methane admixture in the nozzle seems to have a perturbing effect at the plasma edge, probably due to a bad mixing into the plasma core.

In Figs. 4.17 (c) and (d) the inaccuracy in the 4s densities on the off-axis positions may be too large, although the total densities (the + symbols) yield a realistic picture.

Concerning the positions at the plasma axis (the solid symbols), we note the following: For the cases of methane and oxygen addition, Fig. 4.17 (a) and (b), the coupling is still reasonable for the metastable states. The densities for the radiative levels (the triangles (up and down)) are no longer equal. The reason for this is not clear. For the cases of hydrogen and the combined addition, Fig. 4.17 (c) and (d), it is just reversed. The densities of the resonant states remain approximately equal, while those of the metastable states have decreased strongly at the position $z=120$ mm. The populating of these states has to be provided by electronic collisional coupling to the resonant states, which appears to be inadequate.

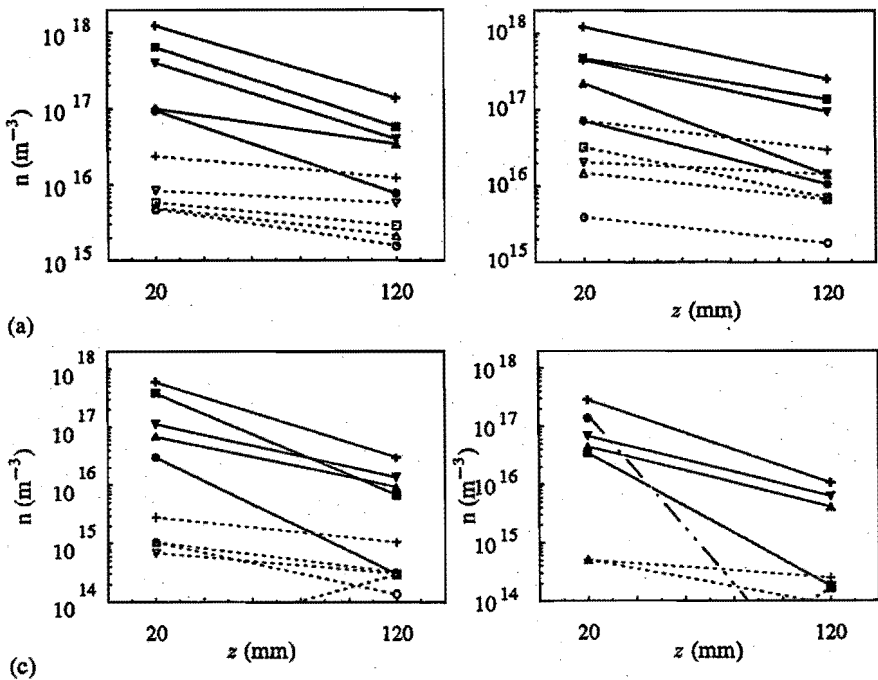
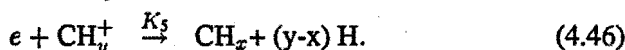
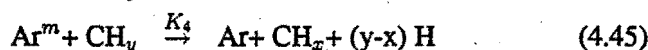
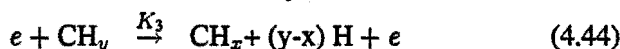
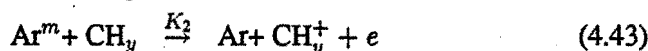
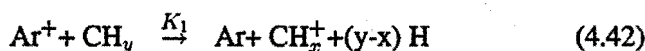


Figure 4.18: Axial decay of the densities of the argon 4s substates upon the addition of various gases: (a) $0.8 \text{ cm}^3 \text{ s}^{-1}$ CH_4 in the nozzle. (b) $0.4 \text{ cm}^3 \text{ s}^{-1}$ O_2 in the nozzle. (c) $3.2 \text{ cm}^3 \text{ s}^{-1}$ H_2 in the middle of the arc. (d) combination

of the gas admixtures (a)-(c). \blacktriangle , \bullet , \blacktriangledown , \blacksquare , $+$, s_2 , s_3 , s_4 , s_5 and total $4s$ density respectively. Two radial positions: solid symbols, solid lines $x=0$ (plasma axis), open symbols, dashed lines $x=40$ mm respectively; Note that here the lines merely serve to connect the associated data points and do not reflect an actually measured dependence.

- For the present small amounts of methane and oxygen admixture, Figs. 4.17 and 4.18 (a) and (b), both the ionization degree of the plasma and the argon $4s$ densities are hardly affected compared with that of a pure argon plasma. The electron densities remain of the order of 10^{19} m^{-3} . This has been established by emission spectroscopy [2] and probe measurements [6] respectively. These findings support the assumption that the argon $4s$ densities are coupled to the ion density. The ion densities are a factor of 10 higher than the argon $4s$ densities. On admixture of methane in the argon plasma the following reactions are of importance:



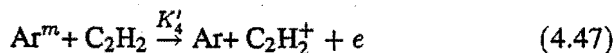
For $y=4$ (starting with methane) rate coefficients are given in the literature (mostly for low-temperature afterglows):

$$K_1 = 1.1 \cdot 10^{-15} \text{ m}^3 \text{ s}^{-1} \quad [4]$$

$$K_3 = 5 \cdot 10^{-15} \text{ m}^3 \text{ s}^{-1} \quad [52]$$

$$K_4 = 0.3 - 0.6 \cdot 10^{-15} \text{ m}^3 \text{ s}^{-1} \quad [53, 5]$$

The cross-section for reaction (4.46) is known to be orders of magnitude larger than that for (4.45) and so this reaction is a important dissociation mechanism. For K_4 no data are available. Penning ionization of CH_4 can most probably be ruled out because of its ionization potential of 12.6 eV, which is 0.9 eV higher than the highest metastable state. The ionization potentials of the CH_x radicals however are 11.1, 10.4 and 9.8 eV for $x=1,2,3$ respectively [54], so Penning ionization of these species can easily occur. No rate coefficients are available but for the comparable reaction on acetylene (ionization potential 11.4 eV),

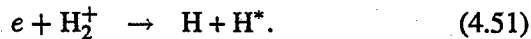
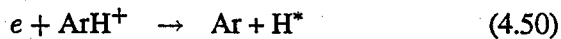
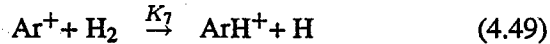
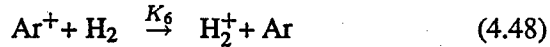


the rate coefficient is known: $K'_4 = 0.56 \cdot 10^{-15} \text{m}^3 \text{s}^{-1}$. [55] Comparing rate constants and densities we may conclude that the role of the metastables is limited and that the most important mechanism for the creation of active (hydro)carbon species is the direct charge exchange with the argon ions followed by dissociative recombination.

- On the admixture of hydrogen, and the combination of the three gases methane, oxygen and hydrogen, Figs. (c) and (d), the following features can be observed:
 - On both axial positions the argon 4s densities are much lower than those for the pure argon plasma.
 - The density profiles are narrower in comparison with pure argon case.

The following reactions are proposed to account for the loss of argon 4s-states:

- Assuming that all 4s-states come from recombination of argon ions, the loss of argon ions by charge transfer followed by dissociative recombination is responsible for the decrease of production of the 4s densities:



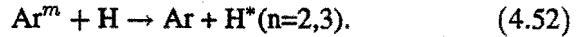
Reactions (4.51) and (4.51) are known to be very effective. For the charge exchange reactions approximate values are given in the literature. In [56] cross-sections of the order of 15 \AA^2 are given for reaction 4.49 (for argon ions with a high energy of 100 eV). For K_7 estimates are given in [57].

$$K_6 = 3 \cdot 10^{-15} \text{m}^3 \text{s}^{-1} \quad [56]$$

$$K_7 = 0.54 \cdot 10^{-15} \text{m}^3 \text{s}^{-1} \quad [57].$$

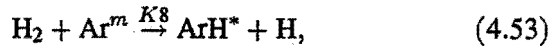
In this view the observed decrease of metastables in the plasma is consistent with the observed decrease of the ion density in argon-hydrogen plasmas [2].

- Direct interaction (excitation transfer) with the $\text{H}^*(n = 2, 3)$ levels [58, 59]:



The typical narrow profiles could be caused by the following mechanisms:

- Again the predominant mechanism may be that the admixture of hydrogen leads to a substantial loss of ions and thus to a lower 4s-density in the core. As a result, the resonance radiation has decreased considerably which leads consequently to a lower production of 4s states in the periphery by radiation capture.
- The mixing of the injected hydrogen into the argon plasma core may be bad, leading to a relatively high reduction of the 4s density in the periphery (again by loss of ionization). Also it could be an indication for the recirculation of H₂, H₂ will be more abundant than atomic hydrogen in the edges of the plasma core. In this case the following loss channel is present:



with $K_8 = 0.11 \cdot 10^{-15} \text{ m}^3\text{s}^{-1}$ [5].

Summarizing, in Fig. 4.19 the axial decay of the total density of the argon 4s states is shown in one figure, for the various gas admixtures. In this case, the results for two radial positions are shown, viz. at the plasma axis ($x=0$) and on the approximate edge of the plasma core ($x=40$ mm).

Also the values for the pure argon plasma are repeated, in this figure. It can immediately be observed that the effect of the admixtures of oxygen and methane on the 4s density is negligible. Moreover, the slope of the axial decrease are about equal to the slope for the case of the pure argon plasma. This indicates that no significant further interaction takes places between these species and the argon 4s metastables in the expansion. The effect of the admixture of hydrogen, and the combination of the three gases is clear. Not only are the values at position $z=20$ mm lower as for the case of the pure argon plasma, but also the slopes of the decrease are steeper. This confirms the influence of the addition of hydrogen on the argon 4s densities.

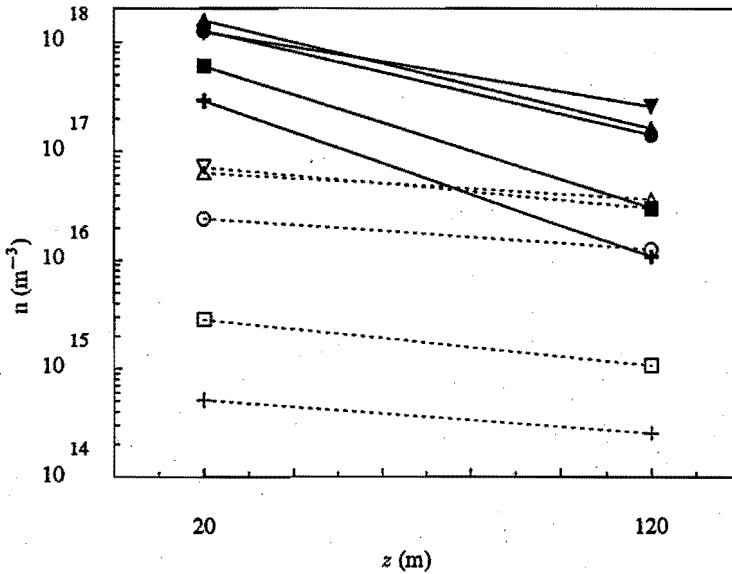


Figure 4.19: Comparison of the axial decay of the total density of the argon 4s state upon the addition of various gases: ▲ standard argon plasma; ● $0.8 \text{ cm}^3 \text{ s}^{-1}$ CH_4 in the nozzle; ▼ $0.4 \text{ cm}^3 \text{ s}^{-1}$ O_2 in the nozzle; ■ $3.2 \text{ cm}^3 \text{ s}^{-1}$ H_2 in the arc; + combination of the three admixtures (diamond condition). Radial positions: solid, open symbols, $x=0, 40$ mm respectively

4.4.3 Density of $\text{H}^*(n=2)$ states in an argon/hydrogen plasma

Attempts have been made to measure also the hydrogen ($n=2$) densities. Using the reactor settings given in Table 4.5 both with the low (40 Pa) as with the high pressure ($6 \cdot 10^3$ Pa) these could not be measured. It appeared that only at high flow rates ($14 \text{ cm}^3 \text{ s}^{-1}$) and an intermediate chamber pressure of 10^3 Pa, they could be measured. (A similar phenomenon has also been observed in emission, where the emission of the H_α appears to be maximum for a pressure of several times 10^2 Pa [60]).

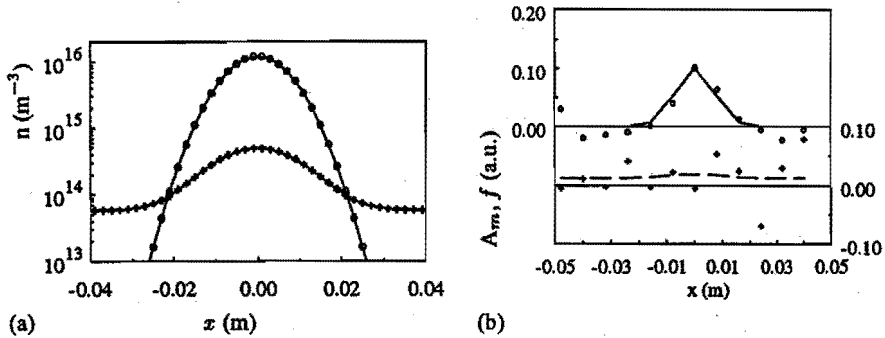
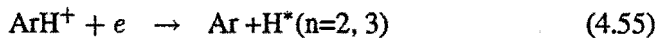
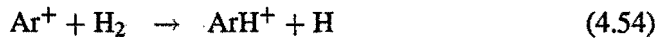


Figure 4.20: (a) Radial density profiles of the $H^*(n=2)$ state upon the addition of $14 \text{ cm}^3 \text{ s}^{-1}$ H_2 in the middle of the arc (in $58 \text{ cm}^3 \text{ s}^{-1}$ argon). \circ $z=20 \text{ mm}$, $+$ $z=120 \text{ mm}$; $p_c=1.1 \cdot 10^3 \text{ Pa}$ and (b) fit quality.

The result of this measurement (with $T=2000 \text{ K}$) is given in Fig. 4.20. As an illustration of the sensitivity of the fit method, and the analysis of the detection limit given in Sec. 4.3.3, the result of the position $z=120 \text{ mm}$ is also given. Using Eq. (4.29), and $\hat{A}_{ki, H_\alpha}=0.441$, $g_k=18$ and $g_i=8$, we find $A_m=6.35 \cdot 10^{-3} \hat{N}_i \hat{l}$. That is a density of $0.3 \cdot 10^{15} \text{ m}^{-3}$ over a length of 5 cm already gives a value for the absorption (of 0.01) in the order of the (statistically reduced) noise. So, at $z=120 \text{ mm}$ the measured absorption data yield $H^*(n=2)$ densities of the order of the detection limit for $H^*(n=2)$ of $\approx 3 \cdot 10^{14} \text{ m}^{-3}$. Unfortunately, in this case it can not be ruled out that the measured absorption values are caused by a systematic error (due to the localized effect of the pixel blurring on the diode array). The source of the $H^*(n=2)$ states is probably the following reaction sequence, with H_2 produced during recirculation in the chamber:



4.5 Conclusions

- 1 An efficient and relatively easy numerical method has been developed for analyzing spectroscopic absorption data for inhomogeneous media. The results prove to be satisfactory; besides density profiles, in the case of accurate measurements also temperature determinations can be done in principle.
- 2 The profile of the $4s$ densities in the expansion can be approximated adequately by a combination of two radial Gauss profiles, a narrow one

- the plasma core and a broad one for the background gas.
- 3 The densities of the argon $4s$ metastables are a factor of ~ 10 lower than the ion densities. So their effect in deposition is limited compared to that of ions.
 - 4 The axial profile of the $4s$ states does not show the typical supersonic expansion behaviour, which can be observed for the densities of the electrons and the neutrals. There is an actual net production of argon $4s$ in the supersonic expansion caused by recombination. Furthermore, most likely transport contributes to the observed high densities.
 - 5 In the subsonic expansion region the $4s$ -densities can be described by a local balance. An uncertainty is the value of the three-particle recombination coefficient and strong dependence on the electron temperature, which is only known approximately.
 - 6 Addition of hydrogen affects the metastable density drastically. Most likely this is due to two reasons: a) the hydrogen-induced loss of ionization; b) the excitation transfer between argon and hydrogen atoms. No interaction with methane was observed, confirming the negligible role of the argon metastables in deposition processes. Addition of small amounts of oxygen has no effect on neither the ion density nor the $4s$ densities.
 - 7 Hydrogen $2s$ metastables can be detected only in specific reactor conditions, a relatively high hydrogen flow and an intermediate chamber pressure.

Acknowledgement

This work was made possible by the financial support of Electricité de France, as a consequence of a collaboration with the Eindhoven University of Technology (Contract nr. M60L04/7B006/EL447). Furthermore the work of J.J. Beulens, M. Schuwer, H. de Jong, T. Kiers, M.J.F. van de Sande and B. Hüsken in developing and building the spectroscopy set-up is gratefully acknowledged.

Bibliography

- [1] G.M.W. Kroesen, *Ph.D. Thesis*, Eindhoven University of Technology, (1988).
- [2] J.J. Beulens, *Ph. D. thesis*, Eindhoven University of Technology, (1991).
- [3] M.C.M. van der Sanden, *Ph. D. thesis*, Eindhoven University of Technology, (1991).

- [4] M.T. Bowers and J.B. Laudenslager, *Principles of Laser Plasmas*, G. Bekefi (ed.), John Wiley & Sons, 98, (1976).
- [5] M. Bourène and J. Le Calvé, *J. Chem. Phys.*, **58** (4), 1452, (1973).
- [6] Zhou Qing, M.C.M. van de Sanden, M.J. de Graaf D.K. Otorbaev, G.J. Meeusen, A.J.M. Buuron, and D.C. Schram, *contribution to the 1993 ISPC-11 conference, Loughborough (UK), August 22-27, (1993).*
- [7] A.J.M. Buuron, D.K. Otorbaev, J.J. Beulens, T. Kiers, M.C.M. van de Sanden H. de Jong, and D.C. Schram, *High Temp. Chem. Processes.*, **2**, 75, (1993).
- [8] E.F.M. van der Held, *Z. Phys.*, **70**, 508, (1931).
- [9] O. Matsumoto, H. Toshima, and Y. Kanzaki, *Thin Solid Films*, **128**, 341, (1985).
- [10] J. Harris, *J. Appl. Phys.*, **56**, 2298, (1990).
- [11] A. Boudina, E. Fitzer, and G. Wahl, *Diamond and Related Materials*, **1**, 380, (1992).
- [12] Y. Tzeng, M. Yoshikawa, M. Murakawa, and A. Feldman, eds., *Proc. 1rst Int. Conf. on Application of Diamond Films. and Rel. Mater.- ADC '91, Auburn, Alabama (U.S.A.) August 17-22, 1991, Materials Science Monographs 73, Elsevier, Amsterdam-Oxford-New York-Tokyo, 475, (1991).*
- [13] M. Frenklach and K.E. Spear, *J. Mater. Res.*, **3**, 133, (1988).
- [14] Y. Mitsuda, Y. Kojima, T. Yoshida, and K. Akashi, *J. Mat. Sci.*, **22**, 1557, (1987).
- [15] Y. Saito, K. Sato, K. Gomi, and H. Miyadera, *J. Mater. Sci.*, **25**, 1246, (1990).
- [16] B. Marcus, M. Mermoux, F. Vinet, A. Campargue, and M. Chevenier, *Surf. Coat. Technol.*, **47**, 608, (1991).
- [17] R. Bleekrode, *Ph.D. Thesis*, University of Amsterdam, (1966).
- [18] A.J.M. Buuron, J.J. Beulens, M.J.F. van de Sande, and D.C. Schram, *Fusion Technol.*, **19**, 2049, (1991).
- [19] W. Lochte-Holtgreven, ed., *Plasma Diagnostics*, North-Holland Publishing Company, Amsterdam, (1968).
- [20] J.W. McConkey, *J. Opt. Soc. Amer.*, **59**, 1262, (1969).
- [21] J. Jolly and M. Touzeau, *J. Quant. Spec. Rad. Trans.*, **15**, 863, (1975).
- [22] Yu.B. Golubovskii, Yu.M. Kagan, and L.L. Komarova, *Opt. Spectrosc.*, **33**, 440, (1972).
- [23] P.A.A. van der Heyden, R.F.G. Meulenbroeks, M.C.M. van de Sanden, and D.C. Schram, to be published, (1993).
- [24] R. Ladenburg, *Z. Phys.*, page 451, (1921).
- [25] S.S. Penner, *Quantitative Molecular Spectroscopy and Gas Emissivities*, Addison-Wesley Reading, Massachusetts, (1958).

- [26] A.C.G. Mitchell and M.W. Zemansky, *Resonance Radiation and Excited Atoms*, Cambridge University Press, Cambridge, (1971).
- [27] S.E. Frish and A.P. Makarov, *Opt. Spectrosc.*, **25**, 447, (1968).
- [28] A.T.M. Wilbers, *Ph. D. Thesis*, Eindhoven University of Technology, (1991).
- [29] R. Ladenburg and F. Reiche, *Ann. Phys.*, **42**, 181, (1913).
- [30] V.M. Lelevkin, D.K. Otorbaev, and D.C. Schram, *Physics of non-equilibrium plasmas*, North Holland Publishing Company, Amsterdam, (1992).
- [31] I.M. Vardavas, *J. Quant. Spec. Rad. Trans.*, **49**, 119, (1993).
- [32] H. W. Drawin and F. Emard, *Beitr. Plasma Phys.*, **13**, 143, (1973).
- [33] R.J. Rosado, *Ph. D. thesis*, Eindhoven University of Technology, (1980).
- [34] T. Holstein, *Phys. Rev.*, **83**, 1159, (1951).
- [35] D.S. Baer and R.K. Hanson, *J. Quant. Spec. Rad. Trans.*, **47** (6), 455, (1992).
- [36] A.T.M. Wilbers, *Ph. D. Thesis*, Eindhoven University of Technology, (1991).
- [37] W.L. Wiese, M.W. Smith, and B.M. Miles, *Atomic Transition Probabilities*, NBS, (1969).
- [38] C.A. Kak and M. Slaney, *Principles of computerized tomographic imaging*, IEEE Press, New York, (1988).
- [39] J.L. Delcroix, C.M. Ferreira, and A. Ricard, *Principles of Laser Plasmas*, G. Bekefi (ed.), John Wiley & Sons, 184, (1976).
- [40] D. Benoy, *Ph. D. Thesis*, Eindhoven University of Technology, (1991).
- [41] B.M. Smirnov, *Ions and Excited Atoms in Plasmas*, (1974).
- [42] M.A. Biondi, *Principles of Laser Plasmas*, G. Bekefi (ed.), John Wiley & Sons, 143, (1976).
- [43] E. Ellis and N.D. Twiddy, *J.Phys.B*, **2**, 1366, (1969).
- [44] J.W.Keto, R.E. Gleason, and G.K. Walters, *Phys. Rev. Lett.*, **33**, 1365, (1974).
- [45] E. Ellis and N.D. Twiddy, *J.Phys.B*, **2**, 1366, (1969).
- [46] L.M. Biberman, V.S. Vorob'ev, and I.T. Yakubov, *Kinetics of Nonequilibrium Plasmas*, Plenum Press, New York, (1987).
- [47] I.I. Sobelman, *Introduction to the Theory of Atomic Spectra*, Pergamon Press, Oxford, (1972).
- [48] R.G. Breene Jr., *The Shift and Shape of Spectral Lines*, Pergamon Press, London, (1961).
- [49] J.M. Vaughan, *Proc. Roy. Soc. A.*, **295**, 164, (1966).
- [50] A. Gleizes, *Beitr. Plasma Phys.*, **22**, 241, (1982).
- [51] A. Funahashi and S. Takeda, *J. Phys. Soc. Japan*, **25**, 298, (1968).
- [52] F. Hummernbrum, H. Kempkens, A. Ruzicka, C. Schiffer H-D. Sauren,

- J. Uhlenbusch, and J. Winter, *Plasma Sources Sci. Technol.*, **1**, 221, (1992).
- [53] L.G. Piper, J.E. Velazco, and D.W. Setser, *J. Chem. Phys.*, **59** (6), 3323, (1973).
- [54] D.R. Lide, ed., *Handbook of Chemistry and Physics*, 72th edition, CRC Press, Inc., Boca Raton, Ann Arbor, Boston, (1991-1992).
- [55] J.L. Delcroix, C.M. Ferreira, and A. Ricard, *Principles of Laser Plasmas*, G. Bekefi (ed.), John Wiley & Sons, 211, (1976).
- [56] R.C. Amme and J.F. McIlwain, *J. Chem. Phys.*, **45** (4), 1224, (1966).
- [57] A.B. Rakshit and P. Warneck, *J. Chem. Phys.*, **73** (6), 2673, (1980).
- [58] M.A.A. Clyne, M.C. Heaven, K.D. Bayes, and P.B. Monkhouse, *Chem. Phys.*, **47**, 179, (1980).
- [59] R.L. Vance and G.A. Gallup, *J. Chem. Phys.*, **72**, 894, (1980).
- [60] M.C.M. van de Sanden, *private communication*, Eindhoven University of Technology, (1993).

Chapter 5

Diamond deposition by an expanding cascaded arc plasma

abstract

With the expanding cascaded arc method, diamond single crystals and continuous films were deposited onto silicon and molybdenum substrates. SEM was used for analyzing the morphology and estimating the deposition rates. Quantitatively, the quality of the deposited diamond was investigated by means of Raman spectroscopy. In the present work an upgrading of the power and flow settings of the deposition reactor was performed, using the conventional 1:100:100 hydrocarbon/hydrogen/argon plasma mixture, and a substrate temperature of 1000 °C. Based on these experiments, successful trials were carried out using the novel oxygen/hydrogen/hydrocarbon/argon plasma mixture. The oxygen to carbon ratio typically had to be of the order of 1:1, in accordance with the values reported in the literature for other types of plasma reactors. In order to try and optimize the deposition rate (while retaining a high quality) the hydrogen flow rate was reduced as far as possible, and the influence of changing the location of admixture of the various gases was investigated. Good quality diamond was deposited reducing the hydrogen flow rate as far as to a 4:1 ratio to the hydrocarbon flow rate. Using this mixture, the highest growth rates were obtained with the substrate at a short distance (4 cm) from the exit of the arc. The maximum growth rate was of the order of 15 nm s⁻¹. The width of the diamond Raman peak was 7.2 cm⁻¹ (a typical value for plasma synthesized diamond). The main advantage however using oxygen as an etching gas is that the substrate temperature required for diamond formation may be much lower. In the present project diamond was deposited at a substrate temperature of 400 °C, but at a low rate of some tenths of nm s⁻¹.

5.1 Introduction

Diamond has a unique combination of physical properties. Among others these are a high hardness and wear resistance, a low friction, optical transparency in a wide wavelength range, a high thermal conductivity (while it is electrically insulating) and biocompatibility. In the form of a continuous coating diamond is suited for a vast field of technological applications [1]. In the last decades the the efforts to synthesize diamond artificially have grown explosively. Up to 1958 the only method to produce artificial diamond crystals was the HP/HT technique in which coal was transformed into diamond by submitting it to simultaneously an extremely high pressure (HP) and a high temperature (HT) [2]. In that year the onset for a low pressure chemical vapour deposition technique for the deposition of diamond was given by Eversole [3]. The major breakthrough for the plasma enhanced diamond chemical vapour deposition techniques was achieved in the early eighties [4, 5, 6]. Extensive surveys of the various methods and recent developments can be found in review papers [7, 8, 9, 10, 11, 12], and in the proceedings of the specific conferences and symposia in this field [13, 14]. The main requirement is the establishment of a superequilibrium of atomic hydrogen, that is an atomic hydrogen concentration much higher than the gas value of the chemical equilibrium for the temperature and the partial gas pressures concerned. The role of the hydrogen radicals is to etch away undesired codeposited graphite and to hinder polymerization in the reacting gases. With all types of plasma discharges this superequilibrium of atomic hydrogen can be achieved. Initially the most common reactors used were hot-filament (HF) reactors and conventional RF, microwave, or DC glow discharges. In these types of plasmas the deposition is governed by diffusion and the deposition rates are limited (up to about $1 \mu\text{m h}^{-1}$). In the last decade other more efficient techniques have been developed *e.g.* the acetylene-oxygen flame (welding torch) [15]. The most recent development is the use of expanding plasma jets, with all types of plasmas (RF microwave, DC arc, ICP) operating as a particle source. Particularly with the DC and ICP jets, revolutionary growth rates have been achieved. A deposition rate of even up to 1 mm h^{-1} has been reported, using a DC arc jet with counterflow injection of liquid alcohols [16].

With the expanding cascaded arc plasma method, in the past [17, 18] diamond single crystals and continuous films were produced at high rates of the order of 10 nm s^{-1} over an area of a few cm^2 . The present project is aimed at optimizing the conditions for high quality diamond deposition with this method. The most common gas mixture used is a hydrogen/methane admixture in the carrier gas (mostly argon). Disadvantages of the gas mixture used are, that the ratio of H:C has to be typically 100:1, and that the substrate temperature has to be of the order of

1000 °C, which makes the method unsuited for many substrate materials. In recent years also successful diamond deposition using other etching gases like oxygen and fluorine has been reported [11, 19, 20] in various types of reactors. The principal gain is that the specific thermodynamic equilibrium conditions needed for the growth of diamond can be satisfied at lower deposition temperatures. In [17] already some successful diamond deposition experiments using oxygen as an additional etching agent were reported, but no reduction in the hydrogen gas flow rate was applied. In the present project firstly the reactor power and flow rates were increased in order to investigate whether a further upgrade of the deposition rate is feasible. In a second stage the hydrogen flow rate was reduced as far as possible, using oxygen as an etching agent. The crystallinity of the deposited carbon material was studied as a function of the ratios H/C, O/C and H/O in the total gas admixture. An additional purpose was the investigation of the effect of these gas ratios on the morphology of the grown crystals. It is reported in the literature (cf. [21]) that by promoting the growth in one specific crystallographic direction, smooth films may be obtained. Furthermore, the influence of changing the injection sites of the gases was investigated. As substrates both molybdenum and silicon wafers were used. Initially the substrate temperature was kept on ~ 1000 °C. Later the most promising trials were repeated for lower substrate temperatures (~ 400 °C). Besides operation at a lower substrate temperature, the use of oxygen in stead of hydrogen has many other advantages like higher growth rates, quality improvement, less power and gas consumption and a safer gas handling. Finally some experiments were carried out using C₂H₂/O₂/Ar and CF₄/CH₄- or CF₄/C₂H₂/Ar plasma mixtures in order to investigate the possibility of growth of diamond with other gas mixtures. The crystallinity and the quality of the deposited diamond were analyzed by Scanning Electron Microscopy (SEM) and Raman spectroscopy. In this chapter, first some properties of diamond and the influence of the deposition conditions will be reviewed. Then we will discuss the experimental set up. Subsequently we will discuss the results of the SEM observations and the Raman spectroscopy, and the influence of various gas mixtures on the quality of the diamond films.

5.2 Structure and properties of diamond

The diamond structure consists of sp^3 hybridized carbon bonds, which build up a tetrahedral crystal lattice ($d_{c-c}=1.54$ Å, angle CCC=109° 28'). The crystal type is face centered cubic (Fig. 5.1), The unit cell is composed of two parallelepipeds. By stacking identical units of structure in different sequences, a number of different modifications (polytypes) arise. The two principal polytypes

are the cubic and hexagonal (lonsdaleite), composed of units in which the atoms form a chair-like or a boat-like configuration respectively [22]. Macroscopically, diamond crystals occur in all kinds of geometrical shapes.

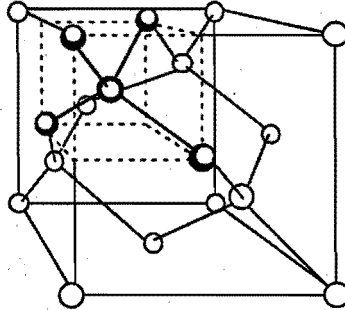


Figure 5.1: *The atomic configuration of diamond, with the atoms (with the solid pattern) expressing the tetrahedral configuration.*

Diamond is very hard (hardness 10^4 kg mm^{-2}), and has a large band gap (5.5 eV) which makes it transparent in large wavelength range, a high resistivity ($10^{16} \Omega\text{m}$) and high thermal conductivity (800 W (mK)^{-1}) [23, 24]. These properties make plasma deposited diamond films suited for a lot of industrial applications. Practical examples are the application on cutting and grinding tools, the application as a heat sink in IC-technology and in diamond coated biomedical components. In [1] an outline of the field of applications is given.

5.3 Diamond nucleation and growth

In order to grow continuous diamond films the nucleation density on the substrate has to be enhanced by pretreatment of the substrate. In our case we applied scratching of the sample with diamond powder and ultrasonic cleaning of the substrate in ethanol. It is obvious that for delicate substrates this pretreatment technique is unsuited. Other methods for nucleation enhancement have been reported such as electrophoretic seeding [25] and the use of halogens [20], which simultaneously modify the substrate. Another important method, favouring deposition on unconventional substrate types like steel, is firstly depositing a DLC (diamond-like carbon, or a-C:H film) (see also Chapter III). A systematic investigation on this method is given in [26]. There are several possible explanations for this type of growth. The first mechanism proposed is that the higher nucleation

density of diamond on amorphous (diamond-like) carbon is achieved by a transformation of the amorphous carbon into diamond. The second is based on the structure of diamond-like carbon films. These films, being either nanocrystalline or amorphous, can be characterized by a high density of defects at the surface, which act as nucleation sites for diamond crystals. However, for the present purpose of studying the deposition of diamond as a function of the reactor settings, the scratching method was adequate.

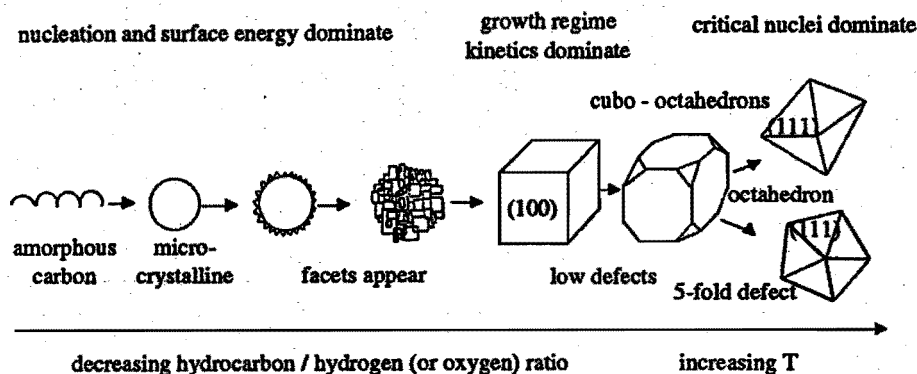


Figure 5.2: Influence of the plasma composition on the crystal shape of plasma synthesized diamond (from [26]).

In the plasma synthesis of diamond the morphology can be tailored by controlling the deposition conditions (Fig. 5.2). Below a certain H/C (or O/C) ratio only graphitic carbon is formed. In the appropriate superequilibrium conditions the formation of diamond is prevalent above that of graphite. From the literature [11] it is known that the ratio of H/C should be about 100:1, and of O/C about 1:1, irrespective of the type of plasma which is used. These findings will appear to be valid also for the cascaded arc deposition technique.

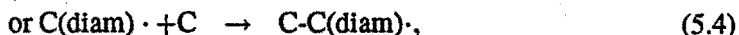
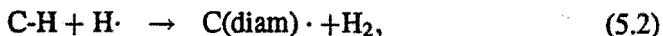
An actual issue is that the diamond films are polycrystalline. This property makes them unsuited for most optical applications. For mechanical applications the surface roughness has to be reduced by a treatment like polishing or laser treatment [27]. The general aim is to produce a monocrystalline layer by epitaxial growth. The latter has only been achieved on substrates of natural diamond (homo-epitaxial growth) [28]. Hetero-epitaxial growth has been out of reach up to now and is also out of the scope of this thesis. Practical requirements necessary for hetero-epitaxial growth are an ultra-high vacuum system and a controlled stepwise growth [29]. Furthermore, the lattice constant of the substrate material has to match that of diamond, and only a few materials e.g. copper fulfill this requirement (but with other drawbacks such as carbon solvability and

a low melting temperature). Hetero-epitaxial growth by the present method may be impossible at all because the growth starts on a limited number of distinct sites on the substrate (the nucleation sites), resulting in a structure of coalescing grains. The grain boundaries act as secondary nucleation sites and the result is a polycrystalline layer. One of the best alternatives to achieve the deposition of flat films is promoting the growth in one crystallographic direction [4, 21, 30]. By variation of the hydrocarbon/hydrogen (or /oxygen ratio) and the substrate temperature the morphology of the deposited crystals may be tuned from cubic to octahedral [26, 31].

Up to now, several questions exist concerning the underlying chemical and physical processes for diamond growth. First of all, graphite is the thermodynamically stable form of solid carbon in the pressure and temperature ranges used in diamond deposition. This fact is based on elementary thermodynamic energy calculations, using the quasi-equilibrium (QE) model for calculating gas compositions above a solid [32]. In the C-H phase diagram [33] the region of stability of diamond lies completely within that of graphite, so the model can not explain why the growth of diamond is prevalent. Additional non-thermodynamic parameters such as sticking coefficients and desorption coefficients have to be included in the model [33], *e.g.* a desorption coefficient of less than unity for H₂ on graphite is proposed, leading to an enhanced etching (by CH₄ formation). The second issue concerns the exact gaseous precursor for diamond deposition. Generally it is assumed that hydrocarbon radicals are relevant. Depending on the deposition reactor used and on the applied diagnostic, different radicals like C₂H₂ [34, 35], C₂H [36], CH₃ [37], CH₂ [38] and CH [39], C₂ [40], C₃ [41] and, recently, C atoms [42]. Mostly, chemical equilibrium models are used to calculate the abundance of the various species. Recently an extensive paper [42] has been presented reviewing the work in this field up to date and extending it to a comprehensive model for an expanding DC plasma jet. A serious limitation of these types of models is that they do not take ionized species and electrons into account. We will briefly summarize the results of these models which are now generally agreed upon. In the conventional HF, RF and microwave methods most likely the CH₃ radical is the dominant growth species [29]. In the methods using an expanding jet, both C and CH₃ radicals may be important species, depending on the relative concentration of atomic hydrogen [42]. The exact value of the latter is determined by the dissociation degree of the injected molecular hydrogen.

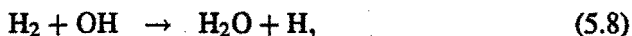
The main surface reaction sequence, leading to the formation of diamond is given in reactions (5.1) through (5.4) [43]:



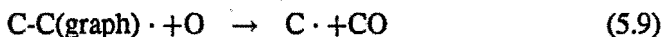


with \cdot denoting a dangling bond, and C(diam) an atom in the diamond configuration. The surfaces of the growing diamond are temporarily hydrogen terminated due to the abundance of the atomic hydrogen (5.1) [29, 35]. After the hydrogen abstraction reaction (5.2), radical adsorption (5.3 or 5.4) occurs, followed by a new cycle of hydrogen adsorption, abstraction and radical absorption reactions. These reactions are all exoenergetic, after energy barriers of the order of 0.5 eV have been passed.

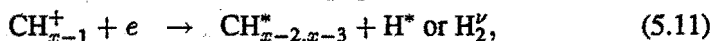
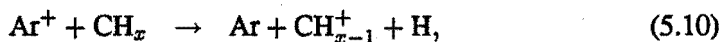
The role of oxygen is explained by the production of CH_3 and H by way of the reactions [43]:



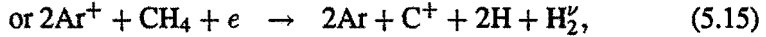
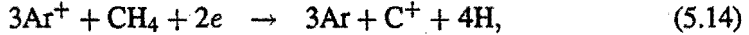
and of dangling bond creation by etching of carbon atoms in the graphite configuration,



It is doubtful whether chemical models give an adequate description of what is actually happening in an expanding plasma jet. Models and observations on the expanding cascaded arc plasma [17, 44] point to an important role for the charged species. Kroesen [44] elaborated a model on the expanding cascaded arc plasma jet, for compositions used for amorphous carbon deposition, in which the effect of charged particles is partly implemented. Beulens [17] measured carbon ions as important species. The mechanism for the production of carbon ions is charge exchange followed by dissociative recombination [17]:



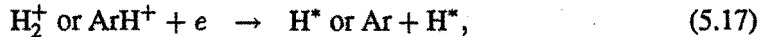
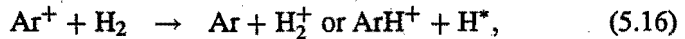
in total,



The species in the right hand side will be electronically or vibrationally excited. Adopting a average value of 4.3 eV for breaking all the C-H bonds of the methane [45], and ionization energies of 15.6 eV (argon) and 11.3 eV (carbon), it can be concluded that these mechanisms lead to a surplus excitation energy for the resulting species of 18.3 eV and 2.7 eV respectively (without taking kinetic energies into account).

From the reactions, it can be concluded that the addition of a small amount of a hydrocarbon (typically 1% for diamond deposition) only slightly affects the plasma ionization degree in the plasma (cf. Chapter IV). A typical carbon ion density in the expansion is 10^{18} m^{-3} (with a chamber pressure of 100 Pa) [17]. The loss by radiative and three-particle recombination in the expansion appears to be negligible [46]. So from these findings, it can be concluded that carbon ions play an important role in the deposition process with the expanding cascaded arc plasma.

However, in the conditions for diamond deposition, this picture is obscured. The admixture of large amounts of hydrogen reduces the ionization degree severely through the following reactions:



In this case the argon ion density in the expansion will be of the order of 10^{16} m^{-3} [47], and the dissociation of the hydrocarbons may be incomplete. Assuming that the ions play an important role in the deposition process, this is another argument for switching to oxygen, which hardly affects the ionization degree [48]. An additional question is still whether the plasma composition in the expanding jet is representative for that close to the substrate. Generally it is accepted that close to the substrate a boundary layers exist with kinetics deviating of that in the plasma jet [42, 43, 49, 50]: In the relatively low temperature boundary gas layer on the substrate stable species CH_4 being the most prevalent, are rapidly produced, followed by CH_3 radicals production by the partial equilibrium of the reaction $\text{CH}_4 + \text{H} \rightleftharpoons \text{CH}_3 + \text{H}_2$. [43]. Furthermore, during recirculation in the chamber hydrocarbons may originate, by association reactions on the walls.

Summarizing, the role of hydrocarbon radicals in the diamond deposition process using the cascaded arc plasma jet can not totally be ruled out. It is also possible that both ions and radicals play a role in a synergetic way.

5.4 Experimental set-up

The cascaded arc was introduced in 1956 by H. Maecker [51]. The composition of the arc itself was already described in Chapter II. In Fig. 5.3 an outline of the expanding cascaded arc set-up used for deposition is shown. The carrier gas argon is injected in the beginning of the arc channel at room temperature at a pressure around 0.5 bar. Standardized to a pressure of 1 bar its flow rate is typically $100 \text{ standard cm}^3\text{s}^{-1}$. A hydrocarbon is injected through the annular anode (the nozzle). As an etching agent hydrogen and/or oxygen can be injected in the middle of the arc or in the nozzle. The anode side of the arc is connected to a vacuum vessel with a pressure of the order of $6 \cdot 10^3 \text{ Pa}$. The vacuum vessel consists of a stainless steel cylinder with a length of 1.2 m, and a diameter of 0.5 m. This vessel can be pumped by a series of two roots blowers with a combined pumping speed of 700 l s^{-1} . The vessel pressure is controlled by a throttling valve in the pumping line and is kept in the range $5 \cdot 10^4 \text{ Pa}$ during operation. A beam of active particles (carbon, hydrogen and oxygen, ions and radicals, and electrons) expands into the vessel. Firstly the particles are accelerated to supersonic velocities of about 4000 m s^{-1} . The expansion and subsequent cooling of the heavy particles occurs approximately adiabatically [46]. The heavy particle temperature decreases from about 8000 K in the arc to about 2000 K in the supersonic expansion. The electron temperature drops from about 14000 K in the arc to about 2000 K. At a distance of some millimeters from the nozzle (depending on the chamber pressure) a shock occurs. After the shock the particles are conveyed subsonically (with velocities of still several hundreds of meters per second) to the substrate where the deposition occurs.

For diamond deposition the chamber pressure typically has to be of the order of $\sim 6 \cdot 10^3 \text{ Pa}$ [17].

The heating of the substrate is supplied by the plasma beam itself. To achieve $1000 \text{ }^\circ\text{C}$, the distance of the substrate to the nozzle has to be of the order of maximum 20 cm. Furthermore, at a larger distance from the nozzle, the plasma beam exhibits a turbulent behaviour due to the relatively high chamber pressure.

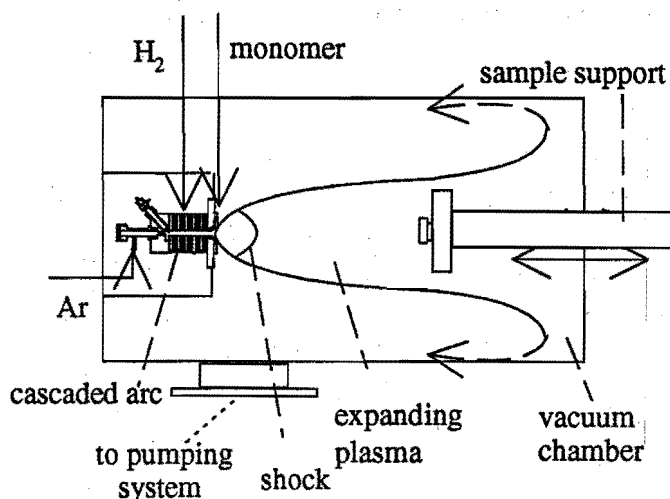


Figure 5.3: Outline of the cascaded arc set-up

In the vacuum chamber recirculation vortices exist. With increasing pressure the residence time of the particles in the vacuum chamber increases, and recirculating particles may pass the substrate several times, leading to an enhanced deposition (and graphite etching) efficiency. This may be another mechanism contributing to the relatively high growth rate and to the better diamond quality, attained at higher chamber pressures (cf. Chapter II).

5.5 Raman Spectroscopy

5.5.1 Introduction

Raman spectroscopy is a suited and fast technique for the analysis of the deposited crystalline carbon materials. The technique is based on the principle that the frequency of light scattered by matter may shift by a small amount depending on the vibrational properties of the matter. The specific advantage of the method is that it can distinguish clearly between the different allotropes of one element, e.g. diamond and graphite in this case, in comparison with for instance Auger electron spectroscopy (AES) or X-ray photo-electron spectroscopy (XPS) where the differences in spectra for various allotropes are small. We will briefly treat the theory of the method followed by a description of the measurement set-up.

A very practical guide on this technique is [52], out of which the theory in the following section is adopted.

5.5.2 Theory of the Raman effect

In the classical approach the Raman effect can be regarded as the scattering of light by a collection of atoms undergoing simple harmonic vibrations, while no account of the quantization of the vibrational energy is taken. When a molecule is subjected to an electric field the atoms acquire an electric dipole moment. For small fields, the induced dipole moment μ_i is proportional to the field strength E .

$$\mu_i = \alpha E. \quad (5.18)$$

The proportionality constant α is the polarizability of the molecule. Electromagnetic radiation generates an electric field which can be expressed as:

$$E = E^0 \cos(2\pi\nu_0 t). \quad (5.19)$$

E^0 is the equilibrium field strength and ν_0 is the angular frequency of the radiation. When a diatomic molecule vibrates harmonically at a frequency ν_v , its vibration as a function of time t can be expressed as

$$q_v = q_0 \cos(2\pi\nu_v t). \quad (5.20)$$

with q_v the elongation of the molecule along the axis and q_0 the equilibrium elongation of the molecule.

A necessary condition for the occurrence of Raman scattering is that the polarizability α changes during the vibration. For small vibrational amplitudes its value will be

$$\alpha = \alpha^0 + \left(\frac{\partial \alpha}{\partial q_v} \right)_0 q_v. \quad (5.21)$$

Substituting Eq. (5.20) in Eq. (5.21), and using Eqs. (5.19) and (5.20), the effect of incident radiation of frequency ν_0 on the induced dipole moment μ_i can be written as:

$$\mu_i = \alpha^0 E^0 \cos(2\pi\nu_0 t) + \left(\frac{\partial \alpha}{\partial q_v} \right)_0 E^0 q_0 / 2 \times [\cos(2\pi(\nu_0 + \nu_v)t) + \cos(2\pi(\nu_0 - \nu_v)t)]. \quad (5.22)$$

The first term in Eq. (5.22) describes the Rayleigh scattering and the remaining terms describe the Stokes and the anti-Stokes Raman scattering. Eq. (5.22) shows that light will be scattered with frequencies:

ν_0 = Rayleigh scattering

and

$\nu_0 \pm \nu_v$ = Raman scattering

In addition, Eq. (5.22) shows that Raman scattering only occurs if:

$$\left(\frac{\delta\alpha}{\delta q_v} \right)_0 \neq 0, \quad (5.23)$$

which means that the polarizability of the molecule must change during a vibration. In reality the polarizability is a tensor of second order. It is given by:

$$\left(\frac{\partial \alpha_{ij}}{\partial q_k} \right)_0 \neq 0 \quad (5.24)$$

which means that incident light with wave vector coordinate q_k induces polarizability changes in the material in the direction of the coordinates i and j (indicating crystallographic axes).

It is clear that all elements will have different specific polarizability changes. Moreover, the type of structure in which the atoms are bonded will be decisive for the determination of the frequencies of the phonons which can occur. In a crystal with a periodic structure only vibrations with discrete frequencies (the normal modes) can occur. This means that different crystal structures of one element can easily be distinguished. In the Raman spectrum sharp and narrow peaks will occur at specific frequencies. The full width at half maximum (FWHM) of the peak is an indication for the perfectness of the crystal and lattice defects will cause a broadening of the peak. An amorphous material will give rise to broad bands in the spectrum. For carbon the Raman peak designation is given in Table 5.1.

Table 5.1: Raman peak designation for carbon. (Adapted from [53])

position (cm^{-1})	typical FWHM (cm^{-1})	shape	assigned to
1150	80	Lorentzian	nanocryst. diamond
1332	2	Lorentzian	natural diamond
1332	7	Lorentzian	plasma deposited diamond
1355	250	Lorentzian	disordered graphite
1470	80	Gaussian	diamond precursor
1470	5	?	C_{60} , C_{70} Buckminster fullerenes [54]
1580	100	Gaussian	graphite

The band at 1470 cm^{-1} is also associated with to the 'bucky-balls' [54], besides to nanocrystalline diamond. Some of our samples exhibited this band. A decisive test however is that using different polarization directions of the incident light the peak should alternately come up or completely disappear. In the testing of our samples the peak intensity was practically independent of the polarization of the incident light [55], so the peak cannot be attributed to full-grown bucky-balls. This finding is also supported by the fact that the presence of oxygen prevents the formation of bucky balls [56] Maybe incomplete balls (curved graphitic sheets) are present in the material. Furthermore, in our samples the 1470 cm^{-1} band is always accompanied by the presence of the 1150 cm^{-1} which is generally assigned to a short range order of tetrahedrally bonded carbon (nanocrystalline diamond). The 1581 and 1355 cm^{-1} graphitic peaks were already addressed in Chapter III. Analog to the 1150 cm^{-1} diamond peak, the presence of the 1355 cm^{-1} band is an indication for the existence of graphitic bonding over a short range.

The results of the diamond deposition experiments have been evaluated with micro-Raman spectroscopy. In this technique the microscope objective serves both for focusing the incident light on the sample as for collecting the scattered light. For solid samples this is the common technique. It has the advantage that the alignment is very easy. Furthermore, by selecting the appropriate magnification, small sections of the samples (*e.g.* single crystals (facets)) can be studied. On the other hand the small spot in this technique hinders an exact interpretation of the overall coating quality [53]. However, because of the transparency of diamond a kind of averaging in depth is obtained. In Fig. 5.4 an outline of the Raman set-up (Dilor XY) is shown (*cf.* Chapter III).

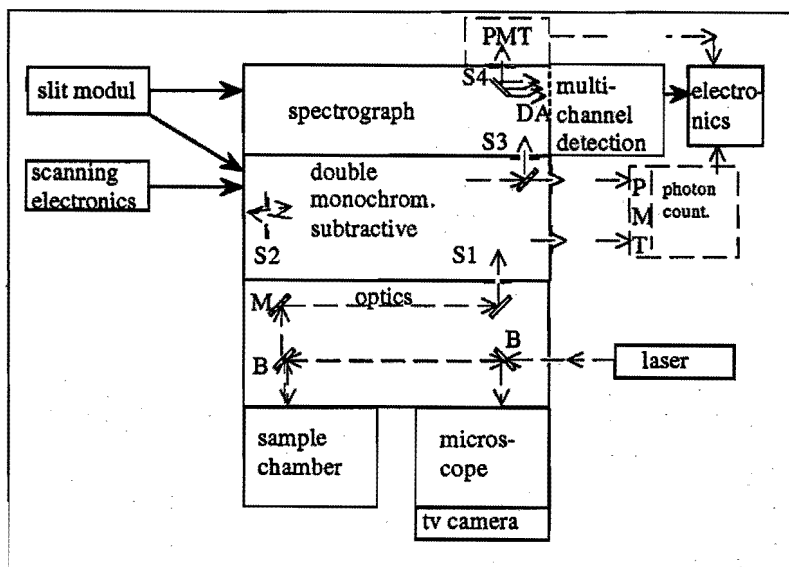


Figure 5.4: Outline of the set-up for micro Raman spectroscopy

The double monochromator is necessary to suppress straylight from the nearby Rayleigh scattering peak (intensity 10^3 to 10^6 times as high as the intensity of the Raman peaks). Depending on the measured intensity, different entrance slit widths (200, 100 and $50 \mu\text{m}$) were chosen, resulting in spectral widths of 6.6, 3.3 and 1.65 cm^{-1} respectively. As these widths are comparable with the peak widths of the diamond Raman peak, deconvolution of the measured diamond peaks was done by fitting the Lorentzian peak convoluted with a Gaussian apparatus profile to the measured data. It should be noted that the Raman scattering efficiency for sp^2 (graphitic) carbon bonds is 50-100 times as high as that for sp^3 (diamond) bonds [43]. The magnification of the objective of the microscope was chosen on $50\times$, resulting in a spot size of $4 \mu\text{m}^2$. As a source, the 514.5 nm line of an argon ion laser was used. In general the laser power was 100 mW. The photo diode array enables fast data-acquisition over a wide wave number range ($\sim 500 \text{ cm}^{-1}$) so the entire interesting region for carbon could be covered in one measurement. Signal-to-noise ratio was improved by averaging over 20 measurements of 1 s duration. Signal detection was done by means of a photo diode array coupled to a PC.

5.6 Results and discussion

5.6.1 Deposition conditions

In Table 5.2 the main parameters with which diamond deposition was obtained in the present project are given, compared to those used in the past [17]. It can be observed that significant extension of the parameter space has been achieved. In the first stage of the present work the power and gas flows were substantially increased (column II, Table 5.2), in order to further increase the deposition rates. The H/C ratio was varied by varying the methane flow from 0.6 to 1.05 cm³s⁻¹. In a second stage the hydrogen was gradually replaced by oxygen. In column III and IV the lower limits of the hydrogen flow rate with which diamond was deposited are given. With this modified gas mixture, lower deposition temperatures come into reach [19]. In order to reduce the substrate temperature, also the power and flow settings had to be reduced. In column IV an optimum setting for these low power trials are given. Furthermore the influence of modifying the admixture locations of the methane and the hydrogen was studied. Hydrogen was admixed in the cathode space, in the middle of the arc, in the nozzle, and in the vessel. Methane was admixed in the nozzle and in the vessel. Oxygen was injected in the middle of the arc, in the nozzle and in the vessel, and, in some preliminary trials, even in the cathode space. Furthermore, the use of C₂H₂ and CF₄ (the latter with fluorine as the etching agent) has been investigated.

Initially, 1 inch wafers of B-doped < 100 >-silicon were used as a substrate, but because of frequent cracking due to non-uniform heating and cooling, most trials were carried out using 1 inch molybdenum disks. With exception of the first few experiments (with hydrogen injection in the middle of the arc), the substrates were scratched with diamond powder (20-40 μm). All substrates were cleaned ultrasonically in ethanol (96 % purity). One striking discovery is that fingerprint contaminations enhance the nucleation of diamond (also reported in [57]). In general, deposition temperatures were measured with an optical pyrometer (Chino-IR-AHIS). Only for the low temperature experiments, a thermocouple measurement had to be used, and corrected to an actual surface deposition temperature. The pressure in the vessel was slightly unstable, and was kept around 6.5·10³ Pa by adjusting the valve to the pumping system (variation ± 3 · 10² Pa) The nozzle-to-sample distance was chosen such that the substrate temperature was about 1000 °C, slightly varying (± 50°C) because the slightly varying pressure (and change in emissivity of the sample).

Table 5.2: Parameter ranges used in the past (column I) and of the present project (column II, III and IV).

		past [17]	parameters upgrading	using oxygen	low power low temp
{Ar}	(cm^3s^{-1})	20-45	58	58	29
{CH ₄ }	(cm^3s^{-1})	0.2-0.4	0.6-1.05	0.8	0.8
{H ₂ }	(cm^3s^{-1})	20-45	35	↓ 1.6	0.4
{O ₂ }	(cm^3s^{-1})	0-0.4	–	0.4-0.3	0.4
I _{arc}	(A)	20-45	45	45	25
V _{arc}	(V)	110-133	128	90	69
P _{arc}	(kW)	3.85-6	5.8	4.1	1.7
Q	(10^{-6}W^{-1})	2.6-1.9	2.4	3.4	1.6
H _{tot} /C	ratio	204	121-71	↓ 8	5
O/C	ratio	0-1	1	1	1
T _s	(°C)	1000	1000	1000	±400
d _{n-s}	(cm)	2-10	12	12, 4	12
p _c	(10 ² Pa)	60	65	65	65
Δt _{depo}	(min.)	60	60	60	60

5.6.2 Crystallinity, morphology and deposition rate of the deposited diamond

The conventional methane/hydrogen/argon plasma

In Table 5.3 the FWHM value is given as a function of the variation of the hydrogen flow rate and injection site. Injection of large amounts of hydrogen in the cathode space was not investigated. The power supply is inadequate to sustain the arc in that case, due to the high plasma resistivity. The reactor settings used are given by column II, Table 5.2.

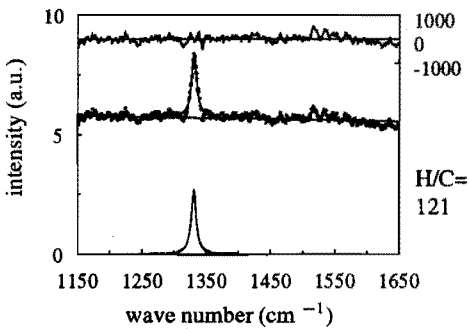
In Figs. 5.5 and 5.6 the fitted Raman spectra (a)-(c) and the morphology (d)-(f) are shown for diamond, deposited with hydrogen admixture in the middle of the arc and in the nozzle respectively. Depending on the substrate pretreatment, both separate single crystals as aggregations of single crystals forming continuous layers were deposited after one hour. In Fig. 5.6 (e) the nucleation enhancement due to the scratches can be noticed clearly. In all cases the predominant crystal habit is cubo-octahedral. The effect of changing the H/C ratio appears to be small. The H/C region in which cubic diamond crystals are formed may be very narrow [31]. Reducing the H/C ratio (Fig. 5.6 (e) and (f)) leads to a sudden

Table 5.3: *FWHM values of the deconvoluted Lorentz diamond peaks as a function of hydrogen flow rate and injection site; -g means: no diamond peak observed, only graphitic bands*

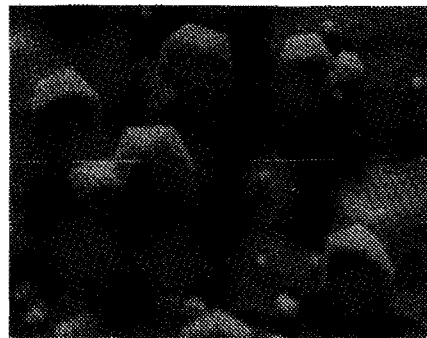
injection site → H _{tot} /C ratio ↓	halfway arc FWHM (cm ⁻¹)	nozzle FWHM (cm ⁻¹)	vessel
121	9.6	6.8	-g
92	10.2	4.8	-g
71	-g	-g	-g

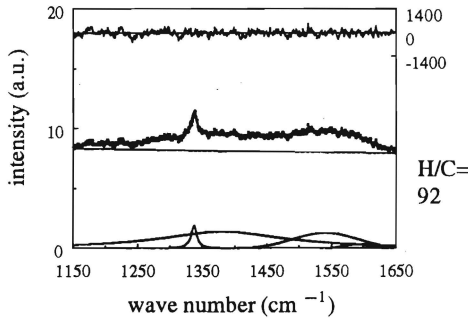
transition to a typical graphitic structure [58].

In most trials the deposition occurred over an annular area with radius of about 1 cm and a few millimeters wide. This may be due to relatively high argon flow (compared to [17]). In the literature [59] it was reported that argon can annihilate nucleation sites for diamond deposition.

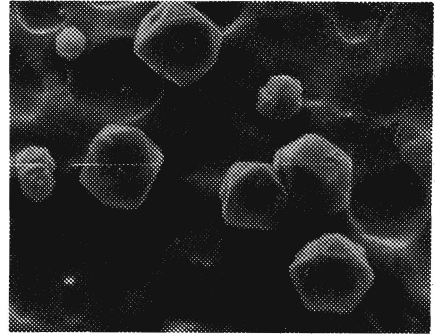
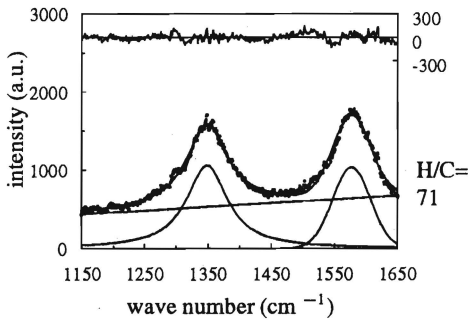


(a)

(d) 1 bar=10 μ m



(b)

(e) 1 bar = 10 μm 

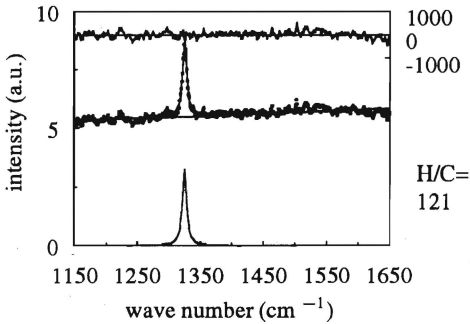
(c)

(cf. Fig. 5.6 (c))

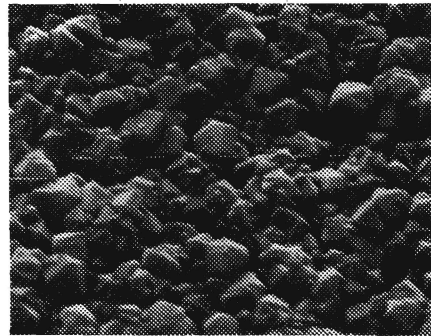
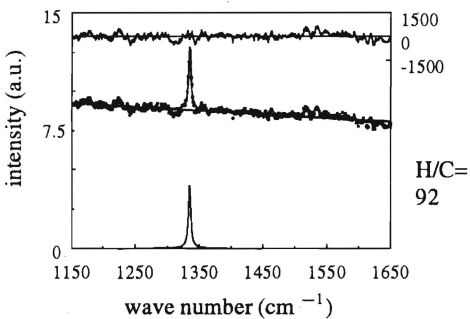
Figure 5.5: (a)-(c) Fitted Raman spectra and (d)-(f) morphology of diamond deposited on silicon (not scratched) with hydrogen injection in the middle of the arc (H means H_{tot}).

Another possible explanation is a non-uniform plasma composition, due to insufficient mixing of the admixed gases into the argon. The maximum growth rates obtained are of the order of $10 \mu\text{m h}^{-1}$ (Fig. 5.5 (b)), which is lower as reported by [17]. It is possible that the loss in deposition rate due to the larger nozzle-substrate distance is larger than the gain by upgrading the power and flow settings. The distribution of the -g's in Table 5.3 confirms the importance of atomic hydrogen for the deposition of diamond. Comparing the sequences of Figs. 5.5 (a) through (c) and 5.6 (a) through (c), and the Raman widths in Table 5.3, it can be observed that the addition of the hydrogen in the nozzle led to somewhat higher quality diamond than injecting it in the middle of the arc. The graphitic components are almost absent and the widths of the diamond peaks are smaller. This may be an indication for the importance of retaining a high ionization degree of the plasma in the diamond deposition process. The ionization

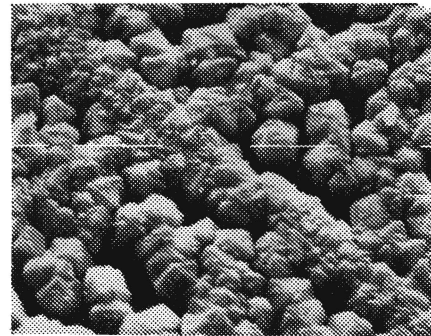
is affected less in the case of hydrogen admixture in the nozzle. Furthermore, again the non-uniform plasma composition may play a role. In the case of Fig. 5.6 (b) the SEM observation is not consistent with the Raman determined crystallinity. The crystals exhibit rough edges, while the Raman width (4.8 cm^{-1}) is the smallest of that sequence. A possible explanation is that both diagnostics are not always applied on the same location on the sample.



(a)

(d) 1 bar = $1 \mu\text{m}$ 

(b)

(e) 1 bar = $10 \mu\text{m}$

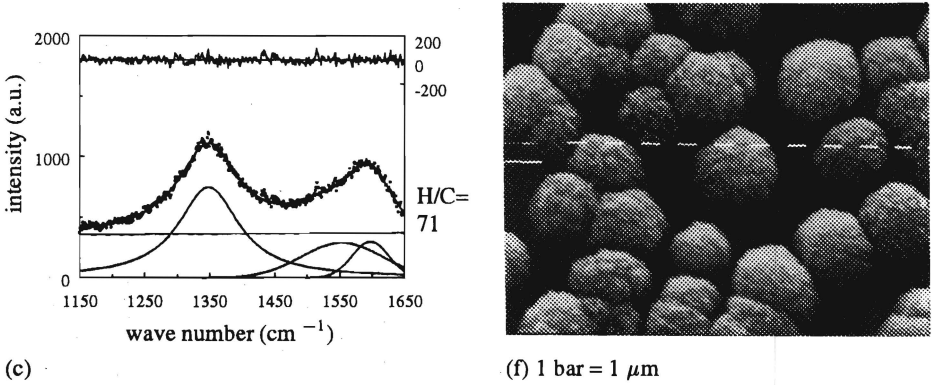


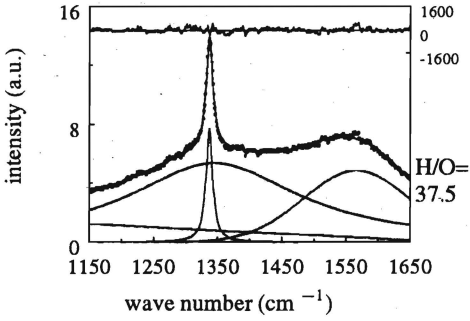
Figure 5.6: (a)-(c) Fitted Raman spectra and (d)-(f) morphology of diamond deposited on silicon with hydrogen admixture in the nozzle.

Effect of replacing the hydrogen with oxygen as an etching agent

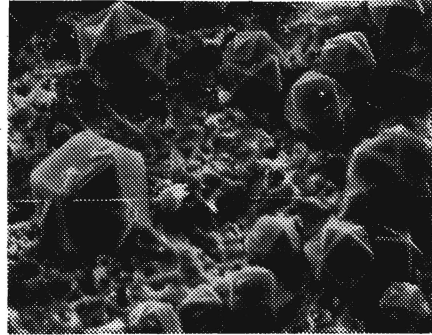
In Table 5.4 the FWHM value is given as a function of the ratio the hydrogen flow rate to the oxygen flow rate (H/O ratio) and the injection site of the oxygen (the hydrogen was injected in the middle of the arc). The O/C ratio was kept on unity. The other reactor settings are given by column III, Table 5.2. In Fig. 5.7 (a) through (e) the Raman spectra, and in fig. 5.7 (f) through (j) the morphology of the deposited diamond is shown. When relevant, the effect of deconvolution with the apparatus profile is also shown.

Table 5.4: FWHM values of the deconvoluted Lorentz diamond peaks as a function of oxygen flow rate and injection site; -g means: no diamond peak observed, only graphitic bands

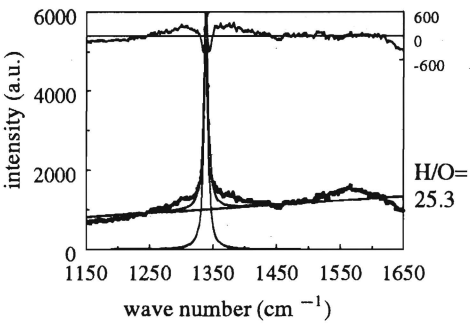
injection site → H _{tot} /O ratio ↓	nozzle FWHM (cm ⁻¹)	vessel
37.5	8.2	-g
25.3	4.6	-g
12.0	6.0	-
8.0	10.2	-g
4.0 (no H ₂)	-g	-



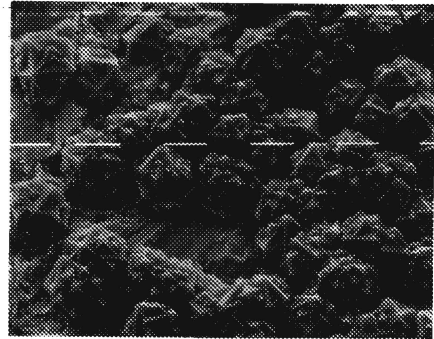
(a)



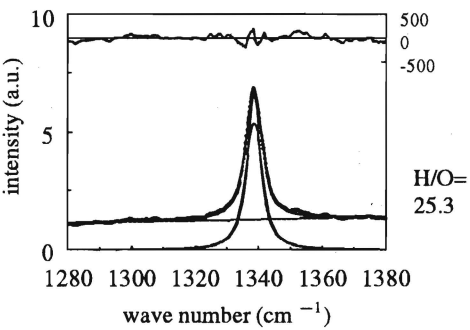
(f) 1 bar = 10 μm



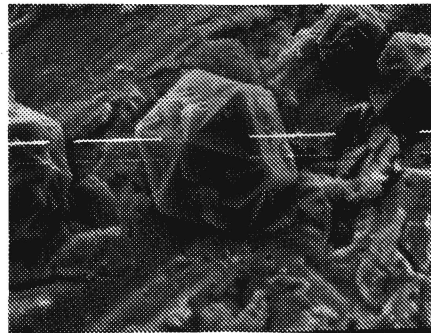
(b1)



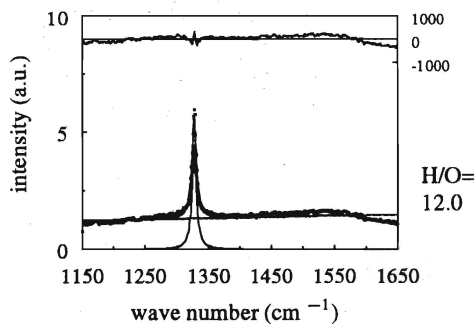
(g1) 1 bar = 10 μm



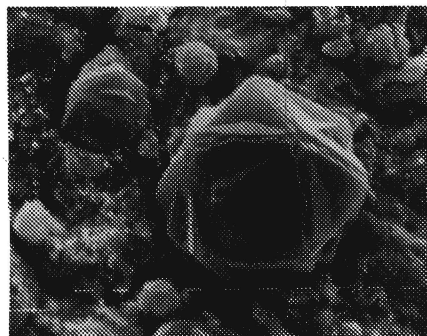
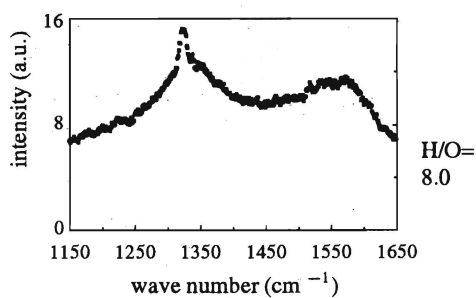
(b2) deconvolution of (b1)



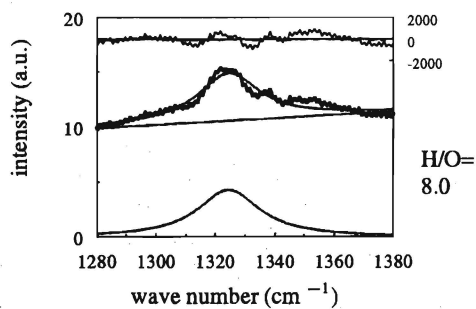
(g2) 1 bar = 10 μm



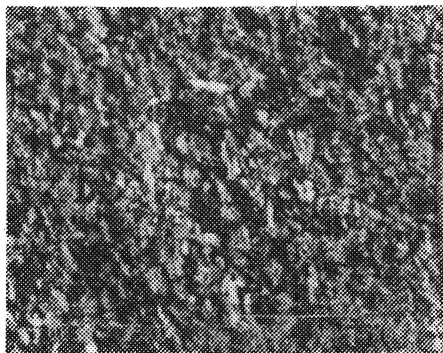
(c)

(h) 1 bar = 1 μm 

(d1)

(i1) 1 bar = 1 μm 

(d2) deconvolution of (d1)

(i2) 1 bar = 10 μm

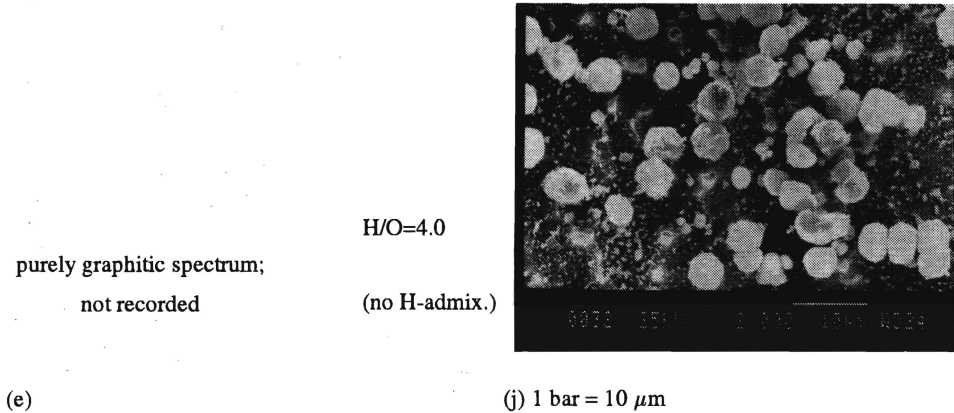


Figure 5.7: Fitted Raman spectra ((a) through (e)) and morphology ((f) through (j)) obtained with hydrogen injection in the middle of the arc and oxygen injection in the nozzle (H means H_{tot} ; $O/C=1$). Fig. (b2) displays the measured diamond peak of fig. (b1), and its deconvoluted shape (the higher one), and the fit quality, and Fig. (d2) that of (d1). Figs. (g1,2) and (i1,2) show two SEM images of the typical diamond shapes associated with the spectrum of Figs. (b1) and (d1) respectively. Substrates: molybdenum

Observing Fig. 5.7 (a) through (e)), there is an optimum H/O ratio (25.3) for obtaining the best quality crystalline material. In the Raman spectrum the graphitic components are almost absent and the width of the diamond peak is at a minimum. Observing the SEM images leads to a similar conclusion. The diamond shown in Fig. 5.7 (g1,2) has the best defined crystal boundaries. No graphitic growth can be observed. Furthermore, again the crystal habit is predominantly cubo-octahedral, almost independent of the variation of the gas ratios, and changing to microcrystalline material for low O/C ratios. Finding reactor settings which lead to the deposition of cubic diamond is desirable in future, with respect to the possibility of depositing a more smooth coating [21].

Total omission of the hydrogen admixture does not lead to diamond deposition with the present reactor settings. In the literature successful diamond deposition with a methane/oxygen/argon mixture [60] has been reported. However, besides a small diamond peak, the Raman spectra exhibit also large graphitic bands. Obviously, the hydrogen radicals out of the methane are sufficient under specific conditions. Generally it is accepted [11], that total omission of hydrogen (e.g. using CO) as a feed gas, can not lead to diamond deposition.

The growth rates are somewhat higher than with the hydrogen/hydrocarbon mixture but still not revolutionary. With a better cooled substrate holder the substrate might be placed closer to the nozzle and even higher power and flow

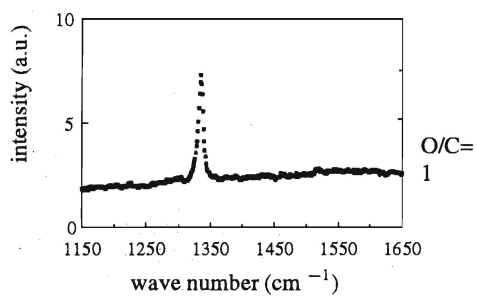
settings might be applied. Furthermore, diamond nucleation and growth seems to be more effective on the molybdenum than on the silicon substrates.

Analysis of the materials, deposited using oxygen in the plasma, with Low Energy Ion Scattering (LEIS) [61], indicated silicon contaminations. Diamond deposited using hydrogen did not show this contamination. For further optimization using oxygen, changes in the gas injection system are recommended. Protection of the substrate by first depositing an amorphous carbon sublayer without the use of oxygen may be necessary.

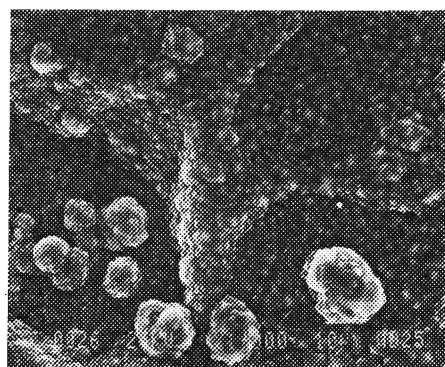
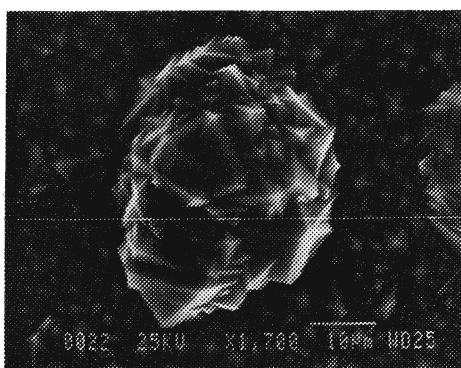
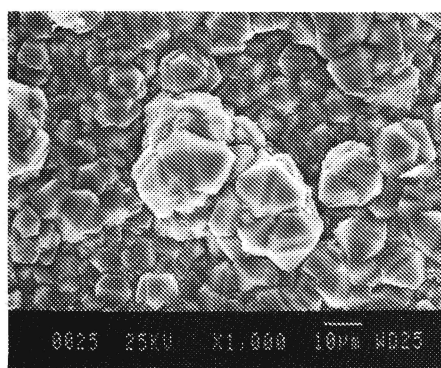
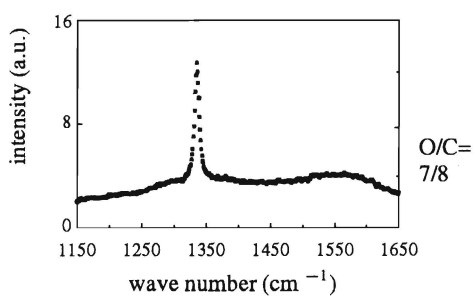
Addition of hydrogen and oxygen in the vessel only led to graphite deposition and will not be discussed any further. Addition of methane in the vessel instead of the nozzle also led to highly crystalline diamond deposition (with a FWHM of 6.5 cm^{-1}).

Optimization of the deposition rate

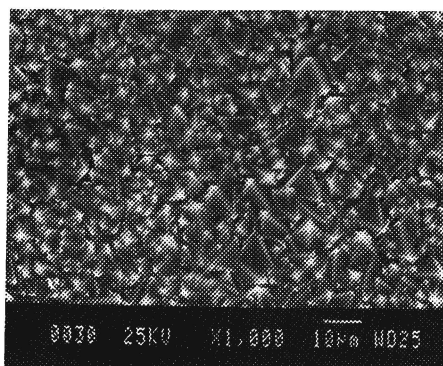
The most promising experiments were repeated at a distance of 4 cm from the nozzle. In this case both the hydrogen and the oxygen was admixed in the cathode space, in order to study the upper limit of the growth rate, simultaneously with the lower limit of the oxygen addition. The idea was that the dissociation of the hydrogen and oxygen gas is more complete in this case, and the required flow rates of these gases can be lower. The hydrogen flow rate was $3.2 \text{ cm}^3\text{s}^{-1}$ and the methane flow rate $0.8 \text{ cm}^3\text{s}^{-1}$. The oxygen flow rate was varied from 0.4 to $0.3 \text{ cm}^3\text{s}^{-1}$. The risk of sputtering cathode material was taken deliberately, as for the present purpose it was of secondary importance. Unfortunately, for this sequence again silicon had to be used as a substrate, by lack of molybdenum. The deposition temperature reached about 1200°C in the center, and the substrates cracked. Nevertheless, on the surrounding pieces diamond was deposited. In Fig 5.8 Raman spectra and SEM micrographs of diamond deposited in these trials are shown. From the SEM images (d) through (f) layer thicknesses of about $50 \mu\text{m h}^{-1}$ can be estimated (on limited areas of some mm^2). In Fig. (d) it can be observed that the film is not uniform in thickness. This may be the result of a non-uniform flow pattern due to the protruding of the (cracked) silicon pieces. Another cause may be cracking of these (thick) layers due to the rapid cooling of the substrate after switching of the plasma. The predominant triangle facets in Fig. (e) indicate a prevalent octahedral crystal habit in this trial. This may be induced by the high deposition temperature in this trial (cf. 5.2).



(a)

(d) 1 bar = 10 μm (e) 1 bar = 10 μm (f) 1 bar = 10 μm 

(b)

(g) 1 bar = 10 μm

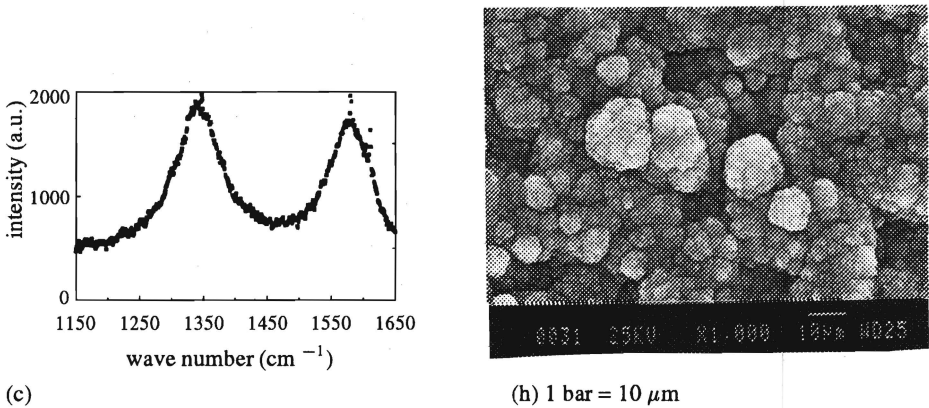


Figure 5.8: (a)-(c) Raman spectra and (d)-(h) SEM micrographs of diamond deposited upon reducing the O/C ratio; both oxygen and hydrogen injected in the cathode space; $d_{n-s} = 4 \text{ cm}$; Silicon substrates.

Table 5.5: FWHM values of the deconvoluted Lorentz diamond peaks as a function of the oxygen flow rate; -g means: no diamond peak observed, only graphitic bands

injection site → O/C ratio ↓	cathode space
1	7.4
7/8	7.2
6/8	-g

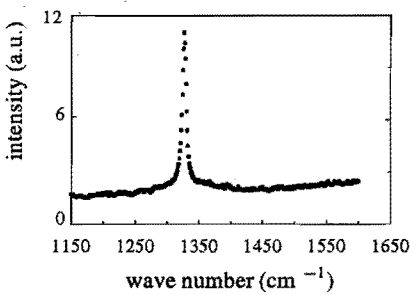
In Table 5.5 the FWHM value of the Raman peaks are summarized. When the oxygen/carbon ratio was reduced to 6/8, a purely graphitic Raman spectrum was obtained (Fig. (c)). Nevertheless, the ballas in Fig. (h) seem to tend to facet formation.

Reduction of power flow and substrate temperature

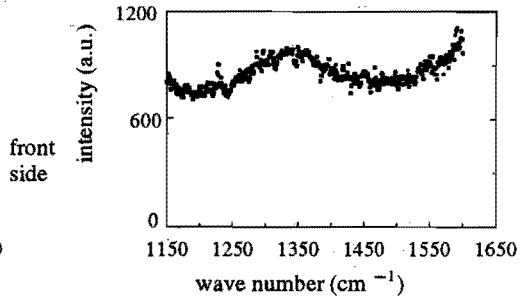
In Fig. 5.9 Raman spectra and SEM micrographs are shown of carbon deposited on different substrate sites with the low power and flow settings given in column IV of Table 5.2. As a substrate, molybdenum was used. The surface temperature had to be estimated by way of a thermocouple measurement of the bulk of the substrate holder. This temperature reached 320 °C. From the experience of simultaneous thermocouple and pyrometer measurements during the graphite project (Chapter III), it appeared that the difference was approximately a factor

5/4. This leads to an estimated real deposition temperature of ~ 400 °C in this case.

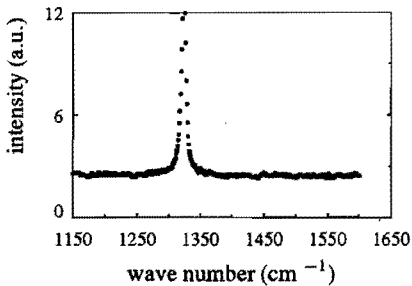
In the Raman spectra of Fig. (5.9) (a)-(b) it can be observed that both graphite and diamond are present on the substrate, depending on the location. In Fig. (e) leaf shaped deposits are shown, which were typical for this trial. Most likely these are graphitic sheets. Bulk structures with facets could not be detected. In Fig. (c) and (d) spectra recorded on the back side of the substrate are shown. Apparently, traces of both materials were present there, too. In the SEM micrograph of the back side (Fig. (f)), some bulk structures with rough facets could be detected. The small dimensions of the structures are in accordance with the expected low growth rate at this temperature. The phenomenon of deposition on the back side appears to be present on some samples out of the other sequences too. It can not be ruled out that the diamond crystals observed in these trials were the residual of deposits of previous trials on the sample holder.



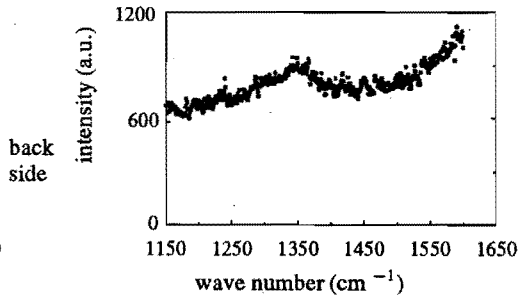
(a)



(b)



(c)



(d)

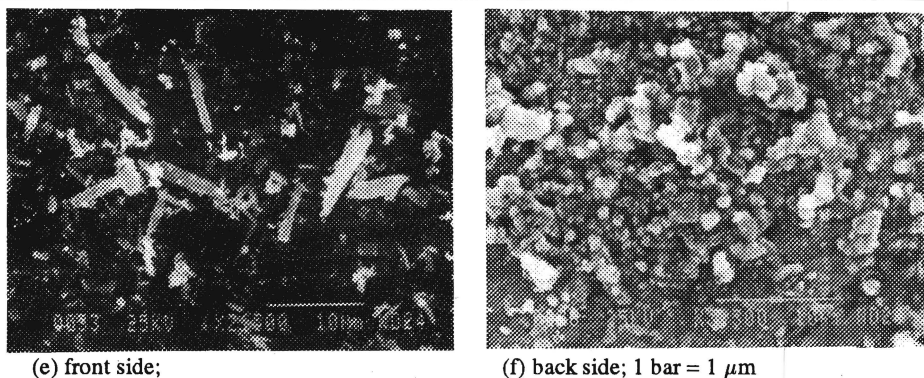


Figure 5.9: (a)-(d) Raman spectra obtained on different substrate locations after deposition with the low power, low flow settings of col. IV, 5.2 Substrate Molybdenum; (e)-(f) SEM images of (e) typical needle shaped carbon deposit (front side of sample), (f) typical bulk structures (on back side of sample)

Application of acetylene, and, fluorine containing gases

Finally, a number of trials have been carried out using C_2H_2/O_2 and C_2H_2/CF_4 mixtures. Only graphitic material could be deposited up to now. The C_2H_2 we used was low grade quality. It is reported that the use of high grade acetylene (without nitrogen) is essential [11]. On using CF_4 it should be noted that the fluorine radicals are already very reactive at the injection site. Injection in the nozzle resulted in the sputtering of copper and subsequent deposition (often in the shape of (diamond like!) FCC crystals) on the substrate. As a spin-off, this may prove to be a suitable method to deposit carbon-metal layers. In order to achieve diamond deposition, besides a change in gas admixture method, further study is necessary to find the appropriate gas ratios. An indication can be found in [20], where successful diamond deposition on Si $\langle 100 \rangle$ wafers is reported, using a low-pressure RF-plasma assisted CVD system. Deposition parameters given are: a chamber pressure of 5 torr, a substrate temperature of $850^\circ C$ and a gas mixture of 8% CF_4 in H_2 .

5.7 Conclusions

- In the cascaded arc deposition method hydrogen can be replaced largely by oxygen as an etching agent. Advantages are a lower power and gas consumption, safer gas handling and a lowering of the deposition temperature. The total omission of the hydrogen is not feasible (only graphitic formation). With the high power and flow settings we have obtained a high growth rate (the estimation is about $50 \mu m h^{-1}$), but only on a limited

annular area (some mm²). Probably, the large argon flow is responsible for this, as it may destroy nucleation sites for diamond. Another explanation is that the mixing of the various gases is insufficient.

- The variation of the location (in the arc) of the admixture of oxygen and hydrogen has only little influence on the quality of diamond. Admixture of these gases in the chamber leads to deposition of graphitic material, confirming the requirement of an abundance of highly reactive radicals in the plasma jet. Admixture of the methane in the chamber also leads to diamond deposition, indicating the possibility of diamond deposition by way of methyl radicals.
- Most likely low power, low temperature diamond deposition is possible with the hydrogen/oxygen/hydrocarbon gas admixture, but the growth rate is rather low. In this case most likely methyl radicals govern the deposition.
- With C₂H₂ or CF₄ no diamond was deposited up to now. Further trying out to find appropriate reactor settings is necessary. The use of high purity gases may be necessary, to avoid nitrogen admixture.
- The use of oxygen and fluorine results in the production of highly reactive radicals already at the injection site. In order to avoid damage to the arc components and contamination of the deposited material the configuration of the gas inlet system should be changed.

Acknowledgement

The important contributions to these results of the Erasmus students C. Chauveau from Université de Paris-Sud, Orsay, and G. Claudio (and friends) from University of Bari (Italy) are gratefully acknowledged. Furthermore, the author wishes to thank Dr. D. Stufkens and Mr. T. Snoeck of the University of Amsterdam for measuring the Raman spectra, Dr. S.N. Mikhailov of the Surface Physics group (Dept. of Physics, Eindhoven UT) for performing the LEIS measurements and Dr. H. Heijligers of the Department of Chemistry (Eindhoven UT) for giving the opportunity of making the SEM images.

Bibliography

- [1] A.R. Badzian, P.K. Bachmann, T. Hartnett, T. Badzian, and R. Messier, *Amorphous Hydrogenated Carbon Films, Eur. Mater. Res. Soc. Symp. Proc. XV*, P. Koidl and L. Oelhafen (eds.), Les Editions de Physique, Paris, 63, (1987).

- [2] F.P. Bundy, H.T. Hall, H.M. Strong, and R.H. Wentorf, *Nature*, **1976**, 51, (1955).
- [3] W.G. Eversole, *U.S. Patent 3 030 188*, (July 23, 1958).
- [4] B.V. Spitsyn, L.L. Bouilov, and B.V. Derjaguin, *J. Cryst. Growth*, **52**, 219, (1981).
- [5] S. Matsumoto, Y. Sato, M. Tsutsumi, and S. Setaka, *J. Mater. Sci.*, **17**, 3106, (1982).
- [6] M. Kamo, Y. Sato, S. Matsumoto, and N. Setaka, *J. Cryst. Growth*, **62**, 642, (1983).
- [7] Y. Catherine and A. Gicquel, *Journée de Formation CIP 91, Dépôt et Gravure Chimiques par Plasma, Antibes (France), june 9-14 1991*, la Groupe de Recherche 57 du CNRS & Société Francaise du Vide, Paris, 333 (1991).
- [8] J.C. Angus, informal contribution to *Proc. 2nd Eur. Conf on Diamond, Diamond-like and Related Materials, Nice, September 2-6, 1991*.
- [9] W.A. Yarbrough and R. Messier, *Science*, **247**, 688, (1990).
- [10] F.G. Celli and J.E. Butler, *Annu. Rev. Phys. Chem.*, **42**, 643, (1991).
- [11] P.K. Bachmann, D. Leers, and H. Lydtin, *Diamond and Related Materials*, **1**, 1, (1991).
- [12] W.L. Brown, W. Lutze, S. Somiya, and L.A. Krysinisky (eds.), *J. Mater. Res.*, **5** (11), (1990).
- [13] P.K. Bachmann *et al* (ed.), *Proc. of Eur. Conf. on Diamond, Diamond-like and Related Materials, 1: Crans-Montana, September 17-19, 1990, 2: Nice, September 2-6, 1991, 3: Heidelberg, September 8-12, 1992*, also in *Diamond and Related Materials and Surf. Coat. Technol.*
- [14] Y. Tzeng, M. Yoshikawa, M. Murakawa, and A. Feldman (eds.), *Proc. 1rst Int. Conf. on Application of Diamond Films. and Rel. Mater.- ADC '91, Auburn, Alabama (U.S.A.) August 17-22, 1991*, Materials Science Monographs, Elsevier, Amsterdam-Oxford-New York-Tokyo; also in *Thin Solid Films* **212** (1992), (1991).
- [15] L.M. Hanssen, K.A. Snail, W.A. Carrington, J.E. Butler, S. Kellogg, and D.B. Oakes, *Thin Solid Films*, **196**, 271, (1991).
- [16] E. Pfender, Q.Y. Han, T.W. Or, Z.P. Lu, and J. Heberlein, *Diamond and Related Materials*, **1**, 127, (1992).
- [17] J.J. Beulens, *Ph. D. thesis*, Eindhoven University of Technology, (1991).
- [18] J.J. Beulens, A.J.M. Buuron, and D.C. Schram, *Surf. Coat. Technol.*, **47**, 401, (1991).
- [19] Y. Liou, A. Inspektor, R. Weimer, D. Knight, and R. Messier, *J. Mater. Res.*, **5** (11), 2305, (1990).

- [20] R. Rudder, *Electronic Letters*, **24**, 1220, (1989).
- [21] Y. Tzeng, M. Yoshikawa, M. Murakawa, and A. Feldman (eds.), *Proc. 1rst Int. Conf. on Application of Diamond Films. and Rel. Mater.- ADC '91, Auburn, Alabama (U.S.A.) August 17-22, 1991*, Materials Science Monographs **73**, Elsevier, Amsterdam-Oxford-New York-Tokyo, 197, (1991).
- [22] A.W. Phelps K.E. Spear and W.B. White, *J. Mater. Res.*, **5** (11), 2277, (1990).
- [23] J. Robertson, *Adv. Phys.*, **35** (4), 317, (1986).
- [24] J.E. Field, *The Properties of Diamond*, Academic Press, London, (1979).
- [25] J.L. Valdes, J.W. Mitchel, J.A. Mucha, L. Seibles, and H. Huggins, *Diamond Deposition: Science and Technology*, **2** (2), 4, (1991).
- [26] K.V. Ravi, C.A Koch, and H.S. Hu, *J. Mater. Res.*, **5** (11), 2356, (1990).
- [27] A. Hirata, H. Tokura, and M. Yoshikawa, *Thin Solid Films*, **212**, 43, (1992).
- [28] G. Janssen, W. Vollenberg, L.J. Gilling, W.J.P. van Enckevort, and J.J.D. Schamineé, *Surf. Coat. Technol.*, **47**, 113, (1991).
- [29] J. Harris, *J. Appl. Phys.*, **56**, 2298, (1990).
- [30] R.E. Clausing, L. Heatherly, L.L. Horton, E.D. Specht, G.M. Begun, and Z.L. Wang, *Diamond and Related Materials*, **1**, 411, (1992).
- [31] Y.-J. Baik and K.Y. Eun, *Thin Solid Films*, **212**, 156, (1992).
- [32] F.W. Smith and G. Ghidini, *J. Electrochem. Soc.*, **129**, 1300, (1982).
- [33] M. Sommer, K. Mui, and F.W. Smith, *Sol. State Comm.*, **69** (7), 775, (1989).
- [34] Y. Tzeng, M. Yoshikawa, M. Murakawa, and A. Feldman (eds.), *Proc. 1rst Int. Conf. on Application of Diamond Films. and Rel. Mater.- ADC '91, Auburn, Alabama (U.S.A.) August 17-22, 1991*, Materials Science Monographs **73**, Elsevier, Amsterdam-Oxford-New York-Tokyo, 475, (1991).
- [35] M. Frenklach and K.E. Spear, *J. Mater. Res.*, **3**, 133, (1988).
- [36] A. Boudina, E. Fitzer, and G. Wahl, *Diamond and Related Materials*, **1**, 380, (1992).
- [37] Y. Matsui, H. Yabe, T. Sugimoto, and Y. Hirose, *Diamond and Related Materials*, **1**, 19, (1991).
- [38] Y. Saito, K. Sato, K. Gomi, and H. Miyadera, *J. Mater. Sci.*, **25**, 1246, (1990).
- [39] Y. Mitsuda, Y. Kojima, T. Yoshida, and K. Akashi, *J. Mat. Sci.*, **22**, 1557, (1987).
- [40] O. Matsumoto, H. Toshima, and Y. Kanzaki, *Thin Solid Films*, **128**, 341, (1985).
- [41] B. Marcus, M. Mermoux, F. Vinet, A. Campargue, and M. Chevenier, *Surf. Coat. Technol.*, **47**, 608, (1991).
- [42] M.E. Coltrin and D.S. Dandy, *submitted (march 1993) to J. Appl. Phys.*

- [43] Y. Matsui, H. Yabe, and Y. Hirose, *Jpn. Journ. Appl. Phys.*, **29** (8), 1552, (1990).
- [44] G.M.W. Kroesen, *Ph.D. Thesis*, Eindhoven University of Technology, (1988).
- [45] D.R. Lide (ed.), *Handbook of Chemistry and Physics*, 72th edition, CRC Press, Inc., Boca Raton, Ann Arbor, Boston, (1991-1992).
- [46] M.C.M. van der Sanden, *Ph. D. thesis*, Eindhoven University of Technology, (1991).
- [47] M.J. de Graaf, R.P. Dahiya, J.L. Jeauberteau, F.J. de Hoog, M.J.F. van de Sande, and D.C. Schram, *Coll. Phys.*, **18** (C5), 387, (1990).
- [48] Zhou Qing, M.C.M. van de Sanden, M.J. de Graaf D.K. Otorbaev, G.J. Meeusen, A.J.M. Buuron, and D.C. Schram, *contribution to the 1993 ISPC-11 conference, Loughborough (UK), August 22-27*, (1993).
- [49] D.W. Brenner, *Phys. Rev. B*, **42** (15), 9458, (1990).
- [50] Y. Matsui, H. Yabe, T. Sugimoto, and Y. Hirose, *Diamond and Related Materials*, **1**, 19, (1991).
- [51] H. Maecker, *Z. Naturforsch.*, **11a**, 457, (1956).
- [52] D.J. Gardiner and P.R. Graves (eds.), *Practical Raman Spectroscopy*, Springer Verlag, (1989).
- [53] P.K. Bachmann and D.U. Wiechert, *Diamond and Related Materials*, **1**, 422, (1992).
- [54] D.S. Bethune, G. Meijer, W.C. Tang, H.J. Rosen, H. Seki W.G. Golden, C.A. Brown, and M.S. de Vries, *Chem. Phys. Lett.*, **179** (1,2), 181, (1991).
- [55] G. Meijer, *private communication*, University of Nijmegen, The Netherlands, (1992).
- [56] J.T. McKinnon, W.L. Bell, and R.M. Barkley, *Combust. and Flame*, **88**, 102, (1992).
- [57] J. Spinnewyn, M. Nesládek, and C. Asinari, *Diamond and Related Materials*, **2**, 361, (1993).
- [58] J.S. Speck, *J. Appl. Phys.*, **67** (1), 495, (1990).
- [59] J.W. Kim, Y.-J. Baik, and K.Y. Eun, *Diamond and Related Materials*, **1**, 200, (1992).
- [60] P. Joeris, C. Benndorf, and S. Bohr, *J. Appl. Phys.*, **71** (9), 4638, (1992).
- [61] S.N. Mikhailov, *private communication* Surface Physics group, Dept. of Physics, Eindhoven University of Technology, 1993.

Chapter 6

Fast deposition of amorphous hydrogenated carbon by an expanding cascaded arc plasma

abstract

Using an expanding cascaded arc plasma jet, amorphous hydrogenated carbon films were deposited on silicon, glass and steel substrates at high rates of tens of nanometers per second and on large areas of up to 50 cm². The present work was aimed at depositing amorphous carbon films suited for optical and protective applications. Films deposited with the common argon/methane or argon/acetylene mixture, tend to delaminate from the substrate when the film is thicker than about $\sim 1 \mu\text{m}$, due to internal compressive stresses. For this reason, also trials using other compounds like C₇H₈ (toluene), CF₄ and H₂, and mixtures of these were used. With the use of toluene, several μm 's thick films, with a good adhesion to the substrate were deposited. With spectroscopic ellipsometry and infrared absorption optical parameters were obtained. Appropriate numerical models were developed for analyzing the data. The hydrogen and oxygen content in the films were determined with nuclear recoil techniques. It appeared that the films deposited with the use of toluene, are mainly polymer-like, have a high hydrogen content (40 at. %), and were partly oxidized (15 at. %). Films deposited with methane and acetylene are more diamond-like, with a lower hydrogen content, and low (2-3 at. %) oxygen incorporation. Refractive indices ranged from 1.3 to 2.2, band gaps are of the order of 1 to 2 eV. By the admixture of hydrogen in the deposition plasma diamond-like films were produced with a larger band gap of 2.2 eV. The corrosion performance of the films was studied by storing them in a humidity cabinet. The corrosion protection of films deposited with hydrocarbon/argon plasma mixtures appeared to be limited. Thick films with a good corrosion performance were produced by admixing a fluorine containing gas in the plasma. Analysis of the infrared absorption spectra showed that these films consist of amorphous fluorinated carbon, with little or no hydrogen incorporation.

6.1 Introduction

Plasma polymerization is a relatively new technique for surface modification and for deposition of amorphous hydrogenated carbon films (a-C:H films) [1, 2, 3]. Compared to conventional gas-phase deposition methods, the plasma deposited films are known to be highly crosslinked. In general the films are insoluble and pinhole free, and adhere well to the substrate up to film thicknesses of $\sim 1 \mu\text{m}$. [1, 4]. The a-C:H films have an extensive field of potential applications, because of their unique combination of specific properties such as hardness, low friction coefficients, chemical inertness, biocompatibility and optical transparency in a wide wavelength range [5]. Some practical applications of a-C:H films are: overcoats on thin-film media for magnetic recording [6], protective and anti-reflection coatings for optical devices, working in the infrared [7], insulating layers in electronic devices [8] and coatings for biomedical purposes [9].

The deposition rate with conventional plasma reactors like RF, microwave or DC glow discharge reactors (a few nanometers per second [10, 11]) however are low and hamper large-scale industrial applications of a-C:H films. In the last decade in our group a method has been developed, using an expanding cascaded arc plasma jet, with which all types of carbon coatings are produced at deposition rates which are orders of magnitude higher [12, 13, 14] than with the conventional methods. For a-C:H films very high growth rates of up to 200 nm s^{-1} were achieved on areas of 100 cm^2 , Conventional gases like methane and acetylene in the argon carrier gas were used [12]. The band gap of plasma deposited a-C:H films are mostly of the order of 1-2 eV. Furthermore, the films tend to delaminate from the substrate at thicknesses larger than about $1 \mu\text{m}$. In the first part of the present project, acetylene (C_2H_2) and toluene (C_7H_8) were used as the hydrocarbon admixture and, in some trials, hydrogen (H_2) was added. The aim of this project was to find parameter settings with which thick films (3-4 μm) could be deposited, with a good adhesion to the substrate, and with optimum combinations of film properties for optical applications. The optical parameters were determined using spectroscopic ellipsometry and infrared absorption spectroscopy. From the results of the latter information on the predominant bonding types in the film was derived. Finally, the hydrogen and oxygen contents in the film were determined by nuclear scattering and recoil techniques.

In a second study the corrosion behaviour of cold-rolled (CRS) steel and electrogalvanized (EGS) steel, coated with a film of amorphous carbon was investigated. Research on the feasibility of depositing films with these qualities on steel for corrosion protection has increased rapidly in the last years. The implications of the possibility of replacing conventional steel protection techniques like galvanization would be enormous. The energy consumption per coated steel area

would decrease drastically, as well the energy necessary for the recycling of the steel. Also from an environmental point of view the advantage of using carbon materials in stead of metallic coatings is obvious. Recently, films deposited with trimethylsilane were reported to have a good corrosion performance [4]. These films were deposited in an RF parallel plate reactor, or in a DC bell-jar-type reactor. The deposition rates obtained (about $1 \mu\text{m h}^{-1}$) are rather low. In the underlying study the possibilities of the cascaded arc method in this field were investigated. The corrosion performance of the coatings was studied as a function of substrate type, pretreatment, gas mixture and gas flow rates. Gases admixed in the carrier gas argon were CH_4 , C_2H_2 , C_7H_8 and CF_4 , and mixtures of these. In order to map the requirements on elemental composition and structure to this specific aim, the films were also characterized using Glow Discharge Optical Spectroscopy (GDOS), Time-of-Flight Secondary Ion Mass Spectrometry (TOFSIMS) and Electron Impedance Spectroscopy (EIS). On some samples, also Scanning Electron Microscopy and X-ray photoelectron spectroscopy (XPS) were carried out. In this chapter, firstly data analysis techniques for the optical diagnostics are treated. Subsequently, the experimental arrangements for deposition, and analysis of the optical, structural and protective properties of the films are adressed. Then the results of the analysis of the films are treated in the same order, that is starting with those of the optical diagnostics and followed by the results on the elemental composition and the corrosion performance.

6.2 Techniques and evaluation methods for analysis of the optical properties of the films

6.2.1 Spectroscopic ellipsometry

With *ex situ* spectroscopic ellipsometry the optical parameters of the deposited films, such as refractive index, absorption coefficient and band gap were determined. The theory of this method has been described extensively in [15]. Briefly, the method determines the change in polarization of linearly polarized light upon reflection on the system film-substrate. This polarization change is expressed in the complex reflection ratio ρ :

$$\rho = R_p/R_s \quad (6.1)$$

R_p and R_s are the complex reflection coefficients for the light components polarized parallel and perpendicularly to the plane of incidence respectively. (For a semi-infinite medium they are directly equal to the Fresnel reflection coefficients

[16].) So ρ is a complex quantity and is generally expressed in the ellipsometric angles Ψ and Δ :

$$\rho = \tan \Psi \exp j\Delta \quad (6.2)$$

In measurement set-ups either a rotating analyzer or a rotating polarizer system is used. In both methods a periodic signal on the detection device arises. By Fourier analysis of this signal the ellipsometric Fourier coefficients a and b are determined. When the polarizer angle is chosen at 45° , these coefficients are related to the ellipsometric angles Ψ and Δ by the following relationships:

$$a = -\cos 2\Psi \quad (6.3)$$

$$b = \sin 2\Psi \cos \Delta \quad (6.4)$$

The parameters refractive index n and the extinction coefficient k , enter the formulas through the Fresnel reflection coefficients R_p and R_s . The band gap can be implied in the formulas using the Tauc relation [5, 12, 17, 18].

$$\sqrt{\alpha E} = G(E - E_g) \quad (6.5)$$

with $\alpha = 4\pi k/\lambda$; λ is the wavelength, E is the photon energy (in eV), E_g is the band gap (in eV), G is a density-of-states coefficient (in $\text{cm}^{-\frac{1}{2}}\text{eV}^{-\frac{1}{2}}$)

Because of the limited thickness of the deposited layers, interference oscillations as a function of wavelength appeared in the signals, due to multiple reflections within the film. The method in which substrate and film considered mathematically by one semi-infinite bulk medium [15] is no longer adequate. The system substrate-layer has to be described by a multilayer system. This prohibits a straightforward calculation of n , k and E_g using the formulas above. The problem can be solved by reversing the solution method. This means that a fit procedure to the measured data can be applied, starting from a given set of thicknesses and optical parameters. From these values the expected values of the coefficients a and b can be calculated and by an iterative mean least-squares algorithm an optimum fit to the measured data can be obtained. Mathematically the multilayer system can be described most conveniently in terms of complex optical impedance factors for each layer [12]. In the past computer programs have been written to analyze the data of He-Ne *in situ* ellipsometry. Recently [19], the program has been adapted for calculations over a large wavelength range. A variable number of parameters can be included in the model: Often the system substrate-layer is extended with a top layer, with different optical parameters. The theory of Bruggeman [20] gives an adequate formulation for

these surface parameters. The top layer is then described by a void fraction and a limited thickness (of some nanometers). However, it appeared that for the present amorphous carbon films, the implication of this top layer did not improve the fit quality, so we omitted it in our calculations.

The following parameters were then included in the fit procedure:

- 1 The thickness of the film d
- 2 The refractive index n , taken constant over the wavelength range.
- 3 The density-of-states factor G
- 4 The optical gap E_g .

The interference oscillations permit an initial film thickness estimates using the equation

$$d = \frac{\lambda_i \lambda_{i+1}}{\lambda_i - \lambda_{i+1}} \frac{1}{2n}, \quad (6.6)$$

with λ_i and λ_{i+1} the wavelength of two successive interference maxima. Initial estimates n , G and E_g can be found (after some practicing) from the amplitude of the fringes, and from the level and the slope of the a and b coefficients.

As a measure for the quality of the fit the least squares error function

$$\chi^2 = \frac{1}{N} \sum_{i=1}^N (a_i^{exp} - a_i^{calc})^2 + (b_i^{exp} - b_i^{calc})^2, \quad (6.7)$$

was adopted, with a and b the Fourier coefficients, N the number of points. Weighing was not applied, because the absolute instrument noise (equal over the entire frequency interval) was predominant over the effect of the relative inaccuracies in a and b .

6.2.2 Infrared absorption spectroscopy

Infrared absorption spectroscopy supplies a means to determine the abundance of bonding types in a coating.

The transmitted intensity I_T through a layer of thickness d is described by the same exponential relationship as the transmission through a gas or plasma:

$$I_T = I_0 \exp(-k \cdot d), \quad (6.8)$$

with I_0 the intensity of the incident beam and k the extinction coefficient. The absorption coefficient α is related to k by $\alpha = 4\pi k/\lambda$.

As in the case of the ellipsometric spectra the measured spectra are disturbed by interference oscillations, caused by multiple reflection in the layer. Furthermore the attenuation of the beam through the substrate has to be taken into

account. This was done by measuring the transmission of an uncoated piece and a coated piece of silicon out of the same wafer. It can easily be deduced that the ratio of the intensity I_0 transmitted through the bare substrate and of the intensity I_{in} transmitted through the substrate, and entering the deposited layer is given by:

$$\frac{I_{in}}{I_0} = \frac{T_2}{T_1} \exp[-\alpha(d_s - d_r)], \quad (6.9)$$

with $T_{1,2}$ the transmission through the bare substrate and the coated substrate respectively. d_s and d_r are the substrate thicknesses in the uncoated and the coated sections respectively, and they will be approximately equal in general. In fact this formula is an illustration of an a-C:H layer as an optical coating. The transmission of the system substrate-coating is often higher than the transmission of the bare substrate. Taking the multiple reflection in the layer into account, Eq. (6.8) is transformed to [15, 21]:

$$\frac{I_T}{I_{in}} = t_3^2 \frac{\exp(-\alpha d)}{1 - 2r_2r_3 \exp(-\alpha d) \cos \phi + (r_2r_3)^2 \exp(-2\alpha d)} \quad (6.10)$$

with t_3 the transmissivity of the coating. r_2 and r_3 are the reflectivities at the coating-substrate and the coating-air interface respectively and are related to the optical parameters n and k by the Fresnel relations. All of the parameters (except the thickness) are a function of frequency (wave number), so $\alpha = \alpha_\nu$, etc.. Using Eqs. (6.9) and (6.10) the measured transmission can now be converted to the real absorption coefficient α_ν . Two approaches are possible: When the thickness and refractive index of the coating and of the substrate are known, α_ν can be solved point by point by a simple computer iteration of Eq. (6.10). For a-C:H materials, the profile of α_ν in a vibration band can be fitted approximately by a Gaussian function [22]. When the thicknesses are not exactly known, the spectrum can be fitted starting from a suited set of initial values for the thicknesses, refractive indices and Gaussian absorption profiles in the vibrational bands. An estimate for the film thickness can be found using Eq. (6.6). A starting estimate for the refractive index is yielded by the amplitude of the interference fringes (with Eq. 6.10). A reasonable assumption is that overall absorption through the layer can be neglected (in the infrared). Inserting these data in formula (6.10) the transmission can be approximated over an entire wavelength range, and by a subsequent least-squares fit, optimum values of the profiles of the absorption coefficient are obtained. In this way the Gaussian absorption bands are convoluted to the measured transmission.

6.3 Experimental

6.3.1 The expanding cascaded arc set-up for deposition

The main features of the expanding cascaded arc technique for deposition, are the separation of the three phases production, transport and deposition of active species. The argon carrier gas enters the cathode space of the cascaded arc at a pressure of about 0.5 bar. A plasma is generated in the channel of a cascaded arc and expands through the annular anode into a vacuum chamber (pressure of the order of 100 Pa). The monomer is injected in the anode and ionized and dissociated by the plasma. In the expanding plasma jet excited and ionized atoms and molecular radicals are transported toward the substrate, where deposition occurs at high rates. To maintain a low deposition temperature (necessary for a-C:H deposition) the substrate support was water-cooled. The exact reactor settings for a-C:H deposition are given in Table 6.1. The inverse power-flow factor Q is a specific parameter in the case of deposition with a plasma jet. It is similar to the W/FM ratio, which is the common parameter in the case of stationary RF and DC deposition methods [4]; W is the power, F is the monomer flow rate and M is the molecular weight of the monomer. The factor Q is defined as F/AW with F , the net carbon flow rate, A the argon flow rate and W the power of the arc. In contrast to *e.g.* in [4], we can not simply state that a high Q factor leads to a precursor-similar structure in the film. In our case the monomer dissociation degree is much higher, and various mechanisms contribute to the observed relationships between reactor settings and carbon film properties. More details on the deposition reactor, the reactor settings and the relations with the deposited materials are given elsewhere [12, 13].

Table 6.1: *The reactor settings and gas flow rates used for a-C:H,F deposition*

I_{arc}	50	A
V_{arc}	90	V
{Ar}	100	cm ³ s ⁻¹
{C _x H _y }	0.3-10.8	cm ³ s ⁻¹
{C ₇ H ₈ }	0.07-0.38	ml/min
{H ₂ }	3, 14	cm ³ s ⁻¹
{CF ₄ }	0.4, 0.6	cm ³ s ⁻¹
$p_{chamber}$	22, 100	Pa
T_s	20-200	°C
d_{n-s}	70	cm

In the present project, two sequences of deposition experiments were carried out. The first sequence was aimed at checking and improving the optical properties of the films, the second at producing films with good anti-corrosive properties. A major demand for both sequences was depositing films with a good adhesion to the substrate. In the first sequence acetylene (C_2H_2) and toluene (C_7H_8) were used as a feed gas. With acetylene a sub-sequence of thin (~ 500 nm) films was deposited, in order to update the results found by Kroesen [12] and Beulens [13] in the past (cf. Chapter II). In a second sub-sequence, thick films (>1 μm) with a good adhesion to the substrate were deposited with the use of toluene. The most promising trials of both sub-sequences were repeated with admixture of hydrogen as an extra feed gas in order to try and deposit more diamond-like films with enhanced sp^3 bonding. In the second main sequence, the corrosion-performance study, films were deposited using various flow rates of the hydrocarbons, and with CF_4 as an extra admixture. In Table 6.1 the range of the applied flow rates is given.

6.3.2 Adhesion improvement by pretreatment

Adhesion of a-C:H films to the substrate is a major issue in the study of the applicability of these films for protective purposes. A distinction can be made between the polymer-like, hydrogen-rich films, which are deposited in low Q -factor trials, and the diamond-like, hydrogen-lean films at the high Q -side of the reactor parameter range [13]. In general polymer-like films are soft and adhere reasonably well to the substrate. Using gaseous precursors like CH_4 and C_2H_2 this is valid for thicknesses of up to about 1 μm . However, using C_7H_8 (toluene), soft films were produced, which adhered well even with thicknesses of several μm s (cf. Sec 6.4.1). The diamond-like films contain internal stresses [17], and have a tendency to delaminate at thicknesses of only a few hundreds of nanometers. It is well-known that a thorough cleaning of the substrate before depositing an a-C:H layer on it is essential for the adhesion of the film. For the glass and silicon substrates 5 minutes ultrasonic cleaning in an organic solvent (trichloroethylene) was carried out. For the cold-rolled (CRS) and electro-galvanized (EGS) steel substrates this treatment has to consist of a few stages. In order to remove stamping oil, at first the substrates were cleaned ultrasonically in trichloroethylene (purity $>99.5\%$) for 5 min. As a second stage, the steel substrates were cleaned in a 100/5 Ar/ H_2 plasma for 5 minutes, with a substrate temperature rising to ~ 300 $^\circ C$. In a recent study [23] it was found that optimum cleaning was achieved by cleaning in a pure hydrogen plasma for 60 min. This may be preceded by cleaning in an oxygen plasma for 2 min. This hydrogen plasma cleaning has the effect that organic residues on the substrate are etched away partly and the residuals are

crosslinked which improves the sticking to the substrate. An important finding reported in [23] is that on the EGS substrates the hydrogen plasma is able to remove the (insulating) oxide layer completely, and that on the CRS substrates it is not.

The actual deposition was divided into two stages. In the first stage of the deposition, the substrate was DC negatively biased for 20 seconds. This can be considered as a third pretreatment stage, in which it was attempted to implant carbon ions in the toplayer of the steel, and create an interlayer of mixed composition. Unfortunately, the bias potential was limited to ~ -200 V, by the high conductivity of the plasma, and it is not sure whether this value is high enough to effectively implant the ions [24, 25]. After switching off the bias the actual deposition was carried out for about 20 seconds.

6.3.3 Diagnostic arrangements

Ellipsometry and spectroscopy

For the ellipsometry a rotating polarizer system with a cascaded arc as a light source [26] was used. The set-up used was that of the group Surface Physics [27]. The angle of incidence was 68.3° , and signal detection occurred by means of a photo diode array. The ellipsometric coefficients a and b were determined over the wavelength range from 300 to 1100 nm (4.5 to 1 eV).

The infrared spectra were recorded with a Bruker IFS 66 Fourier transform interferometer (of the EPG plasma physics group), with a resolution of 4 cm^{-1} using a cascaded arc as a light source.

Nuclear recoil techniques for determining the atomic H/C and O/C ratios

In order to determine the hydrogen content and possible oxygen incorporation in the films (both bonded and not bonded), nuclear recoil techniques using a beam of high energy α -particles, produced by the AVF-cyclotron of the Department of Physics of the Eindhoven University of Technology was utilized. In each measurement two techniques were used simultaneously, Nuclear Back Scattering (NBS) for calibration purposes and (non-coincident) Elastic Recoil Detection Analysis (ERDA) for the actual concentration determination. Experiments were carried out on a selection of the samples. Two different experimental configurations, beam energies and detection methods were used, for the detection of the heavy elements oxygen and carbon, and the light element hydrogen, respectively. In Fig. 6.1 the measurement set-up for the determination of the carbon and oxygen contents in the layers is shown (adopted from [28]).

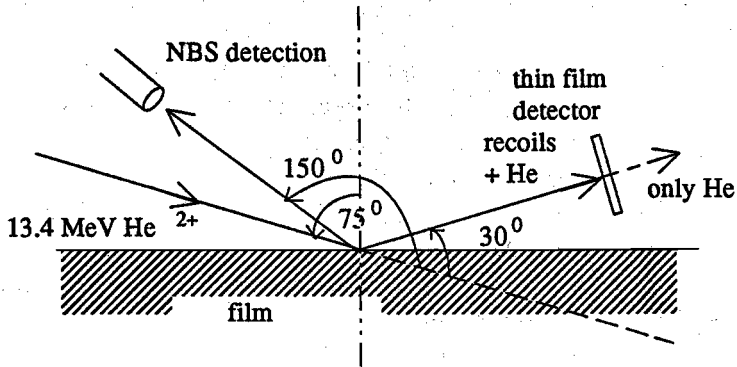


Figure 6.1: Measurement set-up for the determination of the carbon and oxygen contents in the films.

The energy of the α particles was 13.4 MeV. The beam spot size was $\sim 3 \text{ mm}^2$. The angle of incidence with respect to the surface normal was 75° . Dose calibration was obtained using NBS under a 150° angle with the through-passing beam, and equalizing for each sample the signal of the silicon substrate. The oxygen content was determined absolutely using ERDA and by comparing the measured signal with that of an SiO_2 sample with a known thickness and oxygen content. The detection of the recoiled particles occurred under an angle of 30° with the through-passing beam. For the detection a thin ($4 \mu\text{m}$) foil detector, type Ortec surface barrier detector, was used. The thin detector stops the heavy recoils, but lets the α -particles pass through, which facilitates the discrimination between the two types of species. Particles, recoiled from deeper layers in the carbon film lose an amount of energy proportional to their depth by electronic stopping. So, by detecting the recoiled particles per energy channel a depth profile of the film was obtained. The signals were integrated over the depth to obtain the total number of atoms per cm^2 . The measurement set-up for the determination of the hydrogen contents is shown in Fig. 6.2 (cf. also [29]).

In this case α particles with an energy of 4 MeV were used. The angle of incidence was 75° with respect to the surface normal. Dose calibration of the signal was obtained using NBS under a 105° scattering angle with the through-passing beam and equalizing for each sample the signal of the Si-substrate. Absolute determination of the hydrogen contents in the films was obtained using

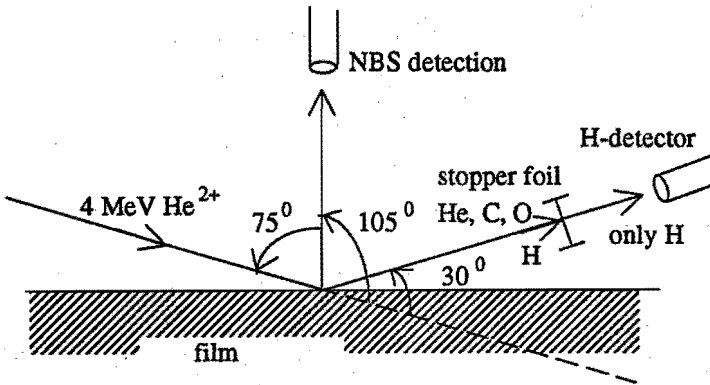


Figure 6.2: *Measurement set-up for the determination of the hydrogen contents in the films*

ERDA and by comparing the signal with that of an Si_3N_4 sample with a known hydrogen content (3.3 at. %). In this case signal detection occurred under a 30° angle with the through-passing beam and the recoiled carbon and oxygen ions and α particles were eliminated by a stopping foil in front of the detector. The scattered H atoms passed through the foil and were detected with a standard PIPS (Passivated Implanted Planar Silicon) detector. In this case no depth profiling was obtained because of the negligible electronic stopping of the hydrogen.

Diagnostics for structure analysis of films for corrosion protection of steel

The diagnostics treated in this section were all carried out by Armco Research and Technology, Middletown (USA) and related companies. The films of the anti-corrosion study were analyzed using Glow Discharge Optical Spectroscopy (GDOS) and Electrochemical Impedance Spectroscopy (EIS). The corrosion performance of the films was tested by storing them in a humidity environment for 96 hours. GDOS renders depth profiles of the elements in the film. In the GDOS diagnostic (cf. e.g. [30]) the film is sputtered by beam of high energy Ar ions. Typical operating parameters were a voltage of 700 V and a current of 30 mA. The device used was a LECO GDS-1000 Glow Discharge Spectrometer. A qualitative picture of the sputtered elements is obtained by observing the optical emission of the glow discharge. In this way a depth profile of the elements in

the film is obtained as a function of time. It should be noted that the GDOS technique has a widely varying sensitivity for the different elements and can only be used for a qualitative analysis. For instance, it appears to be very insensitive to hydrogen. On the other hand it is known that small amounts of nitrogen in a plasma can lead to strong optical emission bands. On a few samples Scanning Electron Microscopy (SEM) was carried out, in order to study the morphology of the films. From correlating the GDOS sputter rate with the thickness of the layer as estimated by SEM observations, an estimate for the growth rate of the films was deduced. Electrochemical Impedance spectroscopy (EIS), [4, 23] yields information on the barrier properties of the films. This is a relatively novel method. The most important parameter is the pore resistance R_{po} . R_{po} is equal to the modulus of the impedance of the system in the limit of zero frequency. This parameter is a direct measure for the porosity of the layer and consequently for the corrosion performance. On a few samples Time-Of-Flight Secondary Ion Mass Spectrometry, (TOFSIMS) was applied for analyzing the toplayer (3 Å). The analysis was performed on a Kratos PRISM instrument. More information on this technique can be found in [31].

6.4 Results and discussion

6.4.1 The optical parameters

In Table 6.2 a survey of the trials aimed at studying the optical parameters is given.

In Fig. 6.3 an example of a representative fit to the measured a and b coefficients is shown. It can be observed that the fit is satisfactory and that the model is adequate for the present purpose. The fit could probably be improved by using the program options of a frequency dependence of the refractive index, and of the top layer. The drawback is that the number of fit parameters increases. Another cause may be the fact that the spectroscopic data are very sensitive to a slight error in the angle of incidence [15]. Moreover, the validity of the Tauc relation is limited. This hinders the selection of the appropriate wavelength range, since this depends again on the (unknown) band gap. So future refinements on the application of this method are desirable. Nevertheless, the accuracy of the fit was sufficient to obtain approximate results on the thicknesses, band gaps and refractive indices of the films.

In Fig. 6.4 the deposition rate as function of the flow rates is given, as obtained from the best-fit thickness of the ellipsometric data (starting from Eq. 6.6). It can be observed that the deposition rate increases almost linearly with the hydrocarbon flow rate up to large values. The area of deposition was ~ 100

Table 6.2: Survey of the trials for the optical applications; $\{CH_4\}$, $\{C_2H_2\}$, $\{C_7H_8\}$ $\{H_2\}$ and $\{CF_4\}$, gas flows, d and R_d , film thicknesses and growth rates as obtained from the ellipsometric fits, t_d , period of deposition, T_s , deposition temperature. All other reactor settings are given in Table 6.1

Sample	$\{C_2H_2\}$ cm^3s^{-1}	$\{C_7H_8\}$ $ml\ min^{-1}$	$\{H_2\}$ cm^3s^{-1}	d (μm)	R_d $(nm\ s^{-1})$	t_d (s)	T_s $(^\circ C)$
E8	—	0.068	—	—	—	180	190
E9	—	0.151	—	720	6.0	120	180
E10	—	0.227	—	1660	5.5	300	200
E11	—	0.302	—	1730	9.6	180	210
E12	—	0.378	—	2300	15.4	150	—
F1	0.36	—	—	370	2.9	125	160
F2	0.90	—	—	370	6.2	59	150
F3	1.90	—	—	395	13.6	29	110
F4	3.6	—	—	265	19.0	14	70
F5	6.6	—	—	310	44.0	7.3	30
F6	10.9	—	—	245	61.0	4.0	30
G1	10.9	—	14	500	15.4	32.5	50
G2	6.6	—	14	50	1	50	50
G3	3.6	—	14	<50	<0.5	26	50
H2	—	0.151	3	2380	9.6	240	—
H3	—	0.151	3	8120	9.0	900	—

cm^2 . In Fig. 6.5 the refractive index and the band gap are shown as a function of the flow rates of acetylene and toluene. G -values were in the order of $150\text{--}300\ cm^{-2}eV^{-1}$. For acetylene the same tendencies for the refractive index and the bandgap as found in the past (cf. Chapter II and [12]) were obtained. For toluene, the refractive index is hardly dependent on flow rate. The actual band gaps are somewhat higher and may be more realistic, because most of the films are transparent for red and orange light. The band gap tends to decrease with an increasing hydrocarbon flow rate. For toluene the same tendency can be noted. For optical purposes the ratio of the diamond-like sp^3 bonding and the polymeric and graphitic sp^1 and sp^2 is of importance. With infrared absorption spectroscopy the prevalent bonding types in the film can be determined. Extensive studies of the assignment of the IR absorption bands observed in a-C:H layers were carried out by Dischler *et al.*, [11, 32, 22]. Table 6.3 gives a selection, summarizing the C-C and C-H bonding types observed in our a-C:H layers.

In Fig. 6.6 (a)-(e) the deconvoluted IR absorption bands are shown as a function of the acetylene flow rate (sequence F, Table 6.2), as obtained with the

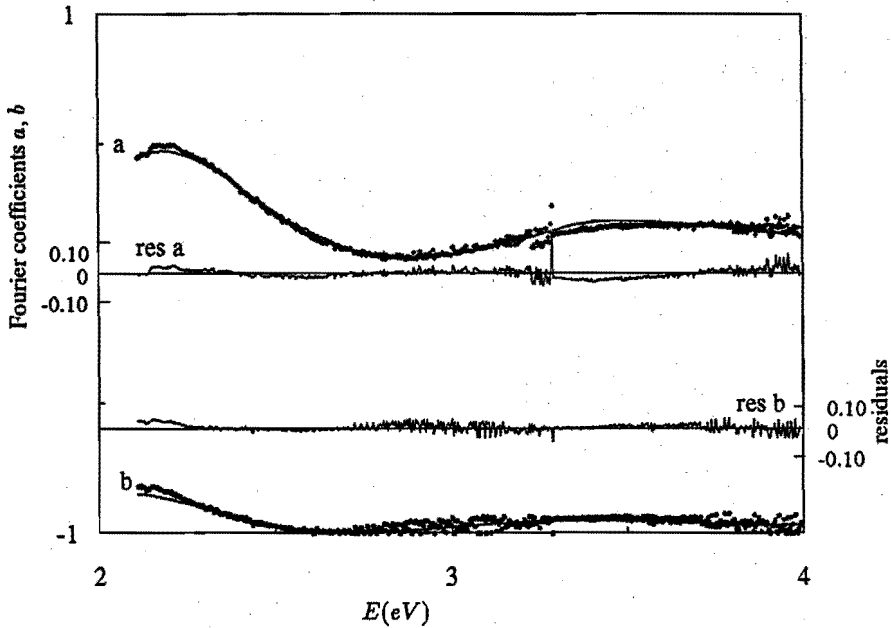


Figure 6.3: Measured and fitted ellipsometric spectrum; sample F6.

method described in Sec. 6.2.2.

It appeared that for all films deposited with C_2H_2 only the sp^3 bands around 2900 cm^{-1} , 1450 cm^{-1} and 1370 cm^{-1} were present. This confirms the finding of Beulens [13] that the films are predominantly diamond-like. In this case the ratio of the integrated intensity of the 2920 cm^{-1} $sp^3CH_{1,2}$ band to the integrated intensity of the 2970 cm^{-1} sp^3CH_3 band can be used as an indication for the degree of crosslinking (more C-C bondings). In Fig. 6.7 (a) the band (integrated) intensity ratio (b) the band widths are given as a function of the acetylene flow rate. The variation with flow rate is small. For the higher flow rates an increase in ratio and width, indicating a more diamond-like and harder film [11] can be noted.

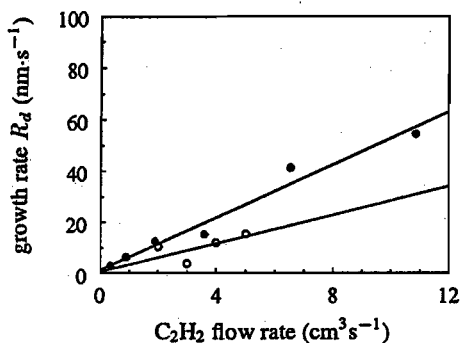


Figure 6.4: Deposition rate R_d as a function of hydrocarbon admixture; \bullet C_2H_2 , \circ C_7H_8 . The flow rate of toluene is given in equivalent acetylene flow ($0.151 \text{ ml min}^{-1}$ C_7H_8 is equivalent to $2 \text{ cm}^3 \text{ s}^{-1}$ C_2H_2).

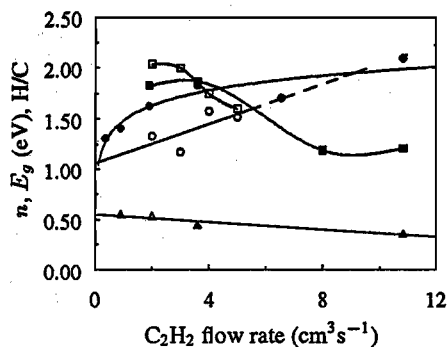


Figure 6.5: \bullet , The refractive index n , \blacksquare band gap E_g , and, \blacktriangle H/C ratio as a function of the equivalent (acetylene) flow rate; solid symbols, acetylene, open symbols, toluene; $1 \text{ cm}^3 \text{ s}^{-1}$ is $Q \approx 5 \cdot 10^{-6} \text{ W}^{-1}$.

Table 6.3: Peak assignment for the infrared C-H absorption bands observed in our a-C:H layers (from [32]). The first block gives the stretching vibrations, the small second block gives the observed bending vibrations (from [13]).

band	frequency (cm^{-1})		assignment
	polymer-like	diamond-like	
H1	3300	3300	$sp^1\text{CH}$
H2	3045	3060	$sp^2\text{CH}$ aromatic
H3	—	3025	$sp^2\text{CH}$ olefinic
H4	3000	3000	$sp^2\text{CH}$ olefinic
H5	—	2970	$sp^3\text{CH}_3$
H6	—	2945	$sp^2\text{CH}_2$ olefinic
H7	2920	2920	$sp^3\text{CH}_2$
H8	2920	—	$sp^3\text{CH}$
H9	—	2875	$sp^3\text{CH}_3$
H10	2850	2850	$sp^3\text{CH}_2$
C2	1620	1600	sp^2 C=C olefinic
C3	1580	1580	sp^2 C=C aromatic
B1	1370	1370	$sp^3\text{CH}$
B2	1450	1450	$sp^{2,3}\text{CH}_2$

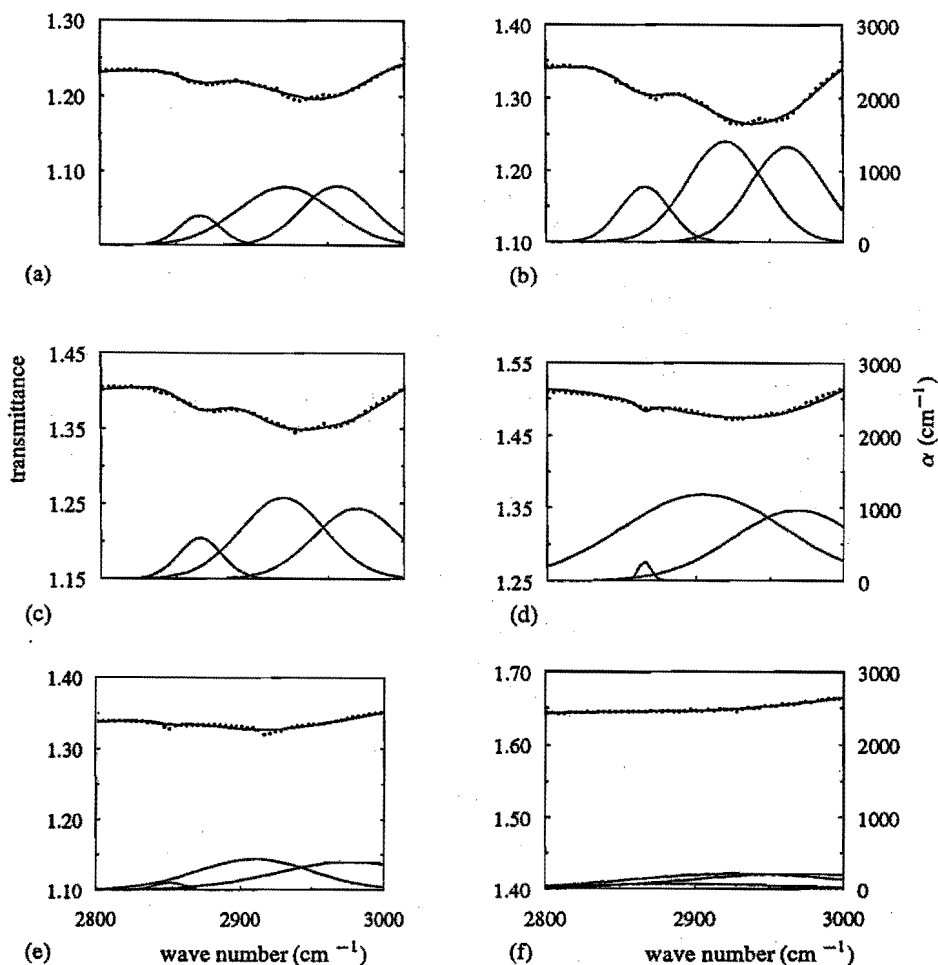


Figure 6.6: Measured transmittance (left hand axis) and fitted IR absorption bands (right hand axis) as a function of the acetylene flow rate, (a)-(f) 0.36, 0.90, 1.9, 3.6, 6.5, 10.8 $\text{cm}^3 \text{s}^{-1}$ respectively

Preliminary trials were carried out (sequence G) in order to improve the optical properties of the deposited films, by admixing various amounts of hydrogen in the plasma, following the experiences from crystalline diamond deposition trials [13]. In Fig. 6.7 the results for three values of the acetylene flow rate, under addition of $14 \text{ cm}^3 \text{s}^{-1}$ of H_2 are shown. It can be observed that the ratio of $sp^3\text{CH}_{1,2}$ to $sp^3\text{CH}_3$ increases with an increasing H/C ratio in the plasma, indicating a more diamond-like film. that is the films become more diamond-like. Only on one film

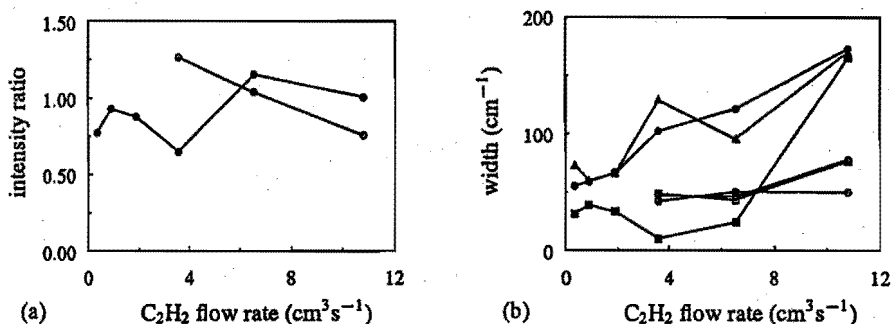


Figure 6.7: (a) • Integrated intensity ratios A_{2920}/A_{2970} and (b) ■, ●, ▲ widths of the 2875, 2920 and 2975 cm^{-1} band respectively, as a function of the acetylene flow rate; Solid symbols: no hydrogen addition; open symbols: with 14 standard $\text{cm}^3 \text{s}^{-1}$ H_2 addition.

(G2) the ellipsometric spectrum was recorded. The refractive index appeared to be low (1.5) but the band gap was enlarged to 1.6 eV (with $G=280 \text{ cm}^{-1} \text{ eV}^{-\frac{1}{2}}$). The growth rate was reduced to about 15 nm s^{-1} , so the hydrogen flow rate may have to be optimized. This results looks promising and future trials with this mixture are recommended.

In Fig. 6.8 (a)-(e) the deconvoluted IR absorption bands are shown as a function of the toluene flow rate (sequence E, Table 6.2). The films deposited with toluene as a feed gas all have a polymeric character. In Fig. 6.8 (f) a typical IR absorption spectrum over a wide wave number range is shown. Besides the $sp^3\text{CH}_x$ bands also the aromatic and olefinic $sp^2\text{CH}$ bands at $3000\text{-}3050 \text{ cm}^{-1}$, the $sp^1\text{CH}$ band at about 3300 and the aromatic $sp^2\text{C}=\text{C}$ band at about 1580 cm^{-1} can be observed. A second band at about 1700 cm^{-1} can be distinguished. This is most probably due to C-O bondings indicating the presence of oxygen in the film. In Fig. 6.8 (a)-(e) the fitted bands around 3000 cm^{-1} are shown. The absolute values of the (integrated) absorption coefficients decrease with higher flow rates; this may indicate that the layers are less dense. In this case besides the intensity ratio of the $2920 \text{ } sp^3\text{CH}_{1,2} \text{ cm}^{-1}$ band and the $2970 \text{ } sp^3\text{CH}_3 \text{ cm}^{-1}$ band, also the ratios with the $sp^1\text{CH}$ band at 3300 and the $sp^2\text{C}=\text{C}$ band at 1580 cm^{-1} give an indication for the degree of crosslinking. In Fig. 6.9 these ratios are given as a function of toluene flow rate. Again the dependence is only weak, and for higher flow rates the films become more diamond-like.

A substantial improvement was again obtained by admixing hydrogen (using a small amount with regard to the lower deposition rate for toluene). In Fig. 6.10 (a) and (b) two IR spectra of trials (H2 and H3) are shown, admixing $3 \text{ cm}^3 \text{ s}^{-1}$ H_2 and $0.151 \text{ ml min}^{-1}$ C_7H_8 in the plasma. The equality of the deconvoluted

absorption bands demonstrates not only the reproducibility of the deposition process but also the correctness of the deconvolution method. The two films have widely different thicknesses, but yield the same values for the absolute absorption coefficients. Trial H3 was carried out aimed at depositing a thick (and protective) film, with good optical properties and a good adhesion. A deposition period of 15 minutes

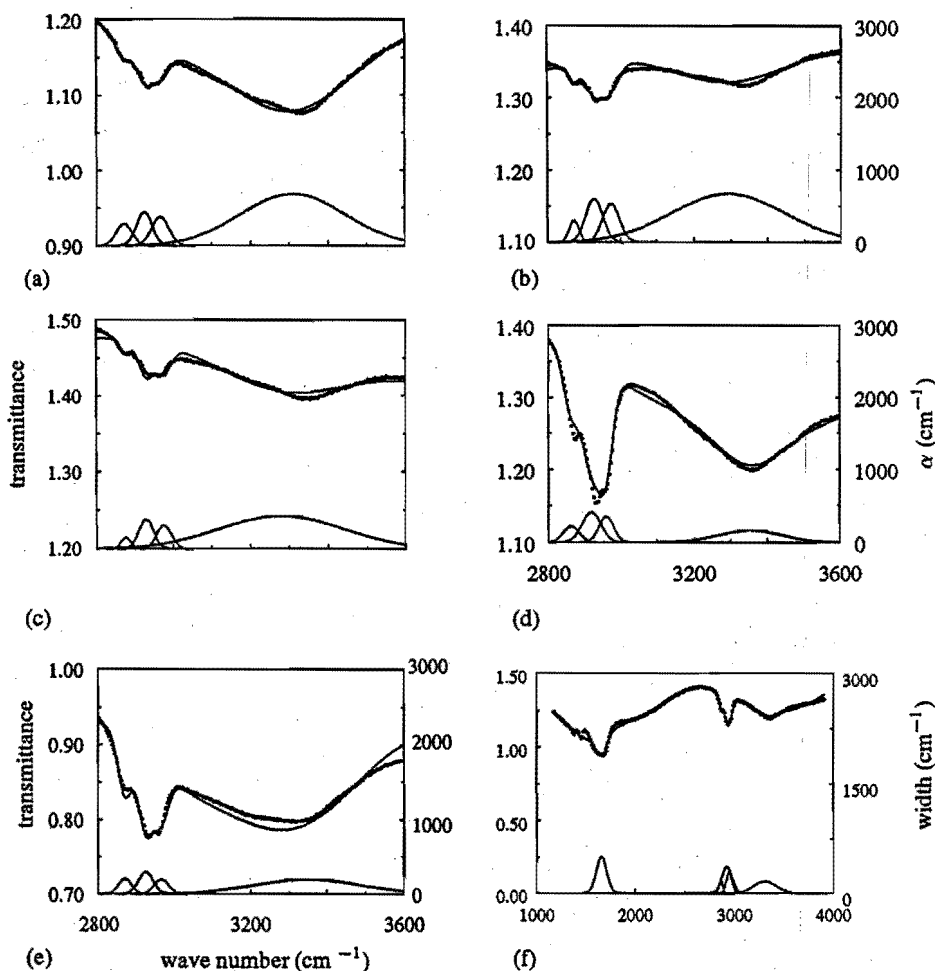


Figure 6.8: IR absorption bands as a function of toluene flow rate, (a-e) 0.08, 0.15, 0.23 0.30, 0.37 ml min^{-1} resp.; (f) Example of a wide wavenumber-range fit of interference fringes and absorption bands (spectrum (d)).

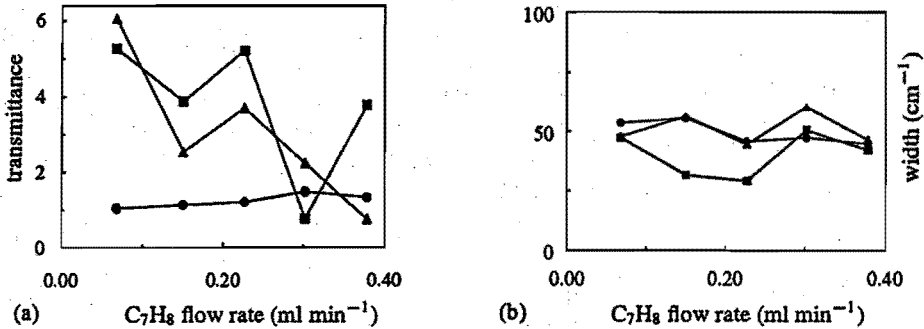


Figure 6.9: Integrated intensity ratios (a) and widths (b) as a function of toluene flow rate. Legend for figure (a): \bullet , A_{2920}/A_{2970} , \blacksquare , $A_{1580}/A_{2920+2970}$, \blacktriangle , $A_{3300}/A_{2920+2970}$. Legend for fig. (b): \square , \circ , \triangle widths of the 2875, 2920 and 2975 cm⁻¹ band respectively.

resulted in a thick (8.1 μm) film with a good adhesion to glass and silicon substrates (trial H3). From the ellipsometry data a refractive index of 1.55 and an optical band gap of 2.2 eV (with $G=600 \text{ cm}^{-1/2} \text{ eV}^{-1/2}$) were determined. Optically the films have are yellow transparent, confirming this value for the optical gap. Similar results have been reported in [33]. In the IR spectrum of the film the $sp^2\text{CH}$ bands at 3000-3050 cm⁻¹, the $sp^1\text{CH}$ band at about 3300 and the $sp^2\text{C}=\text{C}$ band at about 1650 cm⁻¹ were not present anymore. The admixture of hydrogen favours the formation of a diamond-like (sp^3 dominated) structure.

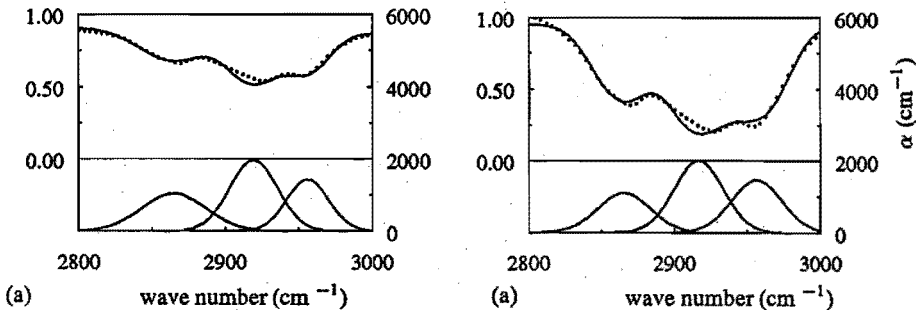


Figure 6.10: Measured transmittance (left hand axis) and fitted IR absorption bands (right hand axis) for two films of different thickness, deposited with equal reactor settings. Gas flow rates: 0.151 ml min⁻¹ C_7H_8 and 3 cm³ s⁻¹ H_2

The actual values of the absorption coefficients (order 500-1000 cm⁻¹) are of the same order as those reported by [32] for RF-deposited a-C:H layers. Unfortunately almost no reports exist in literature how the deconvolution actually

has been carried out.

In principle the exact number density of bondings C_H (and also C_c) per cm^2 can be calculated from the absolute values of the absorption coefficients, and in this way a density determination should be possible. To this end following formula (e.g. [34]) can be used:

$$C_H = A_s \int \frac{a_\nu}{\nu} d\nu, \quad (6.11)$$

with A_s the oscillator strength, ω the wavenumber. The value of A_s can be averaged over the three CH_x modes and is then $\sim 10^{21} \text{ cm}^{-2}$. It should be noted that a_ν is the dimensionless absorptance, that is the absorption coefficient α_ν times the thickness d . Substituting the absorption coefficient yields the number of C-H bondings per cm^3 . Rather low values of the order of 10^{22} cm^{-3} are then obtained. The C-C vibrations are lying in the range $700\text{-}1500 \text{ cm}^{-1}$ [11], and in the actual measurements which were done on Si substrates, we could not resolve them due to severe absorption of this substrate material. In [11], densities for a-C:H layers of typically 2 g cm^{-3} are reported, with comparable values for the C-H absorption bands.

6.4.2 The H/C and O/C ratio

In Fig. 6.11 some typical carbon/oxygen-ERDA spectrum are shown. The high intensity peak at about 5.4 MeV is caused by elastically recoiled C-atoms which pass through the thin foil detector and only reflect a relative impression of the layer thickness. The inelastically recoiled carbon atoms (with emission of gamma radiation) exhibit an intensity distribution independent of the recoil energy, showing that the film is homogeneous over the thickness.

The slowly decreasing low-energy edge of especially the carbon signals may be due to layer thickness or density variations (besides the gradual decrease seen for the reference oxide which is due to the variation of the cross-section with energy). In Fig. 6.12 some typical hydrogen-ERDA spectra are shown. In this technique depth profiling can only be obtained using the variation in electronic stopping of the incoming α -particles with depth and the subsequent variation in energy of the recoiled hydrogen ions.

In the actual case the layer thickness was insufficient and the measured signals reflect the apparatus profile of the detection device. From the ERDA signals integrated over the energy channels, the total numbers of carbon, oxygen and hydrogen atoms per cm^2 and their ratios were obtained. In Table 6.4 the results are summarized. It should be noted that for these measurements special thin films of about 50 nm were required. So the trials denoted in column I of Table 6.4

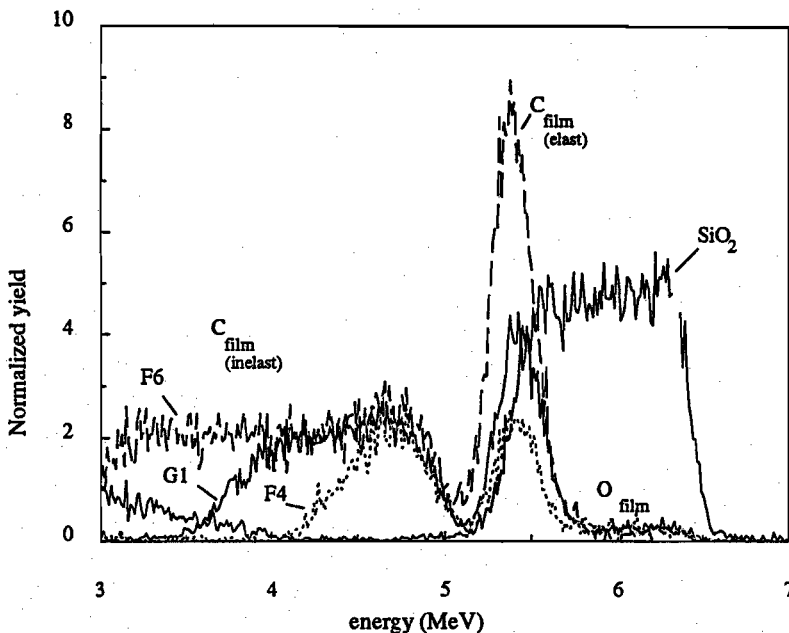


Figure 6.11: Carbon-oxygen ERDA spectra of samples F4, F6 and G1; the deposition settings can be found in Table 6.2.

are reproductions of those in Table 6.2, with a very short deposition time (a few seconds). The ERDA measurements for carbon and oxygen were carried out one day after the deposition of the films. Also the hydrogen content for samples E9, H2 and F2 was measured on this day. The hydrogen content for the other samples were measured three months later. As a check the H/C ratio of sample F1 was determined in both measurement sequences. The H/C ratios were 0.56 and 0.57 respectively, giving an indication for the good reproducibility of the results of this technique and indicating that the hydrogen contents in the film do not change substantially in time.

It can be observed that with increasing acetylene flow (F1 through F6) the hydrogen contents in the film decrease, indicating an increasing diamond-like character, in agreement with the IR results and [13]. The absolute values of the H/C ratio are much lower than in [13], where a different measurement technique was applied. The actual values around 0.5 are of the same order as, again, the ones reported in [11]. In general the oxygen content in the films is small. The high oxygen content for sample E9, deposited with toluene as a feed gas may be due to the relatively large amount of double and triple carbon bonds in the deposited film.

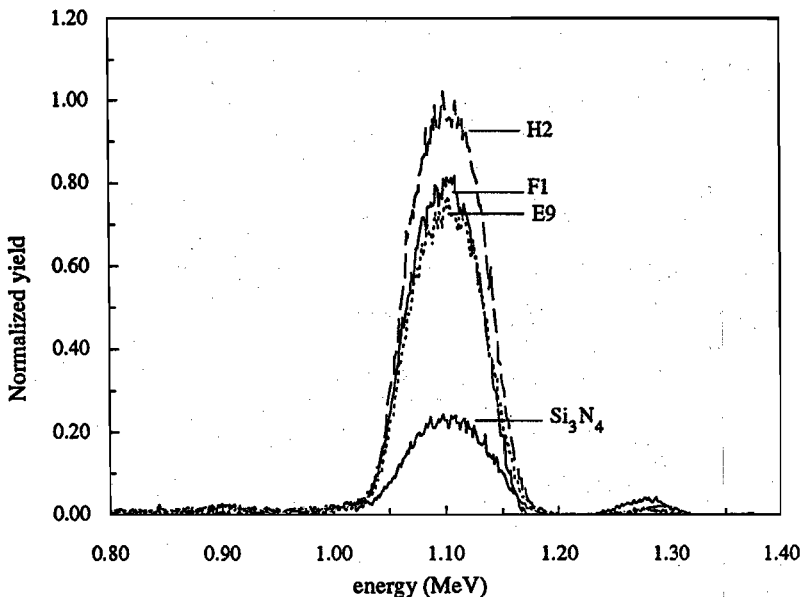


Figure 6.12: Hydrogen ERDA spectra of samples E9, F1 and H2; the deposition settings can be found in Table 6.2.

Table 6.4: Results of the ERDA measurements; flow rates C_7H_8 in $ml\ min^{-1}$, other (gas) admixtures in $cm^3\ s^{-1}$

sample	feed gas + flow rate	C number ($10^{15}\ cm^{-2}$)	O number ($10^{15}\ cm^{-2}$)	H number ($10^{15}\ cm^{-2}$)	O/C	H/C
F1	0.9 C_2H_2	300	4.5	168	0.015	0.56, 0.57
F4	3.6 C_2H_2	830	25	374	0.030	0.45
F6	10.8 C_2H_2	2400	36	860	0.015	0.36
G1	10.8 C_2H_2 + 14 H_2	1600	43	400	0.027	0.25
E9	0.151 C_7H_8	290	64	156	0.22	0.54
H2	0.151 C_7H_8 + 3 H_2	480	37	210	0.076	0.44

By exposure to air these are easily oxidized. Possibly, the oxygen was already dissolved in the liquid toluene. The actual values of the atomic number densities per cm^2 allow a rough estimate of the density of the films. Assuming a film thickness of $\sim 50\ nm$ densities of the order of $2\ g\ cm^{-3}$ can be calculated. (So by introducing a coupling factor, the results of the IR transmission measurements and the ERDA measurements can in principle be related to each other.)

6.4.3 The application of a-C:H layers for anti-corrosion protection

Morphology

In Table 6.5 a survey of the trials aimed at producing a good anti-corrosive film is given. The films of trials D5 through D12 were deposited on large substrates (25 cm²) and these were analyzed by several techniques. Only for D7 a stable thermocouple temperature measurement was obtained, but the other temperatures can be estimated to be of the same order (depending on deposition time).

Table 6.5: Survey of the trials for the protective applications; {CH₄}, {C₂H₂}, {C₇H₈} and {CF₄} gas flows, d and R_d film thicknesses and growth rates from the GDOS experiments, t_d duration of deposition, V_{bias} negative bias voltage applied during the first 20 seconds of the actual deposition, T_s deposition temperature. For trial sequence A, and trials D1-D4: chamber pressure $p_c = 10^2$ Pa area of deposition $A_d \simeq 25$ cm² For trials D5-D12: $p_c = 22$ Pa, $A_d \simeq 100$ cm²; All other reactor settings are given in Table 6.1

Sample	{CH ₄ } cm ³ s ⁻¹	{C ₂ H ₂ } cm ³ s ⁻¹	{C ₇ H ₈ } ml.min ⁻¹	{CF ₄ } cm ³ s ⁻¹	d (μ m)	R_d (nms ⁻¹)	t_d (s)	V_{bias} (V)	T_s ($^{\circ}$ C)
D5	-	3.0	-	-	610	12	50	-70	70
					450	9			
D6	-	6.0	-	-	910	30	30	-110	-
					850	28			
D7	-	3.0	-	0.6	1060	21	50	-50	110
					830	17			
D8	-	6.0	-	0.6	1000	22	45	-50	-
					830	19			
D9	-	1.5	-	0.6	480	8	60	-100	-
					270	4			
D10	-	-	1.0	-	540	9	60	0	-
					450	7			
D11	-	-	0.4	-	1440	36	40	-800	-
					2090	52			
D12	-	-	0.4	0.6	60	0.5	120	-10	-

Results of the GDOS

In 6.13 a representative GDOS spectrum (trial D7) is shown. As the sputter rate is approximately constant for films of the same type it can be deduced that ~ 1 μ m of an amorphous carbon film is sputtered in about 35 s. From this relation estimates of the growth rates and thickness (also given in Table 6.5) of the films for all trials were deduced.

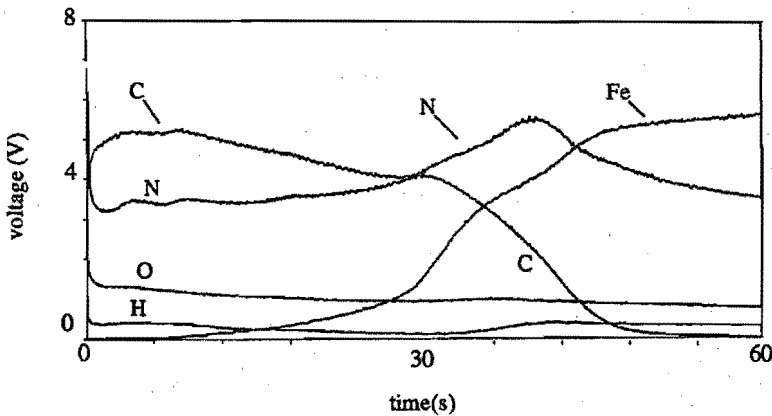


Figure 6.13: Typical GDOS spectrum of a coated CRS substrate (trial D7)

The GDOS spectrum reveals some specific features. The peak in the first seconds is an artefact during stabilization of the ion beam. Contaminations of oxygen, nitrogen and iron can be observed. The former are probably due to residual gases in the deposition chamber. The latter is an indication for a porous film. Physical sputtering of iron during the deposition of the film is very unlikely, in view of the low bias potential and thus ion energy. Furthermore, it can be observed that the substrate film interface appears diffuse. This may be a consequence of the third pretreatment, the bombarding of the substrate with carbon ions, but more likely it is also an artefact of the method (rapid simultaneous sputtering of film and substrate). All the films deposited on CRS substrates showed a spectrum similar to the one of Fig. 6.13, with slight variations in contaminations signals. In films deposited at a higher chamber pressure, these signals were relatively lower (as expected).

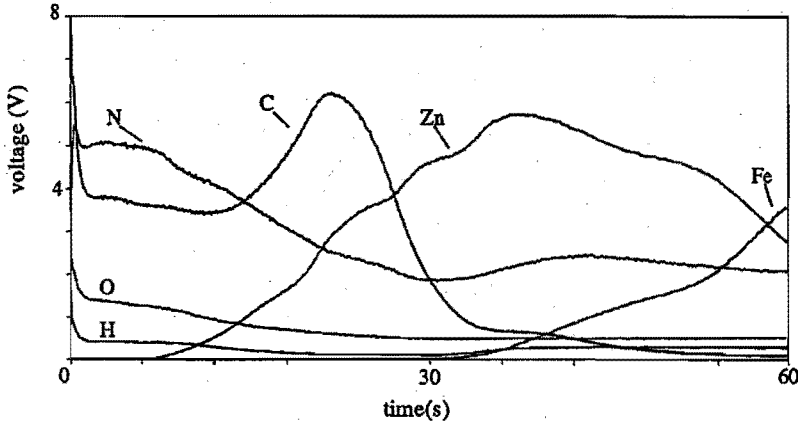


Figure 6.14: Typical GDOS spectrum of a coated EGS substrate (trial D7)

In Fig. 6.14 a spectrum, representative for the same film grown on a EGS substrate is shown. Besides the contaminations already mentioned, a very interesting feature can be observed in the substrate-film region. The carbon signal shows a strong increase. This may be an artefact due to the conductivity of the substrate. However, secondly, it appeared that the film deposited on EGS was always thinner than the one deposited on CRS. A possible explanation for these two features may be the following: It is known [23] that both films are covered with a thin insulating oxide layer. Upon cleaning with a hydrogen plasma, on zinc this oxide is easily reduced. On CRS however the insulating oxide layer is still present. This leads us to distinguish deposition on an conducting and an insulating substrate. The deposited carbon layer also has a high resistivity [5]. The observed two phases layer on zinc, can be explained by a two phase deposition proces: at first on the conductive substrate, and secondly, when the resistance (both electrically as well as thermally) of the growing film has reached a specific limit, a phase transition to another type of material, with relatively less carbon. The deposition on CRS is always one-phased, because the substrate is insulating everywhere. The influence of the conductivity of the substrate can also be responsible for the difference in observed film thickness. As the absolute value of this difference is approximately constant, it points to some kind of incubation time before the growth starts on zinc. This indicates that the initial growth is different on CRS and CGS substrates. This initial growth mechanism may have a large influence on the subsequent growth mode of the bulk of the film.

Results of the TOFSIMS

In Fig. 6.15 the positive ion spectrum for a typical a-C:H film, deposited with a low flow of methane (low Q -factor) is shown. The predominant radicals are C_2H_3 , C_3H_5 and with a lower intensity C_2H_5 , C_3H_7 , C_4H_9 . The former two point to an abundance of carbon sp^2 bondings over the sp^3 bonding form, indicated by the latter three species. This finding is consistent with the results of the IR measurements (Sec. 6.4.1), which shows that low Q -factor films are polymer-like. Some aromatic compounds were found, too. In the negative ion spectrum of this film large contaminations of oxygen and nitrogen, and also chlorine and sulphur were found. As TOFSIMS is a surface sensitive technique, this points to reactions of the top layer with the ambient air. It is known that on the surface of plasma deposited films, highly reactive free radicals exist [31].

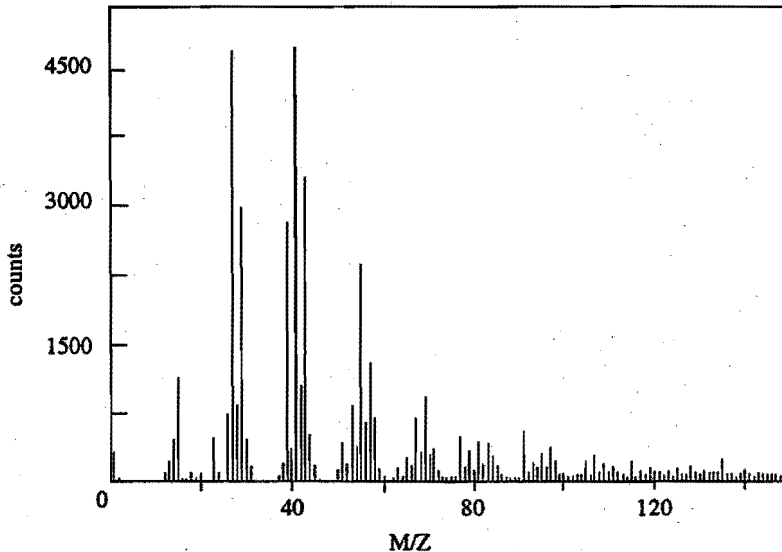


Figure 6.15: Positive ions TOFSIMS spectrum of a typical polymer-like a-C:H coating on a CRS substrate.

Results of the corrosion performance studies

In Fig. 6.16 the qualitative results of the corrosion tests are shown. Bare CRS substrates show severe corrosion in this test (Fig. 6.16 (d)). The corrosion performance of films deposited with an argon/hydrocarbon plasma (e.g. D11) is moderate, particularly of the thicker films. Most probably the adhesion is a very important factor, in addition to the film composition. Samples D7 and D9

showed a good corrosion resistance. These were films produced with acetylene, with additional admixture of CF_4 .

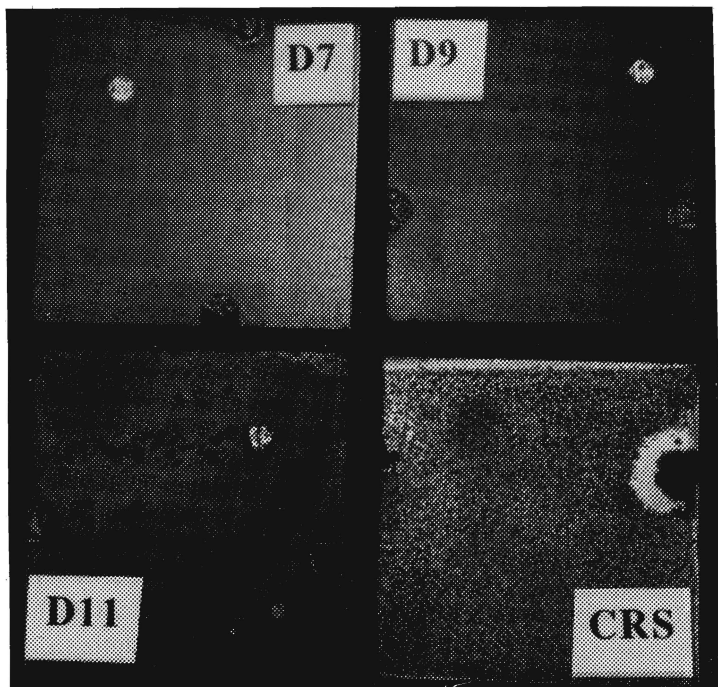


Figure 6.16: Photographs of the result of the corrosion tests on the $a\text{-C:H,F}$ coated CRS substrates. The deposition parameters are given in Table 6.5.

In Fig. 6.17 the IR transmission spectrum of the film (on a silicon reference sample) is given. It appeared that no C-H bands at all could be observed anymore. Only the C-F band at 1200 cm^{-1} [35] is present. Recent XPS measurements [13] indicated a content of 10 at. % F, 3% N, 12 % O and 75 % C for sample D7(CRS) [36]. In Fig. 6.18 the growth rates on the CRS substrates are shown as a function of the hydrocarbon flow rate.

Upon the admixture of CF_4 the following peculiarities can be noted:

- 1 As shown by the IR spectrum of CF_4 assisted deposition of $a\text{-C:H}$ films, the saturation of the carbon bondings was partially provided by F-atoms, in stead of H-atoms.
- 2 The growth rate was of the same order as in the trials without CF_4 addition (compare ▼ and ▲ in Fig. 6.18).

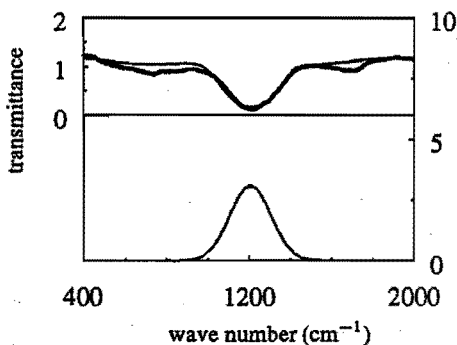


Figure 6.1: Typical IR absorption spectrum of an a-C:F film deposited with a flow of $0.15 \text{ ml}\cdot\text{min}^{-1}$ C_7H_8 and $0.4 \text{ cm}^3\text{s}^{-1}$ CF_4 .

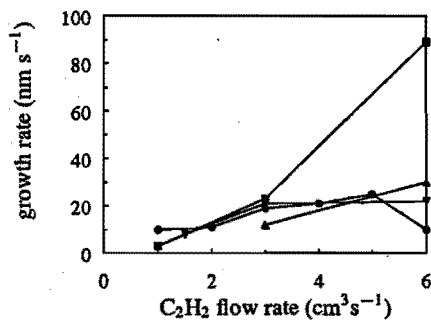


Figure 6.2: Growth rate (on CRS substrates) as a function of various gas admixture flow rates, \blacksquare C_2H_2 , \bullet CH_4 ($p_c=100$ Pa); \blacktriangle , \blacktriangledown C_2H_2 , $\text{C}_2\text{H}_2 + 0.6 \text{ CF}_4$ ($p_c = 22$ Pa);

The first effect may have led to lower internal stresses, diminishing the delamination, which would lead to direct exposure of the CRS substrate to the environment. The second finding implies that, in order to obtain a high quality film, the growth rate does not necessarily have to be reduced. It is possible that the growth mechanism for films deposited with the use of CF_4 is different, due to the simultaneous etching by the fluorine radicals. This hypothesis is supported by recent findings in the deposition of a-Si:H films [37]. It is assumed that the initial growth of the film plays a major role in determining the subsequent growth type of the bulk of the film. A model is suggested in which the initial growth occurs from specific preferential gettering sites of the arriving species (in analogy to the nucleation sites in diamond deposition). The initial growth sites expand to islands, and subsequently to columnar grains. In the course of the deposition these grains coalesce to each other, causing grain boundaries with unsaturated bonding types or even dangling bonds. In the a-Si:H samples an aging effect was observed, coinciding with an increasing oxygen content in the layer. This is probably due to the gradual diffusion of ambient air through the voids, throughout the film, and subsequent passivation of the grain boundaries. It is assumed that this island growth model is also valid for the growth of a-C:H films, and that the voids promote the diffusion of corrosive species to the substrate. The effect of the addition of an etching gas like fluorine may be that, the initial growth takes place in a different mode, leading to a morphology, different from the grain model. A more gradual and regular structure may arise, without or with lesser voids, minimizing the diffusion of ambient air. These assumptions are confirmed

by the following SEM images. In Fig. 6.19 (a) and (b) images of samples D11 and D7 are shown. It can be observed that For D11 a typical columnar growth mechanism has occurred, which starts from island growth and results in columnar grains with curved domes on top [38]. Typical for this growth mode are the existence of voids. In Fig. (b) for the film deposited with CF_4 a very smooth film was obtained. It appears that by the simultaneous etching by the fluorine radicals and subsequent reorganization of the nanostructures, the columnar growth mechanism can be avoided, resulting in more uniform and dense film. The mobility at the surface can be enhanced by a chemical mechanism [39].

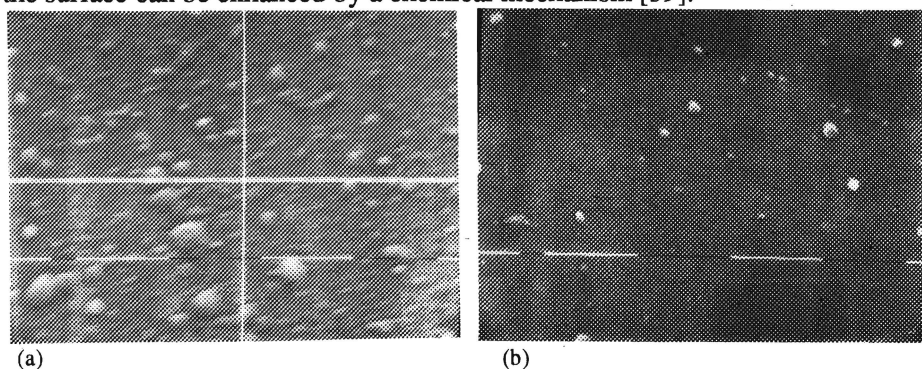


Figure 6.19: SEM micrographs of an $a\text{-C:H}$ (D11) and an $a\text{-C:F}$ film. A striking difference in the film structure can be noticed. The deposition parameters are given in Table 6.5.

As a third explanation it is possible that the substrate is etched by the fluorine radicals creating a very high density of defects, which act as gettering sites, resulting in a more uniform growth (the growth of separate columns is avoided). A similar effect can be noted in the case of diamond deposition. An enhanced nucleation density on the substrate ends up in the growth of smoother films. In [40] successful utilization of the high etching activity of fluorine on silicon for this purpose was reported.

Results of the EIS

As a second diagnostic, the films on the EGS samples were subjected to EIS. In Fig. 6.20 the modulus of the impedance $\|Z\|$ is shown as a function of frequency, for various trials. The values for the best CRS films D7 and D9 however, were not very high. The highest value was obtained for film D11. On CRS the protection of this film was low. This is another indication that the growth mode on CRS is deviating from that on EGS. D11 was produced with a relatively high flow of toluene (low Q -factor), without admixture of fluorines. The only factor deviating from other trials using toluene, was the bias in the pretreatment stage. This

reached a high value of ~ -800 V, because of the increased impedance of the plasma in this trial. This was a consequence of the loss of ionization, caused by the high concentration of hydrocarbons in the plasma [13].

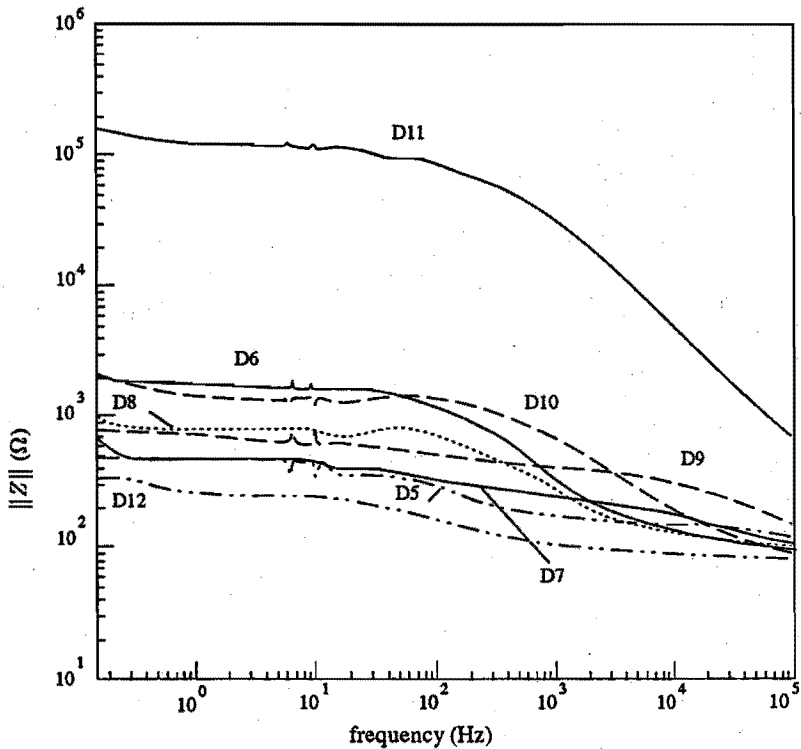


Figure 6.20: EIS spectra of *a-C:H* coatings on EGS substrates

Acknowledgement

The authors gratefully acknowledge the collaboration with Armco research and technology (Middletown, Ohio) and related companies, where all measurements of the corrosion study were carried out. Furthermore they wish to thank all the persons of the Dept. of Physics, Eindhoven University of Technology who were involved in the other measurements, that is the Surface Physics group (Prof. H.H. Brongersma), Dr. C. Flipse, P. Musters, the Nuclear Physics group (Prof. M.J.A. de Voigt), Dr. L. v. Ijzerendoorn, and the group EPG Plasmaphysics (Prof. F.J.

de Hoog), Ir. H. den Boer, and, Dr. J.J. Beulens of Daresbury Laboratory (U.K.) for the XPS measurements.

Conclusions

- 1 Polymerlike and diamond-like a-C:H coatings can be deposited at high rates of tens of nm s^{-1} with the cascaded arc deposition technique using acetylene as a carrier gas. Using toluene results in the deposition of polymer-like films.
- 2 In general the adhesion of the films deposited with toluene is very good, even for films with a thickness of several μms . Using acetylene results in films with a moderate adhesion.
- 3 The optical and protective properties of the films can be improved, by admixing additional feed gases to the argon/hydrocarbon plasma. Addition of hydrogen leads to more diamond-like films with a larger optical band gap.
- 4 To obtain a high corrosion resistance, the addition of a fluorine containing gas is beneficial. Three explanations are offered:
 - The deposition process consists of a simultaneous etching and redeposition, to an enhanced surface mobility and resulting in a different growth morphology is obtained, leading to a less porous structure.
 - By etching of the substrate by the fluorine radicals the number of sites from which the growth starts, is increased, resulting in a more uniform growth.
 - the incorporation of fluorines leads to a-C:F films with much smaller internal stresses compared with those of a-C:H films, and avoiding delamination.
- 4 Different film types were obtained on the CRS and the EGS substrates. This may be reduced to a distinction in insulating and conductive substrate type. On the latter the initial growth appears to require an incubation period, and the actual film growth occurs in two phases, phase I on the conductive substrate, and phase II on the insulating a-C:H layer of phase I.
- 5 A thick film is not a prerequisite for a high corrosion resistance. On the contrary, these films tend to delaminate from the substrate, providing gangways for the corrosive species.
- 6 The initial growth of the a-C:H film may be the main factor in determining the subsequent film morphology. By controlling the growth in this stage, the film properties for the bulk of the film may be predefined.

Bibliography

- [1] H.K. Yasuda, *Plasma Polymerization*, Academic Press, Orlando, Florida, (1985).
- [2] J.J. Beulens, G.M.W. Kroesen, D.C. Schram, C.J. Timmermans, P.C.N. Crouzen, H.Vasmel, H.J.A. Schuurmans, C.B. Beijer and J. Werner, *J. Appl. Polym. Sci.: Appl. Polym. Symp.*, **46**, 527, (1990).
- [3] D.C. Schram, G.M.W. Kroesen and J.J. Beulens, *J. Appl. Polym. Sci.: Appl. Polym. Symp.*, **46**, 1, (1990).
- [4] A. Sabata, W.J. van Ooij, D. Surman and H.K. Yasuda, paper submitted to *Progr. Org. Coat.*, febr. (1993).
- [5] J. Mort and F. Jansen (eds.), *Plasma Deposited Thin Films*, CRC Press, Inc., Boca Raton, Florida, (1986).
- [6] H-C. Tsai and D. B. Bogy, *J. Vac. Sci. Technol. A*, **5** (6), 3287, (1987).
- [7] N.I. Chapliev, T.V. Kononenko, A.A. Smolin and V.E. Strelnitsky, *Surf. Coat. Technol.*, **47**, 730, (1991).
- [8] H. Lorenz, J. Lechner and I. Eisele, *Surf. Coat. Technol.*, **47**, 746, (1991).
- [9] K. Enke, *Mater. Sci. Forum*, **52/53**, 559, 1990.
- [10] S. Orzesko, Bholu N. De, J.A. Woollam, J.J. Pouch, S.A. Alterovitz and D.C. Ingram, *J. Appl. Phys.*, **64** (8), 4175, (1988).
- [11] B. Dischler, A. Bubbenzer and P. Koidl, *Appl. Phys. Lett.*, **42** (8), 636, (1983).
- [12] G.M.W. Kroesen, *Ph.D. Thesis*, Eindhoven University of Technology, (1988).
- [13] J.J. Beulens, *Ph. D. thesis*, Eindhoven University of Technology, (1991).
- [14] A.J.M. Buuron, J.J. Beulens, P. Groot, J. Bakker and D.C. Schram, *Thin Solid Films*, **212**, 282, (1992).
- [15] R.M.A. Azzam and N.M. Bashara, *Ellipsometry and Polarized Light*, North Holland, Amsterdam, The Netherlands, (1977).
- [16] E. Hecht and A. Zajac, *Optics*, Addison Wesley Publishing Company inc. Inc., seventh printing, (1982).
- [17] J. Robertson, *Adv. Phys.*, **35** (4), 317, (1986).
- [18] D.R. McKenzie, D. Muller, B.A. Pailthorpe, E. Kravtchinskaia Z.H. Wang, D. Segal, P.B. Lukins, P.J. Martin P.D. Swift, G. Amaratunga, P.H. Gaskell, and A. Saeed, *Diamond and Related Materials*, **1**, 51, (1991).

- [19] R.M.A. Driessens, *Master's Thesis*, Eindhoven University of Technology, (1993).
- [20] D.A.G. Bruggeman, *Ann. Phys. (Leipzig)*, **24**, 636, (1935).
- [21] E. Verhoeven, *Internal Report Eindhoven University of Technology*, VDF/NT 92-13, (1992).
- [22] B. Dischler, A. Bubenzler and P. Koidl, *Sol. State Comm.*, **48** (2), 105, (1983).
- [23] W.J. van Ooij, A. Sabata and Ih-Houng Loh, *Eur. Symp. Mod. Pass. Films Rel. Res. Loc. Corr., Paris, Febr. 15-17, 1993*, Proc. Inst. Mater., EFC Series. (Eur. Fed. Corr.), (1993).
- [24] J.C. Pivin and T.J. Lee, *Diamond and Related Materials*, **1**, 650, (1992).
- [25] J. Koskinen, *J. Appl. Phys.*, **63** (6), 2094, (1988).
- [26] A.T.M. Wilbers, *Ph. D. Thesis*, Eindhoven University of Technology, (1991).
- [27] H.F. van Rooijen, *Master's thesis*, Eindhoven University of Technology, (1992).
- [28] L. van IJzerdoorn, H.A. Rijken, S.S. Klein and M.J.A. de Voigt, *Appl. Surf. Sci.*, **70/71**, 58, (1993).
- [29] W.-K. Chu, J.W. Mayer and M.A. Nicolet, *Backscattering Spectrometry*, Academic Press Inc. (London) Ltd., (1978).
- [30] A. Bengtson and L. Danielsson, *Proc. 6th Int. Conf Thin Films, Stockholm (Sweden), August 13-17 (1984)*, Elsevier Sequoia, The Netherlands, 231 (1984).
- [31] W.J. van Ooij and A. Sabata, *Surf. Interface Anal.*, **19**, 101, (1992).
- [32] B. Dischler, R.E. Sah, P. Koidl, W. Fluhr and A. Wokaun, *7th Int. Symp. Plasma Chem.*, C.J. Timmermans (ed.), Eindhoven, (1985).
- [33] M. Rubin, C.B. Hopper, N-H. Cho and B. Bhushan, *J. Mater. Res.*, **5** (11), 2538, (1990).
- [34] F. Fujimoto, *Jpn. J. Appl. Phys.*, **23** (7), 810, (1984).
- [35] J.R. Hollahan, Th. Wydeven and C.C. Johnson, *Appl. Opt.*, **13** (8), 1844, (1974).
- [36] J.J. Beulens, *private communication*, Daresbury Laboratory (U.K.), (1993).
- [37] G. Meeusen and P. Haaland, *private communication*, Eindhoven University of Technology, (1993).
- [38] R. Messier, *J. Vac. Sci. Technol. A*, **4** (3), 490, (1986).
- [39] M.J. Brett, *J. Vac. Sci. Technol. A*, **6** (3), 1749, (1988).
- [40] R. Rudder, *Electronic Letters*, **24**, 1220, (1989).

Summary

This thesis concerns the plasma deposition of carbon materials, ranging from amorphous carbon to the crystalline forms graphite and diamond. As a result of the wide variation in properties, these materials cover an extensive field of potential technological applications.

In the deposition method a cascaded arc plasma is used as a particles source. In the arc channel a thermal argon plasma is generated with an ionization degree of the order of 10 %. The exit of the arc is connected to a vacuum chamber with a relatively low pressure. A hydrocarbon compound is admixed in the plasma and by energy transfer processes from the argon to the hydrocarbon, a beam of argon atoms and ions and (hydro)carbon ions and radicals is created, expanding supersonically into a vacuum chamber. On a substrate placed in this beam, a layer of carbon is deposited. With this method high deposition rates are achieved; in general, the rates are several tens of nanometers per second on areas of some cm^2 for the crystalline carbon forms, to about 100 cm^2 for amorphous carbon. The potential for applications on a large scale of the deposition of carbon films with this method has been studied. Their suitability for thermomechanical, optical and protective applications has been investigated. The properties of each of these materials are dependent on the reactor settings during deposition. A distinction is made between the three forms of plasma deposited carbon, based on some principal differences in their properties.

Graphite has good thermoconductive and thermomechanical properties and is electrically conductive. The plasma deposition of graphite is treated as a possible means for *in situ* repair of erosion damage on the plasma-facing components in a fusion reactor. Amorphous (nanocrystalline graphite) and crystalline graphite are deposited at high rates of several hundreds and several tens of nanometers per second respectively. By experiments with a pulsed, high-power laser it appears that the crystalline types of graphite have the highest thermal shock resistance, with a maximum of 2.8 MJ m^{-2} (in a 10 ms pulse). For the deposition of crystalline graphite the substrate temperature has to be high, typically of the order of $800\text{-}1000 \text{ }^\circ\text{C}$, and the use of acetylene and hydrogen as feed gases is beneficial. Probably the C_2 radicals play an important role.

In contrast with graphite, both amorphous carbon and diamond are electrically insulating. As a result, they are transparent over a wide wavelength range. Furthermore, both diamond and amorphous carbon are hard materials. These properties make them particularly suited to serve as a coating material.

The deposition of diamond has been optimized using a novel type of plasma mixture. Compared to the conventional 1:100:100 methane/hydrogen/argon plasma, the large amount of hydrogen, needed as an agent for preventing the

deposition of other forms of carbon, can be replaced by a small amount of oxygen. The O/C ratio in the plasma typically has to be of the order of 1:1, and the H/C ratio in the plasma can be reduced as far as to an 8:1 ratio. By Raman spectroscopy and Scanning Electron Microscopy (SEM) it appears that the quality of the diamond is high. The maximum deposition rates are of the order of $50 \mu\text{m h}^{-1}$ on some mm^2 . The dependence of the morphology of the crystals on the H/C and O/C ratio in the plasma is discussed. The substrate temperature for diamond deposition with this plasma mixture can be reduced from 1000 to 400 °C, but with a decrease of the growth rate.

Films of amorphous hydrogenated carbon (a-C:H) were deposited onto cooled substrates of silicon, glass and steel (temperature 20-200 °C). High rates of tens of nanometers per second on large areas (up to 100cm^2) were achieved. Compounds used are CH_4 , C_2H_2 , CF_4 , C_7H_8 (toluene), H_2 , and mixtures of these. Aimed at optical applications, several μm 's thick films, with a good adhesion to the substrate were deposited with the use of toluene. With spectroscopic ellipsometry and infrared absorption spectroscopy the optical parameters were determined. The system substrate-film often gives rise to interference fringes in the spectra. An appropriate numerical model is treated, which takes these fringes into account and permits the determination of the refractive index, the band gap and the film thickness. The hydrogen and oxygen content in the films were determined with nuclear recoil techniques. For both the admixture of acetylene and toluene, it appears that the refractive index and the amount of diamond-like bonds increases, while the band gap and the hydrogen content decrease. The most relevant parameter for many optical applications, the band gap, decreases from 2.0 to 1.2 eV. By the admixture of hydrogen in the deposition plasma the films become more diamond-like, while the band gap remains relatively high (1.6 eV).

The initial growth mechanism of amorphous carbon films on steel appears to be different on different types of steel. The conductivity of the substrate is probably an important factor. In order to obtain films with a good corrosion performance, the admixture of a fluorine-containing gas in the hydrocarbon/argon plasma is beneficial. The analysis of the infrared absorption spectra shows that fluorine has been incorporated in these films. From SEM observations it appears that these films have a more uniform and smooth structure than a-C:H films.

By means of absorption spectroscopy an important plasma physical aspect of the present method has been investigated, *viz.* the role of argon metastables in the excitation transfer to the admixed species. An experimental set up using a cascaded arc as a continuum light source with optical multichannel detection is presented. Some specific aspects in employing these components for absorption spectroscopy are treated. Measurements were done on the strong argon lines in the range between 790 and 860 nm, and on the 656.3 nm H_α line. An efficient

numerical method, using Abel integration in stead of Abel inversion has been developed for obtaining radial density and temperature profiles. For a pure argon plasma the densities of the Ar($3p^54s$) metastable and resonance states are of the order of 10^{18} to 10^{16} m^{-3} at a pressure of 40 Pa. These densities are lower than the ion densities by a factor of 10, which implies that the contribution of the metastables to the energy transfer from argon tot the admixed hydrocarbon is small. The decay of the densities of the metastables and resonance states in axial direction is also calculated using a local quasi steady state model. It appears that the (re)capture of resonance radiation is keeping up the population density of the argon $4s$ states.

The effect of the admixture of various gases used in deposition experiments, such as hydrogen, oxygen and methane on the Ar($4s$) metastable and resonant states is treated. The addition of methane has only a slight effect on the argon $4s$ densities. This means that energy transfer from argon metastables to methane is not particularly effective. The addition of hydrogen to an argon plasma leads to a rapid disappearance of the argon $4s$ states in an indirect way, by the decrease of the argon ion density upon hydrogen admixture.

Samenvatting

Dit proefschrift behandelt het met behulp van een plasma deponeren van koolstofachtige materialen, variërend van amorf koolstof tot de kristallijne vormen grafiet en diamant. Door de brede variatie in eigenschappen hebben deze materialen een uitgebreid veld van mogelijke technologische toepassingen. In de depositiemethode wordt een cascadeboogplasma gebruikt als deeltjesbron. In de boog wordt een thermisch argonplasma gegenereerd, met een ionisatiegraad in de orde van 10%. Een koolwaterstofverbinding wordt toegevoegd aan het plasma en na energie-overdrachtsprocessen van het argon naar de koolwaterstof wordt een bundel van argonatomen en -ionen en kool(waterstof)ionen en -radicalen gecreëerd, die supersoon expandeert in een vacuumvat. Op een ondergrond (het substraat) die in deze bundel wordt geplaatst, wordt een laagje van koolstof gedeponerd. Met deze methode worden hoge depositiesnelheden bereikt; in het algemeen bedragen deze enige tientallen nanometers per seconde op oppervlaktes van enige vierkante centimeters voor de kristallijne vormen, en op oppervlaktes van ongeveer 100 cm² voor amorf koolstof. De mogelijkheid van toepassingen op grote schaal van de depositie van koolstof films met deze methode is onderzocht. De geschiktheid van de lagen voor thermo-mechanische, optische en beschermende toepassingen is onderzocht. Een onderverdeling wordt gemaakt tussen de bovengenoemde drie hoofdvormen van plasma-gedeponerd koolstof, gebaseerd op de verschillen in hun eigenschappen. De eigenschappen van elk van deze materialen zijn afhankelijk van de instellingen van de depositiereactor.

Grafiet heeft een goede warmtegeleiding en uitstekende thermo-mechanische eigenschappen en, is elektrisch geleidend. De plasma-depositie van grafiet wordt behandeld als een mogelijke methode voor *in situ* reparatie van erosieschade aan de componenten in een kernfusiereactor. Amorf (nanokristallijn) en kristallijn grafiet worden gedeponerd met hoge snelheden van respectievelijk enige honderden en enige tientallen nanometers per seconde. Bij experimenten met een gepulste, hoog-vermogen laser blijkt dat de kristallijne grafietvormen de hoogste thermische schokresistentie hebben, te weten maximaal 2.8 MJ m⁻², in een pulsduur van 10 ms. Voor de depositie van kristallijn grafiet moet de substraat temperatuur hoog zijn, typisch in de orde van 800 tot 1000 °C, en is het gebruik van acetyleen als bijmenggas en toevoeging van waterstof bevordelijk. Vermoedelijk spelen C₂ radicalen een belangrijke rol.

In tegenstelling tot grafiet zijn zowel amorf koolstof als diamant elektrisch isolerend. Tengevolge daarvan zijn zij doorzichtig over een groot golflengte gebied. Verder zijn zowel amorf koolstof als diamant harde materialen. Deze eigenschappen maken hen bijzonder geschikt om te dienen als coating materiaal.

De depositie van diamant is geoptimaliseerd voor een nieuw type plasma-

mengsel. Vergeleken met het conventionele 1:100:100 methaan/waterstof/argon plasma kan de grote hoeveelheid waterstof die benodigd is om de depositie van andere vormen van koolstof te verhinderen vervangen worden door een kleine hoeveelheid zuurstof. De O/C verhouding in het plasma moet typisch van de orde 1:1 zijn, en de H/C verhouding kan teruggebracht worden tot de waarde 8:1. Met behulp van Ramanspectroscopie en elektronenmicroscopie blijkt dat de kwaliteit van het diamant goed is. Maximale groeisnelheden liggen in de orde van 50 $\mu\text{m}/\text{uur}$ op een gebied van enige mm^2 . De morfologie van de kristallen als functie van de H/C en O/C verhouding in het plasma wordt besproken. De substraattemperatuur voor diamantdepositie met dit plasmamengsel kan teruggebracht worden van 1000 naar 400 $^{\circ}\text{C}$, maar met verlies van groeisnelheid.

Laagjes van amorf waterstofhoudend koolstof (a-C:H) werden gedeponereerd op gekoelde substraten van silicium, glas and staal (temperatuur 20-200 $^{\circ}\text{C}$). Snelheden van enige tientallen nanometers per seconde en op grote gebieden tot aan 100 cm^2 zijn bereikt. Stoffen die gebruikt worden zijn CF_4 , C_2H_2 , CF_4 , C_7H_8 (tolueen), H_2 en mengsels daarvan. Voor optische toepassingen zijn met het gebruik van tolueen laagjes met een dikte van verscheidene micrometers, met een goede hechting aan het substraat gedeponereerd. Met spectroscopische ellipsometrie en infrarood-absorptiespectroscopie zijn de optische parameters bepaald. Het systeem substraat-laag geeft vaak aanleiding tot interferentie effecten in de gemeten spectra van beide technieken. Een numeriek model wordt behandeld, dat deze effecten verdisconteert en dat de bepaling van de brekingsindex, bandafstand en laagdikte mogelijk maakt. De waterstof- en zuurstofconcentratie in de laagjes zijn bepaald met kernfysische technieken. Voor zowel de bijmenging van acetyleen als die van tolueen blijkt dat de brekingsindex en de hoeveelheid diamantachtige bindingen toeneemt, terwijl de bandafstand en het waterstofgehalte in de laagjes afneemt bij een toenemende koolwaterstof bijmenging in het plasma. De belangrijkste parameter voor veel optische toepassingen, de bandafstand, neemt af van 2.0 naar 1.2 eV. Door waterstof in het depositieplasma bij te mengen worden de laagjes meer diamantachtig, terwijl de bandafstand relatief groot blijft (1.6 eV).

Het initiële groeimechanisme van amorfe koolstoflagen op staal blijkt verschillend te zijn op verschillende types staal. De geleiding van het substraat is waarschijnlijk een belangrijke factor. Om laagjes met een goede roestwerende werking te verkrijgen is het bevordelijk een fluorhoudend gas in het koolwaterstof/argon plasma bij te mengen. Analyse van de infrarood absorptiespectra toont aan dat in deze laagjes fluor wordt ingebouwd. Uit SEM observaties blijkt dat dergelijke laagjes een meer uniforme en egale opbouw hebben dan a-C:H laagjes.

Door middel van absorptiespectroscopie is een belangrijk plasmafysisch as-

pect van de depositiemethode onderzocht, te weten de rol van argon-metastabielen in de overdracht van excitatie-energie van argon naar de bijgemengde stoffen. Een experimentele opstelling met een cascadeboog als continuïtmlichtbron en met een optische meerkanaals detectie wordt gepresenteerd. Enige specifieke aspecten van het gebruiken van deze componenten voor absorptiespectroscopie worden behandeld. Metingen zijn verricht aan de sterke argon lijnen in het golflengtegebied tussen 790 en 860 nm, en aan de 656.3 nm H_{α} lijn. Een efficiënte numerieke methode, die gebruikt maakt van Abel-integratie in plaats van Abel-inversie is ontwikkeld voor het verkrijgen van radiale dichtheid- en temperatuurprofielen. Voor een plasma van puur argon zijn de dichtheden van de Ar(4s) metastabiele en resonante toestanden in de orde van 10^{18} tot 10^{16} m^{-3} bij een druk van 40 Pa. Deze dichtheden zijn een factor 10 lager dan de ionendichtheden, hetgeen betekent dat de bijdrage van de metastabielen tot de energieoverdracht van argon naar de bijgemengde koolwaterstofverbinding klein is. De afname van de metastabiele en resonante toestandsdichtheden in axiale richting wordt ook berekend met een lokaal quasi-evenwichtsmodel. Het blijkt dat de invangst van straling de bezetting van de argon 4s toestanden op peil houdt. Het effect van de bijmenging van de verschillende gassen die gebruikt worden in de depositie-experimenten, zoals waterstof, zuurstof en methaan op de dichtheden van de argon 4s metastabiele en resonante toestanden wordt behandeld. De bijmenging van methaan heeft slechts een gering effect op de argon 4s dichtheden. Dit betekent dat de energie-overdracht van argon-metastabielen naar methaan niet effectief is. De bijmenging van waterstof in een argonplasma leidt indirect tot een aanzienlijke afname van de argon 4s dichtheden, door de aantasting van de argon-ionendichtheid in dit geval.

Dankwoord

Om alle mensen te bedanken die of een of andere wijze hebben bijgedragen aan de tot stand koming van dit proefschrift zijn twee pagina's nu eigenlijk niet meer voldoende. Dat aantal staat in geen verhouding tot hun werkelijke inbreng.

Allereerst wil ik mijn promotor Daan Schram danken voor de gelegenheid die hij me gegeven heeft om in zijn groep promotie-onderzoek te verrichten. Zijn stimulerende en originele ideeën, en zijn positieve kritiek hebben in belangrijke mate bijgedragen aan de resultaten die in dit proefschrift beschreven worden. Voorts ben ik hem dankbaar voor de grote mate van vrijheid die hij me geboden heeft zowel bij planning als uitvoering, waarbij hij nooit de menselijke kant uit het oog verloor. Mijn co-promotor Richard van de Sanden wil ik bedanken voor zijn begeleiding en intensieve betrokkenheid bij het onderzoek, vooral wat betreft de spectroscopie, en voor het nauwgezet corrigeren van dit proefschrift. Hetzelfde geldt Djoomart Otorbaev, voor wat betreft het spectroscopische gedeelte van dit promotie-werk.

De mensen die ik vervolgens wil bedanken zijn de technische medewerkers van onze groep, zonder wier kunde en degelijkheid dit werk onmogelijk tot stand was gekomen. Ries van de Sande, die ik nogal eens met een haastklus overviel die nog sneller alweer uitgevoerd was. De technici die in belangrijke mate hebben bijgedragen aan de goed werkende opstelling, Ton Kiers en Herman de Jong, Ton voor zijn uitstekende besturingsprogramma en Herman voor zijn uiterst kundige en breed onderbouwde hulp, of beter leiding, bij de uitlijning. Bertus Hüsken, de onmisbare (letterlijk) computerspecialist, die voor een crash zijn hand niet omdraait (tot voor kort...). Daarnaast wil ik ook Marius en zijn collega's bedanken voor de degelijke uitvoering van de technische klussen. Vervolgens veel dank aan Johan Wevers die mij de weg heeft gewezen in kleine oorzaken-grote gevolgen land van Latex, en ook Danny Benoy.

Sjaak Beulens, die mij wegwijs heeft gemaakt in het depositie-onderzoek, zijn werk was ook in belangrijke mate de basis, waarop ik heb voortgebouwd. Met name de opbouw van de spectroscopie-opstelling is voor een groot deel in zijn promotie uitgevoerd. Daarbij wil ik ook Gerrit Kroesen bedanken, in wiens promotiewerk de basis voor het depositie-onderzoek is gelegd, en tevens voor de toepassing en de programmatuur van de ellipsometrie en John Gielen, die als mijn opvolger ook heeft meegewerkt aan de laatste experimenten.

Jeanne wil ik graag bedanken voor het vlotte administratieve werk, en haar positieve en relativerende inbreng.

Vervolgens wil ik de mensen bedanken die een en ander ook financieel mogelijk hebben gemaakt, om te beginnen de mensen van het vroegere NET-project en die van ECN Petten, die onze groep in het contract voor het grafietproject

hebben betrokken, te weten Prof. C.H. Wu van NET en Dr. B. v.d. Schaaf van ECN petten. Naast een wetenschappelijke uitdaging op een zeer boeiend terrein betekende dit project de financiële basis voor dit promotie- onderzoek. Dhr. G. Pasmans die daarna de voortzetting van mijn contract waarborgde, dank ik. Jaap van der Laan, Pieter Groot en Co Bakker van ECN Petten, die mijn wetenschappelijke collega's waren en met wie het zeer prettig werken was, en die de laser thermische schoktesten en de foto's (in hfst. II en III) hebben verzorgd. Vervolgens de twee bedrijven die op soortgelijke wijze tot een ondersteuning en stimulering van het onderzoek in onze groep hebben bijgedragen, te weten Shell Amsterdam met als afgezant Paul Crouzen, en DSM Geleen, Dr. R. Hardeveld. Daarnaast werden interessante uitdagingen aangegeven door de firma's Armco (Middletown (USA)) en Hauser (Venlo) door resp. Dr. W.J. van Ooij en Dr. Münz. De firma Armco en aanverwante instituten wil ik bedanken voor het uitvoeren van de metingen over corrosiewering. De spectroscopiemetingen in hoofdstuk IV waren mogelijk door de steun van Electricité de France. In het kader van het Erasmus uitwisselingsproject kwam Christian Chauveau van de Université d'Orsay stage doen, gevolgd door een student uit Bari, Gianfranco Claudio (p...m...). Beide Erasmus studenten hebben voor een groot deel de diamant depositie uitgevoerd, en daarvoor, en voor de prettige samenwerking wil ik hen graag bedanken.

Tenslotte wil ik iedereen bedanken voor de fijne en stimulerende sfeer waarin ik heb mogen werken: Zhou Qing, mijn zeer verdraagzame kamergenoot, Bart en Joost, ook nog voor hun ondersteuning in de laatste fase, Danny en Frank, idem, Ralph, Richard, John, Hans, Mark, Gijs, Jeanne, Daan en Sjaak, en de mensen van de parallelgroep, en met name Hans, ook nog voor de metingen. Verder alle studenten en buitenlandse gasten, en dan met name Gerard, Rene en Rene, Jeroen, Djoomart, Sergej en Peter, die ook op de meest onmogelijke tijden aanwezig waren, en met wie het prettig werken was. Verder wil ik graag Ruth Gruyters bedanken voor het maken van een aantal mooie plaatjes, de mensen van de repro, en de conciërges.

Natuurlijk was dit werk nooit tot stand gekomen zonder de inbreng van mensen in mijn persoonlijke omgeving in de afgelopen jaren. Ik wil afsluiten met mijn vrienden te bedanken voor hun steun, en, mijn ouders, aan wie dit werk is opgedragen.

Curriculum vitae

15 juni 1957 geboren te Roosendaal

- mei 1975 Eindexamen gymnasium- β ,
Norbertuscollege, Roosendaal
- 23 maart 1983 Ingenieursexamen Technische Natuurkunde,
Technische Universiteit, Eindhoven
- 15 augustus 1983 Vervangende dienstplicht (als programmeur),
- 1 maart 1985 Afd. Gynaecologie en Verloskunde,
St. Lambertus ziekenhuis, Helmond
- oktober 1985 Onderzoekswerk voor Pulsarr, Eindhoven
- maart 1986 (Dr. R.Rosado)
- september 1986 (avond)studie Autonome Vormgeving,
-juni 1988 Akademie voor Industriële Vormgeving Eindhoven
- oktober 1988 Programmeerwerk voor Fa. Roossen
- mei 1989 (Geluidstechniek), Helmond
- 15 augustus 1989 - Wetenschappelijk medewerker,
Afdeling Technische Natuurkunde,
Technische Universiteit, Eindhoven,
o.l.v. Prof. D. Schram.

STELLINGEN

behorend bij het proefschrift

PLASMA DEPOSITION OF CARBON MATERIALS

door

A.J.M. Buuron

1 oktober 1993

1

Bij de depositie van dunne lagen met behulp van expanderende thermische plasma's spelen ionen een belangrijke rol. Voor een volledige beschrijving van het depositieproces moeten in de bestaande chemische en thermodynamische evenwichtsmodellen dan ook de invloed van geladen deeltjes en afwijkingen van evenwichtsbezettingen in rekening gebracht worden.

C.H. Kruger, *Plasma Chem. Plasma Process.*, 9, 4, 435 (1989).

Dit proefschrift, hoofdstuk 5.

2

Het supersone gedeelte van een expanderend boogplasma kan niet gemodelleerd worden door middel van een lokaal botsing-stralingsmodel. Het transport van metastabielen is dominant t.o.v. de lokale productie- en destructieprocessen.

Dit proefschrift, hoofdstuk 4.

3

Het depositierendement van expanderende thermische plasma's en de kwaliteit van het gedeponeerde materiaal kunnen worden opgevoerd door de keuze van een geschikte depositiegeometrie waarin recirculatiecellen boven het substraat gecreëerd worden.

4

Door de gepulste bijmenging van een etsend medium zoals waterstof, zuurstof of een halogeen in een depositieplasma kan de etsen-deponerenbalans, vereist voor de depositie van kristallijne materialen, geoptimaliseerd worden.

5

Absorptiespectroscopie met behulp van een thermische boog als continuümlichtbron kan benut worden als een snelle on-line methode voor de detectie van luchtverontreiniging.

6

Volledig Lokaal Thermodynamisch Evenwicht in een plasma met een hoge elektronendichtheid wordt verstoord door het toenemende stralingsverlies in de flanken van de resonante spectraallijnen.

7

De opvatting dat de aarde de enige planeet in het heelal is waarop intelligent leven tot ontwikkeling gekomen is, getuigt van een hedendaagse vorm van antropocentrisme.

8

De huidige algemene fixatie op korte-termijn economisch voordeel berokkent ernstige schade aan de fundamentele behoeften van de mensheid en haar omgeving, en is bovendien op termijn onrendabel.

9

De opkomende trend om wetenschappelijke onderzoekers in dienst te nemen als "vrijwilliger" met behoud van wachtgeld of uitkering is bedreigend voor de fundamentele wetenschap als onafhankelijk maatschappelijk instituut.

10

In de huidige wereld waarin overbevolking het primaire probleem dreigt te worden, dient kinderbijslag niet langer als een vanzelfsprekende voorziening te gelden.

11

Ondanks de toenemende vergrijzing van de bevolking wordt daar niet op ingespeeld met het aanbrengen van adequate voorzieningen voor de verzorging en de verpleging van behoeftige ouderen. Het gevolg daarvan is dat meer en meer levenspartners hun laatste levensjaren in gedwongen scheiding moeten doorbrengen.

12

Het percentage studiestakers kan teruggedrongen worden door de invloed van tijdelijke of secundaire motieven bij de studiekeuze te verminderen. Dit kan bereikt worden door de standaard toepassing van meer betrouwbare indicatoren zoals een beroepskeuzetest.

13

Plasmatechnologie biedt perspectieven voor toepassing in de kunstwereld. Niet alleen kan chemisch etsen vervangen worden door plasma-etsen, maar bovendien betekent het plasma-schilderen (het zogenaamde "plasma-painting") voor de (beter-gesitueerde) kunstenaar een revolutionair nieuw medium.

14

Met het veelvuldige gebruik van het †-teken bij auteursnamen in publicaties worden de ongezonde kanten van het bedrijven van wetenschap overdreven.